



**VICTORIA  
UNIVERSITY**

**SPECTROSCOPY OF THULIUM  
DOPED SILICA GLASS**

by

**David Allan Simpson  
BSc.(Hons) Victoria University**

Submitted for the degree of

**Doctor of Philosophy**

Optical Technology Research Laboratory

School of Electrical Engineering

Victoria University

Australia

*This thesis is dedicated to my mother Wendy Simpson.*

*“The physicist Leo Szilard once announced to his friend Hans Bethe that he was thinking of keeping a diary: ‘I don’t intend to publish. I am merely going to record the facts for the information of God.’ ‘Don’t you think God knows the facts?’ Bethe asked. ‘Yes’ said Szilard. ‘He knows the facts, but He does not know this version of the facts.’”*

Hans Christian von Baeyer, *Taming the Atom*

# ABSTRACT

## SPECTROSCOPY OF THULIUM DOPED SILICA GLASS

by David Allan Simpson

The increasing demand for bandwidth in optical fibre communication systems has prompted a significant research effort into developing efficient fibre based optical amplifiers at operating wavelengths neighbouring the erbium-doped fibre amplifier. Of the possible candidates, thulium-doped fibre amplifiers appear best suited to serve this need with amplification available from 1460 to 1530 nm. However, the current limitation with these devices is that the amplifying transition can only provide sufficient gain when doped into host materials with relatively low phonon energies. The ultimate goal for thulium-doped amplifiers is to incorporate the ion into a host material which can be easily integrated into standard communication systems without compromising gain; this thereby involves, to some degree, a silica based host material. To date, optical amplification in the telecommunication S-band using thulium-doped silica fibres has been inefficient due to the high phonon energy associated with Si-O bonds in the glass. This work undertakes a systematic study on the effects of network modifiers on the S-band amplifying transition in an effort to improve the radiative quantum efficiency in silica based glasses. To this end, the techniques employed in this investigation included modifying the glass network with elements which may act to reduce the local phonon energy surrounding the thulium ( $\text{Tm}^{3+}$ ) ion and co-doping the  $\text{Tm}^{3+}$  ions with sensitising ytterbium ( $\text{Yb}^{3+}$ ) ions.

The network modifying technique was successful in improving the quantum efficiency of the S-band transition, with  $\text{Al}_2\text{O}_3$  being the most effective network modifying element. The incorporation of 9 mol% of  $\text{Al}_2\text{O}_3$  resulted in a 260% increase in the quantum efficiency of the S-band amplifying transition, when compared to pure silica glass. The other network modifying elements studied included germanium, antimony and tin, and although variations in the shape and position of certain energy

transitions were observed in comparison to the alumino-silicate glasses, no significant improvements to the S-band amplifying transition were observed. A limited  $\text{Tm}_2\text{O}_3$  concentration study also provided details about the mechanisms affecting the  $^3H_4$  manifold population under direct and in-direct pumping. The direct pumping of the  $^3H_4$  manifold confirmed that the well known cross relaxation process, which originates from the  $^3H_4$  manifold, has little effect on the  $^3H_4$  population for  $\text{Tm}_2\text{O}_3$  concentrations up to 1950 ppm. The first demonstration in silica glass of in-direct pumping of the  $^3H_4$  manifold at 1586 nm was demonstrated using an energy transfer up-conversion process. The energy transfer up-conversion process was established in alumino- and germano-silicate host materials and may provide an alternate pumping solution for the S-band amplifier as it acts to increase the population inversion of the amplifying transition.

Promising results were also obtained from the second proposed technique which involved co-doping  $\text{Tm}^{3+}$  with an additional rare earth ion, namely  $\text{Yb}^{3+}$ , in the silica glass host. The spectroscopic measurements established, for the first time in alumino-silicate glass, the double energy transfer mechanism between  $\text{Yb}^{3+}$  and  $\text{Tm}^{3+}$  ions, under 980 nm excitation. The identification of this mechanism in alumino-silicate glass is an important step towards amplification from the  $^3H_4$  manifold of  $\text{Tm}^{3+}$ . The rate equation model developed to describe the up-conversion luminescence from  $\text{Tm}^{3+}$  under 980 nm excitation also established excited state absorption as a populating mechanism of the  $^3H_4$  manifold, thereby identifying two populating mechanisms which act to increase the population inversion of the S-band amplifying transition. The fluorescence lifetime of the lower amplifying  $^3F_4$  manifold was found to increase by a factor of two under 980 nm excitation as a result of the energy transfer from  $\text{Yb}^{3+}$  to  $\text{Tm}^{3+}$  ions. This observation underlines the importance of optimising the efficiency of the second energy transfer up-conversion process as well as the excited state absorption process, in these glass types. Unfortunately, the low  $\text{Tm}_2\text{O}_3$  concentration of the samples used in this investigation prevented the determination of the quantum efficiency of the S-band transition. Solutions to address this shortcoming are discussed in the future directions of this work.

I, David Allan Simpson, declare that the PhD thesis entitled

**“SPECTROSCOPY OF THULIUM DOPED SILICA GLASS”**

is no more than 100,000 words in length, exclusive of tables, figures, appendices, references and footnotes. This thesis contains no material that has been submitted previously, in whole or in part, for the award of any other academic degree or diploma. Except where otherwise indicated, this thesis is my own work.

Signature\_\_\_\_\_

Date\_\_\_\_\_

## ACKNOWLEDGMENTS

Throughout this journey I have had the opportunity and pleasure of meeting and working with many amazing people whom I wish to thank.

First of all, I wish to thank the staff in the School of Electrical Engineering at Victoria University. Your help, assistance and friendship made working at the university a pleasure.

I would particularly like to thank the technical team within the Optical Technology Research Laboratory: Donald Ermel, Hayrettin Arisoy and Abdurrahman Kuzucu. Not only did they provide me with the tools and necessary equipment needed to complete this work, their lively conversations helped to keep my sense of humor and sanity intact.

I would like to extend a big thank you to my principal supervisor Professor Greg Baxter for all of his wisdom, support and friendship throughout my undergraduate and PhD studies. Greg provided me with the fantastic opportunity to work in France with the team at LPMC, for which I am extremely grateful. Although extremely busy, Greg still managed to be there to listen and give advice and support when needed. I would also like to thank Greg for his valuable assistance in preparing this document.

My thanks also extends to my co-supervisor Associate Professor Stephen Collins, who has the unique ability to “drop everything” to have a conversation about work or any other concern, which was extremely helpful on many occasions. I also wish to thank Stephen for his valuable contribution in preparing this document.

I wish to thank my friends and colleagues who have made this journey more enjoyable than I could have imagined. In particular, I would like to thank Bernhard Koziol, Betty Kouskousis and Anbhawa Nand for the good times and late nights spent at Uni. The many helpful discussions and late night pizzas were much appreciated.

I also wish to thank my two closest colleagues and friends Dr. Thinh Nguyen and Dr. Steven Trpkovski, for all their help and support throughout this long journey. I would particularly like to thank Thinh for taking me under his wing in the early days and teaching me the tricks of the trade. And to Steve thanks for the endless laughs and games of table tennis, you certainly made the experience enjoyable.

I am also extremely grateful to the team at the LPMC, in Nice France, in particular, Dr. Bernard Dussardier, Dr. Gerard Monnom, Dr. Wilfried Blanc and Dr. Basile Faure. I thoroughly enjoy working with your group and the many help discussions we had. I also enjoyed the alcoholic beverages consumed on the Promenade des Anglais!

I would also like to thank the team at my new place of employment, Quantum Communications Victoria, for their support in the final stages of completing this work. In particular, I would like to thank Dr. Shane Huntington for giving me the freedom and time required to finish the write up.

To my mentor and friend Keith Gibbs I wish to extend a big thank you. This thesis would not have been possible without you. You are a pleasure to work with, I thoroughly enjoyed all of the discussions we had and I am grateful to you for getting so actively involved in this research, your infinite spectroscopic knowledge and enthusiasm has transformed the way I view and conduct research and for that I am also extremely grateful.

Finally, I would like to thank the most important people in my life. To my partner Claire Rollinson, thank you for all of your love, support and patience you have given me over the past eight years, I could not have done this without you. To my mum Wendy, who has been a constant source of inspiration to me throughout my life and has encouraged and supported me to no end, I thank you. And to my dad Laurie, sister Julianne and my nephews and nice, Joel, Brodie and Erin, thank you for all of your love and support and for believing in me.

# CONTENTS

<b>1</b>	<b>Introduction</b>	<b>1</b>
1.1	Optical communication . . . . .	1
1.2	Amplification in the S-band . . . . .	6
1.2.1	Semi-conductor optical amplifiers . . . . .	6
1.2.2	Raman amplifiers . . . . .	7
1.2.3	Thulium-doped fibre amplifiers . . . . .	8
1.3	Scope of thesis . . . . .	10
<b>2</b>	<b>Spectroscopy of rare earth ions</b>	<b>15</b>
2.1	Electronic structure . . . . .	16
2.2	Radiative transitions . . . . .	18
2.3	Non-radiative transitions . . . . .	20
2.4	Energy level broadening mechanisms . . . . .	22
2.5	Ion-ion interactions . . . . .	24
2.5.1	Cross relaxation . . . . .	24
2.5.2	Energy transfer up-conversion . . . . .	26
2.5.3	Excited state absorption . . . . .	26
2.5.4	Sensitised luminescence . . . . .	26
2.5.5	Fluorescence quenching . . . . .	27
2.6	Thulium . . . . .	27
2.6.1	$^3F_4$ manifold . . . . .	30
2.6.2	$^3H_5$ manifold . . . . .	31
2.6.3	$^3H_4$ manifold . . . . .	31
2.6.4	$^3F_{2,3}$ manifolds . . . . .	32
2.6.5	$^1G_4$ manifold . . . . .	33
2.7	Ytterbium . . . . .	33
<b>3</b>	<b>Experimental arrangements and techniques</b>	<b>35</b>
3.1	Absorption characteristics of rare earth doped optical fibres . . . . .	35
3.2	Rare earth ion concentration in optical fibres . . . . .	37
3.3	Refractive index profiles . . . . .	38
3.4	Fluorescence lifetime measurements . . . . .	40
3.5	Steady state luminescence intensities . . . . .	44
3.6	Luminescence spectra . . . . .	44
<b>4</b>	<b>Thulium-doped silica fibres</b>	<b>46</b>
4.1	Introduction . . . . .	46
4.2	Fabricated fibre samples . . . . .	49
4.3	Absorption measurements . . . . .	51

4.3.1	Alumino-silicate fibres . . . . .	51
4.3.2	Germano-silicate fibres . . . . .	54
4.3.3	Co-doping effects of Sb and Sn . . . . .	56
4.4	Fluorescence lifetime measurements . . . . .	58
4.4.1	Alumino-silicate fibres . . . . .	58
4.4.2	Germano-silicate fibres . . . . .	64
4.4.3	Co-doping effects of Sb and Sn . . . . .	64
4.5	Tm <sup>3+</sup> concentration . . . . .	65
4.5.1	<sup>3</sup> H <sub>4</sub> manifold . . . . .	66
4.5.2	<sup>3</sup> F <sub>4</sub> manifold . . . . .	68
4.6	Energy transfer up-conversion in Tm <sup>3+</sup> -doped silica fibres . . . . .	71
4.6.1	Alumino-silicate fibres . . . . .	75
4.6.2	Germano-silicate fibres . . . . .	81
4.7	Conclusion . . . . .	88
<b>5</b>	<b>Fluorescence decay in Tm<sup>3+</sup> -doped silica fibre</b>	<b>90</b>
5.1	Introduction . . . . .	90
5.1.1	Direct transfer . . . . .	91
5.1.2	Fast diffusion . . . . .	92
5.1.3	Diffusion-limited relaxation . . . . .	93
5.1.4	Inhomogeneous broadening effects . . . . .	95
5.2	Single exponential fitting . . . . .	98
5.2.1	<sup>3</sup> H <sub>4</sub> manifold . . . . .	98
5.2.2	<sup>3</sup> F <sub>4</sub> manifold . . . . .	99
5.3	Stretched exponential fitting . . . . .	101
5.3.1	<sup>3</sup> H <sub>4</sub> manifold . . . . .	101
5.3.1.1	Tm <sup>3+</sup> concentration . . . . .	102
5.3.1.2	Alumino-silicate fibres . . . . .	103
5.3.1.3	Germano-silicate fibres . . . . .	105
5.3.2	<sup>3</sup> F <sub>4</sub> manifold . . . . .	106
5.3.2.1	Tm <sup>3+</sup> concentration . . . . .	107
5.3.2.2	Alumino-silicate fibres . . . . .	108
5.3.2.3	Germano-silicate fibres . . . . .	110
5.4	Conclusion . . . . .	111
<b>6</b>	<b>Thulium:Ytterbium-doped silica fibres</b>	<b>113</b>
6.1	Absorption measurements . . . . .	114
6.2	Up-conversion luminescence under 980 nm excitation . . . . .	115
6.2.1	<sup>3</sup> F <sub>4</sub> manifold . . . . .	120
6.2.2	<sup>3</sup> H <sub>4</sub> manifold . . . . .	123
6.2.3	<sup>1</sup> G <sub>4</sub> manifold . . . . .	123
6.2.4	810 nm luminescence . . . . .	131
6.3	Fluorescence lifetime measurements . . . . .	132
6.3.1	Direct pumping . . . . .	132
6.3.1.1	<sup>2</sup> F <sub>5/2</sub> manifold . . . . .	132
6.3.1.2	<sup>3</sup> F <sub>4</sub> manifold . . . . .	135

6.3.1.3	$^3H_4$ manifold . . . . .	136
6.3.2	In-direct pumping . . . . .	136
6.3.2.1	$^3F_4$ manifold . . . . .	137
6.3.2.2	$^1G_4$ manifold . . . . .	140
6.3.2.3	810 nm luminescence . . . . .	142
6.4	Conclusion . . . . .	146
<b>7</b>	<b>Conclusion</b>	<b>147</b>
7.1	Suggestions for future work . . . . .	149
<b>A</b>	<b>List of publications</b>	<b>163</b>
A.1	Journal articles . . . . .	163
A.2	International Conferences . . . . .	163
A.3	National Conferences . . . . .	164

## LIST OF FIGURES

1.1	Schematic diagram of an optical fibre . . . . .	1
1.2	Attenuation of silica glass . . . . .	3
2.1	Lanthanide series of the elements . . . . .	15
2.2	Non-radiative decay rate as a function of energy gap for various glass and crystal host materials . . . . .	22
2.3	Example of a cross relaxation process in $\text{Tm}^{3+}$ . . . . .	25
2.4	Simplified energy level diagram of $\text{Tm}^{3+}$ in silica glass . . . . .	28
2.5	Simplified energy level diagram of $\text{Yb}^{3+}$ in silica glass . . . . .	34
2.6	Absorption and emission spectrum of $\text{Yb}^{3+}$ -doped silica glass . . . . .	34
3.1	Attenuation measurement system used to obtain the absorption spec- trum of rare earth doped fibres. . . . .	36
3.2	Refractive index profile of a $\text{Tm}^{3+}$ -doped alumino-silicate fibre . . . . .	38
3.3	Refractive index profile of a $\text{Tm}^{3+}$ -doped germano-silicate fibre . . . . .	39
3.4	Fluorescence lifetime experimental arrangement . . . . .	43
3.5	Fitting of the fluorescence decay waveforms . . . . .	43
3.6	Experimental arrangement used to measure the counter-propagating luminescence from an optical fibre sample . . . . .	44
4.1	Tetrahedral structure of $\text{SiO}_4^{2-}$ . . . . .	47
4.2	3 - dimensional structure of $\text{SiO}_2$ . . . . .	48
4.3	Absorption spectra of $\text{Tm}^{3+}$ -doped alumino-silicate fibres . . . . .	52
4.4	${}^3F_4$ peak absorption wavelength as a function of $\text{Al}_2\text{O}_3$ concentration . . . . .	53
4.5	Absorption spectra of $\text{Tm}^{3+}$ -doped germano-silicate fibres . . . . .	55
4.6	Absorption spectra of $\text{Tm}^{3+}$ -doped alumino-silicate fibres co-doped with $\text{Sb}_2\text{O}_3$ and $\text{SnO}_2$ . . . . .	57
4.7	Trend of the ${}^3H_4$ lifetime with increasing $\text{Al}_2\text{O}_3$ concentration . . . . .	59
4.8	Trend of the ${}^3F_4$ lifetime with increasing $\text{Al}_2\text{O}_3$ concentration . . . . .	60
4.9	${}^3F_4$ and ${}^3H_4$ manifold lifetime as a function of $\text{Al}_2\text{O}_3$ concentration . . . . .	60
4.10	Trend of the ${}^3H_4$ lifetime with increasing $\text{Tm}_2\text{O}_3$ concentration . . . . .	66
4.11	Trend of the ${}^3F_4$ lifetime with increasing $\text{Tm}_2\text{O}_3$ concentration . . . . .	69
4.12	${}^3F_4$ lifetime as a function of incident pump power . . . . .	70
4.13	Possible energy transfer up-conversion process which can occur from the ${}^3F_4$ manifold . . . . .	71
4.14	Counter-propagating up-conversion luminescence spectrum of a $\text{Tm}^{3+}$ -doped silica fibre pumped at 1586 nm . . . . .	74
4.15	Possible energy transfer processes that can populate the ${}^3H_4$ manifold in $\text{Tm}^{3+}$ -doped silica glass . . . . .	75
4.16	Log-log plot of the up-conversion luminescence at 810 nm vs. 1800 nm luminescence for three alumino-silicate fibres . . . . .	76

4.17	Semi-log plots of the luminescence from the $^3H_4$ manifold in $Tm^{3+}$ -doped alumino-silicate fibres under direct and in-direct excitation . . .	79
4.18	Single exponential fit to the measured decay from the $^3H_4$ manifold of the alumino-silicate sample Al-8, under in-direct excitation at 1586 nm. . . . .	81
4.19	Log-log plot of the up-conversion luminescence at 810 nm vs. 1800 nm luminescence for two germano-silicate fibres . . . . .	82
4.20	Semi-log plots of the luminescence from the $^3H_4$ manifold in $Tm^{3+}$ -doped germano-silicate fibres under direct and in-direct excitation . . .	84
4.21	Measured relative intensities of the up-conversion luminescence from the $Tm^{3+}$ -doped germano-silicate and alumino-silicate samples under 1586 nm pumping . . . . .	86
5.1	Single exponential fit to the $^3H_4$ manifold decay of a $Tm^{3+}$ -doped alumino-silicate fibre . . . . .	98
5.2	The first four e-fold times from the $^3H_4$ manifold decay of $Tm^{3+}$ -doped alumino-silicate fibres . . . . .	99
5.3	Single exponential fit to the $^3F_4$ manifold decay of a $Tm^{3+}$ -doped alumino-silicate fibre . . . . .	100
5.4	The first four e-fold times from the $^3F_4$ manifold decay of $Tm^{3+}$ -doped alumino-silicate fibres . . . . .	100
5.5	Stretched exponential fit to the $^3H_4$ manifold decay of a $Tm^{3+}$ -doped alumino-silicate fibre . . . . .	101
5.6	Stretched exponential power for the $^3H_4$ manifold as a function of $Al_2O_3$ concentration . . . . .	104
5.7	Stretched exponential fit to the $^3F_4$ manifold decay of a $Tm^{3+}$ -doped alumino-silicate fibre . . . . .	107
5.8	Stretched exponential power for the $^3F_4$ manifold as a function of $Al_2O_3$ concentration . . . . .	109
6.1	Absorption spectrum of a $Tm^{3+}/Yb^{3+}$ -co-doped silica fibre. . . . .	114
6.2	Double energy transfer between $Yb^{3+}$ and $Tm^{3+}$ ions under 980 nm excitation . . . . .	116
6.3	Proposed mechanism for the population of the $^1G_4$ manifold via a three step energy transfer up-conversion process in $Tm^{3+}/Yb^{3+}$ -co-doped silica fibre under 980 nm excitation. . . . .	117
6.4	Counter-propagating luminescence spectra of the $Tm^{3+}/Yb^{3+}$ -co-doped fibre samples under 980 nm excitation . . . . .	118
6.5	1060 nm intensity as a function of incident pump power for a $Tm^{3+}/Yb^{3+}$ -co-doped silica fibre . . . . .	119
6.6	Log-log plot of the 1800 nm luminescence from $Tm^{3+}$ vs. the 1060 nm luminescence from $Yb^{3+}$ , for three $Tm^{3+}/Yb^{3+}$ -co-doped alumino-silicate fibres . . . . .	120
6.7	Energy manifold labelling for the rate equation analysis of the $Tm^{3+}/Yb^{3+}$ -co-doped system . . . . .	121

6.8	Log-log plot of the 475 nm luminescence from $\text{Tm}^{3+}$ vs. the 1060 nm luminescence from $\text{Yb}^{3+}$ , for three $\text{Tm}^{3+}/\text{Yb}^{3+}$ -co-doped aluminosilicate fibres . . . . .	124
6.9	Spectral overlap of the $\text{Yb}^{3+}$ fluorescence from the ${}^2F_{5/2} \rightarrow {}^2F_{7/2}$ transition with the calculated ESA transitions of $\text{Tm}^{3+}$ . . . . .	127
6.10	Log-log plot of the 475 nm luminescence from $\text{Tm}^{3+}$ vs. the 1060 nm luminescence from $\text{Yb}^{3+}$ , for three $\text{Tm}^{3+}/\text{Yb}^{3+}$ -co-doped aluminosilicate fibres . . . . .	129
6.11	Log-log plot of the 810 nm luminescence from $\text{Tm}^{3+}$ vs. the 1060 nm luminescence from $\text{Yb}^{3+}$ , for three $\text{Tm}^{3+}/\text{Yb}^{3+}$ -co-doped aluminosilicate fibres . . . . .	131
6.12	Semi-log plot of the normalised fluorescence decay from the ${}^2F_{5/2}$ manifold under 980 nm excitation . . . . .	133
6.13	Fluorescence lifetime of the ${}^2F_{5/2}$ manifold as a function of incident pump power at 980 nm for three $\text{Tm}^{3+}/\text{Yb}^{3+}$ -co-doped aluminosilicate fibres . . . . .	134
6.14	Semi-log plot of the normalised fluorescence decay from the ${}^3F_4$ manifold under 980 nm excitation . . . . .	137
6.15	Semi-log plot of the normalised fluorescence decay from the ${}^1G_4$ manifold under 980 nm excitation . . . . .	140
6.16	Semi-log plot of the normalised fluorescence decay at 810 nm under 980 nm excitation . . . . .	143

## LIST OF TABLES

1.1	Tm <sup>3+</sup> -doped fibre amplifiers developed to date . . . . .	9
2.1	Fluorescence lifetimes and multi-phonon decay rates for the energy manifolds of Tm <sup>3+</sup> -doped silica glass . . . . .	29
2.2	Fluorescence lifetimes and multi-phonon decay rates for the energy manifolds of Tm <sup>3+</sup> -doped ZBLAN glass . . . . .	29
3.1	Experimental configuration for the measurement of the fluorescence lifetime of the excited states of Tm <sup>3+</sup> and Yb <sup>3+</sup> . . . . .	41
4.1	Core dopants of the Tm <sup>3+</sup> -doped silica fibres . . . . .	49
4.2	Measured peak absorption wavelengths and FWHMs for the energy manifolds of Tm <sup>3+</sup> -doped alumino-silicate fibres . . . . .	52
4.3	Measured peak absorption wavelengths and FWHMs for the energy manifolds of Tm <sup>3+</sup> -doped germano-silicate fibres . . . . .	55
4.4	Measured peak absorption wavelengths and FWHMs for the energy manifolds of Tm <sup>3+</sup> -doped alumino-silicate fibres co-doped with Sb <sub>2</sub> O <sub>3</sub> and SnO <sub>2</sub> . . . . .	57
4.5	1/e lifetime of the <sup>3</sup> H <sub>4</sub> and <sup>3</sup> F <sub>4</sub> manifolds in Tm <sup>3+</sup> -doped alumino-silicate fibre . . . . .	59
4.6	1/e lifetime of the <sup>3</sup> H <sub>4</sub> and <sup>3</sup> F <sub>4</sub> manifolds for the Tm <sup>3+</sup> -doped germano-silicate fibres . . . . .	64
4.7	1/e lifetime of the <sup>3</sup> H <sub>4</sub> and <sup>3</sup> F <sub>4</sub> manifolds for the Tm <sup>3+</sup> -doped alumino-silicate fibres co-doped with Sb <sub>2</sub> O <sub>3</sub> and SnO <sub>2</sub> . . . . .	65
4.8	Percentage decrease in the <sup>3</sup> F <sub>4</sub> manifold lifetime over the pump power range 3 - 16.4 mW . . . . .	70
4.9	Energy mismatch of the two energy transfer up-conversion processes from the <sup>3</sup> F <sub>4</sub> manifold in various Tm <sup>3+</sup> -doped crystals . . . . .	72
4.10	The fitted ‘slow’ amplitude from the Tm <sup>3+</sup> -doped alumino-silicate fibres . . . . .	80
4.11	The fitted ‘slow’ amplitude from the Tm <sup>3+</sup> -doped germano-silicate fibres . . . . .	85
5.1	Characteristic lifetimes and stretched exponential powers of the <sup>3</sup> H <sub>4</sub> manifold for the Tm <sup>3+</sup> -doped alumino-silicate fibres as a function of Tm <sub>2</sub> O <sub>3</sub> concentration . . . . .	102
5.2	Characteristic lifetimes and stretched exponential powers of the <sup>3</sup> H <sub>4</sub> manifold as a function of Al <sub>2</sub> O <sub>3</sub> concentration . . . . .	104
5.3	Characteristic lifetimes and stretched exponential powers of the <sup>3</sup> H <sub>4</sub> manifold for the Tm <sup>3+</sup> -doped germano-silicate fibres . . . . .	105

5.4	Characteristic lifetimes and stretched exponential powers of the ${}^3F_4$ manifold for the $\text{Tm}^{3+}$ -doped aluminosilicate fibres as a function of $\text{Tm}_2\text{O}_3$ concentration . . . . .	107
5.5	Characteristic lifetimes and stretched exponential powers of the ${}^3F_4$ manifold for increasing $\text{Al}_2\text{O}_3$ concentrations . . . . .	109
5.6	Characteristic lifetimes and stretched exponential powers of the ${}^3F_4$ manifold for the $\text{Tm}^{3+}$ -doped germanosilicate fibres . . . . .	110
6.1	Core dopants of the $\text{Tm}^{3+}/\text{Yb}^{3+}$ -co-doped silica fibres . . . . .	114
6.2	Parameters obtained by fitting the steady state rate equation model to the 475 versus 1060 nm luminescence data . . . . .	129
6.3	Fluorescence lifetimes of the ${}^2F_{5/2}$ manifold under 980 nm excitation .	133
6.4	Fluorescence lifetimes of the ${}^3F_4$ manifold under direct excitation at 1586 nm . . . . .	135
6.5	Fluorescence lifetimes of the ${}^3H_4$ manifold under direct pumping at 780 nm . . . . .	136
6.6	Fluorescence lifetime of the ${}^3F_4$ manifold under in-direct excitation at 980 nm . . . . .	138
6.7	Fluorescence lifetime of the ${}^1G_4$ manifold under in-direct excitation at 980 nm . . . . .	141
6.8	Stretched exponential lifetimes and powers from the ${}^1G_4$ manifold decay under in-direct pumping at 980 nm . . . . .	142
6.9	Amplitude and characteristic lifetimes obtained from the double exponential fit of the 810 nm fluorescence decay under in-direct pumping at 980 nm . . . . .	143

# Chapter 1

## INTRODUCTION

### 1.1 Optical communication

The development of optical fibre communication systems over the past 40 years has revolutionised the way in which the world transmits and receives information. Proposals for optical communication via dielectric waveguides or optical fibres were made almost simultaneously in 1966 by Kao and Hockham [1] and Werts [2]. An optical fibre is a thin glass structure typically the thickness of a human hair. The innermost region of an optical fibre, known as the ‘core’, transmits light while the outer region of the optical fibre, known as the ‘cladding’, prevents light from the core leaking out, as depicted in Figure 1.1.

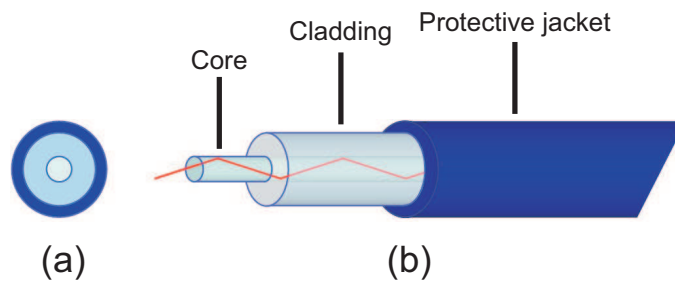


**Figure 1.1:** Schematic diagram of an optical fibre illustrating light being guided along the core: (a) cross section (b) side on view.

The core of an optical fibre is designed in such a way that it has a higher refractive index than the cladding. This is usually achieved by co-doping the silica glass with dopants such as germanium, aluminium, boron or phosphorus. In fibres with large core diameters of the order of 100s of micrometres, the confinement of light is based on total internal reflection at the core/cladding interface. In smaller diameter core fibres of the order of a few micrometres, the confinement relies on establishing a

waveguide. As an optical waveguide, the fibre can support one or more confined transverse modes by which light can propagate along the fibre [3]. Fibres supporting more than one mode are termed multi-mode fibre, whereas fibres which support only one mode are known as single or mono-mode fibre. As little light propagates in the cladding, signals can travel great distances, although impurities in the glass can degrade and attenuate the signal.

Early attempts to fabricate optical fibres in the 1960s produced fibres with extremely high attenuation of  $\sim 1000$  dB/km. However by the 1970s, optical fibre losses had been reduced to below 5 dB/km at mid infra-red wavelengths, which was comparable to the loss in existing co-axial cable technology. Research in the early 1970s into semi-conductor technology coincided with the interest in optical fibres and by the late 1970s research groups had begun to establish complete optical communication systems. The early communication systems were comprised of a semi-conductor laser diode as the light source, multi-mode optical fibre as the transmission medium and a semi-conductor photodiode as a detector. Limitations of such systems included chromatic dispersion or pulse broadening caused by the multi-mode optical fibre and fibre attenuation problems caused by the operating wavelengths (0.8 - 0.9  $\mu\text{m}$ ) which was limited by the range of available light sources.

Throughout the 1970s and early 80s, silica glass was studied in much greater detail, with particular attention being paid to the three mechanisms responsible for attenuation in silica glass fibres: intrinsic absorption, scattering and geometric effects. Intrinsic absorption in silica glass occurs even in its most pure form and is associated with vibrations of chemical bonds such as the silicon-oxygen bond [4]. The minimum intrinsic absorption of silica glass in the infra-red region is highlighted in a typical attenuation spectrum for silica glass shown in Figure 1.2.

Rayleigh scattering of light is one of the aforementioned causes of attenuation in silica glass fibres. The amorphous nature of glass results in localised variations in the density and homogeneity of molecules within the glass. These variations can be

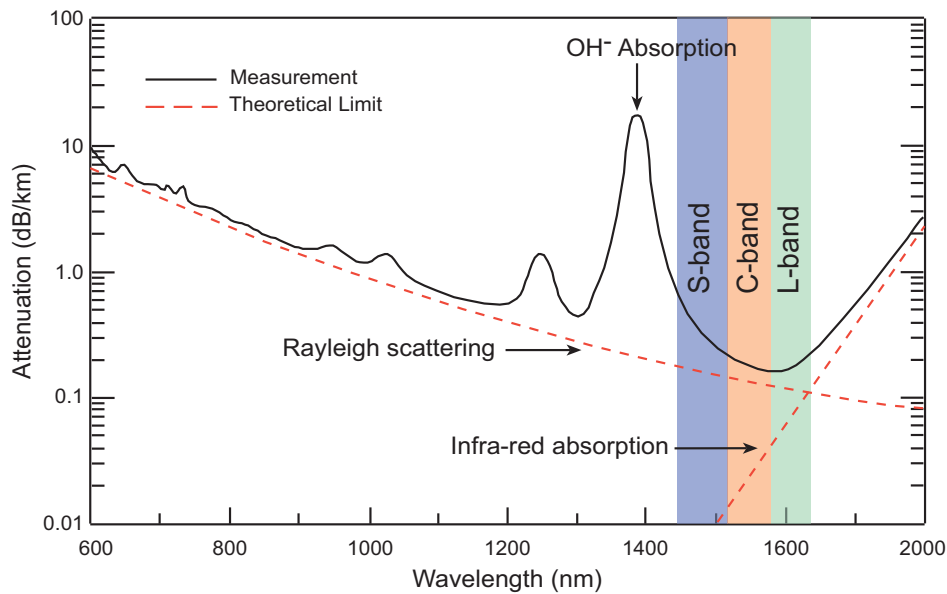


**Figure 1.2:** Attenuation of silica glass [5]. The shaded region represents the 3<sup>rd</sup> telecommunication window, as described in the text. Note: the peak in the measured loss spectrum at 1380 nm is due to impurities known as hydroxyl ions or ( $\text{OH}^-$ ) ions. The resonant frequency of the  $\text{OH}^-$  vibrations occurs at  $2.73 \mu\text{m}$  (outside the transparency range of silica glass), however the overtones and combination bands of this resonance lie around 1380, 1230 and 950 nm [4], consequently care needs to be taken to reduce the number of  $\text{OH}^-$  ions during fabrication.

modelled as small scattering objects whose size is much smaller than the wavelength of light. Lord Rayleigh found that the scattering of light is proportional to  $\lambda^{-4}$ , and hence the loss due to Rayleigh scattering becomes increasingly important as the wavelength decreases. This theoretical limit of scattering loss in silica glass is also highlighted in Figure 1.2. The large scattering loss for wavelengths less than 800 nm provides incentive to work at wavelengths greater than 800 nm. It is clear that Rayleigh scattering has little effect for wavelengths beyond 2000 nm and it would follow that even longer wavelengths may provide reduced attenuation. However, in the case of silica glass, the intrinsic absorption in the infra-red region begins to dominate Rayleigh scattering. Thus researchers are now looking into other glass compositions which are based on the light and heavy halides such as fluoride and chalcogenide glasses. These types of glasses exhibit less intrinsic absorption in the infra-red to mid-infra-red regions compared to the silica based glasses, but unfortunately exhibit poor mechanical, thermal and chemical properties, compared to silica.

Geometric effects such as bending can also cause attenuation in silica glass fibres. Under the appropriate bending conditions, light propagating along the core of the fibre can be lost into the cladding. Bending loss is usually classified as macroscopic or microscopic. Macroscopic bending refers to large scale bending and is usually associated with storing or deploying optical fibres. A standard 125  $\mu\text{m}$  silica glass fibre can usually be bent around a 25 mm radius with negligible loss and will not fracture or break unless the radius is less than 10 mm. Microscopic bending occurs when the fibre is sheathed with a protective coating. The stresses in the cabling process cause small axial distortions (micro-bends) to appear randomly along the fibre [4]. These micro-bends couple light between the guided modes of the fibre and can cause the light to couple out. In general, both macro and microscopic bending losses are less than those described for Rayleigh scattering and intrinsic absorption.

After consideration of these attenuation mechanisms it became clear that transmission at longer wavelengths in single mode fibre (SMF) would result in less signal attenuation and reduced signal dispersion. The low loss region extending from 1450 to 1600 nm, deemed the 3<sup>rd</sup> telecommunication window, emerged as the most practical for long haul telecommunication systems. This window has since been split into several distinct bands, the main bands of interest are the Short-band (S-band), the Centre-band (C-band) and Long-band (L-band). The wavelength designations for these bands are 1460-1530 nm, 1530-1565 and 1565-1625 nm, respectively, as highlighted in Figure 1.2.

Although signal attenuation and dispersion problems had been addressed, there were still a number of practical problems which needed to be overcome before a clear picture of the future of optical communications could be formed. Signal regeneration was proving to be one of the biggest hurdles. The regeneration process involved converting the optical signal into an electrical signal, amplifying the electrical signal and then converting the amplified electrical signal back into an optical signal. This process created enormous bottlenecks at the repeater stations and severely limited the performance of the optical system. In 1987, a group from the

University of Southampton demonstrated the first all optical fibre amplifier, using an erbium-doped silica fibre [6]. The erbium-doped fibre amplifier (EDFA) offers optical amplification over a broad wavelength range from 1530 - 1600 nm. The advent of the optical fibre amplifier offered new and far reaching opportunities for modern telecommunication networks. The main reason for their very strong impact is that optical amplifiers are unique in two respects: they amplify input signals of different bit rates and formats and can be used to achieve simultaneous amplification of multi-wavelength optical signals over a wide spectral range [7]. Some other advantages of optical fibre amplifiers and in particular EDFAs include:

- high gain,
- high power conversion efficiency,
- high saturation power,
- low noise,
- low crosstalk,
- low coupling loss and
- low cost.

Modern optical communication systems now offer terabits per second transmission over tens of kilometres before optical regeneration is required [8]. While this may seem like an enormous amount of information carrying capability, the birth of the internet has seen an exponential growth in the amount of information carried over these transmission systems. To manage the increasing demand for bandwidth, researchers are now looking to expand existing optical systems, by amplifying in the telecommunication S- and L-bands. Of the new bands to open up, perhaps the most important is the S-band. The S-band has comparable or better attenuation characteristics in standard SMF than the L-band and exhibits less sensitivity to bending loss. Furthermore, the S-band exhibits better dispersion characteristics in SMF than both the C- and L-bands. However, developing an S-band optical amplifier has proven to be more of a challenge than first thought.

## 1.2 Amplification in the S-band

Three major technologies have been studied in the hope of bringing the same effective means of optical amplification to the S-band as the EDFA has for the C-band and L-band. Semi-conductor optical amplifiers (SOAs), lumped (or discrete) Raman amplifiers (LRAs) and thulium-doped fibre amplifiers (TDFAs) have all been proposed as candidates to provide optical amplification in the telecommunication S-band from 1460 - 1530 nm. The following sections review each of these technologies and their potential to offer cost-effective long haul transmission in the S-band. More detailed reviews can be found in the literature [9, 10, 11, 12].

### 1.2.1 Semi-conductor optical amplifiers

Semi-conductor optical amplifiers (SOAs) have a similar structure to Fabry-Perot laser diodes but employ anti-reflection coatings on the end faces instead of highly reflective mirrors. SOAs are electrically pumped and optical amplification is achieved by stimulated emission of photons caused by the recombination of electron-hole pairs in the gain material. The centre wavelength and gain bandwidth of SOAs depend on the type of semi-conductor material used. Typical 3 dB gain bandwidths range from 20-30 nm, although bandwidths of up to 60 nm have been reported [13]. The various semi-conductor materials available permit optical amplification across a broad wavelength range, from 1300 - 1600 nm and the refined fabrication process of semi-conductor components makes SOAs much more cost effective than traditional EDFAs. The main challenge associated with this technology is that SOAs suffer from low gain, high noise figures, moderate polarisation dependence and high non-linearity. The high non-linearity presents the greatest problem for optical communications as these devices develop high bit rate and multiplex signal handling sensitivities. The high noise figures associated with these devices are further exacerbated by the high coupling losses that are incurred when connecting SOAs to standard single mode fibre (typically 3 dB at each end). A challenge also exists in coupling the different modes of propagation brought about by the difference in geometries between the fibres and SOAs.

## 1.2.2 Raman amplifiers

Raman gain in optical fibres occurs from the transfer of power from one optical beam to another through the transfer of energy of a phonon. A phonon arises when a beam of light couples with the vibrational modes of the medium. In this instance the optical fibre is the amplifying medium making the gain provided by Raman amplifiers dependent on the optical fibre's composition. In silica fibres, the Raman gain bandwidth is over 260 nm, with the dominant peak occurring at 86 nm from the pump wavelength. This makes Raman gain available across the entire transmission spectrum of the fibre as long as a suitable pump source is available. The gain presented by the Raman effect in fused silica glass is polarisation dependent; therefore gain only occurs if both the signal and pump beams are of the same polarisation [14]. To ensure that gain is maintained and to avoid polarisation dependent loss, the signal and pump are usually transmitted through non-polarisation maintaining fibre. Raman amplifiers are often developed in dispersion compensating fibre, which provides Raman gain 5 to 10 times greater than standard step index single mode fibre [15]. Broadband amplification and gain flattening can also be achieved by pumping at multiple wavelengths. As Raman amplifiers use the optical fibre as the gain medium, the Raman amplification does not suffer from the same implementation (deployment) challenges as the SOA discussed above. However, some of the issues facing this technology include:

- double Rayleigh scattering,
- short upper state lifetime,
- amplified spontaneous emission,
- four wave mixing (pump-pump) and (pump-signal),
- polarisation dependent gain,
- inter-band Raman scattering and
- poor pump conversion efficiency.

Various techniques have been developed to overcome the issues of the short upper state lifetime, four wave mixing and polarisation dependent gain [16]. However, the very nature of Raman amplification places theoretical limits on the amount of double Rayleigh scattering, inter-band Raman scattering and pump conversion efficiency.

### 1.2.3 Thulium-doped fibre amplifiers

Thulium-doped fibre amplifiers (TDFAs) achieve gain in a similar manner to EDFAs, by stimulated emission from the rare earth ions doped into the fibre core. However, the energy level structure of thulium ( $\text{Tm}^{3+}$ ) leads to many important differences in comparison with its erbium counterpart.  $\text{Tm}^{3+}$  produces stimulated emission from a transition that terminates above the ground state. This makes  $\text{Tm}^{3+}$  inherently less efficient, so optimising the pump source and glass host is particularly important. The spectroscopic properties of  $\text{Tm}^{3+}$  also lead to silica being a poor host material for optical amplification. Some of the spectroscopic challenges facing the amplifying transition in  $\text{Tm}^{3+}$  are listed below:

- non-radiative transitions dominate the decay from the upper and lower amplifying manifolds;
- the lower amplifying manifold has a longer lifetime than the upper amplifying manifold, making the transition self-terminating;
- competing transitions reduce the gain from the S-band amplifying transition;
- at high  $\text{Tm}^{3+}$  concentrations a cross relaxation process can quench the population in the upper amplifying manifold, reducing the gain and
- amplified spontaneous emission from the upper amplifying manifold also reduces the gain.

Despite these complications researchers have observed amplification in the S-band region of the 3<sup>rd</sup> telecommunication window. TDFAs have been established in a range of host materials and operated under a variety of different pumping schemes; Table 1.1 lists the TDFAs developed to date.

Host material	Pumping Scheme (nm)	Small signal gain (dB)	Operational bandwidth	Reference
fluoride	1047	>18	1480 - 1510 nm	[17]
fluoride (ZBLAN)	1047	>20	1453 - 1483 nm	[18]
fluorozirconate	1047	>20	1455 - 1485 nm	[19]
fluoride (ZHBLANLiP)	1064	>18	1453 - 1488 nm	[20]
fluoride (ZBLAN)	1064	>22	1465 - 1485 nm	[21]
fluoride (ZBLAN)	1410	>26	1480 - 1510 nm	[22]
fluorozirconate	1047/1560	>20	1478 - 1505 nm	[23]
fluorozirconate	800/1050	26	N/R	[24]
fluoride (ZBLAN)	1050/1550	>28	N/R	[25]
fluoride	1238/1400	>10	1470 - 1500 nm	[26]
fluoride	800/1400	>11	1470 - 1500 nm	[27]
ZBLAN	800/1400	>17	N/R	[28]
fluoride based	1410/1560	>25	1480 - 1510 nm	[29]
fluoride ZBLANLi	690/1560	>10	1470 - 1500 nm	[30]
fluoride ZBLANLi	690/1400	>10	1470 - 1500 nm	[30]
tellurite	795/1064	>10	1460 - 1520 nm	[31]
multi-component silicate	1405/1560	>20	1460 - 1520 nm	[32]
bismuth silica compound*	1047/1560	>6	1450 - 1520 nm	[33]
silica*	1047	8	1470 - 1530 nm	[34]
silica*	1060	1	1450 - 1520 nm	[35]

\* Fibres which can be fusion spliced to existing telecommunication fibre.

**Table 1.1:** TDFAs developed to date. Note: N/R is not reported in the literature.

The improved pumping efficiency of TDFAs (50% [36]), over LRAs (<8% [37]), and improved noise handling capabilities over SOAs places them as the preferred candidate for a cost effective S-band amplifying solution. The main obstacle facing this technology is the incorporation of these amplifiers into existing telecommunication networks. Of the TDFAs listed in Table 1.1, only three are capable of being fusion spliced to existing telecommunication fibre. The thermal and chemical properties of the other glass types prevent them from being fusion spliced to standard silica glass fibres; hence fibre coupling connectors are required at each input and output. To overcome this problem researchers are looking into new glass materials which may offer improved chemical and thermal properties when compared to the fluoride and tellurite materials, but do not compromise gain. Another alternative is to try and improve the efficiency of these amplifiers in the preferred standard silica glass host. This thesis addresses some of the host related issues facing efficient S-band optical amplification in  $\text{Tm}^{3+}$  -doped silica fibres and in particular focuses on addressing the relatively short fluorescence lifetime of the upper  $^3H_4$  manifold which is the limiting factor in obtaining efficient amplification in the S-band. The research also investigates energy transfer up-conversion processes which may also enhance the efficiency the S-band amplifying transition.

### 1.3 Scope of thesis

The increasing demand for bandwidth in optical fibre communication systems has prompted a significant research effort into developing efficient fibre based optical amplifiers at operating wavelengths neighbouring the EDFA. Of the possible candidates,  $\text{Tm}^{3+}$  -doped fibre amplifiers appear best suited to serve this need with amplification available from 1460 to 1530 nm. However, the current limitation with these devices is that the amplifying transition can only provide sufficient gain when doped into a host materials with relatively low phonon energies. Unfortunately, these glass types are incompatible with existing silica based telecommunication fibre making implementation into the optical network difficult. The ultimate goal for  $\text{Tm}^{3+}$  -doped amplifiers is to incorporate the ion into a host material which can be

easily integrated into standard communication systems without compromising gain; this thereby involves, to some degree, a silica based host material.

To date, optical amplification in the telecommunication S-band using  $\text{Tm}^{3+}$  -doped silica fibres has been relatively inefficient as detailed in Table 1.1. The inefficiency of the  ${}^3H_4 \rightarrow {}^3F_4$ , S-band transition in these glass types is attributed to the relatively high phonon energy associated with Si-O bonds in the glass. This high phonon energy causes strong non-radiative quenching of the  ${}^3H_4$  excited state, thereby reducing the radiative quantum efficiency of the amplifying transition. To overcome the non-radiative quenching of  $\text{Tm}^{3+}$  in silica glass, the ion requires an environment with lower phonon energies; this can be accomplished by breaking the Si-O bonds and replacing them with other less energetic bonds in a process known as network modification. A significant amount of effort has been invested in the network modification process in  $\text{Tm}^{3+}$  -doped silica glasses, with the majority of work focusing on lengthening the fluorescence lifetime of the  ${}^3F_4$  manifold to maximise the efficiency of the 2  $\mu\text{m}$  laser. The greatest improvement has been achieved by Cole who demonstrated that the addition of 26.7 mol % of germanium and 0.9 mol % of  $\text{Al}_2\text{O}_3$  to the silica glass host increases the  ${}^3F_4$  manifold lifetime from 388  $\mu\text{s}$  to 944  $\mu\text{s}$ . This work helped to establish the network modifying technique as an effective way to improve the fluorescence properties of the  $\text{Tm}^{3+}$  ion. Other network modifying elements have since been studied in  $\text{Tm}^{3+}$  -doped silica glasses, including aluminium, lead and tantalum [38, 39, 40].

The objective of this thesis was to systematically study the effects of network modifiers on the S-band amplifying transition in an effort to improve the radiative quantum efficiency in silica based glasses. The approach taken involved investigating two possible techniques to improve the efficiency of the S-band amplifying transition. The first technique employs the network modification process and studies the effects of co-doping silica with aluminium, germanium, antimony and tin. The addition of these network modifiers can act to break the Si-O bonds and replace them with less energetic bonds thus providing the  $\text{Tm}^{3+}$  ion with a lower local phonon energy

environment. The spectroscopic measurements of the absorption spectra and fluorescence lifetimes of the fibres allow the effectiveness of each network modifying element to be assessed.

The second technique investigates co-doping  $\text{Tm}^{3+}$  ions with other rare earth elements, in particular  $\text{Yb}^{3+}$  ions. Work done on  $\text{Tm}^{3+}/\text{Yb}^{3+}$  -co-doped systems has shown that under 980 nm excitation, double energy transfer can occur from the  $\text{Yb}^{3+}$  (donor) ion to the  $\text{Tm}^{3+}$  (acceptor) ion [41, 42]. In terms of the S-band amplifying transition in  $\text{Tm}^{3+}$ , this process has the potential to improve the efficiency as it acts to populate the upper amplifying ( ${}^3H_4$ ) manifold whilst depopulating the lower amplifying ( ${}^3F_4$ ) manifold. These processes have been studied in a range of host materials [43, 44, 45]; however a thorough investigation of these energy transfer processes has not been undertaken in silica glass. This research investigates the  $\text{Tm}^{3+}/\text{Yb}^{3+}$  -co-doped system in silica glass and assesses its potential for improving the efficiency of the S-band amplifying transition in  $\text{Tm}^{3+}$ . The spectroscopic measurements on these fibres will allow the populating mechanisms of the system to be identified and characterised.

The thesis reviews the electronic properties of rare earth elements in Chapter 2. The chapter focuses on the effects of the host material on the electronic configuration of the rare earth elements, with a particular emphasis on glass host materials. The non-radiative and radiative decay mechanisms of excited state manifolds are discussed, along with various forms of energy transfer processes. The chapter concludes with a general overview of the two rare earth elements studied in this thesis, namely thulium and ytterbium. The electronic configuration of the respective rare earth ions are presented and discussed in terms of their existing and potential applications.

Chapter 3 describes the experimental techniques used to characterise the spectroscopic properties of the  $\text{Tm}^{3+}$  and  $\text{Tm}^{3+}/\text{Yb}^{3+}$  -co-doped silica fibres. The chapter begins by describing the experimental configuration used to measure the attenuation

of the rare earth doped fibres and discusses the steps involved in relating the measured data to the  $\text{Tm}_2\text{O}_3$  and  $\text{Yb}_2\text{O}_3$  concentrations present in the fibre core. The technique used to obtain the refractive index profiles of optical fibres is presented along with the experimental setup used to measure the fluorescence lifetimes of the excited states of  $\text{Tm}^{3+}$  and  $\text{Yb}^{3+}$ . The chapter concludes with a description of the experimental arrangement used to measure the emission spectra from the rare earth doped optical fibres.

Chapter 4 presents the experimental results of the  $\text{Tm}^{3+}$  -doped silica fibres. The characterisation of these fibres began by studying the absorption spectrum of each fibre sample; these measurements enabled the concentration of  $\text{Tm}^{3+}$  ions to be established and provided initial evidence of host modification. The fluorescence lifetimes of the  $^3H_4$  and  $^3F_4$  manifolds are reported as a function of co-dopant and  $\text{Tm}_2\text{O}_3$  concentration to evaluate the effectiveness of the co-dopants and to identify any energy transfer processes which can occur between the excited state manifolds. The chapter concludes with a study of a beneficial energy transfer up-conversion process which originates from the  $^3F_4$  manifold.

In Chapter 5, the suitability of fitting a single exponential function to the fluorescence decay from the  $^3H_4$  and  $^3F_4$  energy manifolds is discussed. Various energy transfer models are considered to describe the non-exponential behaviour of the fluorescence decay; however, the data are consistent with the explanation that the non-exponential decay is caused by variations in the multi-phonon decay rates at localised sites throughout the silica glass network. The  $\text{Tm}^{3+}$  -doped fibres are then analysed on the basis of this explanation.

Chapter 6 investigates the  $\text{Tm}^{3+}/\text{Yb}^{3+}$  -co-doped system in alumino-silicate glasses and assesses the potential of the system to improve the quantum efficiency of the S-band amplifying transition in thulium. The fluorescence lifetimes of the  $^2F_{5/2}$  manifold of  $\text{Yb}^{3+}$  and the  $^3H_4$ ,  $^3F_4$  and  $^1G_4$  manifolds of  $\text{Tm}^{3+}$  are reported as a function of  $\text{Yb}^{3+}$  concentration to establish any limiting energy back transfer processes. The

measurement of the up-conversion luminescence intensities from the excited state manifolds of  $\text{Tm}^{3+}$  and  $\text{Yb}^{3+}$ , as a function of pump power, allowed modelling of the population dynamics of the system to be undertaken.

Chapter 7 begins with a discussion of the major outcomes from the previous three chapters. The chapter then explores possible directions of this research towards the realisation of an efficient  $\text{Tm}^{3+}$  -doped silica based fibre amplifier and summarises the successes and failures of the current research in meeting its objectives.

## Chapter 2

### SPECTROSCOPY OF RARE EARTH IONS

In order to model and predict the behaviour of rare earth doped optical fibre devices, it is first necessary to understand the spectroscopic properties of rare earth elements. This chapter reviews the fundamental atomic properties of trivalent rare earth ions and their behaviour in glass host materials.

Rare earth elements are categorised by a group of 15 elements known as the Lanthanides and are most stable when in their triply ionised form. The trivalent (3+) ionisation of these elements preferentially removes 6s and 5d electrons, leaving an electronic structure identical to xenon plus a certain number (1-14) of 4f electrons, i.e.  $1s^2, 2s^2, 2p^6, 3s^2, 3p^6, 3d^{10}, 4s^2, 4p^6, 4d^{10}, 4f^N, 5s^2, 5p^6$  and  $6s^0$ , where  $N = 1, \dots, 14$  [46]. The remaining 4f electrons are therefore shielded partially by the outer 5s and 5p shells. This shielding results in  $4f \rightarrow 4f$  optical transitions which are relatively sharp and for the most part are insensitive to the host material, unlike many of the optical transitions which take place in transition metals such as  $\text{Cr}^{3+}$ . Lanthanide elements in their triply ionised form will be referred to as rare earth ions from this point forth. The rare earth elements of particular interest for this work are highlighted in Figure 2.1.

57 La	58 Ce	59 Pr	60 Nd	61 Pm	62 Sm	63 Eu	64 Gd	65 Tb	66 Dy	67 Ho	68 Er	69 Tm	70 Yb	71 Lu
----------	----------	----------	----------	----------	----------	----------	----------	----------	----------	----------	----------	----------	----------	----------

**Figure 2.1:** Lanthanide series of the elements.

## 2.1 Electronic structure

The  $4f^N$  configuration of a rare earth ion is composed of a number of electronic states. A  $4f$  electron can be excited to a higher lying orbital, such as  $5g$ , or it can be excited within the  $4f^N$  set of states. The spread of  $4f^N$  energy levels arises from various atomic interactions between electrons and can be found by solving the time dependent Schrödinger equation. The weak interaction of the  $4f$  electrons with electrons from other ions allows a Hamiltonian to be written for an individual rare earth ion [47].

$$H(t) = H_{free\ ion} + V_{site} + V_{EM}(t) + V_{Vibrational}(t) + V_{ion-ion}(t), \quad (2.1)$$

where  $H_{free\ ion}$  is the Hamiltonian of an ion in complete isolation,  $V_{site}$  is the Hamiltonian which describes the influence of the environment of a rare earth ion,  $V_{EM}(t)$  describes the interaction of an ion with an electromagnetic field,  $V_{Vibrational}(t)$  describes the interaction of an ion with the vibrations of the surrounding lattice and  $V_{ion-ion}(t)$  describes the interactions between rare earth ions. The interaction terms in Equation 2.1 are weak when compared to the free ion Hamiltonian  $H_{free\ ion}$  and can therefore be treated as separate perturbations. The first two terms in Equation 2.1 are discussed as static perturbations; these perturbations are time independent and give rise to the observed electronic structure of a rare earth ion. The techniques for solving these terms are well accepted and can be found readily in the literature [48, 49, 50, 51]. The last three terms in Equation 2.1 are treated as dynamic perturbations; these perturbations are time dependent and result in transitions between the states established by the static interactions. Dynamic perturbations are discussed further in Sections 2.3 and 2.5.

The free ion Hamiltonian  $H_{free\ ion}$  can itself be broken up into several components, i.e.

$$H_{free\ ion} = H_{cf} + H_{rc} + H_{so}, \quad (2.2)$$

where  $H_{cf}$  is the crystal field Hamiltonian, which describes the interaction of an orbiting electron with the nucleus and the effective centrally symmetric field from all other electrons. The  $H_{rc}$  term describes the residual Coulomb interaction of the  $4f$  electrons with each other once the centrally symmetric contribution has been removed and  $H_{so}$  is the spin orbit coupling term as described below.

By employing a crystal field approximation to the free ion Hamiltonian the solutions can be constructed from hydrogenic states, resulting in the total orbital angular momentum  $L$  and total spin  $S$  being ‘good’ quantum numbers (i.e. exact eigenvalues of the Hamiltonian). The  $H_{rc}$  term in the free ion Hamiltonian causes a splitting of the  $4f^N$  electronic orbital state into a number of different states with different energies characterised by the angular and spin quantum numbers  $L$  and  $S$ . Russell-Saunders coupling (LS coupling) is most often used to describe the states of the lanthanides. In this scheme,  $L$  and  $S$  are vectorially added to form the total angular momentum  $J$  and the states are labelled  $^{2S+1}L_J$ . The third and final term in Equation 2.2,  $H_{so}$ , represents the spin orbit coupling of the LS states and gives rise to a further splitting of the LS terms into J levels. In the case of rare earth ions, the spin orbit coupling and residual Coulomb splitting can be the same order of magnitude, which results in L and S not always being good quantum numbers and the eigenstates of the system being a superposition of the Russell-Saunders LS states, a situation known as intermediate coupling [52]. This has caused some confusion particularly in the case of the thulium ion when trying to label energy manifolds. The energy manifolds can either be labelled according to their dominant LS contribution, as is experimentally observed, or in accordance with the zero spin orbit convention. Under the dominant LS contribution convention the first and third excited states of the  $\text{Tm}^{3+}$  ion located at 6000 and 12500  $\text{cm}^{-1}$  would be labelled as  $^3F_4$  and  $^3H_4$ , respectively, whereas the zero spin orbit convention would label these states as  $^3H_4$  and  $^3F_4$ , respectively. This thesis adopts the dominant LS contribution convention.

The host material has the least influence on the electronic structure of the rare earth ion and changes the positions of the energy levels only slightly. The static

effects of the host on the rare earth ion can be treated by replacing the host with an effective crystal field potential at the ion site. The potential is usually expanded in a power series of tensor operator components  $C_q^{(k)}$  that transform as spherical harmonics [47], i.e.

$$V_{site} = \sum_{ikq} B_q^k [C_q^{(k)}]_i, \quad (2.3)$$

where  $B_q^k$  are the crystal field components ( $k \leq 6$  for  $f$  electrons) and the sum over  $i$  is carried out over all the  $4f$  electrons of the ions. The even  $k$  terms in the expansion split the free ion  $J$  multiplets into Stark components generally separated by 10 - 100  $\text{cm}^{-1}$ . The odd  $k$  terms admix higher lying states of opposite parity into the  $4f^N$  configuration. This admixture does not affect the position of the energy levels, but it has a very important effect on the strengths of the optical transitions between the levels [47].

## 2.2 Radiative transitions

The majority of rare earth optical transitions which are observed in the visible region of the electromagnetic spectrum occur between states which belong to the  $4f^N$  configuration. For intra- $f$ -shell transitions the initial and final states have the same parity; this would imply that the electric-dipole process is forbidden. However, in cases where the site symmetry is not a centre of inversion (as is usually the case with glass), the site interaction Hamiltonian (see Equation 2.3) can contain odd-parity terms, thereby introducing a degree of electric-dipole strength into the intra- $f$ -shell transitions. The odd  $k$  terms in Equation 2.3 determine the intensity of a particular transition, whilst the even  $k$  terms determine the positions of the Stark components for each multiplet and therefore the wavelength at which emission or absorption occurs. Using some simplifications, Judd and Ofelt have provided a way to treat conveniently the spectral intensities of intra-configurational transitions of  $4f$  ions in solids. In this approximation, the transition strength is written in the form

$$S_{ij} = e^2 \sum_{t=2,4,6} \Omega_t |\langle j \| U^{(t)} \| i \rangle|^2 = 4\pi\epsilon_0 \frac{3hc n(2J_i + 1)}{8\pi^3 \bar{\nu}} \frac{1}{\chi} \int \sigma_{i,j}(\nu) d\nu, \quad (2.4)$$

where  $\Omega_t$  are co-efficients reflecting the effect of the crystal field, electronic wavefunctions and the energy level separation, while  $|\langle j || U^{(t)} || i \rangle|$  are doubly reduced matrix elements of the tensor operator  $U^{(t)}$ . The tensor operator  $U^{(t)}$  is a quantum mechanical operator for an electric dipole transition from state  $|i\rangle$  to  $|j\rangle$ .

The matrix elements are virtually independent of the host material and have been tabulated in [53, 54]. The host dependence is contained in the three intensity parameters  $\Omega_t$  ( $k = 2, 4, 6$ ), known as Judd-Ofelt parameters. These parameters are usually determined empirically by performing a least squares fit of Equation 2.4 to the integrated absorption bands obtained from a measured spectrum. Once the parameters have been determined, the strength of any radiative transition can be calculated for that dopant and host combination. The electric dipole probability, which corresponds to the probability of spontaneous emission from an excited state can also be determined through the knowledge of the transition strength, which is given by Equation 2.5.

$$A_{i,j} = \frac{1}{4\pi\epsilon_0} \frac{64\pi^4 n \bar{\nu}}{3hc^3(2J_i + 1)} \chi S_{ij} , \quad (2.5)$$

where  $n$  is the index of refraction of the host,  $\epsilon_0$  is the permittivity of a vacuum,  $h$  is Plank's constant,  $c$  is the speed of light in a vacuum,  $\bar{\nu}$  is the mean photon frequency,  $J_i$  is the  $J$  value of the initial state,  $\chi$  is the local correction factor and  $S_{ij}$  is the transition strength.

Equation 2.5 can be used to estimate the radiative spontaneous lifetime for an excited state by simply summing the electric dipole probabilities corresponding to all of the possible transitions originating from the excited state. The radiative lifetime of an excited state can then be written as:

$$\frac{1}{\tau_{rad}} = \sum_j A_{ij} . \quad (2.6)$$

The Judd-Ofelt calculations of the radiative lifetime of  $4f$  energy levels, is particularly useful when trying to identify the quantum efficiency of particular transitions. However, it should be noted that the accuracy of Judd-Ofelt analysis is limited to around 10 to 15 %.

## 2.3 Non-radiative transitions

The transition strengths and radiative lifetimes predicted by Judd-Ofelt theory are made for transitions which are virtually independent of the energy separation between the initial and final states. However, experiments throughout the 1960s showed that the fluorescence in various host materials could be observed only for energy separations greater than  $1000 \text{ cm}^{-1}$  [53]. This revealed the existence of a competing process termed non-radiative decay. Non-radiative transitions involve the absorption and emission of phonons (quanta of vibrational energy in the host material) whereas radiative transitions involve the absorption and emission of photons (quanta of electromagnetic radiation). When electronic states are close enough to be bridged by emission or absorption of one or two phonons, non-radiative decay will occur rapidly and efficiently. This phenomenon is responsible for the thermalisation of energy manifolds.

In many cases the energy separation between excited manifolds in rare earth ions exceeds that which can be accounted for by the absorption/emission of a single phonon. In cases such as these, the energy gap can be bridged by the simultaneous absorption/emission of a multiple number of phonons in a process known as multi-phonon relaxation. The requirement to excite several phonons simultaneously results in the probability of multi-phonon emission being many orders of magnitude less than the probability for the emission or absorption of a single phonon. However, multi-phonon processes can still be significant as the electron-phonon interaction is strong and phonons have a density of states that typically is 11 orders of magnitude larger than that of photons [55]. In general, if less than 5 phonons are required to bridge an energy gap, the rate of multi-phonon emission is comparable with the ra-

diative emission rates. One of the simplest theoretical formulations used to describe multi-phonon decay in crystals was developed by Kiel [56] and extended by Riseberg and Moos [57]. The multi-phonon decay rate from level  $i$  to the next lowest level  $j$  is given by:

$$A_{ij}^{nr} = C [n(T) + 1]^p \exp(-\alpha \Delta E_{ij}), \quad (2.7)$$

where  $C$  and  $\alpha$  are host dependent parameters,  $p$  is the number of phonons required to bridge the energy gap  $\Delta E$  and  $n(T)$  is the Bose-Einstein occupation number for the effective phonon mode, which is given by:

$$n(T) = \frac{1}{\exp\left(\frac{\hbar\omega}{k_B T}\right) - 1}, \quad (2.8)$$

where  $\hbar\omega$  is the maximum phonon energy for a given vibration mode and is host dependent,  $k_B$  is Boltzmann's constant and  $T$  is the temperature in Kelvin.

The integer number of phonons,  $p$ , in Equation 2.7, is given by the ratio of the energy gap  $\Delta E_{ij}$  to the maximum phonon energy of the host material:

$$p = \frac{\Delta E_{ij}}{\hbar\omega}. \quad (2.9)$$

The host dependent parameter  $\alpha$  is defined as:

$$\alpha = (h\omega)^{-1} \left( \ln \frac{p}{g(n(T) + 1)} - 1 \right), \quad (2.10)$$

where  $g$  is the electron-phonon coupling constant.

The host dependent parameters for a range of glasses have been compiled by Reisfeld and Jørgensen [58]. Using these values and Equation 2.7, the multi-phonon decay rate as a function of energy gap can be obtained, as seen in Figure 2.2. The vertical markers in Figure 2.2 indicate the energy separation between the lowest Stark level of the  $i^{th}$  excited manifold, to the highest Stark level from the next lowest,  $j^{th}$  manifold, for each excited state of  $\text{Tm}^{3+}$ .

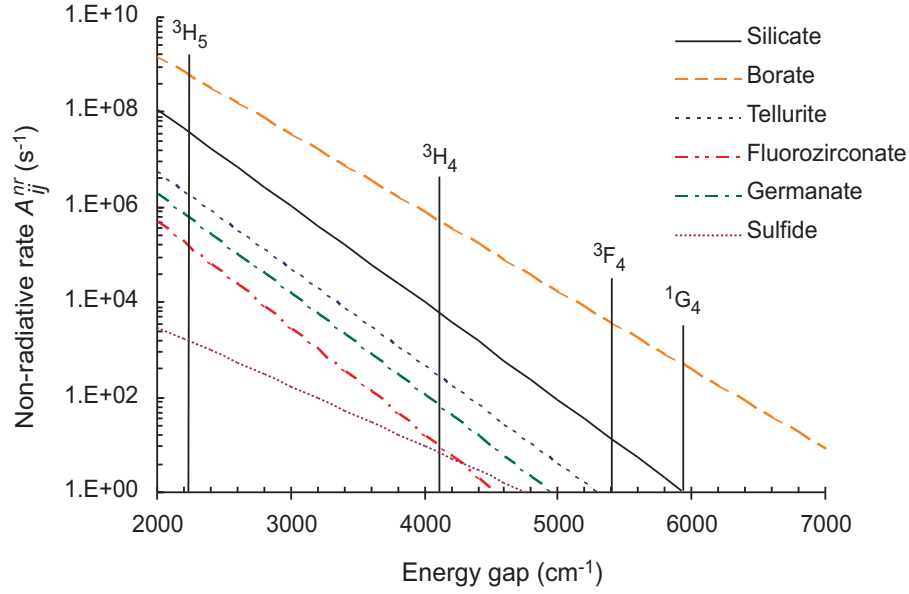


**Figure 2.2:** Non-radiative decay rate as a function of energy gap for various glass and crystal host materials. The vertical lines indicate the energy gap between the lowest Stark level of the  $i^{th}$  excited manifold, to the highest Stark level from the next lowest,  $j^{th}$  manifold, for each excited state of  $Tm^{3+}$ .

Since the excited states of  $Tm^{3+}$  exhibit multi-phonon decay, the experimentally observed decay rate of a particular excited state is given by the addition of the radiative and multi-phonon decay rates:

$$\frac{1}{\tau_i^{obs}} = A_i^{obs} = \sum_j (A_{ij}^R + A_{ij}^{nr}), \quad (2.11)$$

where  $\tau_{obs}$  represents the observed lifetime of the excited state and  $A_i^{obs}$ ,  $A_{ij}^R$  and  $A_{ij}^{nr}$  represent the observed, radiative and non-radiative decay rates, respectively.

## 2.4 Energy level broadening mechanisms

The energy levels of rare earth ions in glass cannot be characterised by a well defined set of energy values. There are several energy broadening mechanisms which give the energy levels of rare earth ions a finite width. The mechanisms which apply equally to all ions at one type of site in a system are termed homogeneous broadening mechanisms and mechanisms which do not apply equally to all ions at a particular site are termed inhomogeneous broadening mechanisms. The simplest form of homogenous

broadening is lifetime broadening which occurs as a consequence of Heisenberg's energy uncertainty principle. Heisenberg's principle states that if an energy manifold has a characteristic lifetime  $\tau$  then the energy of that particular manifold can only be known to within  $\Delta E \geq \hbar/2\tau$ . The energy manifolds of rare earth ions have typical lifetimes of  $10^{-3}$  -  $10^{-8}$  s; therefore the amount of broadening as a result of this effect is relatively small ranging from  $10^{-8}$  -  $10^{-4}$   $\text{cm}^{-1}$  (or 0.1 - 100 kHz). A much larger contribution to the homogeneous linewidth of an energy manifold comes from transitions which occur between Stark levels in a single manifold. If the energy separation between Stark levels is small (a few  $100 \text{ cm}^{-1}$ ), energy can be absorbed from, or emitted to, vibrational modes of the host. These transitions usually involve a single mode of vibration and occur on a rapid time scale giving homogeneous linewidths to the Stark levels of 1 - 300  $\text{cm}^{-1}$  (or 30 - 9000 GHz) [52].

Inhomogeneous broadening arises when the sites occupied by the rare earth ions are not identical. In crystals, the effect of inhomogeneous broadening is small as the rare earth ions occupy almost identical sites. If imperfections exist in the crystal structure then the effects of inhomogeneous broadening may be observed. Random imperfections in a structure produce random variations in the  $B_q^k$  term in the crystal field potential Hamiltonian. These variations will therefore affect the position of the energy manifolds of the ions, but only slightly. In crystals, rare earth ions are observed to absorb and emit energy with well defined sharp spectral lines revealing the positions of each Stark energy level within an energy manifold. In glasses, inhomogeneous broadening becomes the dominant broadening mechanism. The disordered nature of glass exposes the rare earth ions to a distribution of possible environments, each with a characteristic set of field parameters. The distribution of fields at individual sites can be large and the energy manifolds of the ions may show considerable differences to their crystalline counterpart [59]. The absorption and emission spectra of rare earth ions observed in glass are often characterised by a continuous broad-band spectrum where the position of the individual Stark levels of the manifold are masked by the inhomogeneous linewidth.

## 2.5 Ion-ion interactions

The radiative and non-radiative processes described in this chapter thus far have been concerned with a single rare earth ion. When the rare earth ion concentration is significantly low, ions are distributed evenly throughout the glass matrix making the interionic distance large, thus preventing any ion-ion interactions from taking place. However, when the rare earth ion concentration is increased or when clustering of the ions occurs, the distance between ions is reduced and interactions between ions can occur. These dynamic interactions are accounted for by the  $V_{ion-ion}$  term in the time dependent Schrödinger equation. Ion-ion interactions involve the transferring or sharing of energy between ions. Various forms of ion-ion interactions are discussed in the following sections.

### 2.5.1 Cross relaxation

The interaction and energy exchange between ions can occur in various forms; in general energy transfer takes place between a pair of ions. The optically excited ion in the pair is referred to as the ‘donor’ ion, whilst the ion receiving the energy is termed the ‘acceptor’ ion. Cross relaxation is a particular form of ion-ion energy transfer where the energy from an excited donor is transferred to a nearby acceptor ion, promoting the acceptor ion to a higher energy state, whilst demoting the donor ion to a lower energy state. Initially, the acceptor ion can be in an excited state or in the ground state. The process requires only that both donor and acceptor ions have two energy levels of approximately the same energy gap. Cross relaxation can involve a single type of rare earth ion, which plays a role of donor and acceptor. For this effect to occur, it is required that the ion has two pairs of equally spaced energy levels. The energy transfer is said to be resonant if the energy gaps are matched. If an energy mismatch exists between the energy gaps, it may be compensated for by the absorption and emission of phonons; energy transfer of this type is termed phonon assisted. Energy transfer processes which require the emission of phonons are exothermic and are much faster than endothermic processes which require the absorption of phonons. [47].

The effects of cross relaxation can be considered as beneficial or detrimental depending on the application. If one desires ions to be in the excited state that results from cross relaxation, the process can be extremely favourable since in some cases every excited donor ion results in two excited ions in an intermediate energy manifold. However, if one desires the ions to be in an excited state from which the cross relaxation takes place, the initially excited donor ions are quenched resulting in a reduction in the efficiency of the transition. An example of a well known cross relaxation process in  $\text{Tm}^{3+}$  is presented in Figure 2.3.

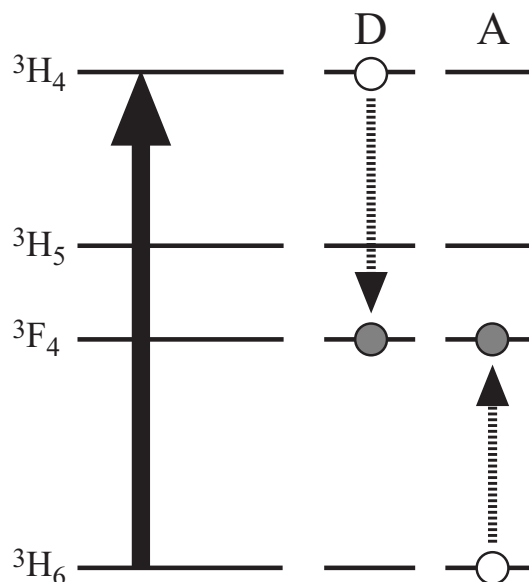


**Figure 2.3:** Example of a well known cross relaxation process in  $\text{Tm}^{3+}$  between the  ${}^3H_4$  and  ${}^3H_6$  manifolds. The donor ion is labelled D and the acceptor ion is labelled A. The white and grey circles represent the ions before and after the energy transfer takes place, respectively.

If an ion excited to the  ${}^3H_4$  manifold interacts with a nearby ion in the ground state  ${}^3H_6$ , the excited ion can transfer part of its energy to the ground state ion, leaving them both in the  ${}^3F_4$  intermediate state. The energy mismatch between the  ${}^3H_4 \rightarrow {}^3F_4$  and  ${}^3H_6 \rightarrow {}^3F_4$  transitions in silica is  $\sim 600 - 700 \text{ cm}^{-1}$  and therefore requires the emission of one phonon to complete the process. This cross relaxation process has been successfully used to increase the quantum and slope efficiencies of the ( ${}^3F_4 \rightarrow {}^3H_6$ )  $2 \mu\text{m}$  lasing transition [60].

### 2.5.2 Energy transfer up-conversion

A special case of cross relaxation is known as energy transfer up-conversion (ETU). This process initially involves both the donor and acceptor ions being in an excited state. A donor ion in an excited state may transfer part or all of its energy to a nearby acceptor ion, prompting the acceptor ion to a higher energy state. From this state the acceptor can relax radiatively or non-radiatively to lower levels or radiatively directly to the ground state in which case the medium is observed to emit fluorescence at an energy greater than that of the incident light; hence the term up-conversion. Any energy mismatches which exist between the energy level pairings can also be accounted for by the absorption or emission of phonons.

### 2.5.3 Excited state absorption

Excited state absorption (ESA) is a process which involves a single ion in an excited state absorbing the energy of an incident pump or signal photon and promoting itself to a higher energy state. Because ESA involves only a single ion in an excited state, it is concentration independent. ETU on the other hand, involves a pair of interacting ions, making the process concentration and pump power dependent. Although, there are distinct differences between ESA and ETU, they are often observed in conjunction with each other.

### 2.5.4 Sensitised luminescence

Ion-ion energy transfer is not restricted to interactions between ions of the same species; energy transfer between ions of different species is also possible. For energy transfer involving two different species, the optically excited ion is referred to as the 'sensitiser' and the ion that receives the excitation is termed the 'activator' [47]. This process can occur in a single step where a particular sensitiser ion absorbs the energy of an incident photon and transfers it to a nearby activator in a similar manner to that described for cross relaxation and energy transfer up-conversion. If the sensitiser concentration becomes high enough, energy migration between sensitiser ions can also occur. In this process a sensitiser ion transfers its energy to

another nearby unexcited sensitiser ion. This process can repeat itself in successive emission/absorption steps until a sensitiser ion finds an activator close enough to complete the final step of the transfer process. In some sensitised systems, this mechanism can be used to improve the quantum efficiency of particular transitions. The ytterbium ion ( $\text{Yb}^{3+}$ ) has been successfully used as a sensitising ion when co-doped with other rare earth ions such as, praseodymium ( $\text{Pr}^{3+}$ ), holmium ( $\text{Ho}^{3+}$ ), erbium ( $\text{Er}^{3+}$ ) and  $\text{Tm}^{3+}$  [61, 62, 63, 64].

### 2.5.5 Fluorescence quenching

Fluorescence quenching is a process that can occur through any of the aforementioned energy transfer processes and has important implications for the performance of luminescence devices as it results in reduced excitation. Fluorescence quenching involves energy being transferred from a donor (sensitiser) ion to an acceptor (activator) ion, but the latter does not fluoresce and relaxes non-radiatively. In this process, the acceptor acts as an energy sink and is sometimes called the deactivator. This results in a reduction in the quantum efficiency of the transition with increasing concentration. Examples of fluorescence quenching have been reported in the literature [65, 66, 67, 68].

## 2.6 Thulium

Thulium is the thirteenth lanthanide element and has 12 electrons in its  $4f$  shell. The energy level diagram of the  $\text{Tm}^{3+}$  ion is shown in Figure 2.4. When doped into silica glass a number of transitions in  $\text{Tm}^{3+}$  become dominated by multi-phonon decay due to the closeness of the next lowest energy level and the relatively high phonon energy of silica glass. Table 2.1 lists the radiative and observed fluorescence lifetimes as well as the radiative, observed and multi-phonon decay rates of each energy manifold of  $\text{Tm}^{3+}$  in silica glass. As a comparison, the same parameters are presented in Table 2.2 for the lower phonon energy ZBLAN glass.

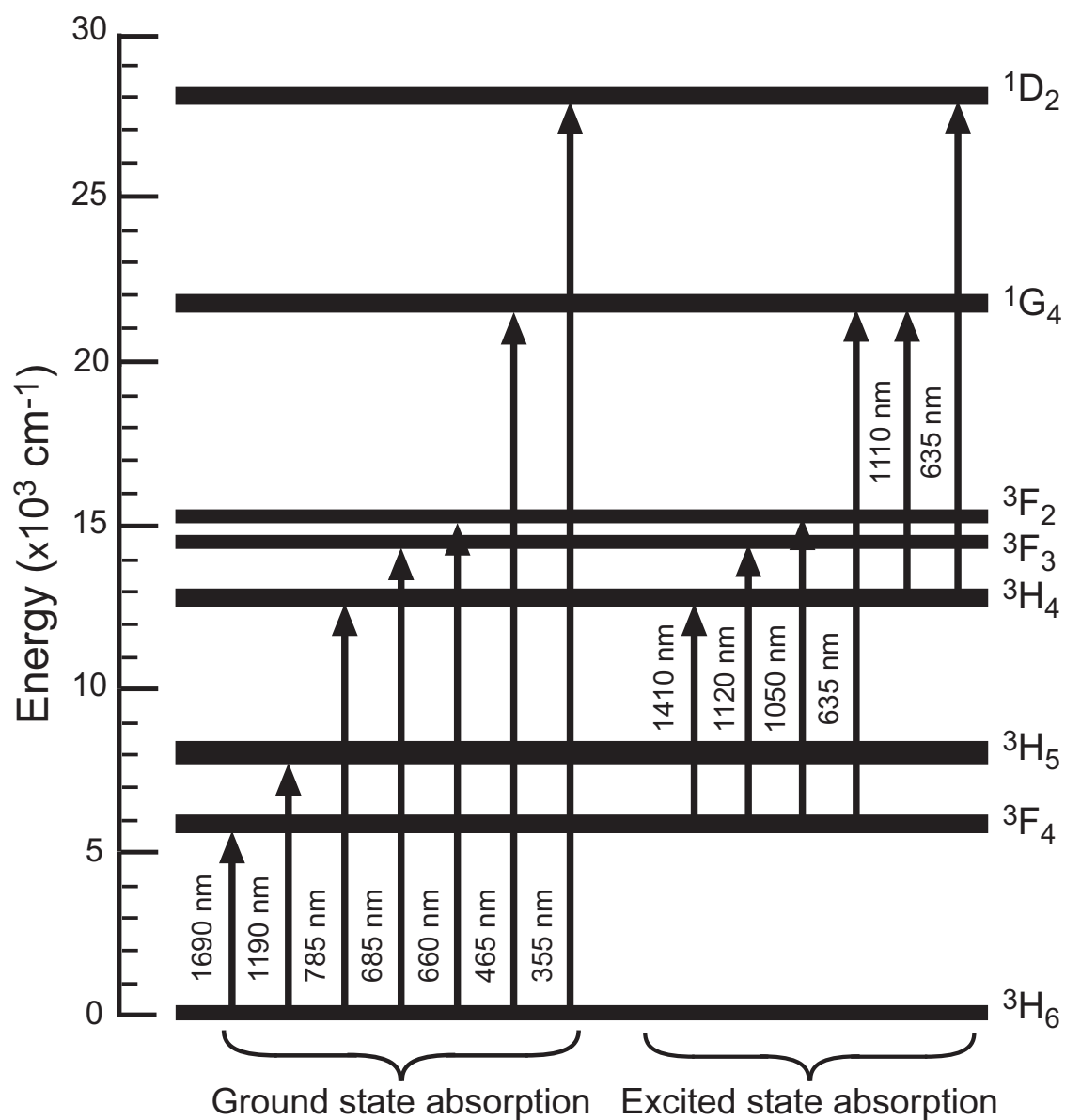


**Figure 2.4:** Simplified energy level diagram of  $Tm^{3+}$  in silica glass, showing the possible ground and excited state absorptions together with the peak central wavelengths [69].

Manifold	$\tau_{obs}$ ( $\mu\text{s}$ )	$A_{obs}$ ( $\text{s}^{-1}$ )	$\tau_{rad}$ ( $\mu\text{s}$ ) [70]	$A_{rad}$ ( $\text{s}^{-1}$ )	$A_{nr}$ ( $\text{s}^{-1}$ )
$^1D_2$	6.5 [71]	153 846	26	38 461.5	115 384
$^1G_4$	260 [71]	3 846	428	2 336.4	1 510
$^3F_2$	N/R	N/R	631	1 584.8	$1.06 \times 10^{11}$
$^3F_3$	N/R	N/R	447	2 237.1	$3.78 \times 10^8$
$^3H_4$	20 [70]	50 000	697	1 434.7	48 565
$^3H_5$	N/R	N/R	3 896	256.7	$3.61 \times 10^7$
$^3F_4$	420 [70]	2 381	4 559	219.5	2 161

**Table 2.1:** Fluorescence lifetimes and multi-phonon decay rates for the energy manifolds of  $\text{Tm}^{3+}$  -doped silica glass. The radiative and observed decay rates were found by taking the reciprocal of the radiative and observed lifetimes, respectively, whilst the non-radiative decay rate is given by the difference between the radiative and observed decay rate. Note: N/R - not reported (refer to text).

Manifold	$\tau_{obs}$ ( $\mu\text{s}$ )	$A_{obs}$ ( $\text{s}^{-1}$ )	$\tau_{rad}$ ( $\mu\text{s}$ ) [70]	$A_{rad}$ ( $\text{s}^{-1}$ )	$A_{nr}$ ( $\text{s}^{-1}$ )
$^1D_2$	56.3 [72]	17762	73	13698.6	$4.0 \times 10^3$
$^1G_4$	817 [72]	1223	908	1101.3	123
$^3F_2$	N/R	N/R	1 234	810.4	$9.16 \times 10^8$
$^3F_3$	N/R	N/R	693	1443.0	$1.81 \times 10^6$
$^3H_4$	1 510 [70]	662	1 519	658.3	4.0
$^3H_5$	N/R	N/R	6 863	145.7	$1.61 \times 10^6$
$^3F_4$	11 200 [70]	89	11 223	89.1	0.2

**Table 2.2:** Fluorescence lifetimes and multi-phonon decay rates for the energy manifolds of  $\text{Tm}^{3+}$  -doped ZBLAN glass. The radiative and observed decay rates were found by taking the reciprocal of the radiative and observed lifetimes, respectively, whilst the non-radiative decay rate is given by the difference between the radiative and observed decay rate. Note: N/R - not reported (refer to text).

The multi-phonon decay rates listed in Tables 2.1 and 2.2 were estimated based on the difference between the radiative and observed decay rates. However, in the case of the  $^3F_2$ ,  $^3F_3$  and  $^3H_5$  manifolds, a measured fluorescence decay time cannot be obtained as the population in these manifolds suffers non-radiative quenching to the next lowest energy manifold resulting in no detectable fluorescence. Therefore, the multi-phonon decay rates were calculated using Equation 2.7 with the values for silica glass of  $C$ ,  $\alpha$  and  $\hbar\omega$  of  $1.4 \times 10^{12}$  Hz,  $4.7 \times 10^{-3}$  cm and  $1100 \text{ cm}^{-1}$  [58], respectively. Whilst the decay rates for ZBLAN were calculated using  $C$ ,  $\alpha$  and  $\hbar\omega$  values of  $1.59 \times 10^{10}$  Hz,  $5.19 \times 10^{-3}$  cm and  $500 \text{ cm}^{-1}$  [58], respectively. The values for the energy gap to the next lowest manifold were taken from [47].

By comparing the observed and radiative lifetimes listed in Tables 2.1 and 2.2 it can be inferred that the radiative quantum efficiency (RQE), defined as  $\eta_{rad} = \tau_{obs}/\tau_{rad}$ , of several  $\text{Tm}^{3+}$  transitions is significantly less in silica glass than in ZBLAN. One of the important aims of this work is to improve the RQE of the  ${}^3H_4$  manifold in  $\text{Tm}^{3+}$ -doped silica glasses, a manifold which is dominated by multi-phonon decay. Such an improvement would have important implications on the S-band amplifier but may also lead to improvements in other active  $\text{Tm}^{3+}$  devices such as the 2  $\mu\text{m}$  and 475 nm lasers. To explore the  $\text{Tm}^{3+}$  ion further, the characteristics of each excited manifold are reviewed in the following sections with an emphasis on their performance in a silica glass host.

### 2.6.1 ${}^3F_4$ manifold

The  ${}^3F_4$  manifold is the first excited state of  $\text{Tm}^{3+}$  and is located  $\sim 6000 \text{ cm}^{-1}$  above the ground state. The  ${}^3F_4 \rightarrow {}^3H_6$  transition produces an extremely wide featureless emission band spanning 1.6 - 2.0  $\mu\text{m}$ . The large linewidth of the emission suggests a strong coupling of the rare earth ion to the lattice [73]. From the values listed in Table 2.1, the  ${}^3F_4 \rightarrow {}^3H_6$  transition operates with a quantum efficiency of  $\sim 11\%$  in silica glass, whilst in glasses with lower phonon energies this transition operates with 100% RQE. The considerably smaller RQE observed in silica glass raises the threshold for lasers operating from the  ${}^3F_4$  manifold, but does not impair slope efficiency, as stimulated emission will dominate non-radiative decay once the laser is above threshold [47]. The increased amount of non-radiative decay in silica glass does, however, place noise restriction on small signal amplifiers operating around 2  $\mu\text{m}$ . The  ${}^3F_4$  manifold can be pumped directly around 1650 nm, or excited through the decay of higher energy manifolds such as the  ${}^3H_5$  and  ${}^3H_4$  manifold. Jackson *et al.* have reported quantum efficiencies greater than 100% by pumping into the  ${}^3H_4$  manifold at 800 nm and relying on the efficient cross relaxation process and multi-phonon decay to populate the  ${}^3F_4$  manifold [38]. Using this technique, Frith *et al.* were able to achieve the highest reported output power at 2.04  $\mu\text{m}$  of 85 W, under 793 nm pumping into a 1.8 m length of  $\text{Tm}^{3+}$ -doped silica fibre [74].

### 2.6.2 ${}^3H_5$ manifold

The  ${}^3H_5$  manifold is located  $\sim 7650 \text{ cm}^{-1}$  from the ground state and  $2250 \text{ cm}^{-1}$  above the  ${}^3F_4$  manifold. The close energy spacing between the  ${}^3H_5$  and  ${}^3F_4$  manifolds results in almost all of the excited state ions in the  ${}^3H_5$  manifold decaying non-radiatively to the  ${}^3F_4$  manifold. The dominance of non-radiative decay eliminates the possibility of radiative emission from the  ${}^3H_5$  manifold, particularly in the case of silica glass hosts where the energy gap can be accounted for with the emission of just two vibrational modes of the glass. The peak absorption wavelength of the  ${}^3H_5$  manifold is around 1200 nm in silica based host materials. However, the broad absorption band also shows reasonable absorption at shorter wavelengths from 1040 to 1060 nm where a range of commercially available high powered pump lasers are available. This allows the  ${}^3F_4$  manifold to be pumped in-directly with relatively cheap and efficient light sources as opposed to pumping the  ${}^3F_4$  manifold directly at 1650 nm. Pumping  $\text{Tm}^{3+}$  between 1040 and 1060 nm also opens up a range of up-conversion processes as can be appreciated by studying Figure 2.4.

### 2.6.3 ${}^3H_4$ manifold

The  ${}^3H_4$  manifold is the third excited state of  $\text{Tm}^{3+}$  and is located at  $\sim 12500 \text{ cm}^{-1}$ , where high powered commercially available laser sources exist. When ions are excited to the  ${}^3H_4$  manifold they may relax via several different routes. Relaxation to the next lowest energy state, the  ${}^3H_5$  manifold, may occur radiatively and/or non-radiatively depending on the host material. The  ${}^3H_4 \rightarrow {}^3H_5$  transition has been demonstrated to lase in ZBLAN glass by various groups over the wavelength range 2250 - 2400 nm [75, 76, 77]. In silica glass however, this transition is dominated by multi-phonon relaxation due to the high phonon energy of the glass (see Table 2.1). The dominance of this multi-phonon relaxation results in a reduced excited state lifetime for the  ${}^3H_4$  manifold. The observed lifetime of the  ${}^3H_4$  manifold in silica is  $\sim 20 \mu\text{s}$ , which is more than an order of magnitude less than the observed lifetime in ZBLAN glass of 1.51 ms.

The radiative transitions from the  ${}^3H_4$  manifold,  ${}^3H_4 \rightarrow {}^3F_4$  and  ${}^3H_4 \rightarrow {}^3H_6$ , result in emission bands spanning 1460 - 1530 and 770 - 820 nm, respectively. The first of these transitions has received enormous interest in recent times as it offers amplification in the sought-after telecommunications S-band. Because the lifetime of the  ${}^3F_4$  manifold is longer than that of the upper  ${}^3H_4$  manifold, the  ${}^3H_4 \rightarrow {}^3F_4$  transition is commonly referred to as a self terminating. It has been pointed out by Quimby and Miniscalco that this does not necessarily preclude laser action [47]. Indeed, amplification of this transition has been observed in a variety of host materials (see Table 1.1). However, this transition is yet to show efficient amplification in silica glass, due to the unfavorable spectroscopic properties of the glass.

The second possible radiative transition  ${}^3H_4 \rightarrow {}^3H_6$  is the dominant radiative relaxation process from the  ${}^3H_4$  manifold. This transition has been operated as a three level laser and amplifier over the wavelength range 803 to 825 nm [78, 79]. In silica glass this transition has a branching ratio of 0.9 [70], indicating that it should provide good performance as a laser or amplifier.

#### 2.6.4 ${}^3F_{2,3}$ manifolds

The  ${}^3F_2$  and  ${}^3F_3$  manifolds are located  $\sim 14\,100$  and  $13\,550\text{ cm}^{-1}$  above the ground state manifold, respectively, and are separated by  $550\text{ cm}^{-1}$ , which is close enough to allow these manifolds to be thermally coupled (i.e. the population of these manifolds is governed by the Boltzmann distribution). Thermalised energy manifolds in rare earth doped materials have been used extensively as a mechanism to measure temperature [80]. However, in the case of  $\text{Tm}^{3+}$ , the close energy spacing between the  ${}^3F_2$  and  ${}^3F_3$  manifolds and the next lowest  ${}^3H_4$  manifold prevents any radiative emission from these manifolds. In silica glass, inhomogeneous broadening masks the absorption peaks from both excited state manifolds resulting in a single broad featureless absorption peak centred around 680 nm. Researchers have pumped this transition at 660 nm in order to excite the  ${}^1D_2$  manifold through an ESA process that can be appreciated by studying Figure 2.4 [64]. TDFAs have also been demonstrated by dual pumping into the  ${}^3F_{2,3}$  and  ${}^3F_4$  manifolds at 690 and 1560 nm [30].

### 2.6.5 $^1G_4$ manifold

The  $^1G_4$  manifold of  $\text{Tm}^{3+}$  is located 20 050  $\text{cm}^{-1}$  from the ground state. Radiative emission from the  $^1G_4$  manifold can occur through a number of possible transitions:  $^1G_4 \rightarrow ^3F_2$  (1630 nm),  $^1G_4 \rightarrow ^3F_3$  (1500 nm),  $^1G_4 \rightarrow ^3H_4$  (1175nm),  $^1G_4 \rightarrow ^3H_5$  (780 nm),  $^1G_4 \rightarrow ^3F_4$  (650 nm) and  $^1G_4 \rightarrow ^3H_6$  (475 nm). The branching ratio for each radiative transition in silica glass has been calculated by Walsh and Barnes using standard Judd-Ofelt techniques [70]. The reported ratios for these transitions are 0.006 (1630 nm), 0.02 (1500 nm), 0.108 (1175 nm), 0.285 (780 nm), 0.069 (650 nm) and 0.51 (475 nm), respectively. To date, the only reported gain from the  $^1G_4$  manifold in silica glass was observed at 475 nm under 1064 nm pumping [24]. Other work in fluorozirconate and crystalline host materials have reported lasing at 475 and 650 nm [81, 82]. The energy separation between the  $^1G_4$  and the  $^3F_2$  manifolds is  $\sim 5\,950\text{ cm}^{-1}$ . In silica glass this energy gap can be accounted for by the emission of 5 phonons; hence the non-radiative decay rate is significantly less than those calculated for the  $^3H_5$  and  $^3F_{2,3}$  manifolds. In silica glass the  $^1G_4$  manifold has a RQE of  $\sim 60\%$ , the highest of any excited state manifold in  $\text{Tm}^{3+}$ .

## 2.7 Ytterbium

Ytterbium is the fourteenth lanthanide element and has 13 electrons in its  $4f$  shell. The ytterbium ion has the simplest energy level structure of all the rare earth ions, with a excited state located  $\sim 10\,000\text{ cm}^{-1}$  from the ground state; all other levels involve transitions in the ultraviolet region of the electromagnetic spectrum. The energy level diagram for  $\text{Yb}^{3+}$  in a silica glass host is shown in Figure 2.5. Due to the large energy gap between the  $^2F_{7/2}$  and  $^2F_{5/2}$  excited state, relaxation from the  $^2F_{5/2}$  manifold is radiative in the majority of host materials. The radiative lifetime of this state has been shown to vary from 700 - 1400  $\mu\text{s}$  depending on the host material [83]. The lack of higher lying energy states reduces the possibility of any energy transfer and ESA processes. The relatively large Stark splitting of the ground and excited state manifold results in broad absorption and emission spectra (see Figure 2.6), permitting lasing over a tunable range from 980 - 1140 nm.

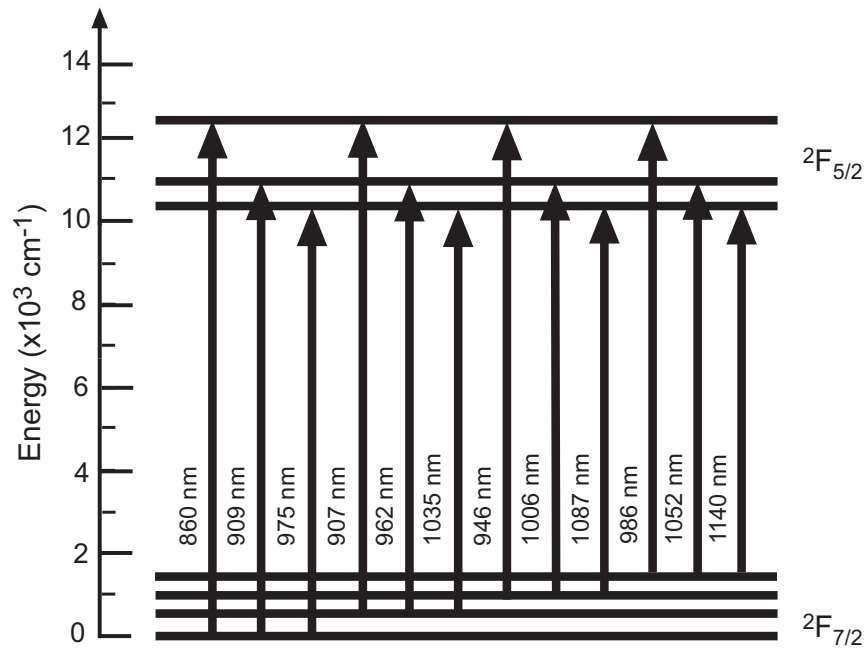


**Figure 2.5:** Simplified energy level diagram of  $Yb^{3+}$  in silica glass.

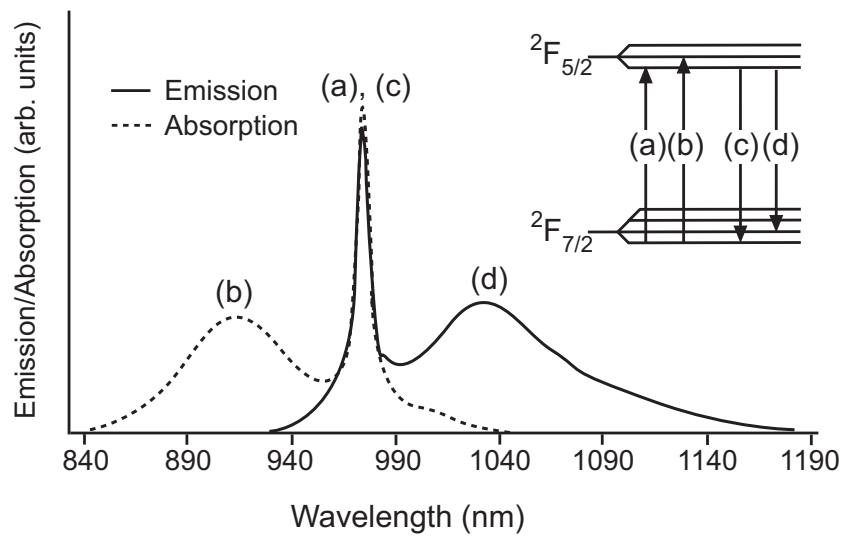


**Figure 2.6:** Absorption and emission spectrum of  $Yb^{3+}$ -doped silica glass [69].

The large absorption and emission cross sections and negligible non-radiative decay of  $Yb^{3+}$  has allowed the development of high power fibre lasers. The highest reported single mode output from a  $Yb^{3+}$ -doped fibre laser to date is 2 kW at 1070 nm [84].

# Chapter 3

## EXPERIMENTAL ARRANGEMENTS AND TECHNIQUES

This chapter reviews the experimental techniques used to characterise the rare earth doped alumino-silicate and germano-silicate fibres fabricated for this work. The details regarding the fabrication of the fibre samples are presented in Chapter 4.

### 3.1 Absorption characteristics of rare earth doped optical fibres

To investigate the absorption properties of rare earth doped glasses, a broadband light source is required to cover the spectral range from 440 - 2000 nm. A tungsten bulb provided sufficient luminescence in the region of interest. The light source was spectrally dispersed using a 0.25 m Jarrell-Ash monochromator. Three grating blazes of 1200, 800 and 600 grooves/mm were used to optimise the three spectral regions of 440 - 1040, 1040 - 1500 and 1500 - 2000 nm, respectively. A resolution of 2 nm was achieved by placing 250  $\mu\text{m}$  slits at the entrance and exit of the monochromator. The monochromatic light exiting the monochromator was focussed, using a  $20\times$  objective, into a length of 1550 nm single mode fibre (SMF). The doped fibre section was then spliced to the 1550 nm SMF. In most cases, the doped fibres had cutoff wavelengths greater than 1600 nm. The length of 1550 nm SMF was used to minimise the number of modes being launched into the doped fibre; this ensured that an accurate account of the attenuation of the fundamental mode was obtained. The light transmitted through the length of doped fibre was detected using various photodiodes. By modulating the light source before entering the monochromator, the lock-in technique could be used to enhance the signal to noise ratio. For the

wavelength ranges 440 - 1040 and 1040 - 1600 nm, Ando Si (AQ-4304) and InGaAs (AQ-2105) detector heads were used, respectively, in conjunction with an Ando (AQ-2034) optical power meter. The optical power meter had a built in lock-in amplifier which allowed light levels as small as tens of picowatts to be detected. For the mid infra-red region of the spectrum, from 1600 - 2000 nm, a Thorlabs (FGA20) photodiode was used in a dual trans-impedance amplifying circuit. A Stanford Research Systems (SRS530) lock-in amplifier was used in conjunction with the photodiode in this configuration. It should also be noted that, for wavelengths greater than 1150 nm, an 1100 nm long pass filter was placed immediately after the exit slit to eliminate unwanted higher orders of the monochromator grating. A schematic diagram of the experimental arrangement is shown in Figure 3.1.

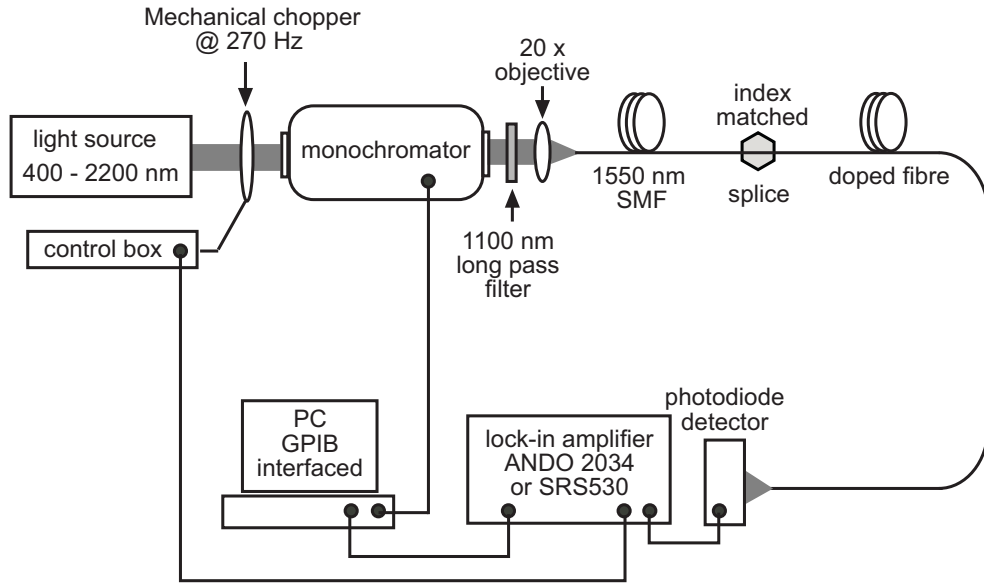


**Figure 3.1:** Attenuation measurement system used to obtain the absorption spectrum of rare earth doped fibres.

To obtain the absorption spectrum the multiple cutback technique was used in conjunction with the following wavelength dependent relationship:

$$\text{loss} \left[ \frac{dB}{km} \right] (\lambda) = \left( \frac{10}{L} \right) \log \left( \frac{I_o(\lambda)}{I(\lambda)} \right), \quad (3.1)$$

where  $I(\lambda)$  is the signal at a particular wavelength from the initial length of fibre,  $I_o(\lambda)$  is the signal at a particular wavelength after the initial length was cutback and  $L$  is the difference in length between the two measurements.

In general, rare earth dopants are confined to the core region of an optical fibre. Therefore, when measuring the absorption of these dopants, the probing light source must travel down the core of the fibre. Any light travelling through the cladding will not experience absorption due to the dopants and can cause significant power measurement errors, particularly in the case of short fibre lengths and high rare earth concentrations. By bending the doped fibre near the splice and applying refractive index matching fluid to the stripped section, the light travelling through the cladding can be guided out into the index matching fluid so that it is not detected at the end of the doped fibre section. Since the cutback method is intensity dependent, it is also important to ensure that the amount of light coupled into the doped fibre remains the same before and after the cutback. For this reason, the coupled and spliced sections of the fibres were untouched throughout the measurement procedure.

## 3.2 Rare earth ion concentration in optical fibres

The rare earth ion concentration of the fabricated samples was estimated by comparing the magnitude of the peaks observed in the absorption spectra to the reported absorption strengths for the particular transitions in silica glass [85]. There is, however, an uncertainty associated with this comparison as the absolute concentration of rare earth ions is related to the host dependent absorption strengths and/or line shapes. Examples of the variation in shape and strength of the absorption spectra of  $\text{Tm}^{3+}$  -doped fibres with different host compositions are shown in Figures 4.3 and 4.5 in Chapter 4. As a result of these variations, comparisons of the rare earth ion concentrations between host glasses of different compositions are open to a large degree of systematic error. With this in mind, concentration values are generally quoted to an accuracy of  $\sim 10\%$ .

### 3.3 Refractive index profiles

The refractive index profile (RIP) of an optical preform or fibre is an important measurement as it allows evaluation of some important parameters of the waveguide such as the numerical aperture (NA) and V parameter. The RIPs of the optical preforms used in this work were measured using a York Industries (P101) refractive index profiler, while the RIPs of the optical fibres were determined using an York (S14) refractive index profiler.

In the first instance, the RIPs of the fabricated fibres were used to ensure the fibre would guide and to calculate the cutoff wavelength, which is the wavelength below which the fibre no longer supports just the single fundamental mode. In addition to these fundamental checks, the RIP was used to determine the core concentration of the co-dopant used to increase the refractive index. This is an extremely useful technique provided the core is free from other index raising co-dopants such as fluorine, boron or large amounts of rare earth ions. Since aluminium was the sole index raising dopant in the aluminosilicate fibres, an estimation of the core  $\text{Al}_2\text{O}_3$  concentration could be obtained with the knowledge that the optical index of silica increases by  $2.3 \times 10^{-3}$  per mol% of  $\text{Al}_2\text{O}_3$  [86]. An example of a measured RIP from a  $\text{Tm}^{3+}$ -doped aluminosilicate fibre fabricated in this work is shown in Figure 3.2.

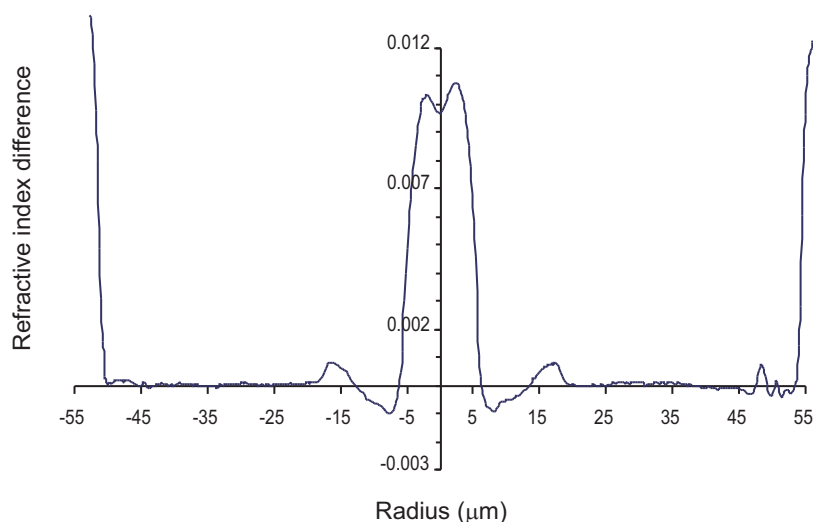


**Figure 3.2:** RIP of a  $\text{Tm}^{3+}$ -doped aluminosilicate fibre.

The RIP profile is typical for an alumino-silicate fibre; there is little ‘burnoff’ in the central core region which indicates that the  $\text{Al}_2\text{O}_3$  does not suffer significant volatilisation during the collapse of the preform. The slight rise in the index in the regions either side of the core may be attributed to small impurities in the gas flow system. The reduction in the index difference at regions just before the core are a result of a single pass with fluorine which was conducted before the deposition of the core. The fluorine was used to vent the preform, eliminating any unwanted contaminants which could have made their way into the core. It should be noted that fluorine was not used in the deposition of the core layers.

The RIP of a germano-silicate fibre fabricated in this work is shown in Figure 3.3. Germano-silicate fibres have been shown to exhibit significant ‘burnoff’ in the central core region and occurs as a result of the high temperatures required to collapse the preform.

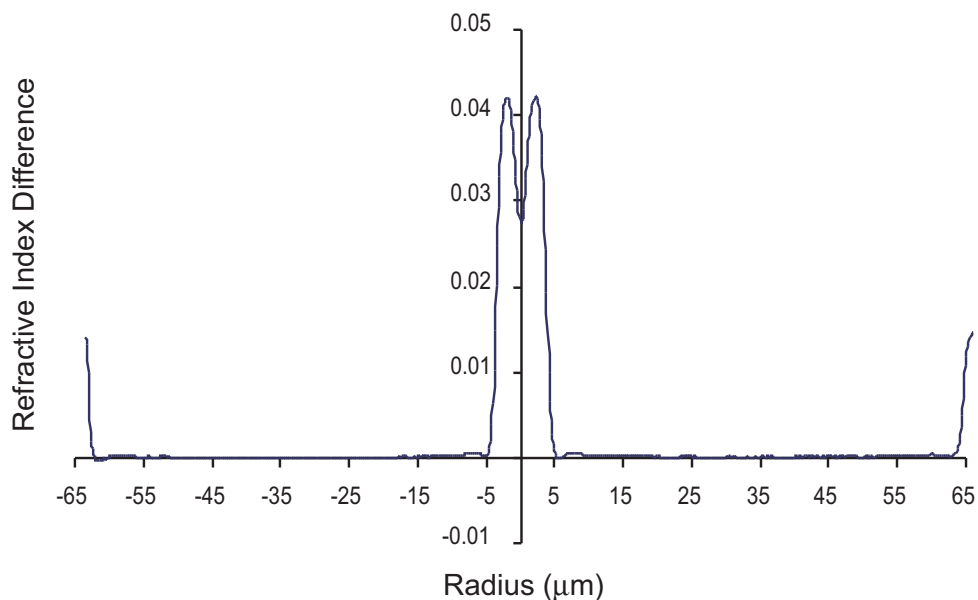


**Figure 3.3:** RIP of a  $\text{Tm}^{3+}$ -doped germano-silicate fibre.

### 3.4 Fluorescence lifetime measurements

Studies of the fluorescence lifetimes of particular energy manifolds required a number of different excitation sources, optical filters and detectors. The appropriate configuration for each manifold studied is listed in Table 3.1. When measuring the fluorescence lifetime of a particular excited manifold, it is preferred that only a small fraction of ions from the ground state are excited to that manifold. If a situation is reached where a significant fraction of the ground state ions are excited (i.e. the ground state population is depleted) and energy transfer processes from the manifold under investigation exist, the measurement of the fluorescence lifetime can become masked by competing effects. To avoid this unwanted regime the energy manifolds were probed using short excitation pulses, which limits the peak power per pulse and does not allow the manifold to saturate. The  ${}^3F_4$  manifold of  $\text{Tm}^{3+}$  and the  ${}^2F_{5/2}$  manifold of  $\text{Yb}^{3+}$  were studied under 30  $\mu\text{s}$  excitation pulses, whilst the  ${}^3H_4$  manifold of  $\text{Tm}^{3+}$  was studied with 3  $\mu\text{s}$  pulses. The repetition rate of the pulses was 40 Hz for all fluorescence lifetime measurements. This repetition rate left ample time ( $> 10 \tau_{lifetime}$ ) for each excited manifold of  $\text{Tm}^{3+}$  and  $\text{Yb}^{3+}$  to decay back to the ground state.

The accurate measurement of a fluorescence lifetime requires the detection system to have a sufficiently fast response time. A general rule of thumb is the response time should be less than 1/10 of the lifetime which is to be measured. The response time of the measurement system is limited by the response time of the detector and amplifying circuitry as well as the time taken to turn the excitation pulses on and off. An Avtech laser diode driver was used to control each laser diode which had an on/off response time of 50 ns, which is more than adequate when trying to determine lifetimes within the range of tens to hundreds of microseconds. The total response time of the system was measured by detecting the light from the laser diode and measuring the time it took to reduce from 90% to 10% of its original value. The measured response times are listed in Table 3.1 for each detector used. In all cases the response time was less than 1/10 of the measured lifetime.

Energy manifold	Pump source	Filter	Detector	Response time
$\text{Tm}^{3+}$ ( $^3F_4$ )	1586 nm laser diode	1500 nm long pass	InGaAs photodiode (FGA20)	13 $\mu\text{s}$
$\text{Tm}^{3+}$ ( $^3H_4$ )	780 nm laser diode	$810 \pm 10$ nm	PMT (R930)	600 ns
$\text{Tm}^{3+}$ ( $^1G_4$ )	980 nm laser diode	$475 \pm 10$ nm	PMT (R930)	600 ns
$\text{Yb}^{3+}$ ( $^2F_{5/2}$ )	980 nm laser diode	$1030 \pm 10$ nm	InGaAs photodiode (FGA10)	13 $\mu\text{s}$

PMT - Photo-multiplier tube

**Table 3.1:** Experimental configuration for the measurement of the fluorescence lifetime of the excited manifolds of  $\text{Tm}^{3+}$  and  $\text{Yb}^{3+}$ . Note: the Thorlabs InGaAs photodiode (FGA20) had a peak sensitivity of  $\sim 1$  A/W near  $1.9 \mu\text{m}$  compared to traditional InGaAs photodiodes for which peak sensitivities occur around  $1.6 \mu\text{m}$ . The peak sensitivity at longer wavelengths was ideal for measuring the fluorescence signal from the  $^3F_4$  manifold of  $\text{Tm}^{3+}$ , which peaks around 1850 nm.

Energy manifolds can be excited either directly or in-directly. Direct excitation involves pumping the energy manifold at a wavelength near the peak absorption for that manifold and monitoring the fluorescence decay at a similar wavelength. This technique provides an accurate account of the decay characteristics of the excited manifold. In-direct pumping, on the other hand, relies on relaxation and up-conversion mechanisms (radiative or non-radiative) to populate the energy manifold of interest. In this case, the fluorescence decay from the manifold can exhibit characteristics of the higher or lower energy manifold feeding it, particularly in the case where the feeding manifold has a considerably longer lifetime. Understanding the true nature of the decay from the energy manifold of interest can then become difficult unless a quantitative rate equation analysis is undertaken to factor in the population effects of the other excited manifolds. With this in mind, a considerable effort was made to excite the energy manifolds directly. With the exception of the  $^1G_4$  manifold of  $\text{Tm}^{3+}$ , each excited manifold in  $\text{Tm}^{3+}$  and  $\text{Yb}^{3+}$  was excited

directly. The  $^1G_4$  manifold was studied indirectly using sequential energy transfer up-conversion processes from  $\text{Yb}^{3+}$  to  $\text{Tm}^{3+}$  ions. The sequential up-conversion process has a lifetime much shorter than the  $^1G_4$  manifold and hence the fluorescence decay is unaffected by the feeding mechanism.

All fluorescence measurements were conducted with the detector located transverse to the doped fibre. Side fluorescence measurement is preferred because reabsorption is minimal as the core of an optical fibre is optically thin. Fibre lengths were kept to 50 mm to minimise the effects of amplified spontaneous emission (if any); although the amplified spontaneous emission signal is confined to the core of the fibre its effect on the side fluorescence still remains. Index matching fluid was also applied to the end of each sample to eliminate any unwanted reflections of the pump or fluorescence. The fibre samples were mounted on a Melles Griot xyz translation stage to enable accurate optimisation of the fluorescence signal. The side fluorescence was collected via an aspheric lens ( $f = 4$  mm) immediately after the splice to the SMF providing the excitation. The fluorescence signal was then passed through the appropriate filter to the appropriate detector (see Table 3.1). The excitation conditions remained as constant as possible for each fibre sample, but due to small variations in the core sizes of the fibres and the splices to the excitation source, these conditions may have varied slightly and therefore the values given for the incident pump power are accurate to within  $\sim 5$  %. The decay waveforms were captured on a Tektronix TDS320 digital oscilloscope and averaged 256 times before being sent to a PC for further processing. Low fluorescence signals were averaged 1024 times to improve the signal to noise ratio. Figure 3.4 shows a schematic diagram of the fluorescence lifetime experimental arrangement.

The characteristic lifetime of each manifold was found by fitting a single exponential function to the measured waveforms with the curve fitting program Tablecurve 2D Ver. 5.0. Before fitting, the detector offset was removed and the data were normalised to the initial voltage. The detector offset was corrected by subtracting the measured voltage just before the excitation pulse occurred, see Figure 3.5.

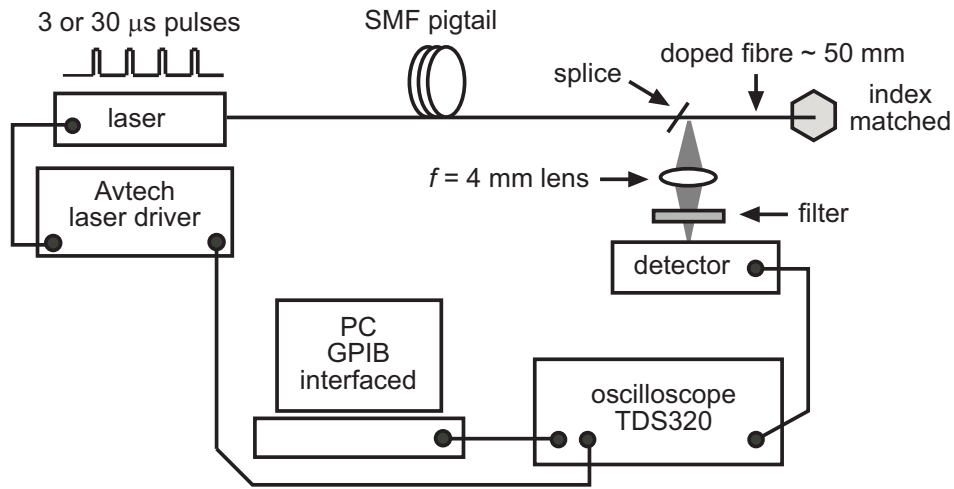


**Figure 3.4:** Fluorescence lifetime experimental arrangement.

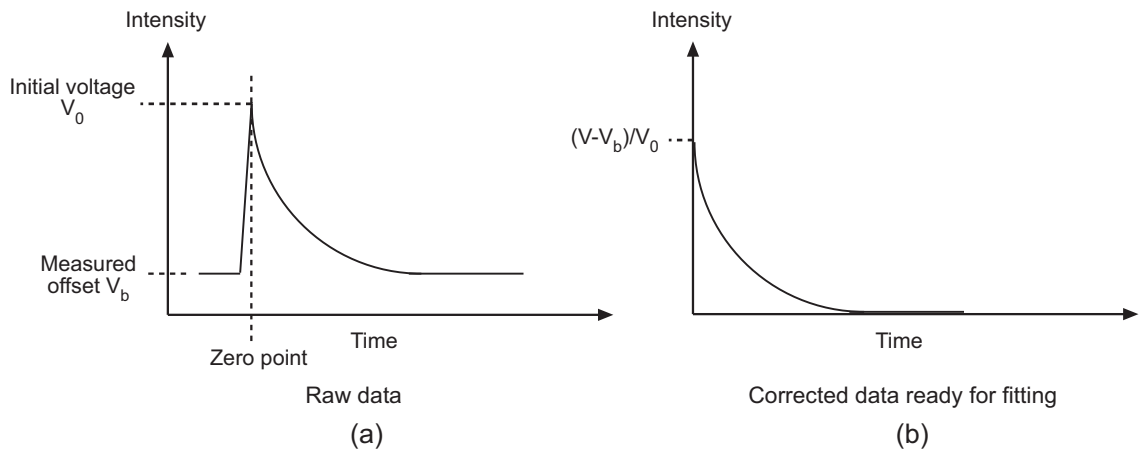


**Figure 3.5:** Fitting procedure for the fluorescence decay waveforms. (a) Simulated raw data from detector and (b) corrected data ready for fitting with offset removed and the signal normalised.

The decay waveforms were measured over a time scale at least 8 times the lifetime of the particular manifold to ensure that 99.96 % of the light from the emitting manifold had decayed. The zero point in time was determined from the trigger pulse from the laser diode driver. The single exponential fitting equation is given by:

$$I(t) = I_0 \exp(-t/\tau_{ife}) \quad (3.2)$$

where  $I_0$  is the initial intensity before the pump excitation is removed and  $\tau_{ife}$  is the fluorescence lifetime.

The suitability of fitting a single exponential function to the decay of rare earth ions in a glass host is discussed at length in Chapter 5.

### 3.5 Steady state luminescence intensities

Steady state luminescence intensity measurements were carried out using a similar arrangement to that shown in Figure 3.4, but with the digital oscilloscope replaced by a lock-in amplifier (SRS530). The excitation sources were operated in quasi-continuous wave mode with 12.5 ms pulses at a repetition rate of 40 Hz to allow for lock-in detection. As the 12.5 ms pulse length is at least 10 times longer than the longest rise time of any excited manifold in the  $\text{Tm}^{3+}$  or  $\text{Yb}^{3+}$  -doped silica system, the intensity of the luminescence represents the intensity under steady state conditions.

### 3.6 Luminescence spectra

The low luminescence light levels radiating from the side of the fibre prevented a side luminescence spectrum from being measured. Instead, counter-propagating luminescence spectra were obtained using a  $2 \times 2$  optical fibre coupler in the experimental arrangement shown in Figure 3.6.

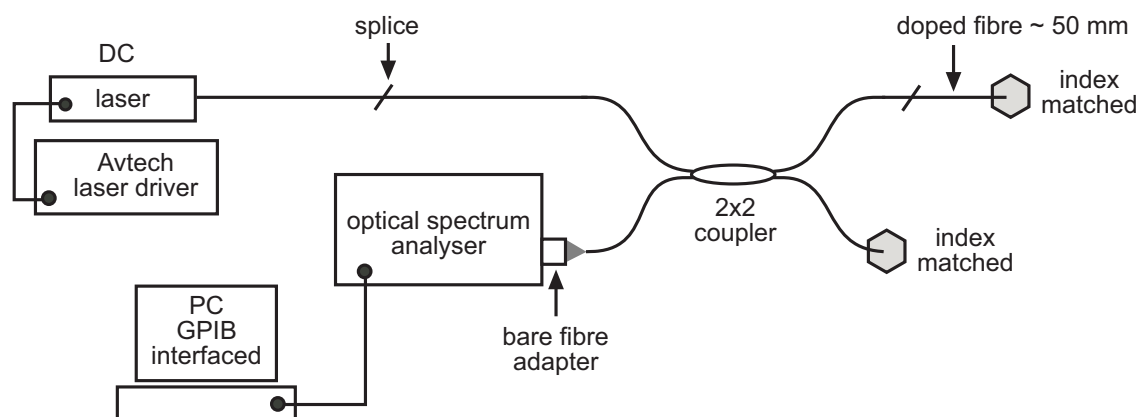


**Figure 3.6:** Experimental arrangement to measure the counter-propagating luminescence spectrum from an optical fibre sample.

The excitation source was operated in continuous wave mode at the maximum operating current of the source. The doped fibre section was spliced to the coupler arm which contained the majority of pump light. The resulting fluorescence which propagates in the forward direction is termed co-propagating fluorescence and the fluorescence which propagates back through the  $2 \times 2$  coupler is termed counter-propagating fluorescence. The drawback to measuring the co- or counter-propagating fluorescence is that the fluorescence is subjected to reabsorption as it propagates through the doped sample, often producing dips at wavelengths where a strong ground state transition exists. The counter-propagating luminescence spectra reported in this work were recorded using an Ando AQ6310B optical spectrum analyser with a resolution of 5 nm.

## Chapter 4

# THULIUM-DOPED SILICA FIBRES

### 4.1 Introduction

The  $\text{Tm}^{3+}$  ion offers a range of fluorescence wavelength bands extending from 0.475 up to 3.5  $\mu\text{m}$  which have, or have the potential for, applications in a variety of fields such as telecommunications, medicine, atmospheric sensing and defence, to name but a few. More notably, the 1.47 - and 2 -  $\mu\text{m}$  transitions of  $\text{Tm}^{3+}$  have attracted the most attention due to their potential application as optical amplifiers and high powered lasers. Unfortunately, in silica glass these transitions are dominated by non-radiative decay, due to the relatively high phonon energy of the glass, which limits the quantum efficiency of both transitions to a few percent. For thulium doped silica based fibres to become a viable solution for the aforementioned applications, considerable improvement in the quantum efficiency of these transitions is required.

Improvements in the quantum efficiency of optical transitions can be achieved by modifying the local environment surrounding the rare earth ion [87, 88, 39]. Such modifications are often achieved by breaking up the structure of atoms surrounding a rare earth ion with other, often larger elements, termed network modifiers. Discussing the role of network modifiers requires an understanding of the basic structure of silica glass. Silica is built from basic structural units, the most common of which is the network former  $(\text{SiO}_4)^{2-}$ . This network former consists of a silicon atom at the centre of a tetrahedron with an O atom bonded to each corner, as shown in Figure 4.1.



**Figure 4.1:** Tetrahedral structure of  $\text{SiO}_4^{2-}$ , showing 4 oxygen atoms surrounding the central silicon atom. [89].

The formation of the glass structure was first proposed by Zachariasen who suggested a set of four rules for glass formation in an oxide in order to obtain a random network [90]. The four rules are listed below:

1. oxygen atoms are linked to no more than two atoms of type A (A = B, Si, As, Ge, etc.);
2. the oxygen co-ordination around A is small (i.e. 3 or 4);
3. oxygen polyhedra share corners but not edges or faces and
4. at least three corners are shared.

This commonly accepted structure of silica glass is therefore tetrahedral units that are tightly connected by their corners through oxygen atoms (bridging oxygens); these random connections form a 3 dimensional structure similar to that shown in Figure 4.2.

The strong electron bond which exists between the silicon and oxygen atoms give silica glass its impressive mechanical strength and thermal properties. The drawback to the silica glass network is that it can accommodate only a small number of rare earth ions before clustering occurs [91]. One explanation of this phenomenon is that



**Figure 4.2:** 3 - dimensional structure of SiO<sub>2</sub>, showing the interconnection of the tetrahedral units [89].

rare earth ions require co-ordination of a sufficiently high number of non-bridging oxygens to screen the electric charge of the ion, but the highly rigid silica glass network cannot sufficiently co-ordinate non-bridging oxygens resulting in a system with a higher enthalpy state. Therefore, rare earth ions tend to share non-bridging oxygens to reduce the excess enthalpy, resulting in the formation of clusters [92]. To accommodate greater amounts of rare earth ions, network modifiers are required to increase the number of available non-bridging oxygen ions in the silica glass network. Network modifiers such as Na<sup>3+</sup> and Al<sup>3+</sup> are often used to facilitate the incorporation of rare earth ions, as their size is substantially greater than the basic network. These modifiers act to break the bridging oxygens to form non-bridging oxygens which can be used to co-ordinate the rare earth ions. Of the network modifiers studied in silica glass to date, aluminium has shown the most favourable characteristics. In studies of Nd<sup>3+</sup> -doped silica glass, clustering of 0.29 mol% of Nd<sub>2</sub>O<sub>3</sub> ions was eliminated with the incorporation of 2.87 mol % of Al<sub>2</sub>O<sub>3</sub> [92]. Aluminium has also been used to improve the efficiency of Er<sup>3+</sup> -doped fibre amplifiers by eliminating the quenching effects from the  ${}^4I_{13/2} \rightarrow {}^4I_{15/2}$  transition [93]. Since the configuration of

$\text{Tm}^{3+}$  is not significantly different from that of  $\text{Er}^{3+}$  and  $\text{Nd}^{3+}$ , one could speculate that similar effects may be observed in  $\text{Tm}^{3+}$  -doped silica glasses.

## 4.2 Fabricated fibre samples

For this research the network modifiers aluminium (Al), germanium (Ge), antimony (Sb) and tin (Sn) were co-doped with silica glass in an effort to modify the local environment of the  $\text{Tm}^{3+}$  ions. The effects of co-doping are examined by studying the spectroscopic properties of the  $\text{Tm}^{3+}$  ion in the different glass host environments using standard spectroscopic techniques. A total of twelve  $\text{Tm}^{3+}$  -doped silica pre-forms and their fibres were fabricated and used in this work. Table 4.1 lists the core dopants of each sample and categorises the samples according to their host composition. The samples were fabricated by a combination of the author, supervisor and the team at the Laboratoire de Physique de la Matière Condensée (LPMC) in Nice, France, using the modified chemical vapour deposition (MCVD) and solution doping techniques [94].

Alumino-silicate samples							
Sample	Network Modifiers	$\text{Tm}_2\text{O}_3$ (ppm)	$\text{Al}_2\text{O}_3$ (mol %)	$\text{SbCl}_4$ (mol/L)	$\text{SnCl}_4$ (mol/L)	P	LPMC Label
Al-1	Al	100	1.9	-	-	-	C019
Al-2	Al	240	3.4	-	-	-	B012
Al-3	Al	450	4.4	-	-	-	C035
Al-4	Al	1850	4.6	-	-	-	C036
Al-5	Al	220	4.8	-	-	-	C034
Al-6	Al	1950	5.4	-	-	-	C040
Al-7	Al	250	9.0	-	-	-	C063
Al-8	Al:P	32000	1 <sup>a</sup>	-	-	yes	Tm11
Al-9	Al:Sb	330	3.6	2.0	-	-	A027
Al-10	Al:Sn	260	2.7	-	1.9	-	A025
Germano-silicate samples							
Sample	Network Modifiers	$\text{Tm}_2\text{O}_3$ (ppm)	Ge	$\text{SbCl}_4$ (mol/L)	$\text{SnCl}_4$ (mol/L)	P	LPMC Label
Ge-1	Ge:Sb	300	yes	3.9	-	-	A030
Ge-2	Ge:Sn	1400	yes	-	1.9	-	A013

**Table 4.1:** Core dopants of the  $\text{Tm}^{3+}$  -doped silica fibres. Note: P refers to the doping of phosphorus, while <sup>a</sup> indicates the solution concentration of  $\text{AlCl}_3$  in mol/L (see text).

The  $\text{Tm}_2\text{O}_3$  concentrations listed in Table 4.1 were estimated by comparing the absorption peak at 785 nm to that obtained by Hanna *et al.* [85] in  $\text{Tm}^{3+}$  -doped silica glass. The absorption peaks were measured using the multiple cutback technique as described in Section 3.1. The RIPs of the  $\text{Tm}^{3+}$  -doped alumino-silicate fibres were used to estimate the  $\text{Al}_2\text{O}_3$  concentration, as discussed in Section 3.3. The  $\text{GeO}_2$  concentration could not be estimated from the RIP as other co-dopants were also used in the fabrication of these samples. The addition of  $\text{Sb}_2\text{O}_3$  and  $\text{SnO}_2$  into the core of the optical preform makes a non-negligible contribution to the RIP. It should be noted here that the  $\text{GeO}_2$  was added to the core during the collapse of the preform. The flow rate of  $\text{GeOCl}_4$  was kept constant during the fabrication of each germano-silicate sample and therefore it is expected that the  $\text{GeO}_2$  concentration should not vary significantly between fibre samples. Phosphorus was added to the Al-8 sample as a glass softening agent; due to the core dopants and high concentration of  $\text{Tm}_2\text{O}_3$ , the concentration of phosphorus and  $\text{Al}_2\text{O}_3$  was unable to be determined. The concentrations of  $\text{SbCl}_4$  and  $\text{SnCl}_4$  given in Table 4.1 are the solution concentrations and for the same reasons described for  $\text{GeO}_2$  their core concentrations could not be estimated from the RIP.

As the primary focus of this work is to improve the quantum efficiency of the  ${}^3H_4 \rightarrow {}^3F_4$  S-band transition, high  $\text{Tm}_2\text{O}_3$  concentrations were avoided, with the exception of Al-8. Many authors have observed cross relaxation in heavily doped thulium glasses [95, 96, 97]. This cross relaxation acts to reduce the lifetime of the  ${}^3H_4$  manifold, which results in a reduction in the radiative quantum efficiency of the  ${}^3H_4 \rightarrow {}^3F_4$  transition.

### 4.3 Absorption measurements

The absorption spectra of a rare earth ion can, in some cases, provide detailed information regarding the position of individual Stark levels within an energy manifold. This is particularly true in the case of crystal host materials where rare earth ions effectively experience the same local environment and therefore exhibit identical absorption and emission characteristics. However, in the case of glasses, the amorphous nature of the structure results in rare earth ions experiencing slightly different local environments. This results in inhomogeneous broadening and limits the ability to identify the individual Stark components. However, valuable information regarding the position of the energy manifold can still be obtained. In this section, absorption spectra of the different fibre types are compared to examine any differences in the position and shape of each absorption transition. Variations in the positions and shapes of the absorption lines are a first step towards identifying whether co-doping with network modifiers actually affects the local environment of the  $\text{Tm}^{3+}$  ion.

#### 4.3.1 Alumino-silicate fibres

The absorption spectra of the fibre samples were measured using the experimental arrangement described in Section 3.1. To limit the number of variables in the comparison of these spectra, fibres samples Al-1, Al-2, Al-5 and Al-7 were initially chosen for comparison as they cover a large  $\text{Al}_2\text{O}_3$  concentration range but have similar  $\text{Tm}_2\text{O}_3$  concentrations. Unfortunately, the full spectrum of Al-1 could not be obtained due to the poor guiding properties of the fibre. The low  $\text{Al}_2\text{O}_3$  concentration of Al-1 resulted in a small index difference between the core and the cladding and hence core light tended to leak into the cladding; this prevented long fibre lengths from being used to obtain the entire spectrum. Therefore, Figure 4.3 shows the absorption spectra for the samples Al-2, Al-5 and Al-7, while Table 4.2 lists the measured peak wavelengths and full width half maxima (FWHM) of each transition.

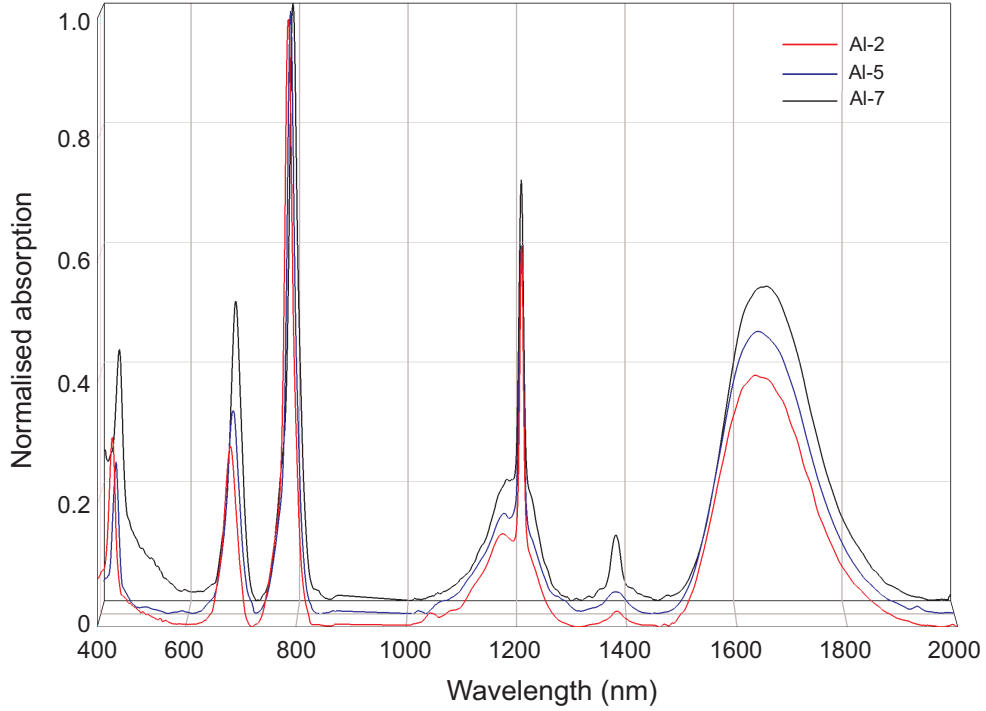


**Figure 4.3:** Absorption spectra of  $\text{Tm}^{3+}$ -doped alumino-silicate fibres Al-2, Al-5 and Al-7 at  $\text{Al}_2\text{O}_3$  concentrations of 3.4, 4.8 and 9 mol %, respectively. Note: the spectra have been normalised to the peak at 786 nm from the  ${}^3H_4$  manifold.

Manifold	Sample	$\lambda_{peak}$ (nm)	FWHM (nm)
${}^1G_4$	Al-2	467.0	11.5
	Al-5	468.0	14.5
	Al-7	468.0	12.5
${}^3F_{2,3}$	Al-2	681.0	27.5
	Al-5	682.0	26.5
	Al-7	682.0	24.5
${}^3H_4$	Al-2	787.0	19.0
	Al-5	787.0	18.0
	Al-7	788.0	19.0
${}^3H_5$	Al-2	1209.5	10.5
	Al-5	1208.5	10.0
	Al-7	1208.5	10.0
${}^3F_4$	Al-2	1632.5	181.5
	Al-5	1641.5	182.0
	Al-7	1660.5	179.5

**Table 4.2:** Measured peak absorption wavelengths and FWHMs for the energy manifolds of  $\text{Tm}^{3+}$ -doped alumino-silicate fibres. Note: the FWHM stated for the  ${}^3H_5$  manifold was determined from the narrow peak centred around 1208 nm.

Figure 4.3 shows the absorption strength from the  $^1G_4$ ,  $^3F_{2,3}$ ,  $^3H_5$  and  $^3F_4$  manifolds increase in comparison to the  $^3H_4$  manifold for increasing  $\text{Al}_2\text{O}_3$  concentration. Host dependent variations in the absorption strength of particular transitions are not uncommon and have been frequently reported in the literature for other rare earth ions, namely  $\text{Er}^{3+}$  and  $\text{Eu}^{3+}$ , in similar host materials [87, 98]. For alumino-silicate glass, Tanabe *et al.* have attributed the increase to the change in the local symmetry of the rare earth ions, in which the non-bridging oxygen ions tend to co-ordinate to the ions, accompanied by the formation of an Al-O-Si bond [87].

The measured peak wavelengths and FWHMs of the  $^1G_4$ ,  $^3F_{2,3}$ ,  $^3H_4$  and  $^3H_5$  manifolds do not show any significant change with increasing  $\text{Al}_2\text{O}_3$  concentration (see Table 4.2), indicating that the Stark energy level positions of these manifolds are largely unaffected by the addition of  $\text{Al}_2\text{O}_3$  into the glass network. The  $^3F_4$  manifold, however, exhibits a significant red shift in the peak absorption wavelength with increasing  $\text{Al}_2\text{O}_3$  concentration. The trend of the  $^3F_4$  peak absorption shift as a function of  $\text{Al}_2\text{O}_3$  concentration is shown in Figure 4.4; although three data points is not ideal it can be suggested that the shift may be linearly dependent on the  $\text{Al}_2\text{O}_3$  concentration over the concentration range studied here.

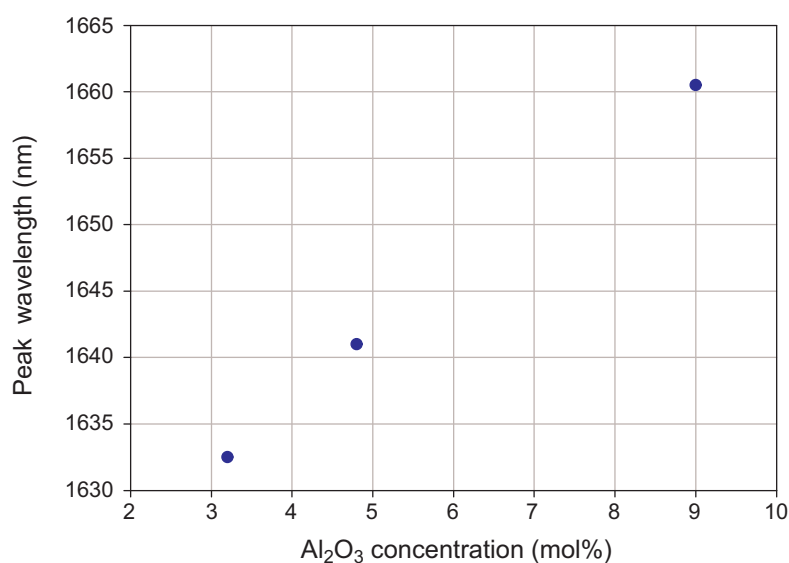


**Figure 4.4:**  $^3F_4$  peak absorption wavelength as a function of  $\text{Al}_2\text{O}_3$  concentration for three alumino-silicate fibres.

The reason for the selective wavelength shift of the  ${}^3F_4$  manifold is unclear; the large line broadening of the  ${}^3F_4 \rightarrow {}^3H_6$  transition reflects the strong coupling of the manifold to the local strain in the silica glass [73]. This strong coupling may result in the  ${}^3F_4$  manifold experiencing a greater propensity to the variations in the strain and crystal field caused by the incorporation of  $\text{Al}_2\text{O}_3$  into the glass network.

The role  $\text{Al}_2\text{O}_3$  plays when incorporated into glass has been proposed by Arai *et al.* in terms of a structural model and solution chemistry [92]. The structural model for aluminium co-doping assumes that aluminium is incorporated into the silica network in two local bonding configurations; the first as a network former in the tetrahedral bonding configuration  $\text{AlO}_{4/2}$  and the second as a network modifier in an octahedral co-ordination of oxygen atoms  $\text{AlO}_{6/2}$ . These two bonding configurations coupled with the tetrahedral configuration of  $\text{SiO}_2$  are expected to surround the rare earth ion and accommodate them into the glass network without sacrificing excess enthalpy. It would appear from the results in Figure 4.3 that the lower energy side of the  ${}^3F_4$  transition is more sensitive to the incorporation of  $\text{AlO}_{4/2}$  and  $\text{AlO}_{6/2}$  molecules. This effect alone may result in the  ${}^3F_4$  manifold exhibiting more non-radiative decay as the energy gap between the ground and excited states has been reduced. However, Arai *et al.* also points out that as the homogeneously dispersed rare earth ions couple with the aluminium to modify the  $\text{SiO}_2$  glass network the Raman spectral features of the glass can vary; this effect can have important implications for the phonon energies of the glass and therefore the excited state lifetimes of the rare earth ion. Section 4.4.1 explores the effect of  $\text{Al}_2\text{O}_3$  on the fluorescence lifetime of the  ${}^3F_4$  manifold and discusses some of the issues raised from this analysis.

### 4.3.2 Germano-silicate fibres

The other major host material studied in this investigation was germano-silicate. Samples Ge-1 and Ge-2 each contained an additional network modifier:  $\text{Sb}_2\text{O}_3$ , in the case of Ge-1 and  $\text{SnO}_2$  in the case of Ge-2. The effects of the additional network modifiers will be discussed in greater detail in Section 4.3.3. The absorption spectra of the Ge-1 and Ge-2 samples have been normalised to the 782 nm peak to aid in

the comparison of these two fibres and are presented in Figure 4.5, while Table 4.3 lists the measured peaks and FWHMs.

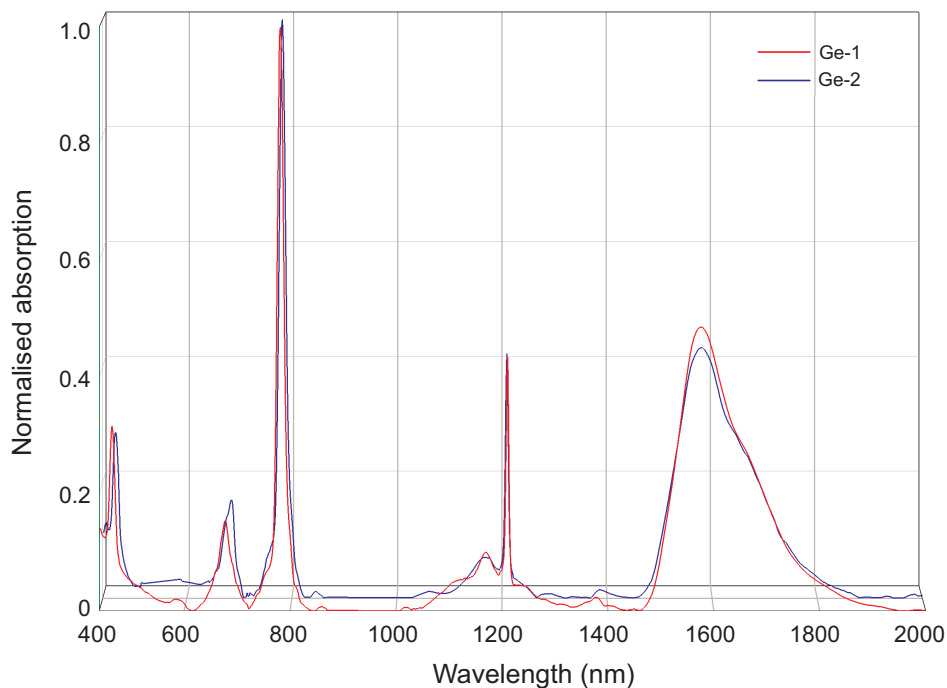


**Figure 4.5:** Absorption spectra of  $\text{Tm}^{3+}$ -doped germano-silicate fibres, normalised to the 782 nm absorption peak.

Manifold	Sample	$\lambda_{peak}$ (nm)	FWHM (nm)
$^1G_4$	Ge-1	464.0	10.0
	Ge-2	464.0	10.0
$^3F_{2,3}$	Ge-1	677.0	26.0
	Ge-2	685.0	26.0
$^3H_4$	Ge-1	782.0	15.0
	Ge-2	782.0	15.0
$^3H_5$	Ge-1	1210.5	6.5
	Ge-2	1209.5	7.5
$^3F_4$	Ge-1	1576.5	160.5
	Ge-2	1580.5	168.0

**Table 4.3:** Measured peak absorption wavelengths and FWHMs for the energy manifolds of  $\text{Tm}^{3+}$ -doped germano-silicate fibres. Note: the FWHM stated for the  $^3H_5$  manifold was determined from the narrow peak centred around 1210 nm.

In general, the germano-silicate fibres exhibited narrower absorption lines and shorter peak absorption wavelengths when compared to the alumino-silicate samples, indicating that germanium has impacted on the local environment surrounding the  $\text{Tm}^{3+}$  ion. The greatest effect was again observed in the  ${}^3F_4$  manifold; with a peak wavelength  $\sim 60$  nm less than the alumino-silicate fibres as well as an  $\sim 20$  nm reduction in the FWHM.

The incorporation of germanium into the silica structure is significantly different to aluminium as Ge is four-coordinated and hence does not significantly alter the tetrahedral structure of the silica network resulting in the  $\text{Tm}^{3+}$  ion being surrounded by an essentially silica environment. This has been verified in the work of Ainslie *et al.* who showed that the emission spectrum of  $\text{Nd}^{3+}$  -doped pure silica glass was identical to that in germano-silicate glass [99]. Thus, it is not surprising that the peak absorption of the  ${}^3F_4$  manifold shifted to shorter wavelengths, as the results from Section 4.3.1 suggest that in the limit of zero  $\text{Al}_2\text{O}_3$  concentration (i.e. pure  $\text{SiO}_2$  glass), the peak absorption should occur around 1617 nm.

### 4.3.3 Co-doping effects of Sb and Sn

Previous work on  $\text{Tm}^{3+}$  -doped antimony glasses has shown some promise in modifying the environment of the  $\text{Tm}^{3+}$  ion and effecting an increase in the fluorescence lifetime of the  ${}^3H_4$  manifold [34]. Unfortunately, the poor mechanical, chemical and thermal properties of these glasses prevent them from being readily spliced to standard telecommunication fibre [100]. The motivation of this investigation was to combine the advantageous properties of the network modifier with the silica glass host to achieve a favorable environment for the  $\text{Tm}^{3+}$  ion in which it would be able to emit with increased efficiency. From the results in Table 4.3, the effect of the additional network modifiers on the local environment of the  $\text{Tm}^{3+}$  appears to be small. If the addition of  $\text{Sb}_2\text{O}_3$  and  $\text{SnO}_2$  had significantly altered the local environment, the peak positions and FWHMs of these samples would not be in such good agreement. The same can also be said for the alumino-silicate fibres doped with  $\text{Sb}_2\text{O}_3$  and  $\text{SnO}_2$ ; see Figure 4.6 and Table 4.4 for the peak positions and FWHMs.

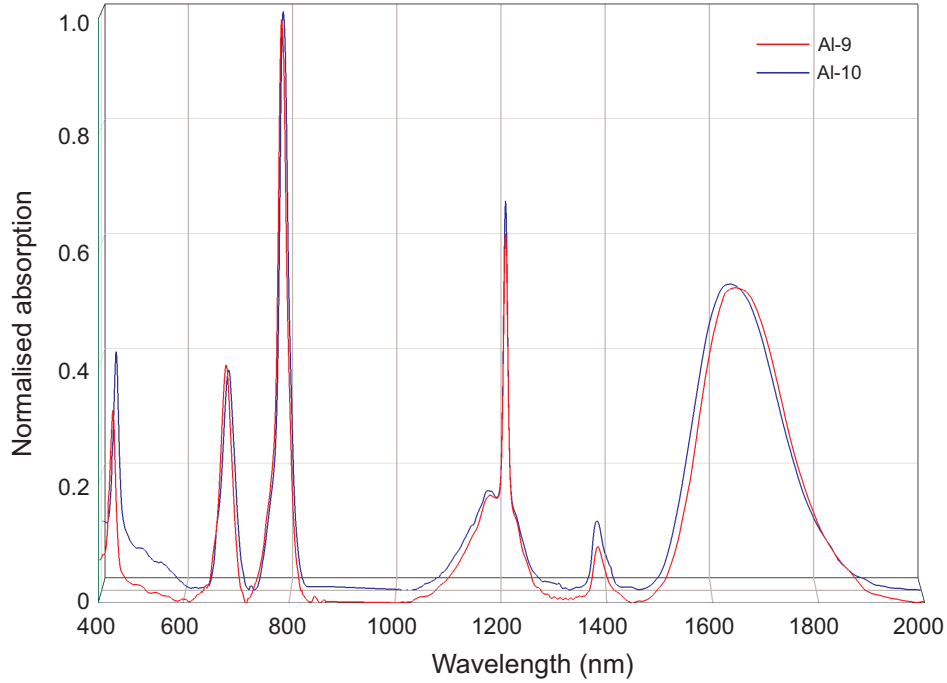


**Figure 4.6:** Absorption spectra of  $\text{Tm}^{3+}$ -doped alumino-silicate fibres co-doped with  $\text{Sb}_2\text{O}_3$  and  $\text{SnO}_2$ . Recall Al-9 is co-doped with  $\text{Sb}_2\text{O}_3$ , whilst Al-10 is co-doped with  $\text{SnO}_2$ .

Manifold	Sample	$\lambda_{peak}$ (nm)	FWHM (nm)
$^1G_4$	Al-9	468.0	12.0
	Al-10	468.0	11.5
$^3F_{2,3}$	Al-9	681.0	26.0
	Al-10	682.0	27.0
$^3H_4$	Al-9	786.0	19.5
	Al-10	786.0	19.5
$^3H_5$	Al-9	1208.5	11.5
	Al-10	1208.5	11.0
$^3F_4$	Al-9	1642.5	200.0
	Al-10	1636.5	195.0

**Table 4.4:** Measured peak absorption wavelengths and FWHMs for the energy manifolds of  $\text{Tm}^{3+}$ -doped alumino-silicate fibres co-doped with  $\text{Sb}_2\text{O}_3$  and  $\text{SnO}_2$ . Note: the FWHM stated for the  $^3H_5$  manifold was determined from the narrow peak centred around 1208 nm.

It can be seen that the peak absorption wavelengths and FWHMs agree with the results reported for the pure alumino-silicate fibre samples, providing further evidence that  $\text{Sb}_2\text{O}_3$  and  $\text{SnO}_2$  do not play effective roles in modifying the local environment of the  $\text{Tm}^{3+}$  ion. The variation in the peak position of the  $^3F_4$  manifold can be attributed to the amount of  $\text{Al}_2\text{O}_3$  present in the fibre core.

## 4.4 Fluorescence lifetime measurements

The quantum efficiency of an excited state transition is governed principally by the ratio of the measured and radiative fluorescence lifetimes. With this in mind, the only way the efficiency of a transition can be improved is to modify one or both of these fluorescence lifetimes. In the previous section it was seen that modifying the host environment surrounding a rare earth ion can result in a slight change in the energy level positions and distribution, but previous studies into the effects of host materials have demonstrated that the radiative lifetime of an energy manifold is relatively insensitive to such variations. Therefore, to effect a change in the efficiency of an excited state transition, changes in the measured fluorescence lifetime are required. Fortunately, the measured lifetime is sensitive to the host material as it is governed by the reciprocal addition of the radiative and non-radiative decay rates. Since the non-radiative decay rate is dependent on the phonon energy of the host material and the energy gap between the excited and next lowest energy manifold, slight variations in the energy gap caused by host dependant shifting of the Stark energy levels coupled with modifications to the local phonon energies experienced by the rare earth ion should see a modification of the non-radiative decay rate. The work presented in the following subsections focuses on the effects of network modifying on the measured fluorescence lifetime of the two important energy manifolds of the S-band amplifier, the  ${}^3H_4$  and  ${}^3F_4$  manifold.

### 4.4.1 Alumino-silicate fibres

The fluorescence lifetime of the alumino-silicate fibres were measured using the experimental arrangement described in Section 3.4. Single exponential fits were applied to the decay waveforms from the  ${}^3H_4$  and  ${}^3F_4$  manifolds to obtain the  $1/e$  characteristic lifetime. The suitability of fitting a single exponential function to the decay of both manifolds is discussed in greater detail in Chapter 5; for now the lifetimes obtained from a single exponential fit allow comparisons to be made between each fibre sample. In general, the decay from the  ${}^3H_4$  manifold was non-exponential, whilst the decay from the  ${}^3F_4$  manifold could be described adequately by the single

exponential fit. It should be noted that all  ${}^3H_4$  manifold decay waveforms were fitted over a time scale of 180  $\mu\text{s}$ , whilst the  ${}^3F_4$  manifold decay waveforms were fitted over 470  $\mu\text{s}$ . The 1/e lifetimes for both energy manifolds are listed in Table 4.5.

Sample	Tm <sub>2</sub> O <sub>3</sub> (ppm)	Al <sub>2</sub> O <sub>3</sub> (mol %)	${}^3H_4$ lifetime ( $\mu\text{s}$ )	${}^3F_4$ lifetime ( $\mu\text{s}$ )
Al-1	100	1.9	16.8 $\pm$ 0.2	384 $\pm$ 2
Al-2	240	3.4	20.0 $\pm$ 0.1	417 $\pm$ 3
Al-3	450	4.4	20.7 $\pm$ 0.1	428 $\pm$ 2
Al-4	1850	4.6	21.0 $\pm$ 0.1	441 $\pm$ 2
Al-5	220	4.8	22.6 $\pm$ 0.2	448 $\pm$ 3
Al-6	1950	5.4	21.2 $\pm$ 0.1	447 $\pm$ 2
Al-7	250	9.0	32.5 $\pm$ 0.2	573 $\pm$ 3
Al-8	32000	1 <sup>a</sup>	15.2 $\pm$ 0.1	397 $\pm$ 1

**Table 4.5:** 1/e lifetime of  ${}^3H_4$  and  ${}^3F_4$  manifolds in Tm<sup>3+</sup>-doped alumino-silicate fibre. Note: <sup>a</sup> is the solution concentration of AlCl<sub>3</sub> in mol/L.

It is evident from the results listed in Table 4.5 that the incorporation of Al<sub>2</sub>O<sub>3</sub> has a lengthening effect on the measured fluorescence lifetime of both energy manifolds. Figures 4.7 and 4.8 illustrate this, showing the trend of the fluorescence lifetimes from both manifolds with increasing Al<sub>2</sub>O<sub>3</sub> concentration.

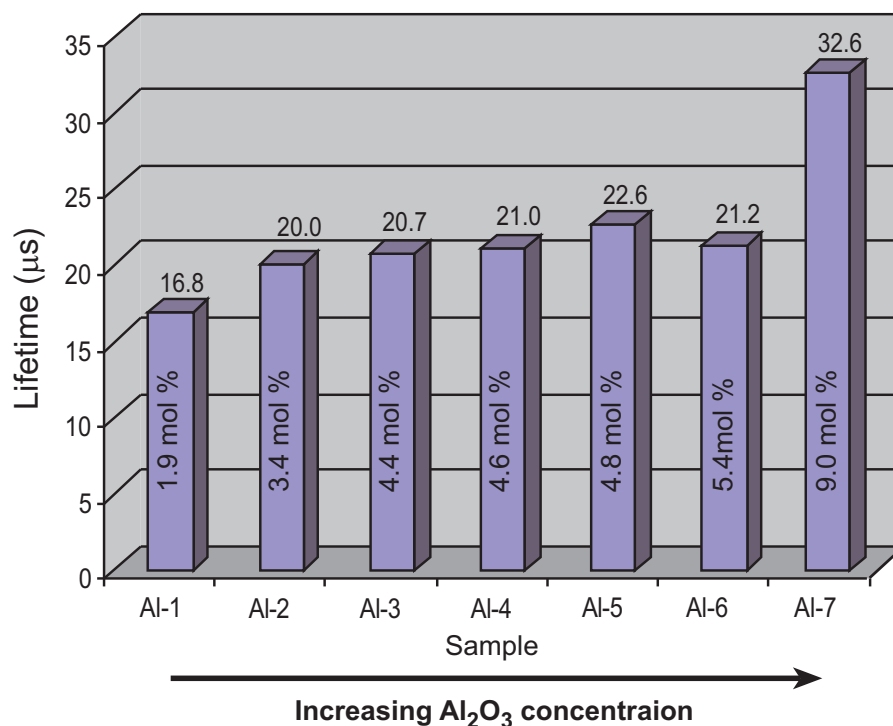


**Figure 4.7:**  ${}^3H_4$  lifetime at various Al<sub>2</sub>O<sub>3</sub> concentrations.

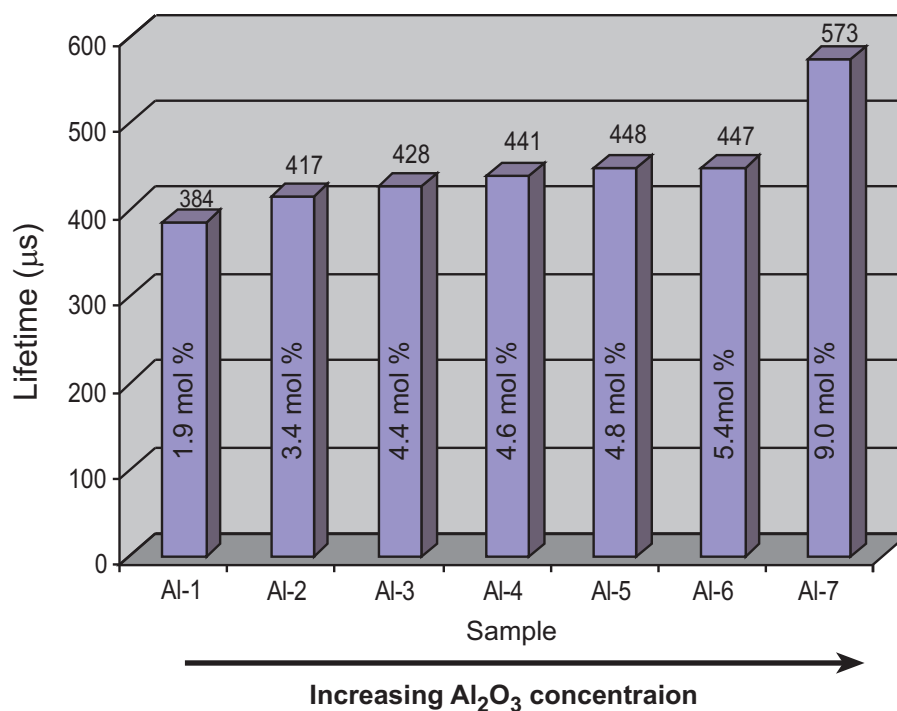


**Figure 4.8:**  $^3F_4$  lifetime at various  $\text{Al}_2\text{O}_3$  concentrations.

Figure 4.9 shows the respective lifetimes for each manifold as a function of  $\text{Al}_2\text{O}_3$  concentration for samples with low  $\text{Tm}_2\text{O}_3$  concentrations ( $\leq 250$  ppm).

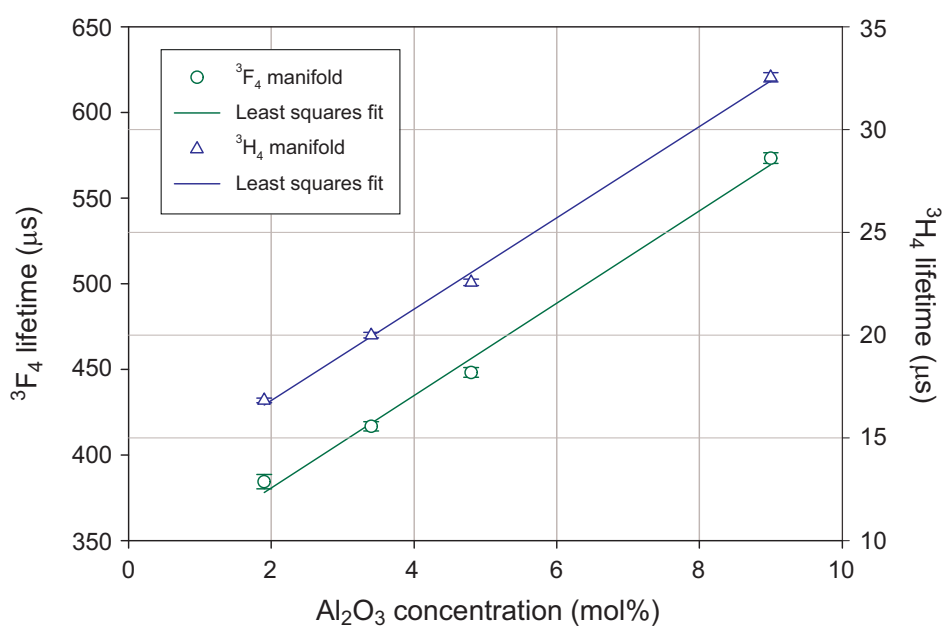


**Figure 4.9:**  $^3F_4$  and  $^3H_4$  manifold lifetime as a function of  $\text{Al}_2\text{O}_3$  concentration, for fibre samples with  $\text{Tm}_2\text{O}_3$  concentration  $\leq 250$  ppm.

These samples provide a more accurate account of the lifetime dependence on  $\text{Al}_2\text{O}_3$  concentration as energy transfer processes which may affect the lifetime are unlikely at such low  $\text{Tm}_2\text{O}_3$  concentrations. The linear fit applied to the data set in Figure 4.9 showed excellent agreement for both energy manifolds over the  $\text{Al}_2\text{O}_3$  concentration range 2 - 9 mol %. The  $^3H_4$  manifold exhibited a slope of  $2.2 \mu\text{s}/\text{mol}\%$  of  $\text{Al}_2\text{O}_3$  with a lifetime of  $12.4 \mu\text{s}$  in the limit of zero  $\text{Al}_2\text{O}_3$  concentration, which is consistent with the  $14.2 \mu\text{s}$  lifetime calculated by Jackson *et al.* for  $\text{Tm}^{3+}$ -doped silica glass [101]. More importantly, the incorporation of 9 mol% of  $\text{Al}_2\text{O}_3$  resulted in a  $\sim 260\%$  increase in the measured fluorescence lifetime, when compared to pure silica glass. This is in agreement with the work of Faure *et al.* on the  $^3H_4$  manifold in similar types of  $\text{Tm}^{3+}$ -doped alumino-silicate fibres [102]. The  $^3F_4$  manifold lifetime was found to increase at a rate of  $27 \mu\text{s}/\text{mol}\%$  of  $\text{Al}_2\text{O}_3$  with a lifetime of  $327 \mu\text{s}$  in the limit of zero  $\text{Al}_2\text{O}_3$  concentration, which is also consistent with the  $334 \mu\text{s}$  calculated lifetime of this manifold in silica glass [101]. With the incorporation of 9 mol% of  $\text{Al}_2\text{O}_3$ , the measured  $^3F_4$  fluorescence lifetime increased by  $\sim 175\%$ , when compared to pure silica glass.

The effect of  $\text{Al}_2\text{O}_3$  on the measured lifetime of the  $^3F_4$  manifold is, however, open to some conjecture. Cole [88] and Wu [103], using two different fabrication techniques, reported that  $\text{Al}_2\text{O}_3$  has little effect on the lifetime of the  $^3F_4$  manifold in  $\text{Tm}^{3+}$ -doped alumino-silicate glasses. The fabrication method used by Cole consisted of a rare earth chelate delivery system in conjunction with the MCVD technique. This technique first deposits a cladding on the inside of a silica substrate tube using the MCVD technique; the core dopants such as  $\text{Tm}_2\text{O}_3$ ,  $\text{Al}_2\text{O}_3$  and  $\text{GeO}_2$  are then deposited and sintered in a similar manner to the cladding to form the core of the optical preform. The preform is then collapsed under high temperature to form a solid glass rod. Wu, on the other hand, used a method which combined Sol-Gel with MCVD, first developed by DiGiovanni [104]. In this process, a cladding is first deposited inside a silica substrate tube using the conventional MCVD technique. The tube is then removed and dip coated with a Sol-Gel containing the core dopant ions. The tube is then drained at a constant rate and placed back into the MCVD lathe

where the core is sintered and the preform is collapsed. Both of these fabrication techniques differ from the MCVD and solution doping technique employed in this investigation. In this technique, the cladding is deposited on the inside of a silica substrate tube using the MCVD process. The core material is then deposited at a temperature hot enough to allow for the oxidation of the reactants ( $SiCl_4 + O_2 \rightarrow SiO_2 + 2Cl_2$ ), but low enough to only partially sinter the soot particles ( $SiO_2$ ). The silica tube is then removed from the lathe and treated with a solution containing the co-dopant ions and left to soak for a period of time, typically a few hours. The solution is then removed and the tube is dried and placed back into the lathe, where the core is sintered and the preform is collapsed. There are, therefore, obvious differences between each fabrication technique. It is apparent from this investigation that  $Al_2O_3$  co-doping of  $Tm^{3+}$ -doped silica fibre has a more pronounced effect on the local environment of the  $Tm^{3+}$  ion when fabricated using the MCVD and solution doping technique compared to the aforementioned fabrication techniques. In other work, Boj *et al.* indicated that the large quantity of Al (14% ions) was incorporated into their  $Tm^{3+}$ -doped Al-Ge- $SiO_2$  sample to increase the fluorescence lifetime of the  $^3F_4$  manifold [105]. However, as their sample also contained a large quantity of Ge (15% ions), it is inconclusive as to which co-dopant was responsible for the increase in the lifetime.

To the best of the author's knowledge, this thesis studies for the first time, the fluorescence lifetime of the  $^3F_4$  manifold as a pure function of  $Al_2O_3$  concentration using the MCVD and solution doping technique. The study showed that an  $\sim 175\%$  increase in the fluorescence lifetime, compared to pure silica glass, could be achieved by incorporating 9 mol% of  $Al_2O_3$  into the glass network. The linear dependence of the fluorescence lifetime with  $Al_2O_3$  concentration, as seen in Figure 4.9, does not appear to saturate over the concentration range studied here; this suggests that even greater improvements in the fluorescence lifetimes may be achieved with the incorporation of greater amounts of  $Al_2O_3$ . Unfortunately, from the point of view of the solution doping technique, the amount of  $Al_2O_3$  which can be incorporated into the core is limited by the solubility of the aluminium chloride salts in the doping

solution solvent. If the solution cannot dissolve the salts completely then they may be incorporated into the core of the preform. Crystallisation of the salts results in clustering and axial variations of the dopant along the length of the preform and fibre, which can lead to unwanted problems such as increased attenuation. Therefore a fabrication method which allows large quantities of  $\text{Al}_2\text{O}_3$  is required to make further advances in the quantum efficiencies of these transitions. It is vital, however, that the fabrication process exhibit similar outcomes to the MCVD and solution doping technique. The realisation of such a technique may have important implications for active  $\text{Tm}^{3+}$  -doped devices in silica glass, such as the S-band optical amplifier and the  $2\ \mu\text{m}$  laser.

The role aluminium co-doping plays in increasing the fluorescence lifetime of the energy manifolds of  $\text{Tm}^{3+}$  is not fully understood. However since both energy manifolds showed similar increases in the fluorescence lifetime with  $\text{Al}_2\text{O}_3$  concentration, it can be concluded that the shifting of the  ${}^3F_4$  manifold with  $\text{Al}_2\text{O}_3$  concentration did not have a significant effect on the lifetime. If the shifting of the  ${}^3F_4$  manifold were to play a significant role, the lifetime of the transition would be expected to decrease as the energy gap between the excited and ground state has been reduced. Therefore another host dependent effect must be responsible for the increase in the lifetime. The most obvious host dependent effect which can result in an increase in the fluorescence lifetime of an energy manifold is the phonon energy of the glass. As seen in Equation 2.7, the maximum phonon energy of the host material determines the non-radiative decay rate of the excited manifold. Furthermore, a reduction in the maximum phonon energy of the host material will result in an increase in the measured fluorescence lifetime. Measured phonon energy spectra from  $\text{Al}_2\text{O}_3$  waveguides show a maximum phonon energy of  $870\ \text{cm}^{-1}$  [106], which is some  $230\ \text{cm}^{-1}$  less than that observed in silica glass. This indicates that in  $\text{Al}_2\text{O}_3$  rich environments the maximum phonon energy experienced by rare earth ions is less than that in silica; this could explain the observed increase in the fluorescence lifetimes of the  ${}^3H_4$  and  ${}^3F_4$  manifolds with increased amounts of  $\text{Al}_2\text{O}_3$ . At high  $\text{Al}_2\text{O}_3$  concentrations, the  $\text{Tm}^{3+}$  ion is surrounded by a significant number of aluminium atoms and experiences

a lower local phonon energy, whereas at low  $\text{Al}_2\text{O}_3$  concentrations the  $\text{Tm}^{3+}$  ion is surrounded by  $\text{SiO}_2$  molecules and experiences a larger phonon energy.

#### 4.4.2 Germano-silicate fibres

The measured 1/e fluorescence lifetimes for the  ${}^3H_4$  and  ${}^3F_4$  manifolds of the germano-silicate fibres are listed in Table 4.6.

Sample	$\text{Tm}_2\text{O}_3$ (ppm)	$\text{SbCl}_4$ (mol/L)	$\text{SnCl}_4$ (mol/L)	${}^3H_4$ lifetime ( $\mu\text{s}$ )	${}^3F_4$ lifetime ( $\mu\text{s}$ )
Ge-1	300	3.9	-	$21.0 \pm 0.1$	$479 \pm 2$
Ge-2	1400	-	1.9	$20.1 \pm 0.1$	$467 \pm 2$

**Table 4.6:** 1/e lifetime of the  ${}^3H_4$  and  ${}^3F_4$  manifolds for the  $\text{Tm}^{3+}$  -doped germano-silicate fibres.

The lifetimes of the germano-silicate samples are in agreement with other values reported for  $\text{Tm}^{3+}$  -doped germano-silicate fibre [107] and are marginally greater than the calculated lifetime in pure silica glass [101]. This indicates that the germano-silicate host material offers no significant advantage in terms of modifying the local environment of the  $\text{Tm}^{3+}$  ion. Of particular interest, is the similarity between the  ${}^3F_4$  manifold lifetimes in both germano- and alumino-silicate host materials despite the considerable difference in the positioning of the Stark energy levels. This observation verifies that the host dependent shifting of the Stark energy levels does not have a major impact on the measured fluorescence lifetime of the  ${}^3F_4$  manifold. This, coupled with the fact that germano-silicate glass suffers from micro-clustering at concentrations at least an order of magnitude less than alumino-silicate glass, indicates that alumino-silicate glass is the preferred host material for improving the efficiency of excited state transitions in  $\text{Tm}^{3+}$ .

#### 4.4.3 Co-doping effects of Sb and Sn

The co-doping with additional network modifiers,  $\text{Sb}_2\text{O}_3$  and  $\text{SnO}_2$  of the germano- and alumino-silicate fibres showed no notable effect on the measured fluorescence

lifetime and hence efficiency of the  ${}^3H_4$  and  ${}^3F_4$  manifolds. Table 4.7 lists the 1/e lifetimes of the alumino-silicate fibres co-doped with  $Sb_2O_3$  and  $SnO_2$ .

Sample	Tm <sub>2</sub> O <sub>3</sub> (ppm)	SbCl <sub>4</sub> (mol/L)	SnCl <sub>4</sub> (mol/L)	${}^3H_4$ lifetime ( $\mu s$ )	${}^3F_4$ lifetime ( $\mu s$ )
Al-9	330	2.0	-	$23.2 \pm 0.2$	$477 \pm 2$
Al-10	260	-	1.9	$20.7 \pm 0.1$	$445 \pm 2$

**Table 4.7:** 1/e lifetime of the  ${}^3H_4$  and  ${}^3F_4$  manifolds for the Tm<sup>3+</sup>-doped alumino-silicate fibres co-doped with  $Sb_2O_3$  and  $SnO_2$ .

The measured fluorescence lifetimes are in agreement with the lifetimes reported in Table 4.5 for the pure alumino-silicate samples. The minor difference in the measured fluorescence lifetimes of the Al-9 and Al-10 fibres can be attributed to the difference in Al<sub>2</sub>O<sub>3</sub> concentration, as described in Section 4.4.1. The equivalent lifetimes and absorption profiles of the  $Sb_2O_3$  and  $SnO_2$  co-doped samples, when compared to the pure germano and alumino-silicate samples, suggests that the local environment and phonon energy of the glasses remain relatively unchanged with the addition of  $Sb_2O_3$  and  $SnO_2$ . Perhaps, with the incorporation of greater amounts of  $Sb_2O_3$  or  $SnO_2$ , changes in the local environment and/or local phonon energy can be achieved, although different fabrication techniques would be required, as the concentration levels studied here were the highest that could be obtained in the solution before saturation occurred.

## 4.5 Tm<sup>3+</sup> concentration

The dopant concentration of a material is a critical parameter in the design of active rare earth doped devices. The concentration can have advantageous and deleterious effects on the performance of an active device depending on the application type, as discussed in Section 2.5. In terms of spectroscopic studies, varying the dopant concentration allows one to study various diffusion and energy transfer processes which may be occurring in the system. In this section, the fluorescence lifetimes of the  ${}^3F_4$  and  ${}^3H_4$  manifolds are examined as a function of Tm<sub>2</sub>O<sub>3</sub> concentration. It

has been established in Section 4.4.1 that the addition of  $\text{Al}_2\text{O}_3$  into the host material significantly alters the fluorescence lifetime of both energy manifolds. Therefore to study the effects of the  $\text{Tm}_2\text{O}_3$  concentration independently, the sample set has been limited to the fibres with similar  $\text{Al}_2\text{O}_3$  concentrations.

### 4.5.1 $^3H_4$ manifold

The trend of the  $^3H_4$  lifetime with increasing  $\text{Tm}_2\text{O}_3$  concentration is shown in Figure 4.10 for fibre samples with  $\text{Al}_2\text{O}_3$  concentrations from 4.4 - 5.4 mol %.

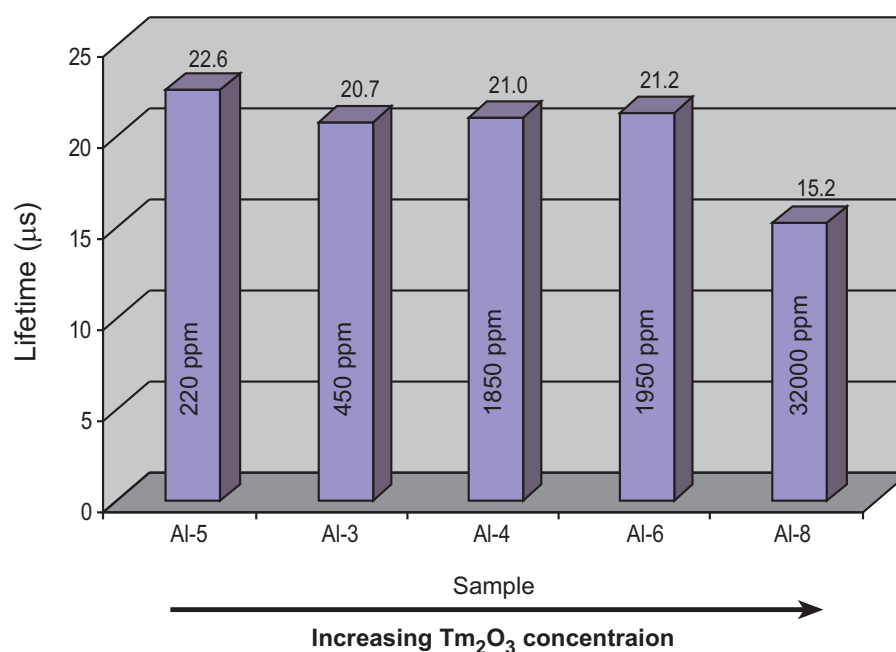


**Figure 4.10:**  $^3H_4$  lifetime at various  $\text{Tm}_2\text{O}_3$  concentrations for fibres with  $\text{Al}_2\text{O}_3$  concentrations from 4.4 - 5.4 mol %.

The chart shows no significant change in the fluorescence lifetime of the  $^3H_4$  manifold for  $\text{Tm}_2\text{O}_3$  concentrations as high as 1950 ppm. However, a  $\sim 29\%$  reduction in the lifetime was observed for the highly concentrated Al-8 sample; this decrease is attributed to the well known cross relaxation process which exists between the  $^3H_4$  manifold and  $^3H_6$  ground state ( $^3H_4, ^3H_6 \rightarrow ^3F_4, ^3F_4$ ). In this process, an excited ion in the  $^3H_4$  manifold transfers part of its energy to a nearby ground state  $\text{Tm}^{3+}$  ion resulting in two excited ions in the  $^3F_4$  manifold. The rate of re-

removal of excited ions from the  ${}^3H_4$  manifold via the cross relaxation process depends on numerous parameters such as the energy mismatch between the  ${}^3H_4 \rightarrow {}^3F_4$  and  ${}^3H_6 \rightarrow {}^3F_4$  transitions, the phonon energy of the glass, the temperature and perhaps most importantly the interionic distance between  $Tm^{3+}$  ions, or in other words, the  $Tm^{3+}$  concentration. As the interionic distance decreases, the probability that an excited ion will be close enough to interact with a nearby ground state ion increases; thereby, increasing the rate at which excited ions are removed from the  ${}^3H_4$  manifold. When this rate becomes significant enough to compete with the non-radiative decay rate, the measured fluorescence lifetime becomes concentration dependent. From the results shown in Figure 4.10, it can be concluded that the cross relaxation rate has a negligible effect on the measured fluorescence lifetime of the  ${}^3H_4$  manifold for  $Tm_2O_3$  concentrations as high as 1950 ppm.

Traditional techniques for estimating the cross relaxation co-efficient are based on studying the variation in the shape of the decay waveform as a function of donor concentration. As the cross relaxation process occurs on a time scale much faster than the radiative and observed fluorescence decay rates, its effects can be studied at the beginning of the decay (typically within the first few microseconds). By increasing the donor concentration, the effects of cross relaxation on the beginning of the decay waveform become more pronounced. The changes in the nature of the decay as a function of donor concentration can be adequately described by the Förster Dexter energy transfer model as well as the Inokuti-Hirayama relationship [108, 109, 110], with both techniques providing an estimation of the cross relaxation co-efficient. Unfortunately, the present study has been limited to fibre samples with relatively low donor concentrations and hence no significant variation in the shape of the decay waveform was observed (see Chapter 5). However, other studies on the cross relaxation process in other host materials have estimated the cross relaxation co-efficient to be  $1.3 - 5.5 \times 10^{-51} \text{ m}^6\text{s}^{-1}$ , depending on the host material [111, 112, 113]. In silica glass, the co-efficient is expected to be higher than those observed in fluoride glasses and crystals as there is considerable energy level broadening in glasses which will reduce the energy mismatches associated with the process.

Furthermore, the high phonon energy associated with silica glass allows the energy mismatches to be overcome with greater efficiency. If the maximum observed coefficient,  $5.5 \times 10^{-51} \text{ m}^6\text{s}^{-1}$ , is taken as an estimate for the coefficient in silica glass, this would equate to a cross relaxation rate of  $20 \text{ s}^{-1}$  for a  $\text{Tm}_2\text{O}_3$  concentration of 2000 ppm (assuming 1000 ppm is equivalent to  $3.1 \times 10^{25} \text{ ions/m}^3$  [114]). If this rate is compared to the radiative and non-radiative decay rates of the  $^3H_4$  manifold, as listed in Table 2.1, it is clear that the cross relaxation process does not compete with the other decay rates at such concentrations. However, if the same calculation is performed for a  $\text{Tm}_2\text{O}_3$  concentration of 32 000 ppm, the cross relaxation rate increases to  $\sim 5400 \text{ s}^{-1}$  and becomes significantly larger than the radiative decay rate from the  $^3H_4$  manifold. In this instance, the observed lifetime of the  $^3H_4$  manifold would decrease. This calculation supports the observed lifetime reduction in the highly concentrated Al-8 fibre sample.

The measurements reported here have important implications for the development of S-band optical amplifiers which operate from the  $^3H_4$  manifold. Previous attempts to fabricate efficient S-band  $\text{Tm}^{3+}$ -doped silica fibre amplifiers have been carried out using relatively low  $\text{Tm}_2\text{O}_3$  concentrations to avoid quenching from the cross relaxation process [34, 35]. The negligible cross relaxation rate at  $\text{Tm}_2\text{O}_3$  concentration at and below 1950 ppm indicates  $\text{Tm}_2\text{O}_3$  concentrations of this order could be used in S-band amplifiers without severe penalty from the cross relaxation process; higher  $\text{Tm}_2\text{O}_3$  concentrations should allow further improvements in the gain of the amplifiers to be realised.

#### 4.5.2 $^3F_4$ manifold

Figure 4.11 shows the trend of the  $^3F_4$  lifetime with increasing  $\text{Tm}_2\text{O}_3$  concentration. The  $^3F_4$  fluorescence lifetime did not show any significant dependence on the  $\text{Tm}_2\text{O}_3$  concentration, although a  $\sim 9\%$  decrease was observed for the most highly concentrated sample. The decrease in the fluorescence lifetime of this sample could be attributed to quenching energy transfer processes and/or energy migration and diffusion processes.

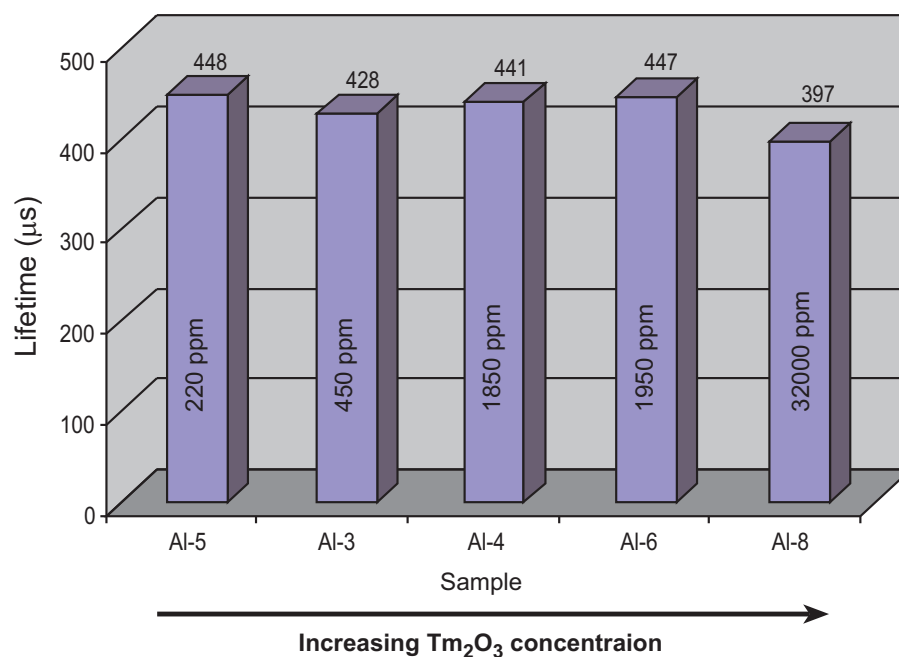


**Figure 4.11:**  ${}^3F_4$  lifetime at various  $\text{Tm}_2\text{O}_3$  concentrations for fibres with similar  $\text{Al}_2\text{O}_3$  concentrations.

Energy migration and diffusion from the  ${}^3F_4$  manifold has been reported in several host materials [97, 115, 116]. However, it is expected that energy migration and diffusion processes can be ignored in this investigation as they become apparent only at much higher  $\text{Tm}_2\text{O}_3$  concentrations than those studied here [115]. There are two possible energy transfer processes which can occur from the  ${}^3F_4$  manifold ( ${}^3F_4, {}^3F_4 \rightarrow {}^3H_5, {}^3H_6$ ) and ( ${}^3F_4, {}^3F_4 \rightarrow {}^3H_4, {}^3H_6$ ); both of which act to quench the population of the  ${}^3F_4$  manifold. Identifying energy transfer up-conversion processes is, in some respects, easier than the aforementioned cross relaxation process. The two possible ETU processes, which can occur from the  ${}^3F_4$  manifold in  $\text{Tm}^{3+}$ , require two excited ions in the  ${}^3F_4$  manifold to exchange energy. This requirement makes both of these processes dependent on the incident pump power, and thus the energy transfer up-conversion processes can be identified by studying the fluorescence lifetime as a function of pump power. The cross relaxation process, on the other hand, requires only a single excited ion in the  ${}^3H_4$  manifold, and therefore the process is independent of pump power and cannot be established by such an experiment. To investigate the possible presence of energy transfer up-conversion processes in  $\text{Tm}^{3+}$ -doped silica fibres, the lifetime of the  ${}^3F_4$  manifold was investigated at different pump powers.

By modulating the 1586 nm excitation source with 12.5 ms pulses at a repetition rate of 40 Hz, significantly larger pump intensities could be obtained from the available laser diode. This condition also allowed the manifold sufficient time to reach a steady state equilibrium, as the pulse length was at least ten times longer than the longest rise time of any excited energy manifold in the  $\text{Tm}^{3+}$ -doped silica system. The laser diode had an operating power range from 0 - 16.5 mW at 1586 nm. The study was undertaken for the two different host materials, germano-silicate and alumino-silicate, with various  $\text{Tm}_2\text{O}_3$  concentrations. The  $^3F_4$  fluorescence lifetime as a function of incident pump power for each fibre sample is shown in Figure 4.12, whilst Table 4.8 lists the percentage decrease in the lifetime of the  $^3F_4$  manifold over the range of incident pump powers.

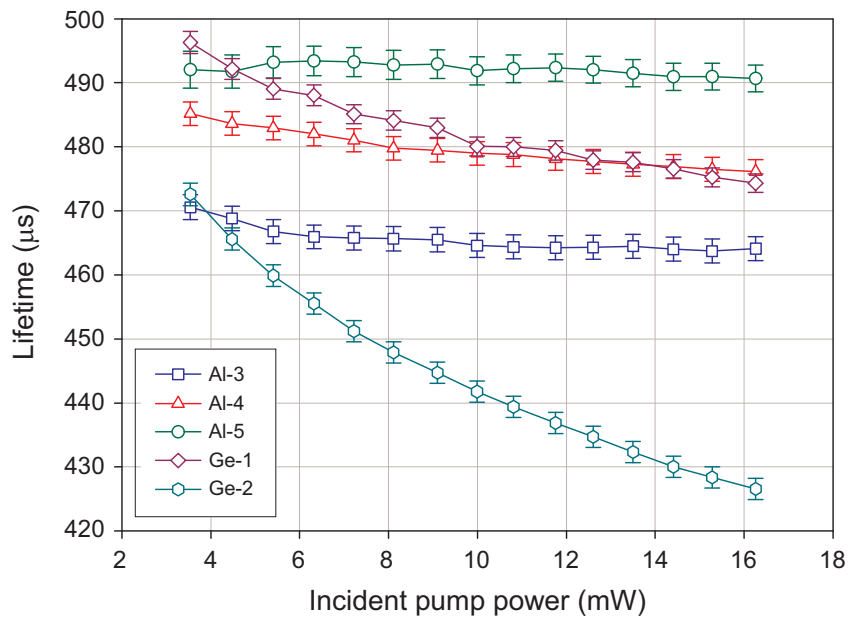


**Figure 4.12:**  $^3F_4$  lifetime as a function of incident pump power for the  $\text{Tm}^{3+}$ -doped alumino- and germano-silicate fibres indicated. Note: the lines are a guide for the eye.

Sample	$\text{Tm}_2\text{O}_3$ (ppm)	$^3F_4$ lifetime decrease (%)
Al-5	200	0.9
Al-3	450	1.0
Al-4	1850	1.9
Ge-1	300	4.4
Ge-2	1400	9.7

**Table 4.8:** Percentage decrease in the  $^3F_4$  manifold lifetime over the pump power range 3 - 16.4 mW.

From Figure 4.12 it can be seen that the lifetime of the  ${}^3F_4$  manifold decreases with increasing pump power. The decrease in the fluorescence lifetime appears to be dependent on both the host composition and the  $\text{Tm}_2\text{O}_3$  concentration. This behaviour is consistent with the presence of energy transfer up-conversion processes. In general, the  ${}^3F_4$  lifetime of the germano-silicate samples showed a greater dependence on pump power compared to the alumino-silicate samples. Although this measurement provides evidence for the presence of the energy transfer up-conversion processes, it does not provide any information about which energy transfer process is operating; this is the focus of the following section.

## 4.6 Energy transfer up-conversion in $\text{Tm}^{3+}$ -doped silica fibres

The energy transfer up-conversion processes relevant to this investigation in  $\text{Tm}^{3+}$ -doped silica fibre are ( ${}^3F_4, {}^3F_4 \rightarrow {}^3H_5, {}^3H_6$ ) and ( ${}^3F_4, {}^3F_4 \rightarrow {}^3H_4, {}^3H_6$ ). Figure 4.13 displays the two possible energy transfer up-conversion processes that quench the population of the  ${}^3F_4$  manifold. The discrete energy levels illustrated in Figure 4.13 represent the Stark energy levels within the energy manifold, showing  $2J+1$  Stark levels in each energy manifold.

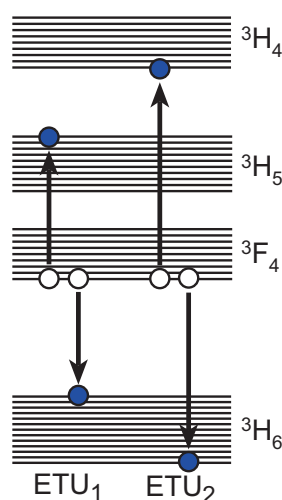


**Figure 4.13:** Possible energy transfer up-conversion process which can occur from the  ${}^3F_4$  manifold. The white and blue circles represent the ions before and after the energy transfer has taken place, respectively.

The final Stark levels relevant for each energy transfer up-conversion process considered here are obtained from the general rule that the actual Stark levels which are involved at the completion of the energy transfer are those that will minimise the absolute value of the energy difference or energy mismatch  $\Delta E_{ab} = \sum E_i - \sum E_f$  between the initial and final multiplets of the process [60]. It can be assumed that only the lower Stark level of each manifold engaged at the initial stage of the energy transfer process is relevant to the calculation of  $\Delta E_{ab}$ . Whilst thermal equilibrium exists between the Stark levels of a manifold, the lower Stark level has a higher proportion of the density of states. The energy mismatch  $\Delta E$  for both energy transfer up-conversion processes are listed in Table 4.9 for a range of different host materials.

Crystal	$\Delta E_{ETU_1}$ ( $\text{cm}^{-1}$ )	$\Delta E_{ETU_2}$ ( $\text{cm}^{-1}$ )
$\text{Y}_3\text{Al}_5\text{O}_{12}$ [117]	1500	-1495
$\text{Y}_2\text{O}_3\text{-Sc}_2\text{-Al}_2\text{O}_3$ [118]	1882	-790
$\text{LiYF}_4$ [119]	2368	-1411
$\text{YVO}_4$ [120]	2277	-1423
$\text{NaLa}(\text{MoO}_4)_2$ [121]	2389	-1387
$\text{YCl}_3$ [95]	N/R	-698
$\text{Ca}_4\text{GdO}(\text{BO}_3)_3$ [113]	N/R	-1345

**Table 4.9:** Energy mismatch of the two energy transfer up-conversion processes in various  $\text{Tm}^{3+}$  -doped crystals. Note: N/R - not reported in the literature.

The positive energy mismatch of  $\text{ETU}_1$  indicates an exothermic transfer process which requires the emission of phonons to conserve energy. The negative energy mismatch of  $\text{ETU}_2$  indicates an endothermic transfer process which requires the absorption of phonons to conserve energy. Based on the values listed in Table 4.9 and given the maximum phonon energy of silica glass is  $1100 \text{ cm}^{-1}$ , at least two phonons would need to be emitted for  $\text{ETU}_1$  to occur and at least one phonon would need to be absorbed to complete  $\text{ETU}_2$ . This implies that  $\text{ETU}_2$  is inherently more efficient than  $\text{ETU}_1$ . However, since exothermic processes are, in general, more probable than endothermic processes most authors report  $\text{ETU}_1 > \text{ETU}_2$  [122, 60]. In silica glass,  $\text{ETU}_1$  may be deemed a fluorescence quenching energy transfer process, as

the majority of ions excited to the  ${}^3H_5$  manifold will decay non-radiatively back to the  ${}^3F_4$  manifold. This process has important consequences for the 2  $\mu\text{m}$  lasing transition as it quenches the excited state population of the  ${}^3F_4$  manifold. Work by Jackson in heavily  $\text{Tm}^{3+}$ -doped silica fibres has shown that fluorescence quenching energy transfer processes such as  $\text{ETU}_1$  can significantly affect the lasing threshold and slope efficiency of the 2  $\mu\text{m}$  laser [60].

The other possible energy transfer up-conversion process, labelled  $\text{ETU}_2$  in Figure 4.13, is of much interest for the operation of an S-band optical amplifier. This energy transfer process acts to increase the population inversion between the upper and lower amplifying manifolds. The  $({}^3F_4, {}^3F_4 \rightarrow {}^3H_4, {}^3H_6)$  process involves the spectral overlap between the excited state absorption from  ${}^3F_4 \rightarrow {}^3H_4$  which occurs at  $\sim 1410$  nm and the  ${}^3F_4 \rightarrow {}^3H_6$  emission which occurs at  $\sim 1800$  nm. Although this energy transfer up-conversion process has been established in several  $\text{Tm}^{3+}$ -doped crystals [95, 121, 122], in some cases, the sharp spectral lines associated with these materials results in a lack of spectral overlap between the  ${}^3F_4 \rightarrow {}^3H_4$  excited state absorption and the  ${}^3F_4 \rightarrow {}^3H_6$  emission, which reduces the efficiency of the energy transfer process. In silica glasses, where the energy levels are inhomogeneously broadened, the spectral overlap is expected to be much stronger and therefore the effect of the energy transfer up-conversion is expected to be greater.

To establish the  $({}^3F_4, {}^3F_4 \rightarrow {}^3H_4, {}^3H_6)$  energy transfer process in  $\text{Tm}^{3+}$ -doped silica fibres, spectroscopic studies were carried out under 1586 nm excitation into the  ${}^3F_4$  manifold. The detection of up-conversion luminescence from the  ${}^3H_4$  manifold would be the first step towards identifying the presence of the  $\text{ETU}_2$  process. When excited at 1586 nm, the  $\text{Tm}^{3+}$ -doped silica fibres were observed to emit up-conversion luminescence centred at 800 nm. The 800 nm luminescence band from the  ${}^3H_4$  manifold was studied here as it is 9 times stronger than the 1480 nm luminescence in silica glass [70]. Figure 4.14 shows the counter propagating emission spectrum obtained from a 20 cm section of the 1850 ppm alumino-silicate sample (Al-4), when pumped with 16.8 mW of light at 1586 nm.

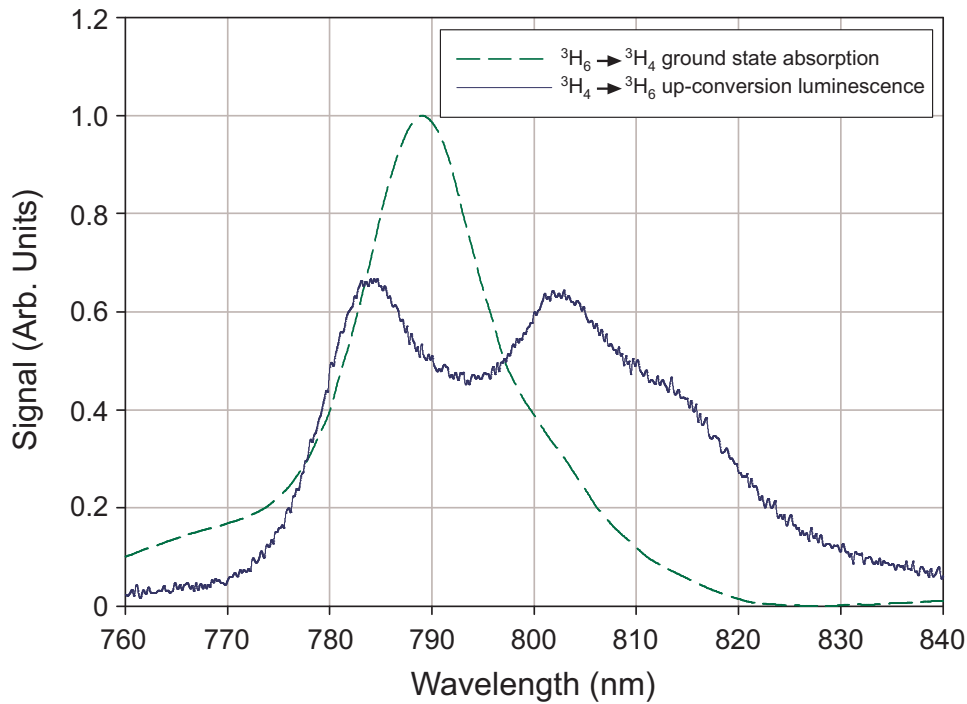


**Figure 4.14:** Counter-propagating up-conversion luminescence spectrum from a 20 cm section of the Al-4 fibre, excited with 16.8 mW at 1586 nm.

The emission spectrum observed is characteristic of the  ${}^3H_4$  manifold. The large dip in the spectrum at  $\sim 790$  nm results from the counter propagating fluorescence being reabsorbed by the strong ground state transition ( ${}^3H_6 \rightarrow {}^3H_4$ ) as the fluorescence propagates back through the doped fibre section. It should be noted that the same experimental arrangement was not used to collect the up-conversion fluorescence signal for the decay analysis; all other measurements were carried out transverse to the doped fibre as described in Section 3.4.

The origin of this luminescence lies in two possible processes: energy transfer up-conversion (ETU<sub>2</sub>) and/or excited state absorption (ESA). In ETU<sub>2</sub>, two pump photons excite two ions to the  ${}^3F_4$  manifold. The excited ions then exchange energy non-radiatively, promoting one excited ion to the  ${}^3H_4$  manifold, whilst demoting the other ion to the  ${}^3H_6$  ground state. In ESA, a pump photon excites an ion to the  ${}^3F_4$  manifold. The excited ion then absorbs the energy of another pump photon promoting itself to the  ${}^3H_4$  manifold (see Figure 4.15).

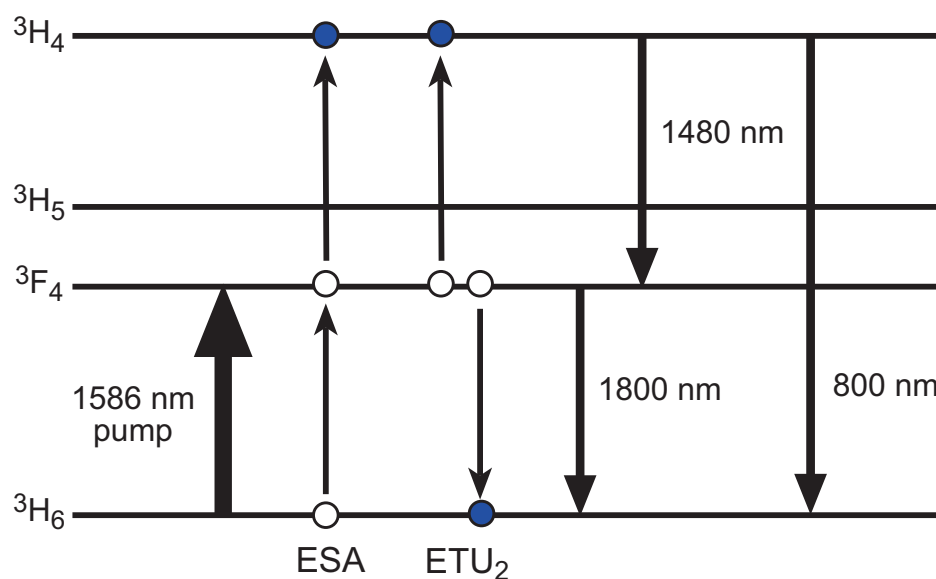


**Figure 4.15:** Possible energy transfer processes that can populate the  ${}^3H_4$  manifold in  $Tm^{3+}$ -doped silica glass, when pumping into the  ${}^3F_4$  manifold. The white and blue circles represent the ions before and after the processes have taken place, respectively.

Both processes illustrated in Figure 4.15 require two pump photons in the process of exciting one ion to the  ${}^3H_4$  manifold. Hence, the luminescence from the  ${}^3H_4$  manifold at 800 nm should be proportional to the square of the population in the  ${}^3F_4$  manifold, i.e. proportional to the square of the luminescence from this manifold at 1800 nm. This was investigated by measuring the integrated steady state luminescence intensities from the 800 and 1800 nm transitions over the range of available pump powers. It should be noted that the luminescence from the 800 nm transition was collected through a  $810 \pm 10$  nm bandpass filter, while the 1800 nm luminescence was collected using a 1500 nm long pass filter.

#### 4.6.1 Alumino-silicate fibres

The  $Al_2O_3$  concentration has been shown to significantly affect the fluorescence lifetimes of the excited state manifolds of  $Tm^{3+}$ . In order to study the energy transfer processes independently, this study was limited to fibres with similar  $Al_2O_3$  concentrations, namely, Al-3, Al-4 and Al-5. Figure 4.16 shows the dependence of the 810 nm luminescence on the 1800 nm luminescence for these fibre samples. The

approximate quadratic dependence observed for all three samples is consistent with the  ${}^3H_4$  manifold being populated by a two photon process.

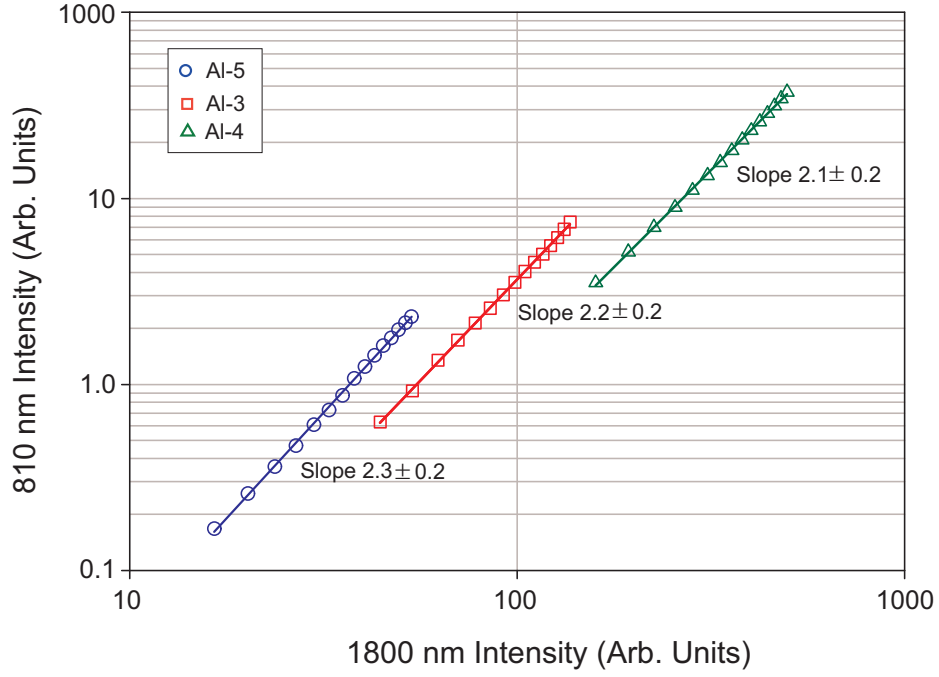


**Figure 4.16:** Log-log plot of the 810 nm luminescence vs. the 1800 nm luminescence, for incident pump powers ranging from 3 - 16.8 mW. The 1800 nm data have been offset to aid comparison. Note: the errors associated with these measurements are not shown as they are smaller than the size of the individual data points presented in the plot.

To distinguish between the two possible populating mechanisms, ESA and  $ETU_2$ , a study was undertaken of the decay characteristics of the up-conversion luminescence. The behaviour of the up-conversion luminescence when the pump excitation has been removed can be described by considering a simple set of rate equations relating the populations of the  ${}^3F_4$  and  ${}^3H_4$  manifolds, namely:

$$\frac{dn_1}{dt} = -\frac{n_1}{\tau_1} - W_{ETU} n_1^2 c , \quad (4.1)$$

$$\frac{dn_2}{dt} = -\frac{n_2}{\tau_2} + \frac{1}{2} W_{ETU} n_1^2 c , \quad (4.2)$$

where  $n_1$  and  $n_2$  represent the relative population of the  ${}^3F_4$  and  ${}^3H_4$  manifolds respectively,  $c$  is the  $Tm_2O_3$  concentration,  $W_{ETU}$  is the ETU co-efficient and  $\tau_1$  and  $\tau_2$  are the fluorescence lifetimes of the  ${}^3F_4$  and  ${}^3H_4$  manifolds, respectively.

The rate equations 4.1 and 4.2 involve several assumptions. Firstly, it has been assumed that any population in the  ${}^3H_5$  manifold will relax rapidly to the  ${}^3F_4$  manifold in a time scale which is short in comparison to the other decay times involved (refer to Table 2.1); thus the  ${}^3H_5$  manifold has been ignored. Secondly, by representing the ETU<sub>2</sub> process with the term  $W_{ETU} n_1^2 c$  we have ignored any energy migration processes, which is justifiable since this process occurs on a much smaller time scale ( $\sim 10^{-10}$  s) [123]. The term which describes the possible ESA from the  ${}^3F_4 \rightarrow {}^3H_4$  manifold does not appear in the rate equations describing the decay of the emission as ESA occurs only in the presence of pump excitation. Therefore studying the decay characteristics of the up-converted luminescence provides a sensitive technique for distinguishing between the ETU<sub>2</sub> and ESA processes. Theoretical calculations by Peterka *et al.* [11] have estimated the ESA cross section at the pump and signal wavelengths (1586 and 1800 nm) to be  $\sim 3 \times 10^{-31}$  and  $\sim 0$  m<sup>2</sup>, respectively. Although relatively large errors are associated with these values, they suggest that ESA does not play a significant role in the up-conversion process at these wavelengths.

As noted in Section 4.4.1, the luminescence decay from the  ${}^3F_4$  manifold is adequately described by a single exponential, implying  $n_1/\tau_1 \gg W_{ETU} n_1^2 c$ . Therefore the solution to Equation 4.1 becomes:

$$n_1 = n_{10} \exp\left(-\frac{t}{\tau_1}\right), \quad (4.3)$$

where  $n_{10}$  represents the initial population of the  ${}^3F_4$  manifold after the pump excitation has been removed.

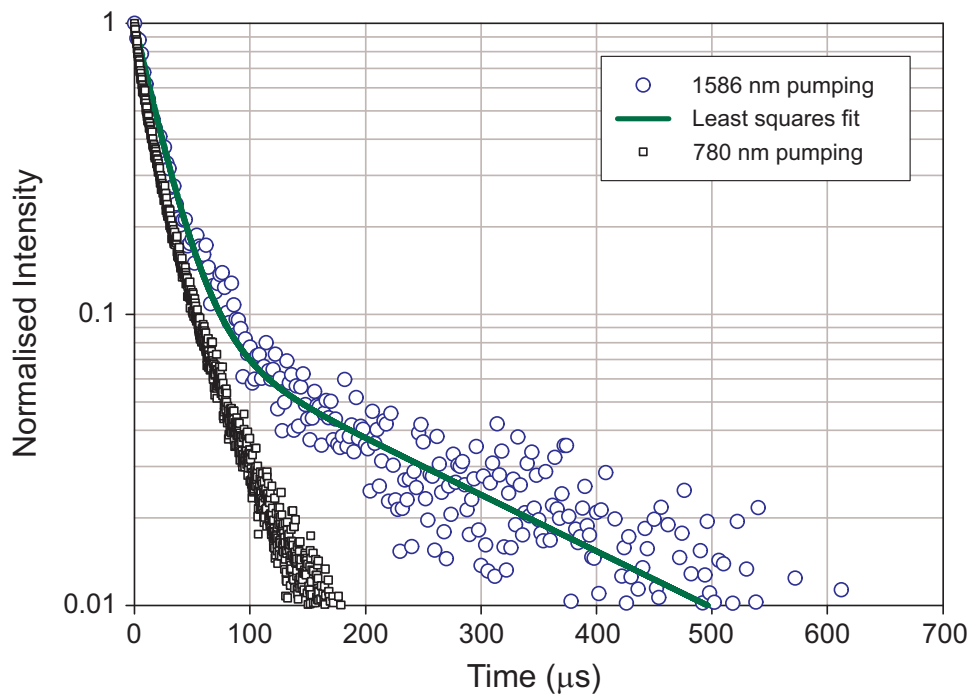
By inserting Equation 4.3 into 4.2, a normalised expression for  $n_2$  can be found:

$$\frac{n_2}{n_{20}} = (1 - A) \exp\left(-\frac{t}{\tau_2}\right) + A \exp\left(-\frac{2t}{\tau_1}\right), \quad (4.4)$$

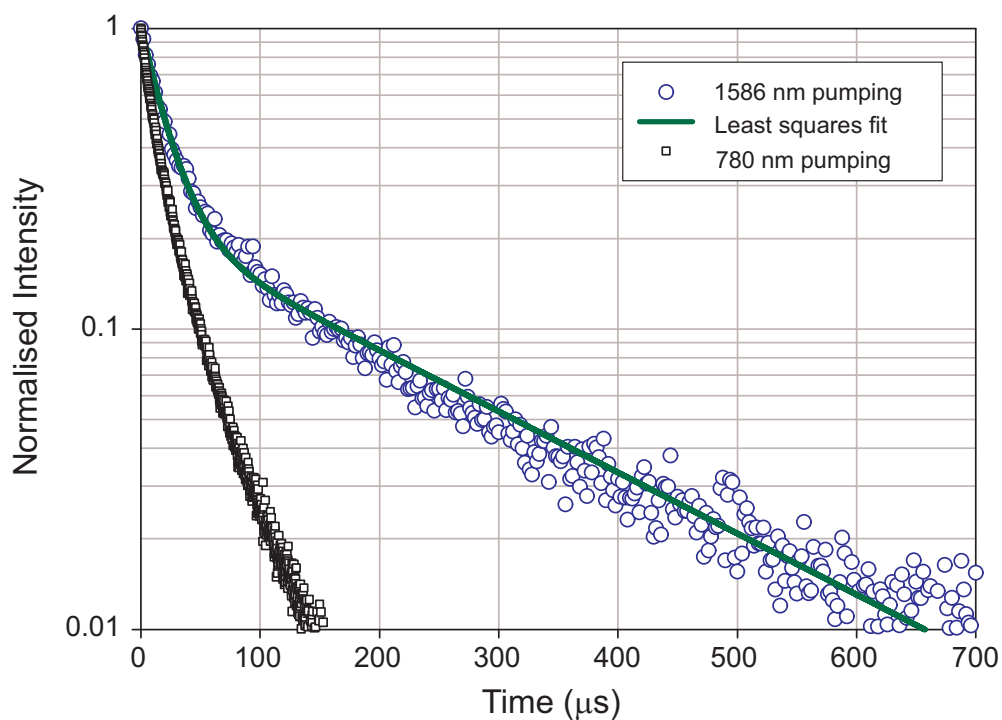
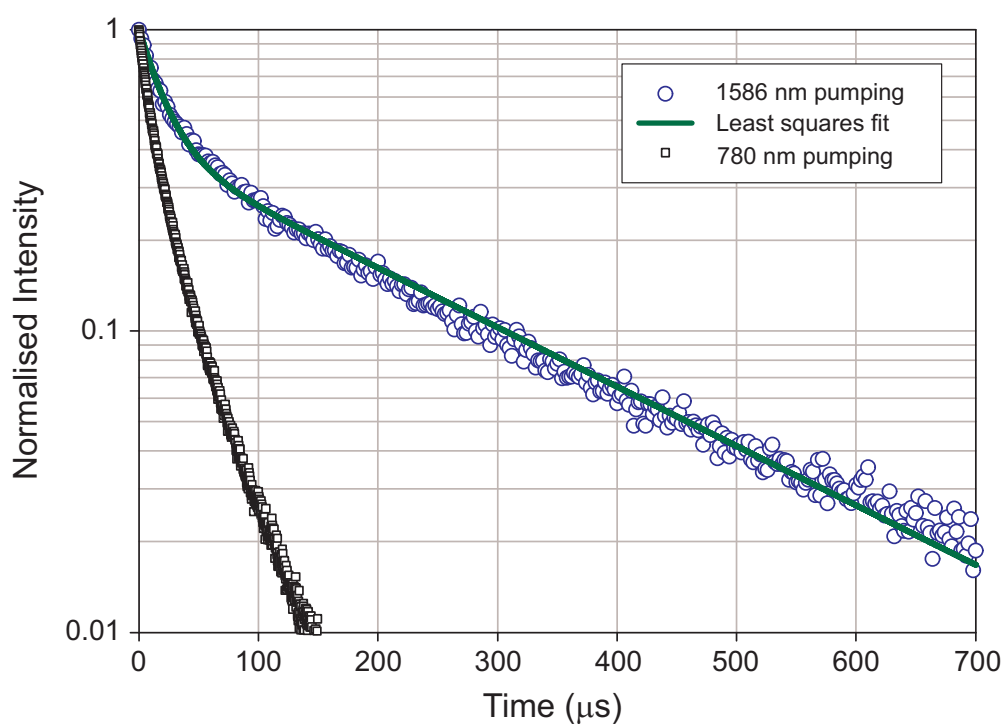
where  $A = \frac{W_{ETU} c n_{10}^2}{(\tau_2^{-1} - 2\tau_1^{-1}) 2n_{20}}$  and  $n_{20}$  represents the initial population of the  ${}^3H_4$  manifold after the pump excitation is removed.

From Equation 4.4 we see that the up-conversion luminescence, resulting from  $ETU_2$ , decays as a double exponential with two characteristic time constants, one being equal to the lifetime of the  ${}^3H_4$  manifold ( $\tau_2$ ) and the other being equal to  $(\frac{1}{2}\tau_1)$  i.e. one half of the  ${}^3F_4$  manifold lifetime. The amplitudes of the respective decay components are given as  $(1 - A)$  for the fast decay component and  $A$  for the slow decay component of the waveform. The ‘fast’ and ‘slow’ amplitudes of the decay waveforms can give an insight into the dominant decay process over time.

Figure 4.17 shows the semi-log plots of the up-conversion luminescence decay under 1586 nm pumping for the Al-3, Al-4 and Al-5 samples and, as a comparison, the decay of the  ${}^3H_4$  manifold under direct excitation at 780 nm is also presented. It is clear from Figure 4.17 that the up-conversion luminescence decay deviates from the natural decay of the  ${}^3H_4$  manifold. Furthermore, the up-conversion luminescence decay shows evidence of two characteristic decay components.



(a) Al-3 - 200 ppm  $Tm_2O_3$

(b) Al-4 - 450 ppm  $\text{Tm}_2\text{O}_3$ (c) Al-5 - 1850 ppm  $\text{Tm}_2\text{O}_3$ 

**Figure 4.17:** Semi-log plots of the luminescence from the  ${}^3H_4 \rightarrow {}^3H_6$  transition. (a), (b) and (c) are the decay curves for samples Al-3, Al-4 and Al-5, respectively. The open circles represent the decay under in-direct excitation at 1586 nm. The open squares represent the decay under direct excitation at 780 nm. The least squares fits are discussed in the text.

A least squares fit using Equation 4.4 was applied to the up-conversion luminescence decay waveforms, with  $\tau_1$  and  $\tau_2$  being the  $1/e$  lifetimes, as listed in Table 4.5, obtained under direct pumping of the  $^3F_4$  and  $^3H_4$  manifolds, leaving  $A$  as the fitting parameter. The least squares fits were in excellent agreement with the measured waveforms. The fitting parameter  $A$  represents the ‘slow’ amplitude of the late exponential, which is due to the energy transfer up-conversion process. The fitted parameter for each fibre sample is listed in Table 4.10.

Sample	Tm <sub>2</sub> O <sub>3</sub> (ppm)	‘slow’ amplitude ( $A$ )
Al-5	200	$0.091 \pm 0.001$
Al-3	450	$0.215 \pm 0.001$
Al-4	1850	$0.401 \pm 0.001$

**Table 4.10:** The ‘slow’ amplitude obtained from the fit to Equation 4.4 for the three Tm<sup>3+</sup> -doped aluminosilicate samples.

The ‘slow’ amplitude provides an indication of the strength of the energy transfer up-conversion process in relation to the natural fluorescence decay rate from the  $^3H_4$  manifold. If the energy transfer up-conversion rate is small in comparison to the natural fluorescence decay rate (i.e.  $n_2/\tau_2 \gg W_{ETU} n_1^2 c$ ) then the up-conversion luminescence will exhibit a relatively small ‘slow’ amplitude. If, on the other hand, the ETU<sub>2</sub> rate dominates the natural fluorescence decay rate (i.e.  $W_{ETU} n_1^2 c \gg n_2/\tau_2$ ) then the ‘slow’ amplitude will approach unity and the up-conversion luminescence will decay as a single exponential in the form  $n_2(t) = A \exp(-2t/\tau_1)$ . This effect was observed for the highly concentrated Al-8 sample (32 000 ppm), as shown in Figure 4.18, where the up-conversion luminescence decay could be described accurately by a single exponential function with a characteristic lifetime equal to  $\tau_1/2$ .

The concentration dependence of the ‘slow’ amplitude can be explained by considering the concentration dependence of the energy transfer and natural fluorescence decay rates. From the fluorescence lifetime results presented in Section 4.4.1 it can be concluded that the natural fluorescence decay rate is concentration independent for Tm<sub>2</sub>O<sub>3</sub> concentrations up to 1950 ppm. The same cannot be said for the energy

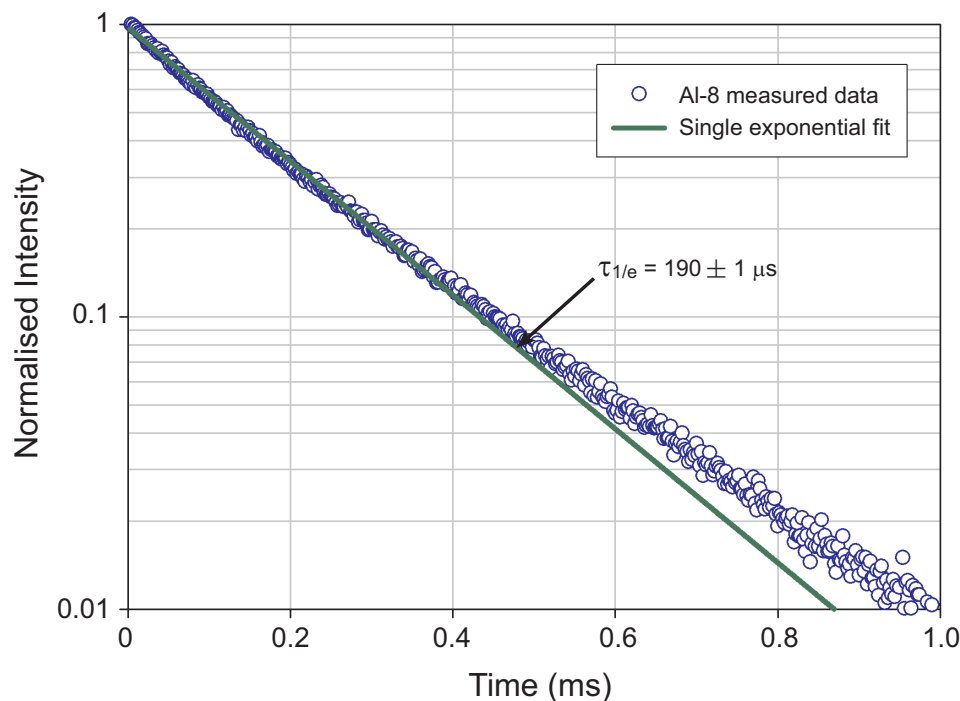


**Figure 4.18:** Single exponential fit to the measured decay from the  $^3H_4$  manifold of the alumino-silicate sample Al-8, under in-direct excitation at 1586 nm.

transfer rate. As the  $Tm_2O_3$  concentration increases, so too does the energy transfer rate. For high  $Tm_2O_3$  concentrations, this rate can begin to compete and then dominate over the concentration independent natural fluorescence decay rate, which will lead to increases in the ‘slow’ amplitude. From the fitted values of  $A$  listed in Table 4.10, it can be concluded that the energy transfer rate is less dominant, although not negligible, than the natural fluorescence decay rate for  $Tm_2O_3$  concentrations up to 1850 ppm.

#### 4.6.2 Germano-silicate fibres

Similar investigations were carried out on the germano-silicate fibres, Ge-1 and Ge-2, to gain an understanding of the strength of the energy transfer up-conversion process in comparison to the alumino-silicate fibres. Figure 4.19 shows a log-log plot of the 810 nm up-conversion luminescence versus the 1800 nm luminescence.

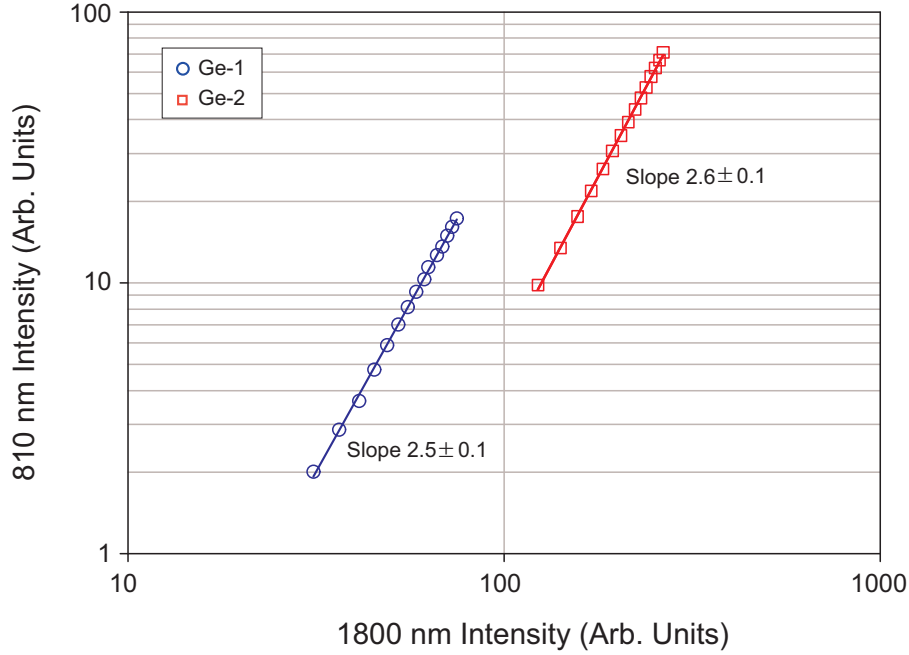


**Figure 4.19:** Log-log plot of the 810 nm luminescence vs. the 1800 nm luminescence, for incident pump powers ranging from 3 - 16.8 mW. The 1800 nm measured data has been offset to aid comparison. Note: the errors associated with these measurements are not shown as they are smaller than the size of the individual data points presented in the plot.

The non-integer values greater than 2, obtained from the slopes of the log-log plots indicate that other energy transfer processes are involved in populating the  ${}^3H_4$  manifold. As energy transfer up-conversion processes require two nearby excited ions to complete the transition their relationship with the up-conversion luminescence is always quadratic. However, processes such as ESA are not dependent on the number of nearby excited ions in a particular manifold but are dependent on the incident pump power. In the case of ESA, the slope of the 810 nm up-conversion luminescence versus the 1800 nm luminescence can take on quite different characteristics to ETU. This phenomenon is able to be observed using simple rate equation analysis, in which the rate equation describing the population of the  ${}^3F_4$  manifold under continuous wave pumping can be written as:

$$\frac{dn_1}{dt} = R_{01}n_0 - \frac{n_1}{\tau_1} - 2W_{ETU}n_1^2c - R_{12}n_1 - \frac{n_2}{\tau_{21}}. \quad (4.5)$$

where  $n_0$ ,  $n_1$  and  $n_2$  are the relative populations of the  ${}^3H_6$ ,  ${}^3F_4$  and  ${}^3H_4$  manifolds, respectively,  $W_{ETU}$  is the energy transfer up-conversion co-efficient,  $c$  is the

$\text{Tm}_2\text{O}_3$  concentration,  $R_{01}$  is the pump rate from the  ${}^3H_6 \rightarrow {}^3F_4$  manifold,  $R_{12}$  is the ESA pump rate from the  ${}^3F_4 \rightarrow {}^3H_4$  manifold and  $\tau_2$  is the lifetime of the  ${}^3H_4$  manifold.

The rate equation describing the population of the  ${}^3H_4$  manifold can be written as:

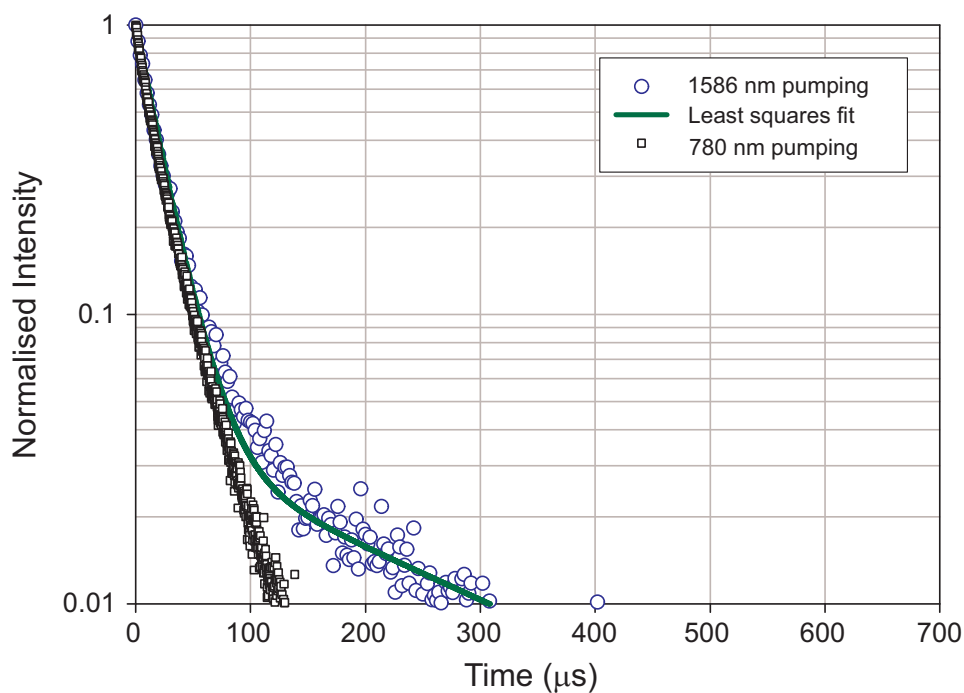
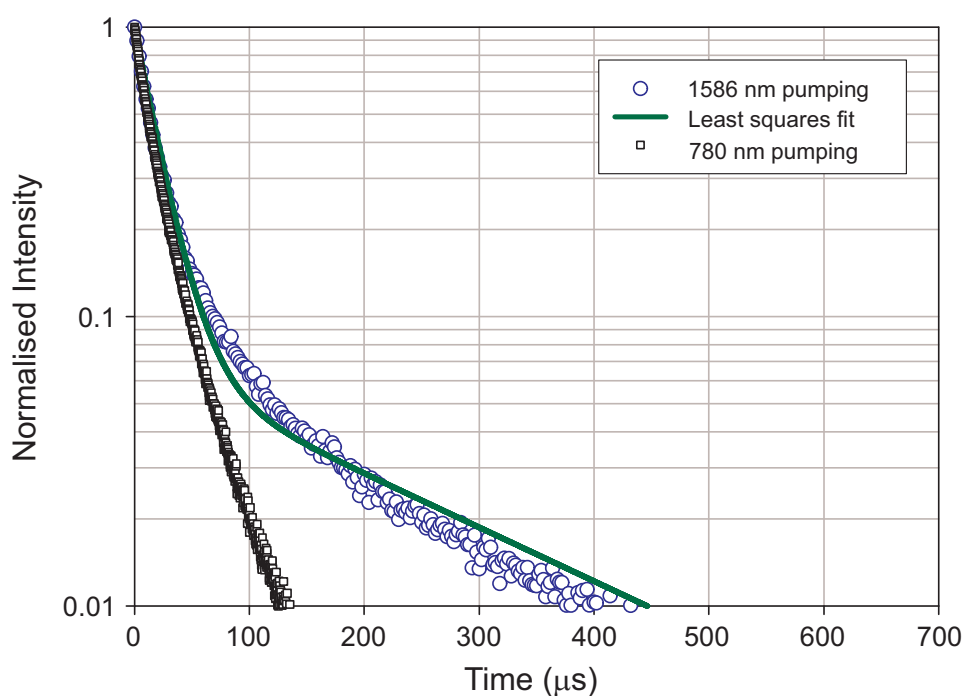
$$\frac{dn_2}{dt} = W_{ETU} n_1^2 c + R_{12} n_1. \quad (4.6)$$

In the steady state these rate equations equate to zero and can be solved analytically. From Equation 4.6 an expression for the up-conversion luminescence ( $n_2$ ) as a function of the down-conversion luminescence ( $n_1$ ) from the  ${}^3F_4$  manifold can be obtained.

$$n_2 = (W_{ETU} n_1^2 c + R_{12} n_1) \tau_2, \quad (4.7)$$

Therefore, in the presence of ESA the up-conversion luminescence from the  ${}^3H_4$  manifold is found to exhibit a greater than quadratic relationship with the down-conversion luminescence from the  ${}^3F_4$  manifold. With this in mind, it can be concluded from the results shown in Figure 4.19 that the up-conversion luminescence from the  ${}^3H_4$  manifold in the germano-silicate fibres is due to two population mechanisms, ETU<sub>2</sub> and ESA. Unfortunately, without a value for ETU<sub>2</sub> or the ESA cross section for the pump wavelength it is not possible to compare the model directly. However, the model is in qualitative agreement with the measured intensities.

Although evidence of ESA has been observed in the study of the steady state luminescence intensity, these effects should not affect the decay characteristics of the up-conversion luminescence, as ESA only occurs in the presence of pump excitation. Hence, the decay analysis used for the aluminosilicate fibres should still hold true for the germano-silicate samples. Figure 4.20 shows the semi-log plot of the up-conversion luminescence decay under 1586 nm pumping for the two germano-silicate samples. Again the least squares fit to Equation 4.4 was applied with the lifetimes  $\tau_1$  and  $\tau_2$  being the 1/e lifetimes, as listed in Table 4.6, obtained under direct pumping of the  ${}^3F_4$  and  ${}^3H_4$  manifolds, respectively.

(a) Ge-1 - 200 ppm  $\text{Tm}_2\text{O}_3$ (b) Ge-2 - 450 ppm  $\text{Tm}_2\text{O}_3$ 

**Figure 4.20:** Semi-log plots of the luminescence from the  ${}^3H_4 \rightarrow {}^3H_6$  transition. (a) and (b) are the decay curves for samples Ge-1 and Ge-2, respectively. The open circles represent the decay under in-direct excitation at 1586 nm. The open squares represent the decay under direct excitation at 780 nm. The least squares fits are discussed in the text.

The fits to the decay waveform show reasonable agreement throughout the decay, although the quality of the fits are less when compared to those obtained for the alumino-silicate samples. This may be attributed to other energy transfer processes occurring which have not been accounted for in the ETU model, an example of which would be ESA of the signal fluorescence. There is some justification for ESA of the signal fluorescence since evidence of ESA was observed in the steady state luminescence investigations. The difference between ESA of the pump and signal fluorescence is that ESA of the pump can only occur during pump excitation and hence when the pump is removed ESA ceases and the excited ions are left to decay naturally to the ground state. ESA of the signal fluorescence, on the other hand, occurs in the presence of fluorescence and therefore there is an opportunity for the excited ions in the intermediate state to be excited to a higher energy manifold by the signal fluorescence for a short period of time after the pump excitation has been removed. This will in turn affect the population of the up-converted manifold as well as the decay characteristics. This may explain the small discrepancy between the measured decay waveform and the ETU model presented here. However, the reasonable agreement with the ETU model still establishes the  $\text{ETU}_2$  process as a populating mechanism of the  ${}^3H_4$  manifold under 1586 nm pumping in germano-silicate fibre. The fitting parameter  $A$  describing the ‘slow’ amplitude is listed in Table 4.11 for the two germano-silicate samples.

Sample	$\text{Tm}_2\text{O}_3$ (ppm)	‘slow’ amplitude ( $A$ )
Ge-1	300	$0.036 \pm 0.001$
Ge-2	1400	$0.067 \pm 0.001$

**Table 4.11:** The ‘slow’ amplitude obtained from the fit to the germano-silicate samples using Equation 4.4.

The ‘slow’ amplitudes are significantly less than those obtained from the alumino-silicate samples. Considering that the fluorescence lifetime of the  ${}^3H_4$  manifold in the germano-silicate samples is similar to the alumino-silicate samples, it can be concluded that the germano-silicate fibres exhibit less  $\text{ETU}_2$  than the alumino-silicate fibres. A crude comparison suggests that the alumino-silicate fibres exhibit

$\sim 2.5$  times more energy transfer up-conversion than the germano-silicate samples, when excited under the same pump conditions at 1586 nm. It is also important to put these results in context with the data presented in Figure 4.12. Under 1586 nm pumping the  ${}^3F_4$  manifold lifetime of the germano-silicate fibre samples showed a greater dependence on pump power. This dependence was attributed to two possible energy transfer up-conversion processes  $\text{ETU}_1$ -( ${}^3F_4, {}^3F_4 \rightarrow {}^3H_5, {}^3H_6$ ) and  $\text{ETU}_2$ -( ${}^3F_4, {}^3F_4 \rightarrow {}^3H_4, {}^3H_6$ ). Unfortunately  $\text{ETU}_1$  relies on the transition from the  ${}^3F_4 \rightarrow {}^3H_5$  manifold which occurs at  $\sim 3 \mu\text{m}$ , a wavelength which is outside the transparency range of silica glass. Therefore quantifying the contribution this process makes to the quenching of the  ${}^3F_4$  manifold is difficult. However, the fact that the germano-silicate fibres exhibit less energy transfer up-conversion to the  ${}^3H_4$  manifold than the alumino-silicate samples implies that the majority of quenching of the  ${}^3F_4$  manifold in germano-silicate fibres occurs as a result of the  $\text{ETU}_1$  process.

Another important observation from the data set was that the germano-silicate fibre samples were found to emit more up-conversion luminescence at 810 nm than the alumino-silicate samples. Figure 4.21 illustrates the difference in the relative intensities from the up-conversion luminescence for samples Al-5 and Ge-1.

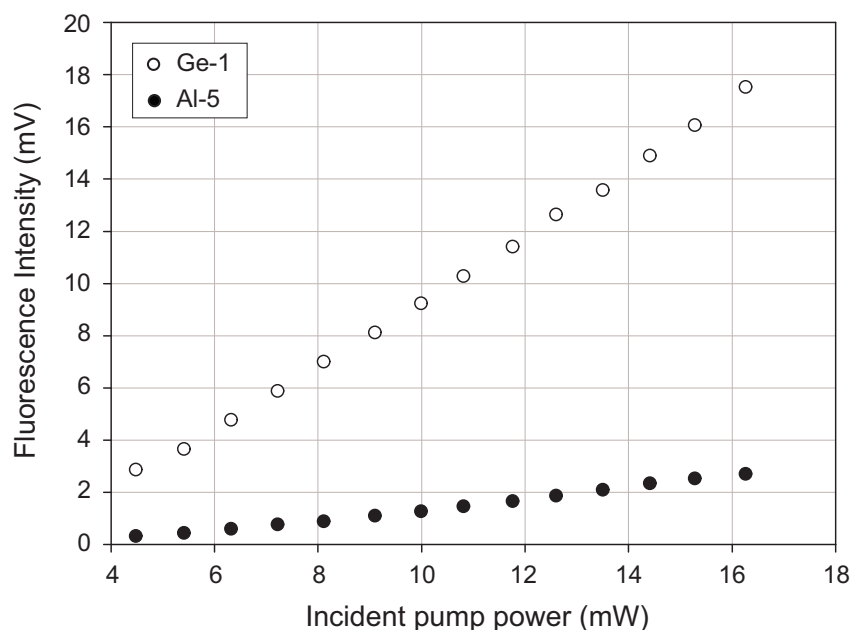


**Figure 4.21:** Measured relative intensities from the up-conversion luminescence of the  $\text{Tm}^{3+}$ -doped germano-silicate and alumino-silicate samples under 1586 nm pumping.

These two fibres are used as the comparison as they have similar  $\text{Tm}_2\text{O}_3$  concentrations. The measured voltage from the photodiode detectors is directly proportional to the relative intensity and hence population from the excited manifold, provided that the detector circuitry is operated within the linear region of the photodiode. The necessary steps were taken to ensure that this was the case.

The higher relative intensities observed in the germano-silicate fibres can be attributed to the populating mechanisms for the two different fibre types. It was established in Section 4.6.1, that up-conversion luminescence at 810 nm from the alumino-silicate fibres resulted solely from the  $\text{ETU}_2$  process. However, the up-conversion luminescence from germano-silicate fibres was linked both to  $\text{ETU}_2$  and ESA. Since the  $\text{ETU}_2$  process was found to be less efficient in the germano-silicate fibres, it must be concluded that ESA in the germano-silicate fibres dominates over  $\text{ETU}_2$  in the concentration range studied here. The significant presence of ESA in the germano-silicate fibres can be attributed to the position of the  ${}^3F_4$  absorption peak. As shown in Section 4.3.2, germano-silicate fibres exhibit a  ${}^3F_4$  absorption peak at significantly shorter wavelengths than the alumino-silicate fibres. Theoretical estimations place the peak ESA cross section from the  ${}^3F_4 \rightarrow {}^3H_4$  transition at 1410 nm [11]. Therefore the  ${}^3F_4$  absorption peak observed in the germano-silicate fibres exhibits significantly more overlap with the ESA cross section of the  ${}^3F_4 \rightarrow {}^3H_4$  transition. This may also provide a plausible explanation as to why ESA was not observed in the  $\text{Tm}^{3+}$ -doped alumino-silicate glass. The  ${}^3F_4$  absorption peak in alumino-silicate glass was measured to be  $\sim 60$  nm longer than in germano-silicate glass, this results in a reduced spectral overlap between the  ${}^3F_4$  manifold and the ESA cross section in comparison to the germano-silicate glasses.

The spectroscopic measurements reported here do not allow the determination of the relative strength of the energy transfer up-conversion co-efficient. In general, determination of this parameter requires a systematic study of the variations in the nature of the luminescence decay from the  ${}^3F_4$  manifold with  $\text{Tm}^{3+}$  concentration. These variations can usually be described well in the energy transfer framework put

forward by Inokuti-Hirayama [108] or Yokota-Tanimoto [124]. Unfortunately, the restricted concentration range studied here limited our ability to study any variations in the fluorescence decay from the  $^3F_4$  manifold. Even so, the identification of this parameter in  $\text{Tm}^{3+}$ -doped silica fibres is made even harder by the fact that two energy transfer up-conversion processes occur out of the  $^3F_4$  manifold. Therefore determining the contribution each process makes to the quenching of the  $^3F_4$  manifold would be extremely difficult and open to significant uncertainty. However, it can be concluded from this investigation that the energy transfer up-conversion process  $\text{ETU}_2-(^3F_4, ^3F_4 \rightarrow ^3H_4, ^3H_6)$  does exist in  $\text{Tm}^{3+}$ -doped silica fibre at  $\text{Tm}_2\text{O}_3$  concentrations as low as a few hundred ppm and this process was found to be more efficient in alumino-silicate glasses compared to germano-silicate glasses.

## 4.7 Conclusion

Modifying the local environment of the  $\text{Tm}^{3+}$  ion in silica glasses has, in some cases, had an advantageous effect on the fluorescence properties of the  $\text{Tm}^{3+}$  ion. The addition of 9 mol % of  $\text{Al}_2\text{O}_3$  to the silica glass network resulted in a  $\sim 260\%$  increase in the fluorescence lifetime of the  $^3H_4$  manifold, when compared to pure silica glass, commensurate with a  $\sim 260\%$  increase in the quantum efficiency of the  $^3H_4 \rightarrow ^3F_4$  S-band transition. A similar percentage increase of  $\sim 175\%$  was observed from the  $^3F_4$  manifold. The increase in the lifetimes of both manifolds was attributed to the modified local environment surrounding the  $\text{Tm}^{3+}$  ion and the lower phonon energy of the Al-O bonds. The addition of  $\text{Al}_2\text{O}_3$  was also shown to affect the energy level structure of the  $\text{Tm}^{3+}$  ion, with the greatest effect observed for the  $^3F_4$  manifold. The peak absorption of this manifold was found to shift by 28 nm with the addition of 9 mol % of  $\text{Al}_2\text{O}_3$ . The cause of the selective shift of the  $^3F_4$  manifold peak is unclear, but may be attributed to the strong electron coupling to the random local strains of the glass. The other co-dopant which was shown to affect the local environment of the  $\text{Tm}^{3+}$  ion was  $\text{GeO}_2$ . Although  $\text{GeO}_2$  exhibited considerable differences in the shapes and positions of the energy manifolds (particularly the  $^3F_4$  manifold) its effect on the fluorescence lifetime of the  $^3F_4$  and  $^3H_4$  manifolds were minimal.

The same can be said for  $\text{Sb}_2\text{O}_3$  and  $\text{SnO}_2$  which were found to have a negligible effect on the absorption or fluorescence properties of the  $\text{Tm}^{3+}$  ion.

The  $\text{Tm}_2\text{O}_3$  concentration studies concluded that the cross relaxation process from the  ${}^3H_4$  manifold has a negligible effect on the decay from this manifold for  $\text{Tm}_2\text{O}_3$  concentrations as high as 1950 and 1400 ppm for aluminosilicate and germanosilicate glasses, respectively. This study went on to establish the ( ${}^3F_4, {}^3F_4 \rightarrow {}^3H_4, {}^3H_6$ ) ETU process in silica based glasses for the first time, to the best of the author's knowledge [125]. Under 1586 nm pumping, the  $\text{ETU}_2$  process was found to be the sole process populating the  ${}^3H_4$  manifold in aluminosilicate glasses, whilst germanosilicate glasses showed evidence of both  $\text{ETU}_2$  and ESA from the  ${}^3F_4$  manifold. In terms of efficiency, the germanosilicate glasses were found to emit more up-conversion luminescence, which was tentatively assigned to the domination of the ESA process in these glasses under 1586 nm pumping. The establishment of the  $\text{ETU}_2$  process may provide an alternative pumping scheme for the S-band optical amplifier in silica glass as it acts to increase the population inversion between the  ${}^3H_4$  and  ${}^3F_4$  manifolds. Future work into optimising the host parameters to maximise the efficiency of the ESA and  $\text{ETU}_2$  processes may enable more efficient  $\text{Tm}^{3+}$ -doped silica fibre S-band optical amplifiers to be realised.

## Chapter 5

# FLUORESCENCE DECAY IN $\text{Tm}^{3+}$ -DOPED SILICA FIBRE

### 5.1 Introduction

This chapter reviews and explores the origin of non-exponential fluorescence decay in rare earth doped materials and presents a study into the origin of the non-exponential fluorescence decay observed from some excited manifolds in  $\text{Tm}^{3+}$  -doped silica fibres. To understand the origin of the non-exponential decay, it is necessary to begin with the simplest form of luminescence decay from an excited manifold known as intrinsic decay. This form of decay occurs when a system of donor ions is excited by a short pulse of radiation. When the number of excited donor ions is small compared to the total number of donor ions, the probability of a neighbouring donor ion being unexcited approaches unity. If the donor ion excitation density, given by  $\phi(\vec{r}, t)$ , denotes the probability of finding a donor ion at position  $\vec{r}$  in an excited state at time  $t$ , then, in the absence of energy acceptor ions and diffusion, the donor ion system  $\phi(t)$  will decay as a single exponential  $\exp(-t/\tau_0)$  where  $\tau_0^{-1}$  is the intrinsic donor ion decay rate.

In addition to intrinsic decay, excited donor ions have been found to relax by (i) direct interaction and energy transfer to acceptor ions and (ii) by the migration of excitation among donor ions. The direct interaction and energy transfer to acceptor ions is a one step process involving resonant energy transfer between donor and acceptor ions. The theory for this process was initially developed by Förster [110] and Dexter [109] for multi-polar coupling and was later extended by Inokuti and Hirayama [108] for exchange coupling. Relaxation via energy migration, on the other

hand, is a multi-step process involving resonant energy transfer from one ion to another ion of the same species in a random walk manner and finally de-exciting to an imperfection in the host material, the theory for which was developed by Dexter and Schulman [123]. It should be noted here, that donor and acceptor ions can represent two different species (or rare earth ions) and in some cases, the rare earth ions take the form of both donor and acceptor ions. For the present discussion, donor and acceptor ions are considered to be  $Tm^{3+}$  ions.

In glass materials both direct energy transfer and energy migration are active. An understanding of how these processes affect the form of the luminescence decay in such systems, may be established in terms of three limiting cases (1) direct transfer - no diffusion, (2) fast diffusion and (3) diffusion-limited relaxation. The theoretical treatment of these three limiting cases have been reviewed in the literature [126] and are summarised below.

### 5.1.1 Direct transfer

In a system which comprises both donor and acceptor ions, direct energy transfer can take place when a donor ion transfers its energy via exchange or multi-polar forces to an acceptor ion. The transfer rates for different donor-acceptor pairings vary significantly since the strength of the donor-acceptor coupling is dependent on the separation between donor-acceptor pairings and the distribution and orientation of acceptor ions [126]. By assuming a random distribution and orientation of acceptor ions, the angular dependence of the transfer rate can be averaged out, leaving the dependence on separation, which for multi-polar interactions is given by [127]:

$$w(R) = CR^{-S}, \quad (5.1)$$

where  $C$  is a constant in m/s,  $R$  is the distance in metres between donor-acceptor ion pairs and  $S$  describes the type of multi-polar coupling. For dipole-dipole coupling  $S = 6$ , dipole-quadrupole  $S = 8$  and quadrupole-quadrupole  $S = 10$ .

The general solution for the decay of the luminescence,  $\phi(t)$ , for multi-polar coupling is then given by:

$$\phi(t) = \phi(0) \exp \left[ (-t/\tau_0) - \frac{4}{3}\pi \Gamma(1 - 3/S) N_a R_0^3 (t/\tau_0)^{3/S} \right], \quad (5.2)$$

where  $\phi(0)$  is the initial excitation,  $R_0 = (C\tau_0)^{(1/S)}$  is the critical transfer distance and is defined as the separation at which the probability for energy transfer between a donor-acceptor ion pair is equal to the intrinsic decay probability  $\tau_0^{-1}$  and finally,  $N_a$  is the concentration of acceptor ions.

A similar expression derived by Inokuti and Hirayama [108] to describe the luminescence decay for exchange coupling is given in Equation 5.3.

$$\phi(t) = \phi(0) \exp \left[ (-t/\tau_0) - \frac{4}{3}\pi^{(3/2)} \Gamma(1 - 3/S) N_a R_0^3 (t/\tau_0)^{3/S} \right]. \quad (5.3)$$

These two relationships show that in the presence of direct energy transfer, the luminescence decay does not exhibit a simple exponential dependence with time. At short times ( $t \ll \tau_0$ ) the decay is non-exponential and proportional to  $1 - \gamma t$  where  $\gamma = \frac{4}{3}\pi^a \Gamma(1 - 3/S) N_a R_0^3 \tau_0^{-3/S}$  and  $a = (3/2)$  and  $1$  for exchange and multi-polar coupling, respectively. whilst at longer times ( $t \gg \tau_0$ ) the decay exhibits an single exponential dependence with a decay rate equal to  $\tau_0^{-1}$ .

### 5.1.2 Fast diffusion

Another form of energy transfer which occurs in systems with high donor ion concentrations is fast diffusion. Fast diffusion refers to the resonant energy transfer between donor ions. In this scheme, the excitation energy is able to migrate through the system by the successive transfer of energy from one donor ion to another, until the excitation comes into the vicinity of an acceptor ion where direct (donor-acceptor) energy transfer can take place. At high donor ion concentrations the average separation between donor ions is small; this allows the migration or diffusion of energy to occur rapidly. The fast diffusion of energy effectively averages out the variations

in the transfer rates for different donor-acceptor ion pairs. The luminescence decay from such a system will therefore exhibit a simple exponential dependence with time.

### 5.1.3 Diffusion-limited relaxation

As opposed to fast diffusion, diffusion limited relaxation is said to occur when the rate of energy diffusion from donor to acceptor ions is slow (but still comparable to the intrinsic decay rate) and when in this regime the system is observed to decay with two competing processes. Excited donor ions in close proximity to acceptor ions will relax predominantly by direct donor-acceptor ion energy transfer, whilst the more distant donor ions must first diffuse into the vicinity of an acceptor ion before relaxation can occur. In systems where the acceptor concentration is low, only a small fraction of the total number of excited donor ions are within the critical transfer distance of an acceptor ion. In this limit, where the average distance between acceptors  $N_a^{-1/3} \gg R_0$ , the donor ion decay will be governed principally by the intrinsic relaxation and the diffusion-limited relaxation to acceptor ions [126].

As the acceptor ion concentration increases, a larger proportion of donor ions are within the critical interaction range of the acceptor ions making energy migration less predominant. Yokota and Tanimoto [124] were the first to obtain a general solution for the donor ion decay function including both diffusion within the donor ion system and donor-acceptor ion energy transfer via dipole-dipole coupling. The solution takes the form:

$$\phi(t) = \phi(0) \exp\left(\frac{-t}{\tau_0}\right) \times \exp\left[-\frac{4}{3}\pi^{3/2}N_a(Ct)^{1/2} \left(\frac{1 + 10.87x + 15.50x^2}{1 + 8.743x}\right)^{3/4}\right], \quad (5.4)$$

where  $x = DC^{-1/3}t^{2/3}$  and  $D$  is the diffusion constant.

For early times during the decay, when  $t \ll C^{1/2}D^{-3/2}$ , often for times  $\ll \tau_0$ , Equation 5.4 reduces to Equation 5.3 and therefore exhibits non-exponential behaviour with time. At longer decay times,  $t \gg \tau_0$ , the diffusion and intrinsic decay processes begin to dominate. In this limit, Equation 5.4 reduces to an exponential

function and decays at a rate approximately equal to  $1/\tau = 1/\tau_0 + 1/\tau_D$ , where  $1/\tau_D$  is the decay rate due to diffusion.

By analysing the luminescence decay from the donor ion system, usually as a function of donor ion concentration, one can determine the appropriate regime of the donor ion system. The distinguishing features of the luminescence decay,  $\phi(t)$ , for each regime are summarised below.

*1. Direct transfer - no diffusion*

- (a) Occurs at low donor ion concentrations;
- (b)  $\phi(t)$  at early times is fast and non-exponential;  $\phi(t \ll \tau_0) \propto 1 - \gamma t^{3/S}$  and
- (c)  $\phi(t)$  at long times becomes exponential as the donor ions that are far from the acceptor ion will decay with their own lifetime:  $\phi(t \gg \tau_0) \propto \exp(-t/\tau_0)$ .

*2. Fast diffusion*

- (a) Occurs at very high donor ion concentrations;
- (b) at high donor ion concentrations the separation between donor ions is small, making the rate of energy transfer/energy migration high and
- (c) the observed decay is purely exponential, since the fast diffusion averages out all of the different donor ion environments:  $\phi(t) \propto \exp(-t/(\tau_0 + \tau_D))$ .

*3. Diffusion-limited relaxation*

- (a) Occurs at high donor ion concentrations;
- (b) the decay at early times, where migration is not important, takes the form for direct donor-acceptor ion transfer:  $\phi(t \ll \tau_0) \propto 1 - \gamma t^{3/S}$  and
- (c) the decay at long times becomes exponential and is characterised by:  $\phi(t \gg \tau_0) \propto \exp(-t/(\tau_0 + \tau_D))$ .

Direct transfer and diffusion-limited relaxation have been shown to result in non-exponential decay of the donor ion system. These two theoretical frameworks are frequently used in the literature to characterise the non-exponential decay from rare earth ions. In recent times, these frameworks have been used to describe the non-exponential decay of the  ${}^3H_4$  and  ${}^3F_4$  manifolds of  $Tm^{3+}$  in a range of different host materials [115, 97, 113, 128, 129, 130]. However, these studies have been restricted to fluoride and crystal host materials, mainly due to their ability to incorporate large  $Tm_2O_3$  concentrations.

Although no quantitative study of the energy transfer processes in  $Tm^{3+}$  -doped silica glass has been undertaken, non-exponential decay from the  ${}^3H_4$  and to a lesser extent the  ${}^3F_4$  manifold, has been reported [107, 88]. Work by Lincoln in low concentration  $Tm^{3+}$  -doped silica fibres demonstrated that non-exponential decay could also occur as a result of the inhomogeneous nature of the glass [107]. The approach taken in that work showed that non-exponential decay of an excited manifold may still occur in the absence of energy transfer mechanisms. The theory behind this approach is discussed in the following section.

#### 5.1.4 Inhomogeneous broadening effects

To understand the effects that inhomogeneous broadening can have on the decay of an excited state manifold, it is convenient to look at the rate equation describing the decay of the population in an excited state. In the absence of any energy transfer processes, the rate equation describing the population of  $N_j$  excited ions in a manifold of energy  $E_j$  can be given as:

$$\frac{dN_j}{dt} = - \sum_{n=1}^{N_j} \left( A_{j,j-1}^n (mp) + \sum_{i, E_i < E_j} A_{j,i}^n (rad) \right), \quad (5.5)$$

where  $A_{j,i}^n (rad)$  is the radiative decay rate of ion  $n$  to a lower lying Stark manifold  $i$  and  $A_{j,j-1}^n (mp)$  is the multi-phonon decay rate of ion  $n$ .

If the radiative and non-radiative decay rates are constant for all excited ions then the  $j^{th}$  manifold will decay as a single exponential, with a characteristic lifetime of  $1/\tau = 1/\tau_{rad} + 1/\tau_{mp}$ , where  $1/\tau_{rad}$  and  $1/\tau_{mp}$  represent the radiative and non-radiative (multi-phonon) decay rates, respectively. However, if there is a non-uniform distribution of either of these two decay rates within the glass, the decay from the manifold will become non-exponential.

As discussed in Section 2.4, inhomogeneous broadening of energy manifolds can result in slight variations in the position of the Stark levels within a manifold. In a situation where the excited and next lowest energy manifold are separated by several thousand  $cm^{-1}$  the transition will be dominated by radiative decay. The slight variation in the position of the energy levels in this case, is considered to have a negligible effect on the decay of the manifold since transitions which are dominated by radiative decay can, in general, be described by a single exponential.

On the other hand, when the energy gap between the excited and next lowest energy manifold is such that multi-phonon emission can occur and dominate, then the decay of the system becomes vulnerable to site-to-site variations. As discussed in Section 2.3, the multi-phonon decay rate is exponentially dependent on the energy gap between the two Stark manifolds; this being the case, any variation between site-to-site energies will have a significant effect on the multi-phonon decay rate. The finite energy differences caused by the site-to-site variation will translate into a finite distribution of possible multi-phonon decay rates and therefore non-exponential decay from the system. The decay of a system dominated by multi-phonon decay across a varying energy gap can be modelled according to [114]:

$$\phi(t) \propto \int g(E) \exp\left(\frac{-t}{\tau_{mp}(E)}\right) dE, \quad (5.6)$$

where  $g(E)$  is the probability of having an energy gap  $E$  and  $\tau_{mp(E)}^{-1}$  is the multi-phonon decay rate which can be approximated by:

$$\tau_{mp(E)}^{-1} = B \exp(-\alpha E), \quad (5.7)$$

where  $B$  and  $\alpha$  are host dependent parameters.

If the assumption is made that energy gap distribution is Gaussian, then the decay of the system can be described by:

$$\phi(t) \propto \int \exp[-(E - (E_0/\zeta))^2 - t B \exp(-\alpha E)] dE, \quad (5.8)$$

where  $(E - (E_0/\zeta))^2$  represents the Gaussian approximation of the energy gap distribution.

Unfortunately, the occurrence of an exponential within the exponential in the integral makes solving this equation extremely difficult. To date, solutions to Equation 5.8 have not been found. Instead, Lincoln demonstrated that a stretched exponential function can be used to characterise these types of decaying systems [114]. The stretched exponential function is frequently used in physics and chemistry to describe non-exponential waveforms and takes the form:

$$\phi(t) = \phi(0) \exp(-t/\tau_{life})^p, \quad (5.9)$$

where  $\phi(0)$  is the initial population of the excited manifold,  $\tau_{SE}$  is the stretched exponential lifetime of the excited manifold and  $p$  is the stretched exponential power (SEP), which ranges from 0 to 1, where 1 represents a single exponential. For  $p$  values  $< 1$  the decay is slower than the comparable exponential decay with the same  $\tau_{life}$  factor.

Therefore, in the case of a stretched exponential function there are three parameters which describe the decay waveform. An important note here is that the stretched exponential function behaviour is implicit in the energy transfer models derived by Förster and Dexter [109], and Inokuti and Hirayama [108]. However in the case of inter-molecular energy transfer, the physical origin of the stretched exponential is

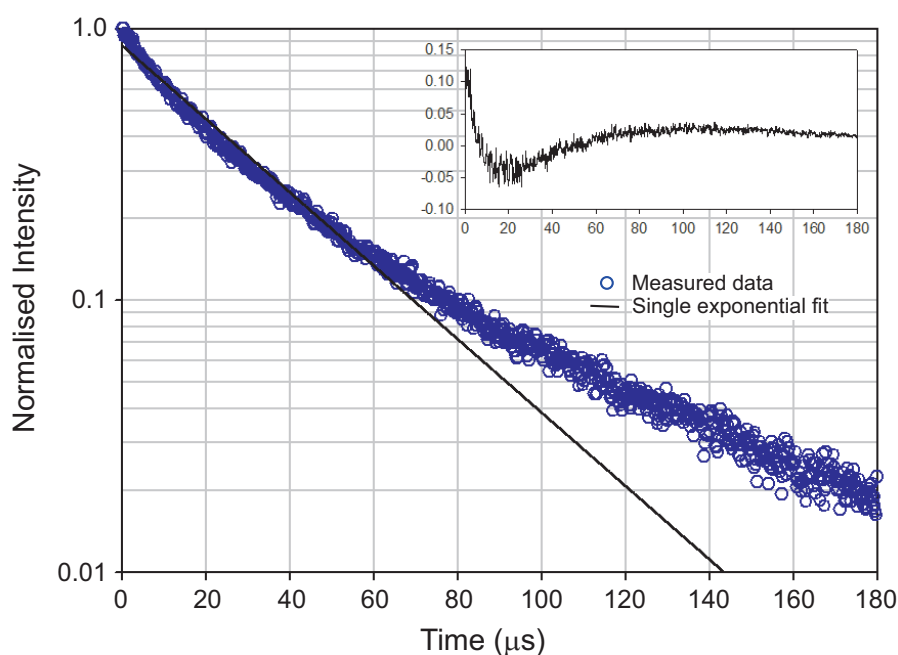
defined [109] and hence the principal parameters driving the stretched exponential decay can be determined. The same cannot be said for the stretched exponential of the form presented in Equation 5.9, for this type of function does not have an exclusive origin for the stretched exponential decay. Therefore, the characteristic lifetime obtained from the fit cannot be interpreted with a great deal of physical meaning. Rather the stretched exponential fit provides an effective tool to compare the shapes and decay time scales from one system to another.

## 5.2 Single exponential fitting

In Chapter 4, single exponential fits were applied to the decay waveforms from the  ${}^3H_4$  and  ${}^3F_4$  manifolds to obtain a characteristic lifetime value which could be compared between each fibre sample.

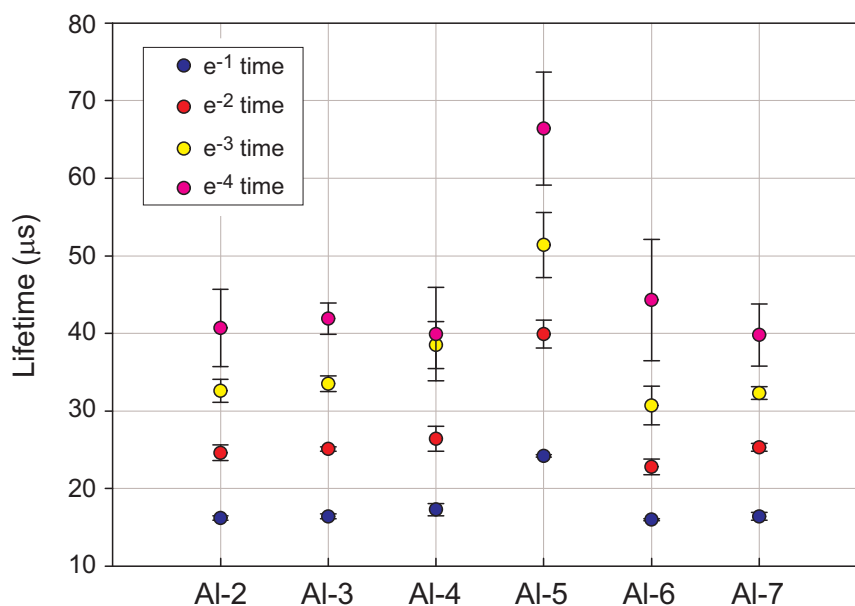
### 5.2.1 ${}^3H_4$ manifold

Figure 5.1 shows an example of a single exponential fit to the decay of the  ${}^3H_4$  manifold for sample Al-7, under 780 nm excitation.



**Figure 5.1:** Single exponential fit to the measured decay from the  ${}^3H_4$  manifold of the alumino-silicate sample Al-7, under 780 nm excitation. The inset of the figure shows the residuals associated with the fit to the single exponential function.

The single exponential fit to the data fails to describe accurately the waveform at the beginning of the decay for  $t < 60 \mu s$ ; this is exemplified in the plot of the residuals shown in the inset of Figure 5.1. The non-exponential nature of the decay from this manifold is further evidenced by the  $1/e$ -fold times for the decay. Figure 5.2 shows the first four e-fold times from the  ${}^3H_4$  manifold decay for six of the  $Tm^{3+}$  -doped alumino-silicate fibre samples.



**Figure 5.2:** The first four e-fold times from the  ${}^3H_4$  manifold decay of  $Tm^{3+}$  -doped alumino-silicate fibres, under 780 nm excitation.

The variation in e-fold times confirms the non-exponential nature of these decay waveforms. The lifetime increase of each e-fold time also indicates that the decay is dictated by longer decay components as it progresses in time.

### 5.2.2 ${}^3F_4$ manifold

The decay waveforms from the  ${}^3F_4$  manifold of  $Tm^{3+}$  are reported frequently as single exponential for reasons discussed later in this chapter. In this section it becomes clear that the decay from this manifold in silica glass does exhibit non-exponential behaviour. Figure 5.3 presents an example of a single exponential fit to the decay of the  ${}^3F_4$  manifold for the alumino-silicate sample Al-7, under 1586nm pumping.

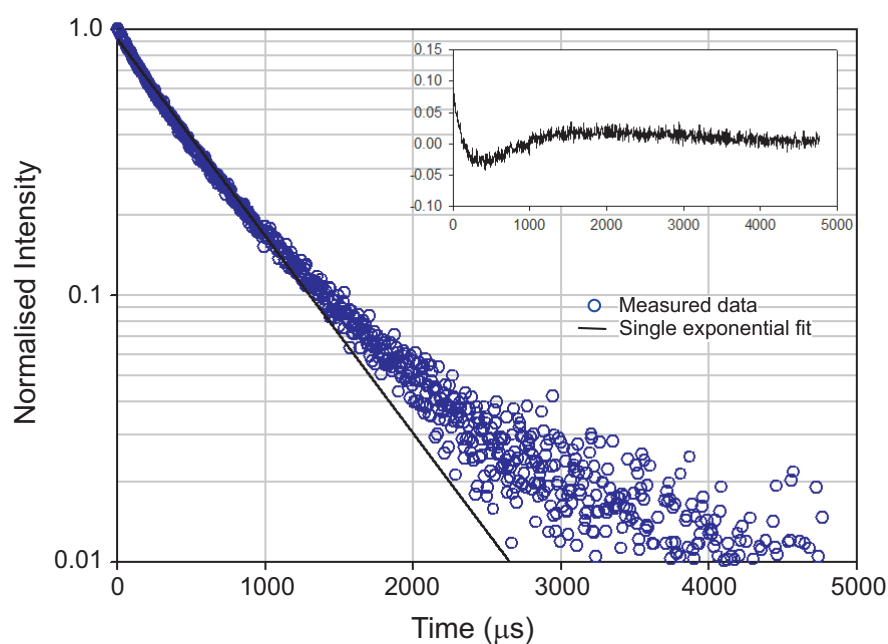


**Figure 5.3:** Single exponential fit to the measured decay from the  $^3F_4$  manifold of the alumino-silicate sample Al-7, under 1586 nm excitation. The inset of the figure shows the residuals associated with the fit to the single exponential function.

From Figure 5.3 it can be concluded that the decay is more exponential than that from the  $^3H_4$  manifold; however, the fit fails to describe the beginning of the decay for times  $> 1000 \mu s$ , as exemplified in the plot of the residuals shown in the inset of Figure 5.3. The first four e-fold times from the  $^3F_4$  manifold decay for six of the  $Tm^{3+}$  -doped alumino-silicate fibre samples is shown in Figure 5.4.

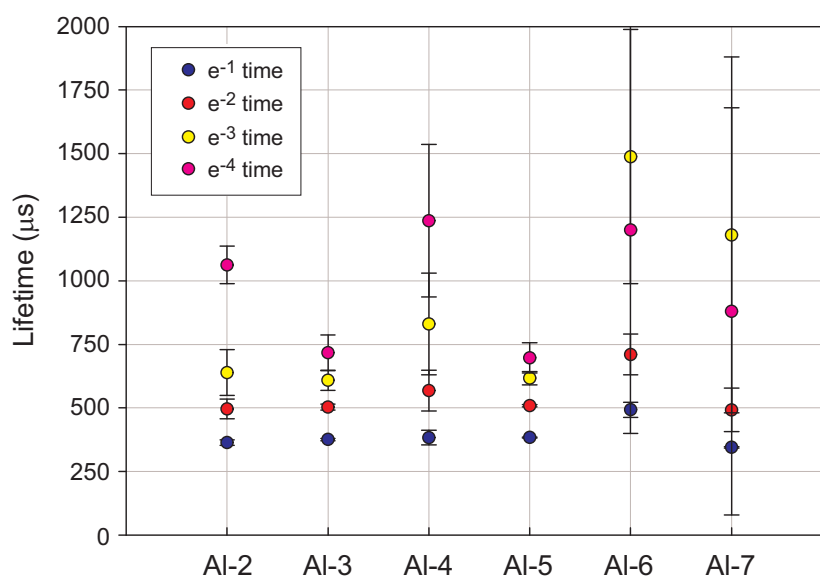


**Figure 5.4:** The first four e-fold times from the  $^3F_4$  manifold decay of  $Tm^{3+}$  -doped alumino-silicate fibres, under 1586 nm excitation.

Although rarely reported in the literature, increases in the e-fold times for the  ${}^3F_4$  manifold in  $Tm^{3+}$  -doped germano-silicate fibres have been observed [88].

### 5.3 Stretched exponential fitting

To explore the non-exponential nature of the decay from both the  ${}^3H_4$  and  ${}^3F_4$  manifolds, a stretched exponential fit is applied to the data to compare the degree of non-exponentiality for each measured waveform. By comparing the amount of non-exponential decay that a particular manifold exhibits, meaningful conclusions regarding the origin of the non-exponential form can be made. The least squares fitting of the stretched exponential function was carried out using the three parameters  $\phi(0)$ ,  $\tau_{SE}$  and  $p$ , as defined in Equation 5.9.

#### 5.3.1 ${}^3H_4$ manifold

Figure 5.5 shows a stretched exponential fit to the  ${}^3H_4$  manifold decay waveform from the alumino-silicate sample Al-7.

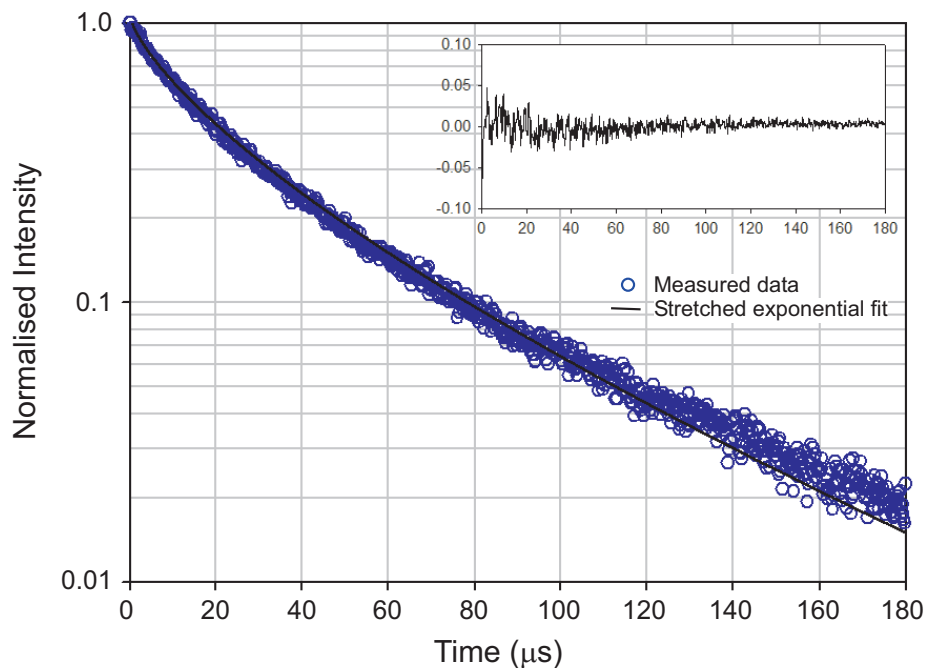


**Figure 5.5:** Stretched exponential fit to the decay from the  ${}^3H_4$  manifold of the alumino-silicate sample Al-7, under 780 nm pumping. The inset of the plot shows the residuals associated with the stretched exponential fit.

The stretched exponential fit described the decay waveform quite accurately over both short and long decay times as seen by the plot of the residuals shown in the inset of Figure 5.5. In the following sections the parameters from the stretched exponential fit are used to investigate the effects of the  $Tm^{3+}$  concentration and host environment on the non-exponential nature of the decay from the  $^3H_4$  manifold.

### 5.3.1.1 $Tm^{3+}$ concentration

In order to determine the origin of non-exponential decay in  $Tm^{3+}$  -doped silica fibres, one of the important comparisons which needs to be made is the degree of non-exponentiality as a function of  $Tm^{3+}$  concentration. If the observed non-exponential decay is a result of inter-molecular energy transfer then, according to the expressions presented in Section 5.1, the decay waveform should become increasingly non-exponential with donor concentration. On the other hand, if the non-exponential decay is a result of the finite distribution of multi-phonon decay rates caused by the inhomogeneous nature of the host material then the degree of non-exponentiality should be independent of donor concentration. Table 5.1 reports the fitted parameters from the stretched exponential fit to the decay of five aluminosilicate fibre samples at various  $Tm_2O_3$  concentrations, under 780 nm pumping.

Sample	$Tm_2O_3$ (ppm)	$\tau_{SE}$ ( $\mu s$ )	SEP ' $p$ '
Al-5	220	$15.9 \pm 0.10$	$0.719 \pm 0.008$
Al-3	450	$15.0 \pm 0.07$	$0.722 \pm 0.007$
Al-6	1850	$15.6 \pm 0.06$	$0.719 \pm 0.006$
Al-4	1950	$15.3 \pm 0.06$	$0.716 \pm 0.005$
Al-8	32000	$10.9 \pm 0.03$	$0.704 \pm 0.005$

**Table 5.1:** Characteristic lifetimes and stretched exponential powers of the  $^3H_4$  manifold as a function of  $Tm_2O_3$  concentration.

The stretched exponential power obtained from the fits show no dependence on the  $Tm_2O_3$  concentration, for concentrations as high as 1950 ppm. This result is in agreement with Chapter 4, which found that the cross relaxation process involving the  $^3H_4$  and  $^3H_6$  manifolds ( $^3H_4, ^3H_6 \rightarrow ^3F_4, ^3F_4$ ) has a negligible effect on the decay dynamics of the  $^3H_4$  manifold at these concentration levels. It can also be concluded,

from the lack of concentration dependence in this sample set, that inter-molecular energy transfer mechanisms are not the cause of the non-exponential behaviour from this manifold.

The highly doped Al-8 sample was the only sample to deviate from the average stretched exponential power. The slight reduction in the power and exponentiality could be attributed to the cross relaxation process originating from this manifold, as the probability of this process occurring increases with concentration. With this in mind, the decay waveform was fitted to both the Inokuti-Hirayama energy exchange expression as well as the Yokota-Tanimoto expression; both fits exhibited similar outcomes to the stretched exponential as expected. However, the phenomenological parameters which arise from the fits give non-physical values, indicative of an inappropriate fit.

This leads to the second most probable cause for the slight reduction in the stretched exponential power, the host composition. Sample Al-8 was co-doped with aluminium and a small proportion of phosphorus, which acted as a glass softening agent to incorporate such high  $Tm_2O_3$  concentrations. The addition of phosphorus to the host composition has been shown to dramatically decrease the fluorescence lifetime of the  $^3H_4$  manifold [35], which indicates that it has a significant impact on the local environment surrounding the  $Tm^{3+}$  ion. It is therefore proposed that the incorporation of phosphorus has modified the local environment which could involve increasing the amount of inhomogeneous broadening and therefore the distribution of possible multi-phonon decay rates in the system. An increase in the amount of inhomogeneous broadening would account for the observed increase in the non-exponentiality of the Al-8 decay waveform.

### 5.3.1.2 Alumino-silicate fibres

To further explore the host materials' effect on the non-exponentiality of the decay waveforms a study was undertaken on the stretched exponential parameters for the range of alumino-silicate fibre samples. The stretched exponential parameters for a

series of alumino-silicate samples with  $Tm_2O_3$  concentrations  $< 500$  ppm containing  $Al_2O_3$  concentrations from 1.9 to 9 mol% are listed in Table 5.2 and displayed as a function of  $Al_2O_3$  concentration in Figure 5.6.

Sample	$Al_2O_3$ (mol %)	$\tau_{SE}$ ( $\mu s$ )	SEP ' $p$ '
Al-1	1.9	$16.8 \pm 0.1$	$0.733 \pm 0.006$
Al-2	3.4	$19.9 \pm 0.1$	$0.723 \pm 0.005$
Al-3	4.4	$20.7 \pm 0.1$	$0.722 \pm 0.004$
Al-5	4.8	$22.5 \pm 0.2$	$0.719 \pm 0.004$
Al-7	9.0	$32.5 \pm 0.2$	$0.697 \pm 0.005$

**Table 5.2:** Characteristic lifetimes and stretched exponential powers of the  $^3H_4$  manifold as a function of  $Al_2O_3$  concentration.

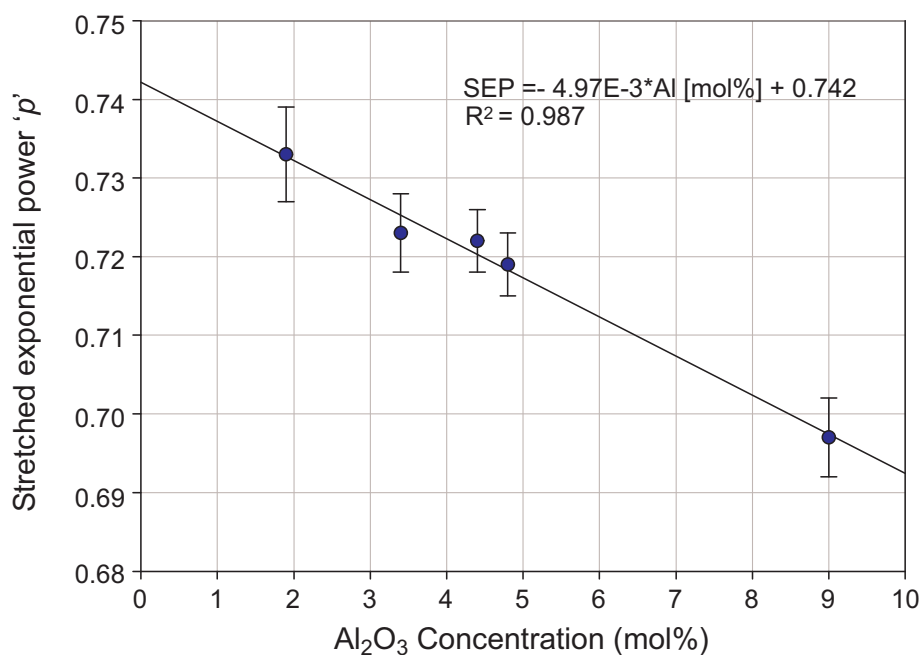


**Figure 5.6:** Stretched exponential power for the  $^3H_4$  manifold as a function of  $Al_2O_3$  concentration, for fibre samples with  $Tm_2O_3$  concentrations  $< 500$  ppm.

The decreasing trend in the stretched exponential power with  $Al_2O_3$  concentration indicates that the host material and local environment surrounding the  $Tm^{3+}$  ion does indeed, play a role in determining the shape and nature of the decay from the  $^3H_4$  manifold. In the theoretical framework considered here, an increase in the non-exponentiality with increasing  $Al_2O_3$  concentration suggests that the site-to-site

variations and distributions of multi-phonon decay rates increases with increasing  $Al_2O_3$  concentration. There is evidence in the literature to support such an argument, with spectroscopic studies of  $Er^{3+}$  and  $Nd^{3+}$  showing that the amount of inhomogeneous broadening of the excited  $^4I_{13/2}$  and  $^4F_{3/2}$  manifolds, respectively, increase with increasing  $Al_2O_3$  concentration in silica glass [131, 92]. Since the fibres studied in this investigation were fabricated using the same technique (MCVD) in a similar host material, it is not unreasonable to expect  $Tm^{3+}$  -doped alumino-silicate glasses to exhibit similar characteristics. An important note here is that no significant inhomogeneous broadening of the energy manifold was observed from the absorption spectra presented in Section 4.3, bearing in mind that the measurement resolution of the spectra was limited to 2 nm. This suggests that modest changes in the local environment may lead to significant changes in the exponentiality of the decay waveform from the  $^3H_4$  manifold. Variation in the local environment surrounding the  $Tm^{3+}$  ion, caused by the addition of  $Al_2O_3$ , may be further exaggerated by the fact that the  $^3H_4$  manifold is dominated by non-radiative multi-phonon decay (see Table 2.1). The strong link to the multi-phonon decay rate results in the  $^3H_4$  manifold being extremely sensitive to changes in the local environment. This sensitivity may prove to be an effective tool in determining the effects of a co-dopant in the silica glass system.

### 5.3.1.3 Germano-silicate fibres

The parameters obtained from stretched exponential fits to the decay waveforms from the  $^3H_4$  manifold of the germano-silicate samples are listed in Table 5.3.

Sample	$\tau_{SE}$ ( $\mu s$ )	SEP ' $p$ '
Ge-1	$17.8 \pm 0.1$	$0.818 \pm 0.008$
Ge-2	$16.4 \pm 0.1$	$0.804 \pm 0.005$

**Table 5.3:** Characteristic lifetimes and stretched exponential powers of the  $^3H_4$  manifold for the two germano-silicate fibres.

The stretched exponential power exhibited in the germano-silicate samples is considerably higher than those reported for the alumino-silicate samples. The increase in the exponentiality can be explained in terms of how the rare earth ion is incorporated into the host material. In germano-silicate glass, the four-coordinated Ge does not alter the tetrahedral silica network sufficiently [91]. By comparison, the structural model put forward by Arai *et al.* for the incorporation of Al suggests that there are two different bonding configurations in a  $SiO_2$  network: (a) a tetrahedral bonding configuration as a network former such as  $AlO_{4/2}$  and (b) an octahedral coordination of oxygen atoms as a network modifier such as  $AlO_{6/2}$ . Therefore combinations of  $AlO_{4/2}$  and/or  $AlO_{6/2}$  coupled with  $SiO_2$  surround the rare earth ion.

The varying local environment surrounding the rare earth has important implications on the transition linewidths, both homogeneous and inhomogeneous. Indeed, Desurvire *et al.* showed in studies on  $Er^{3+}$  -doped silica glass, that the inhomogeneous broadening of the  ${}^4I_{14/2} \rightarrow {}^4I_{15/2}$  was greater in alumino-silicate glasses compared to germano-silicate glass [132, 133]. It is expected that the  $Tm^{3+}$  -doped silica glasses studied here would exhibit similar characteristics, as they were fabricated using the same technique. In this case, decay waveforms which are dependent on the inhomogeneous broadening of the host in germano-silicate fibres will exhibit a greater degree of exponentiality than those in alumino-silicate glass as the site-to-site variation and hence distribution of possible multi-phonon decay rates is reduced.

### 5.3.2 ${}^3F_4$ manifold

In this section, the non-exponential decay of the  ${}^3F_4$  manifold is explored in greater detail with respect to the host composition and  $Tm_2O_3$  concentration. A stretched exponential fit to the  ${}^3F_4$  manifold decay of the Al-7 sample, under 1586 nm pumping, is shown in Figure 5.7.

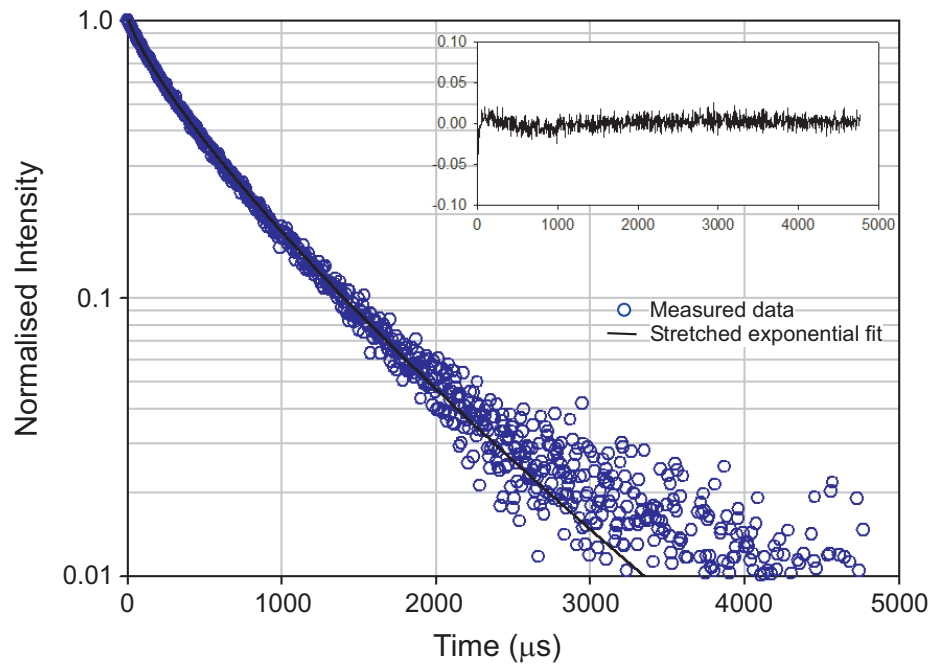


**Figure 5.7:** Stretched exponential fit to the decay from the  ${}^3F_4$  manifold of the aluminosilicate sample Al-7, under 1586 nm pumping. The inset of the plot shows the residuals associated with the stretched exponential fit.

The fit again describes the decay waveform well at both early and late times, as indicated by the plot of the residuals in the inset of Figure 5.7. To explore the origin of non-exponentiality from the  ${}^3F_4$  manifold, a similar study was carried out into the effects of the  $Tm_2O_3$  concentration and host composition.

### 5.3.2.1 $Tm^{3+}$ concentration

Table 5.4 reports the fitted parameters from the stretched exponential fit to the decay of five aluminosilicate fibre samples at various  $Tm_2O_3$  concentrations.

Sample	$Tm_2O_3$ (ppm)	$\tau_{SE}$ ( $\mu s$ )	SEP ' $p$ '
Al-5	220	$367 \pm 2$	$0.781 \pm 0.006$
Al-3	450	$347 \pm 1$	$0.785 \pm 0.004$
Al-6	1850	$361 \pm 1$	$0.794 \pm 0.008$
Al-4	1950	$366 \pm 1$	$0.795 \pm 0.005$
Al-8	32000	$355.5 \pm 0.5$	$0.879 \pm 0.0007$

**Table 5.4:** Characteristic lifetimes and stretched exponential powers of the  ${}^3F_4$  manifold for increasing  $Tm_2O_3$  concentrations.

It may be argued that the non-exponential decay from the  ${}^3F_4$  manifold is a result of the energy transfer up-conversion processes which were established in Section 4.6. However, if this were the case then the degree of non-exponentiality would increase with increasing  $Tm_2O_3$  concentration. The stretched exponential powers listed in Table 5.4 show a variation of  $< 2\%$  for  $Tm_2O_3$  concentrations ranging from 220 - 1950 ppm. It can therefore be concluded that the energy transfer up-conversion processes originating from the  ${}^3F_4$  manifold have a negligible effect on the decay characteristics of the  ${}^3F_4$  manifold at such concentrations. This is not a surprising result, as the energy transfer up-conversion process, established in Section 4.6, is less efficient than the cross relaxation process and no significant change was observed for that process.

A significant increase in the stretched exponential power was observed for the highly concentrated Al-8 sample. The  $\sim 10\%$  increase in the stretched exponential power is attributed to the high  $Tm_2O_3$  concentration. At  $Tm_2O_3$  concentrations of the order of several thousand ppm, the system can be considered to be in the fast diffusion regime. In this regime, donor  $Tm^{3+}$  ions can transfer energy rapidly throughout the system, effectively averaging out the variations in the multi-phonon decay rate caused by the site-to-site variations. The averaging of the multi-phonon decay rate distribution results in a decay which has a greater exponential dependence with time. This regime has a more pronounced effect on the  ${}^3F_4$  manifold, because the manifold is dominated less by multi-phonon decay compared to the  ${}^3H_4$  manifold and exhibits a longer intrinsic decay time.

### 5.3.2.2 Alumino-silicate fibres

The stretched exponential parameters for the series of alumino-silicate samples with  $Tm_2O_3$  concentrations  $< 500$  ppm containing  $Al_2O_3$  concentrations from 1.9 to 9 mol% are listed in Table 5.5 and displayed as a function of  $Al_2O_3$  concentration in Figure 5.8.

Sample	$Al_2O_3$ (mol %)	$\tau_{SE}$ ( $\mu s$ )	SEP ' $p$ '
Al-1	1.9	$306 \pm 6$	$0.77 \pm 0.01$
Al-2	3.4	$332 \pm 2$	$0.774 \pm 0.005$
Al-3	4.4	$347 \pm 3$	$0.785 \pm 0.004$
Al-5	4.8	$367 \pm 2$	$0.781 \pm 0.006$
Al-7	9.0	$475 \pm 2$	$0.781 \pm 0.008$

**Table 5.5:** Characteristic lifetimes and stretched exponential powers of the  ${}^3F_4$  manifold for increasing  $Al_2O_3$  concentration.

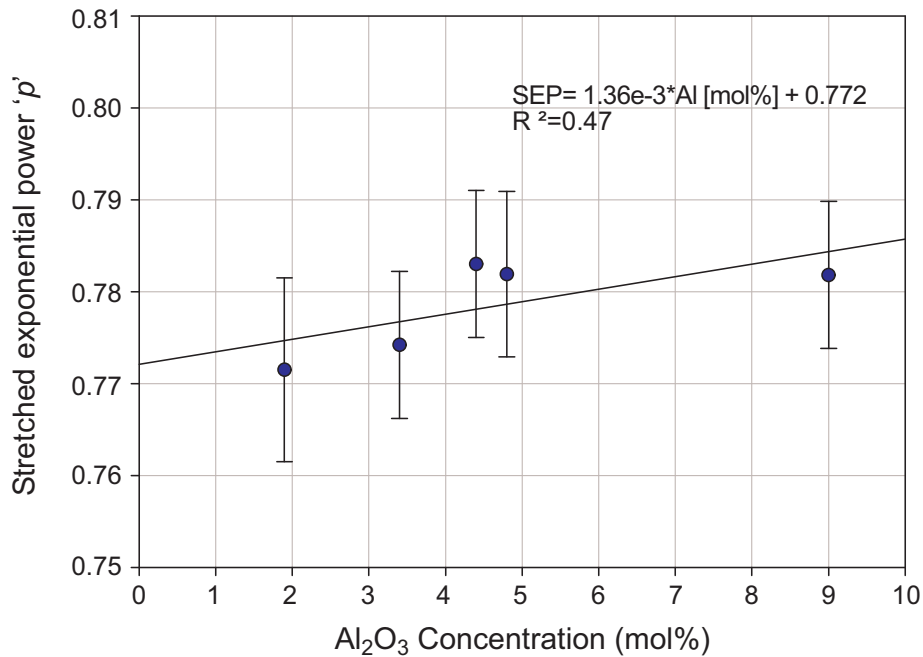


**Figure 5.8:** Stretched exponential power for the  ${}^3F_4$  manifold as a function of  $Al_2O_3$  concentration, for fibre samples with  $Tm_2O_3$  concentrations  $< 500$  ppm.

From the data presented in Figure 5.8 a slight positive slope is observed. However, the linear fit applied to the data results in a poor fit and a slope consistent with zero, when measurement errors are considered. The stretched exponential power of the  ${}^3F_4$  manifold was found to be significantly higher ( $\sim 10\%$ ) than the  ${}^3H_4$  manifold. This can be explained by considering the multi-phonon contribution to the overall decay rate for each manifold. The energy gap from the  ${}^3F_4$  manifold to the  ${}^3H_6$  ground state is  $\sim 5400\text{ cm}^{-1}$ , whereas the energy gap from the  ${}^3H_4$  manifold to the next lowest Stark manifold ( ${}^3H_5$ ) is  $\sim 4150\text{ cm}^{-1}$ . Therefore, the decay from the  ${}^3H_4$  manifold is more sensitive to variations in the multi-phonon decay rate

caused by site-to-site variations. Many researchers have reported single exponential decay from the  ${}^3F_4$  manifold [95, 134, 97], in low phonon energy glasses, where this transition is dominated by radiative decay as the energy gap cannot be bridged by the simultaneous emission of multiple phonons. Hence, site-to-site variations caused by the host material have little to no effect on the decay of the manifold and the manifold will decay as a single exponential. Researchers have also reported single exponential decay of the  ${}^3F_4$  manifold in crystals [115]; in these cases the single exponential nature of the decay arises from the fact that the sites occupied by rare earth ions are the same throughout the crystal which results in little or no inhomogeneous broadening of the energy levels. With no inhomogeneous broadening, all excited ions in a particular manifold will decay with constant radiative and non-radiative decay rates.

### 5.3.2.3 Germano-silicate fibres

The parameters obtained from the stretched exponential fit to the decay waveforms from the  ${}^3F_4$  manifold of the germano-silicate samples are presented in Table 5.6.

Sample	$\tau_{SE}$ ( $\mu s$ )	SEP 'p'
Ge-1	$419 \pm 2$	$0.853 \pm 0.004$
Ge-2	$387 \pm 1$	$0.815 \pm 0.004$

**Table 5.6:** Characteristic lifetimes and stretched exponential powers of the  ${}^3F_4$  manifold for the two germano-silicate fibres.

The fluorescence decay from the  ${}^3F_4$  manifold in the germano-silicate glass again exhibited a greater degree of exponentiality than those observed in the alumino-silicate glass. This result is consistent with the explanation offered in Section 5.3.1.3, regarding the difference between the incorporation of the  $Tm^{3+}$  ion in a host material of germano-silicate as opposed to alumino-silicate. The cause of the difference between the stretched exponential power of Ge-1 and Ge-2 ( $\sim 4\%$ ) is unclear. One possible explanation may be the difference in  $Tm_2O_3$  concentration. In germano-silicate glass, the incorporation of rare earth ions is made difficult by the tetrahedral structure of the network and lack of non-bridging oxygens. Hence, rare earth ions in

germano-silicate glasses tend to cluster at concentrations much less than aluminosilicate glasses [92]. With this in mind, the reduction in stretched exponential power observed with the increase in the  $Tm_2O_3$  concentration, may indicate that the energy transfer up-conversion processes established in Section 4.6 affect the decay dynamics of this manifold for  $Tm_2O_3$  concentrations  $\gtrsim 1950$  ppm. However, this effect is considered to be minimal since the ETU rate was found to be greater in the aluminosilicate fibres where no variation in the shape of the decay was observed with increasing  $Tm_2O_3$  concentration.

## 5.4 Conclusion

In the majority of cases, the fluorescence from rare earth ions can be described well by fitting a single exponential function to the decay waveform. The single exponential fit is justified when the majority of ions decay with the same radiative and non-radiative decay rates. In a disordered host material such as glass, this requirement still holds true for excited manifolds which are dominated by radiative decay. On the other hand, excited manifolds which are dominated by multi-phonon decay have been found to exhibit non-exponential behaviour, regardless of dopant concentration. In these situations the non-exponential nature of the decay cannot be explained by ion-ion interactions and/or clustering.

In the present study, the non-exponential nature of the decay from the  $^3H_4$  and  $^3F_4$  manifolds in  $Tm^{3+}$  -doped aluminosilicate host materials, was explained in terms of multi-phonon decay occurring across varying energy gaps caused by site-to-site variations in the glass network. Stretched exponential fits were found to accurately describe the non-exponential nature of the decays as well as providing a comparative figure for the degree of non-exponentiality exhibited by a particular decay waveform. The stretched exponential power for the  $^3H_4$  manifold of  $Tm^{3+}$  in the aluminosilicate glass was found to decrease with increasing  $Al_2O_3$  concentration. This effect was attributed to the increase in site-to-site variations and distribution of possible multi-phonon decay rates caused by the incorporation of  $Al_2O_3$  into the

glass network. The results suggest that the  $^3H_4$  manifold of  $Tm^{3+}$  may be used as a probing source to gain information about the relative amount of site-to-site variation and average local environment experienced by a  $Tm^{3+}$  ion. Although no quantitative information could be obtained from this analysis, it may provide a simple technique for assessing the effects of co-doping in particular disordered host materials. It should be noted that this technique is not limited to  $Tm^{3+}$ ; other rare earth ions that have energy manifolds which are dominated by multi-phonon decay will also serve as excellent probing sources for the assessment of the effects of different host modifiers.

## Chapter 6

# THULIUM:YTTTERBIUM-DOPED SILICA FIBRES

The second approach taken to improve the quantum efficiency of the  $\text{Tm}^{3+}$  -doped fibre amplifier in silica glass was to co-dope  $\text{Tm}^{3+}$  ions with a strong sensitising ion in the form of  $\text{Yb}^{3+}$ . Studies of  $\text{Tm}^{3+}/\text{Yb}^{3+}$  co-doped systems date back to the 1960s and 70s where Hewes *et al.* [41] and Ostermayer *et al.* [42] carried out extensive studies on the up-conversion characteristics of  $\text{Tm}^{3+}/\text{Yb}^{3+}$  in  $\text{YF}_3$  crystals. Researchers have since studied the properties of  $\text{Tm}^{3+}/\text{Yb}^{3+}$  co-doped systems in a range of host materials [43, 44, 135, 45, 136], although work that has been carried out on such systems in silica based glasses has been limited. Hanna *et al.* reported on the up-conversion properties of  $\text{Tm}^{3+}/\text{Yb}^{3+}$  -co-doped silica glass under excitation at 1060 and 800-860 nm and found that the poor up-conversion efficiencies of the system were a result of the short excited state lifetimes of  $\text{Tm}^{3+}$  [64]. However, from the results shown in Section 4.4.1, 3-fold increases in the fluorescence lifetimes of the  $^3H_4$  and  $^3F_4$  manifolds can be achieved in these glass types through the incorporation of large amounts of  $\text{Al}_2\text{O}_3$ . This, coupled with the development of high-powered semi-conductor laser sources at 980 nm, which enables the peak absorption of  $\text{Yb}^{3+}$  to be optically pumped efficiently, suggests that an improvement in the up-conversion efficiencies in silica-based materials may now be realised.

In this chapter the up-conversion properties of  $\text{Tm}^{3+}/\text{Yb}^{3+}$  co-doped aluminosilicate fibres under excitation at 980 nm are presented. The population mechanisms for the up-conversion processes are established and studied at three different  $\text{Tm}^{3+}/\text{Yb}^{3+}$  concentration ratios. The lifetimes of the excited states of  $\text{Tm}^{3+}$  and  $\text{Yb}^{3+}$  are also reported and studied as a function of  $\text{Yb}_2\text{O}_3$  concentration.

## 6.1 Absorption measurements

A total of three  $\text{Tm}^{3+}/\text{Yb}^{3+}$  co-doped aluminosilicate fibres were fabricated for this study using the MCVD and solution doping techniques. The core concentrations of the fibres are listed in Table 6.1 along with the  $\text{Tm}^{3+}/\text{Yb}^{3+}$  concentration ratios.

Sample	$\text{Tm}_2\text{O}_3$ (ppm)	$\text{Yb}_2\text{O}_3$ (ppm)	Ratio $\text{Tm}^{3+}/\text{Yb}^{3+}$	$\text{Al}_2\text{O}_3$ (mol%)	LPMC label
TmYb-1	100	430	1:4	3.8	C05
TmYb-2	100	940	1:9	3.8	C08
TmYb-3	120	1400	1:12	3.2	C017

**Table 6.1:** Core dopants of the  $\text{Tm}^{3+}/\text{Yb}^{3+}$  -co-doped silica fibres.

The absorption spectrum of the TmYb-1 sample is shown in Figure 6.1.

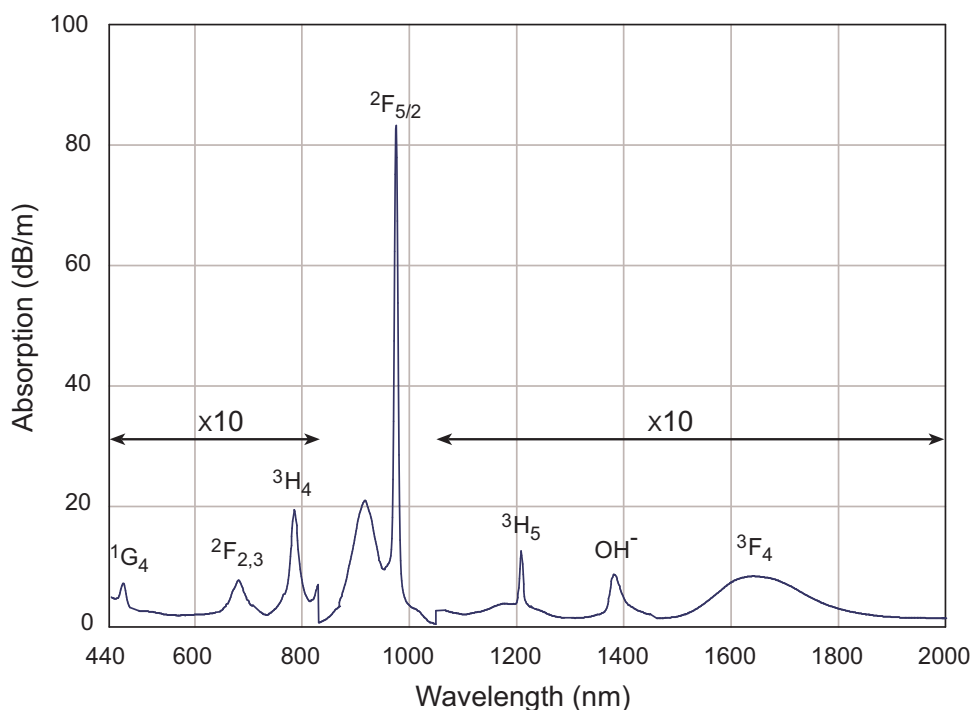


**Figure 6.1:** Measured absorption spectrum of the  $\text{Tm}^{3+}/\text{Yb}^{3+}$  -co-doped silica fibre sample TmYb-1. The energy level designations for each absorption peak are also presented. Note: the measured absorption has been magnified by a factor of 10 in the regions designated by the arrows.

The absorption spectrum displayed similar characteristics to the  $\text{Tm}^{3+}$  -doped silica fibre spectra shown in Section 4.3.1, apart from the absorption peaks present at 920 and 976 nm. These peaks are attributed to the  $\text{Yb}^{3+}$  ion and are significantly stronger than those associated with  $\text{Tm}^{3+}$  as can be seen by the scaling factor of 10 in Figure 6.1. The  $\text{Tm}_2\text{O}_3$  and  $\text{Yb}_2\text{O}_3$  concentrations given in Table 6.1 were estimated from the absorption peaks at 786 and 920 nm, respectively. The refractive index profiles of the fibre samples were used to obtain the  $\text{Al}_2\text{O}_3$  concentrations.  $\text{Al}_2\text{O}_3$  was used to modify the core region of the fibre, as it has been established that it has a lengthening effect on the fluorescence lifetimes of the  $^3H_4$  and  $^3F_4$  manifolds. The  $\text{Al}_2\text{O}_3$  also helps to distribute the rare earth ions homogeneously throughout the glass host and provides the refractive index difference needed to guide light along the fibre. High  $\text{Tm}_2\text{O}_3$  concentrations were avoided in this study as the cross relaxation processes between  $\text{Tm}^{3+}$  ions may mask the energy transfer properties from the energy exchange between  $\text{Yb}^{3+}$  and  $\text{Tm}^{3+}$  ions. No other standard modifiers of silica, such as germanium, phosphorus or fluorine were used in the fabrication process.

## 6.2 Up-conversion luminescence under 980 nm excitation

The approach taken in this investigation is to use a double energy transfer process to further enhance the quantum efficiency of the S-band transition in  $\text{Tm}^{3+}$ . The proposed double energy transfer process has the added advantage of populating the upper amplifying  $^3H_4$  manifold whilst depopulating the lower amplifying  $^3F_4$  manifold, as shown in Figure 6.2.

The double energy transfer mechanism involves the energy transfer of an excited ion in the  $^2F_{5/2}$  manifold of  $\text{Yb}^{3+}$  with a nearby ground state  $\text{Tm}^{3+}$  ion, which excites the ground state  $\text{Tm}^{3+}$  ion to the  $^3H_5$  manifold. Due to the close proximity of the  $^3F_4$  manifold, multi-phonon decay quickly relaxes any population in the  $^3H_5$  mani-

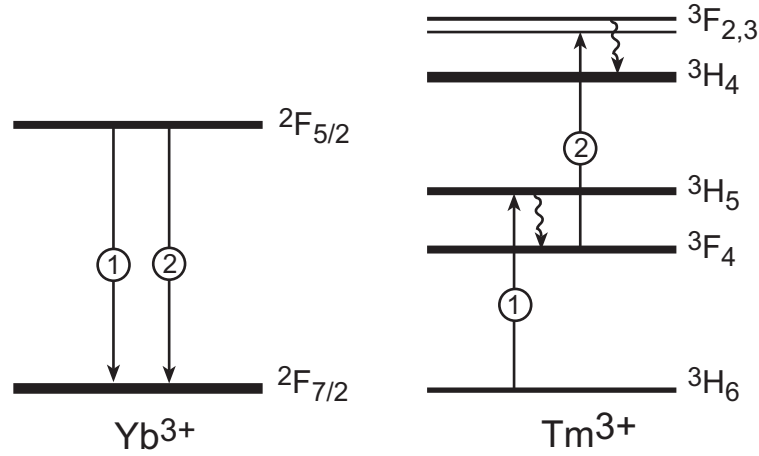
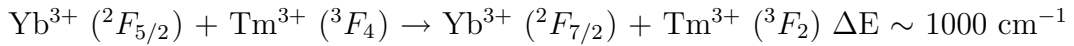
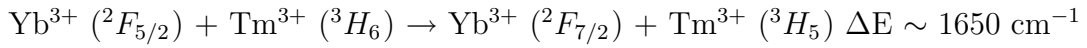


**Figure 6.2:** Double energy transfer between  $\text{Yb}^{3+}$  and  $\text{Tm}^{3+}$  ions under 980 nm excitation, illustrating how the  ${}^3H_4$  manifold of  $\text{Tm}^{3+}$  is populated.

fold to the relatively long lived  ${}^3F_4$  manifold. A second energy transfer from another excited  $\text{Yb}^{3+}$  ion can then populate the  ${}^3F_2$  and  ${}^3F_3$  manifolds of  $\text{Tm}^{3+}$ . Again, multi-phonon decay quickly relaxes any population in the  ${}^3F_2$  and  ${}^3F_3$  manifolds to the  ${}^3H_4$  manifold. The non-resonant nature of each energy transfer step necessitates the assistance of phonons. The energy mismatch for each up-conversion step is given below for  $\text{Tm}^{3+}/\text{Yb}^{3+}$  in  $\text{YF}_3$  [42]:



From the absorption spectra of the fibre samples used in this investigation these mismatches are estimated to be  $\sim 1124 \pm 4$  and  $\sim 822 \pm 33 \text{ cm}^{-1}$ , respectively. The reduction in the energy mismatches in silica glass may be attributed to the energy level broadening caused by the amorphous nature of the glass. The positive energy mismatch associated with these processes requires the emission of phonons to conserve energy. The reduced energy mismatches coupled with the relatively high phonon energy of silica glass suggests that efficient energy transfer can take place in silica glass environments, although these advantages may be negated by the reduction in the radiative lifetimes of the excited manifolds.

When optically pumped at 980 nm, the  $\text{Tm}^{3+}/\text{Yb}^{3+}$  -co-doped silica fibres produced

blue emission, which was clearly visible with the naked eye. Blue luminescence under 980 nm pumping in  $\text{Tm}^{3+}/\text{Yb}^{3+}$  -co-doped systems has been observed in many host materials and is reported to originate from the  $^1G_4$  manifold of  $\text{Tm}^{3+}$  by the successive three step energy transfer process illustrated in Figure 6.3 [64, 137, 138].

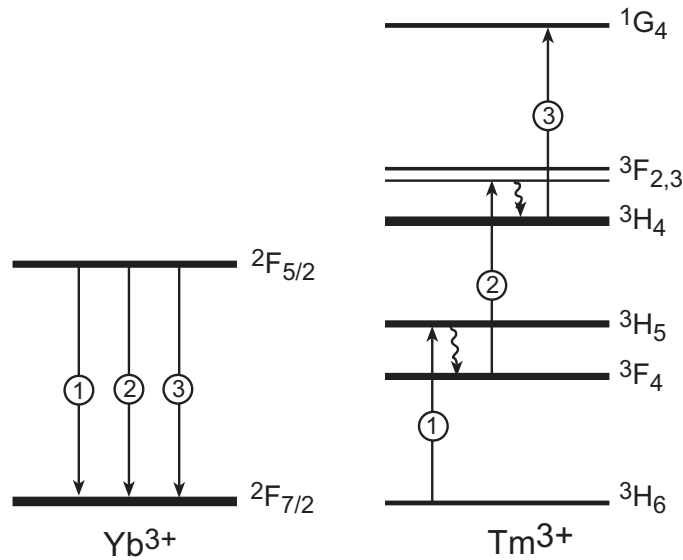
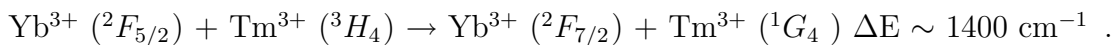


**Figure 6.3:** Proposed mechanism for the population of the  $^1G_4$  manifold via a three step energy transfer up-conversion process in  $\text{Tm}^{3+}/\text{Yb}^{3+}$  co-doped silica fibre under 980 nm excitation.

The three step process involves the double energy transfer mechanism shown in Figure 6.2 with an additional step, which involves a third energy transfer from another excited  $\text{Yb}^{3+}$  ion to a neighbouring excited  $\text{Tm}^{3+}$  ion in the  $^3H_4$  manifold. The resultant transfer culminates in an excited  $\text{Tm}^{3+}$  ion in the  $^1G_4$  manifold. The energy mismatch for the third energy step for  $\text{Tm}^{3+}/\text{Yb}^{3+}$  in  $\text{YF}_3$  [42] is:



From the absorption spectra measured in this work the mismatch is estimated to be  $955 \pm 15 \text{ cm}^{-1}$ , in alumino-silicate glass.

The counter-propagating up-conversion luminescence spectrum for each fibre sample, in the wavelength range of 450 - 900 nm is shown in Figure 6.4.

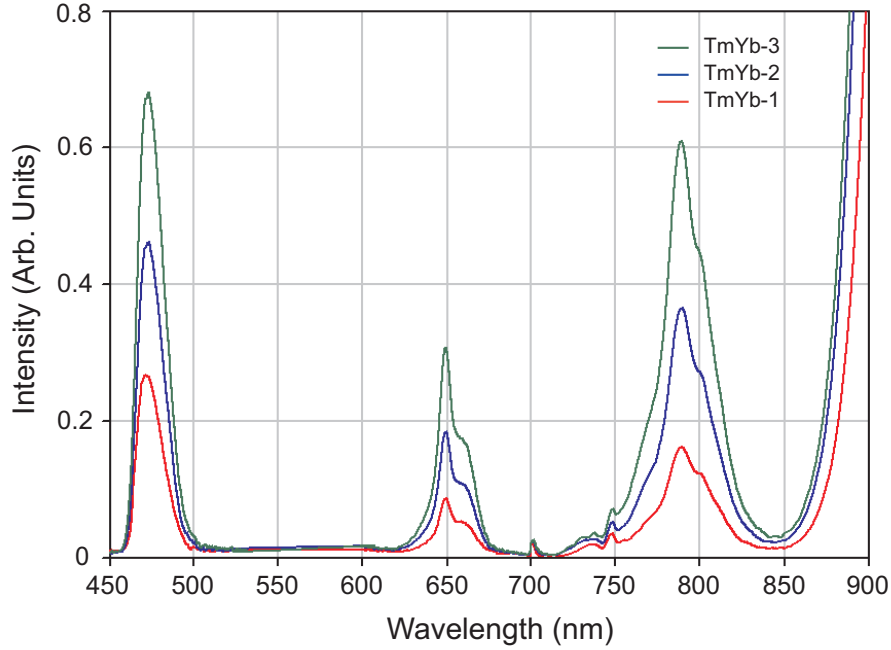


**Figure 6.4:** Counter-propagating luminescence spectra of the  $\text{Tm}^{3+}/\text{Yb}^{3+}$ -co-doped fibre samples under 980 nm excitation. Note: sample lengths were all kept to 20 cm and the incident pump power in each case was 128 mW.

The up-conversion luminescence spectra show three distinct fluorescence bands centred around 475, 650 and 780 nm, which are attributed to the transitions from the  ${}^1G_4 \rightarrow {}^3H_6$ ,  ${}^1G_4 \rightarrow {}^3F_4$  and ( ${}^1G_4 \rightarrow {}^3H_5$  &  ${}^3H_4 \rightarrow {}^3H_6$ ) manifolds, respectively. Unfortunately, low fluorescence intensity levels prevented the  ${}^3H_4 \rightarrow {}^3F_4$  and  ${}^3F_4 \rightarrow {}^3H_6$  counter propagating spectra from being measured. Even so, the presence of the three luminescence bands at visible wavelengths confirms energy transfer between  $\text{Yb}^{3+}$  and  $\text{Tm}^{3+}$  ions is taking place under 980 nm excitation. A fourth fluorescence band which begins to rise around 880 nm is attributed to the strong  $\text{Yb}^{3+}$  fluorescence band which spans  $\sim 300$  nm and peaks at 980 and 1040 nm as seen in Figure 2.6.

To understand the origin of the luminescence bands, the dependencies of the up-conversion luminescence bands were studied as a function of the  $\text{Yb}^{3+}$  excited state population for a range of incident pump powers. The number of pump photons,  $n$ , required to produce an up-converted photon in the  $\text{Tm}^{3+}/\text{Yb}^{3+}$ -co-doped system can be determined easily, as the up-conversion intensity has an  $n$  power dependence

on the density of excited ions in the  ${}^2F_{5/2}$  manifold of  $\text{Yb}^{3+}$ . In the majority of cases, authors report the up-conversion luminescence as a function of incident pump power to obtain the number ‘ $n$ ’ which is valid when the density of excited ions in the  ${}^2F_{5/2}$  excited manifold is directly proportional to the incident pump power. This condition is satisfied when only a small number of ions are excited from the ground state manifold. However, when the ground state is excited with increasingly large input powers it can become depleted, resulting in a saturated excited state population. In such a case, the density of excited ions is no longer directly proportional to the incident pump power and comparisons with the up-conversion luminescence become invalid. A more accurate account of the density of ions in an excited state can be obtained by measuring the fluorescence intensity from the excited manifold. The fluorescence intensity is directly proportional to the density of excited ions under all input pumping regimes; therefore comparison between the fluorescence intensities of the excited state and up-conversion luminescence states provides a better account of the populating mechanism and number ‘ $n$ ’ over a large range of incident pump powers. This is an important distinction which needs to be made as in this work, saturation effects in population of the  ${}^2F_{5/2}$  manifold were observed for incident pump powers  $> 20$  mW in the lowest  $\text{Yb}_2\text{O}_3$  concentrated samples (see Figure 6.5).

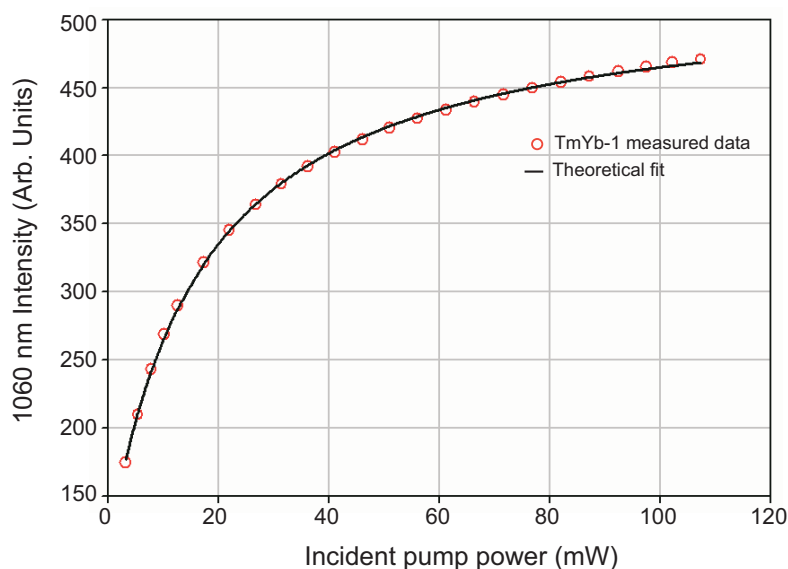


**Figure 6.5:** 1060 nm fluorescence intensity as a function of incident pump power for the TmYb-1 fibre sample. Note: the theoretical fit was obtained from the solution to the rate equation describing a simple two level system.

Since the fluorescence intensity at 1060 nm is directly proportional to the density of excited ions in the  ${}^2F_{5/2}$  manifold of  $\text{Yb}^{3+}$ , the number of pump photons required for a particular up-conversion process is obtained readily from the slope of the up-conversion intensity versus the fluorescence intensity at 1060 nm.

### 6.2.1 ${}^3F_4$ manifold

To establish the first energy transfer step, the fluorescence intensity at 1800 nm from the  ${}^3F_4$  manifold of  $\text{Tm}^{3+}$  was compared to the fluorescence intensity at 1060 nm from  $\text{Yb}^{3+}$ . Figure 6.6 shows the log-log plot of the 1800 nm luminescence versus the 1060 nm luminescence for the three fibres.

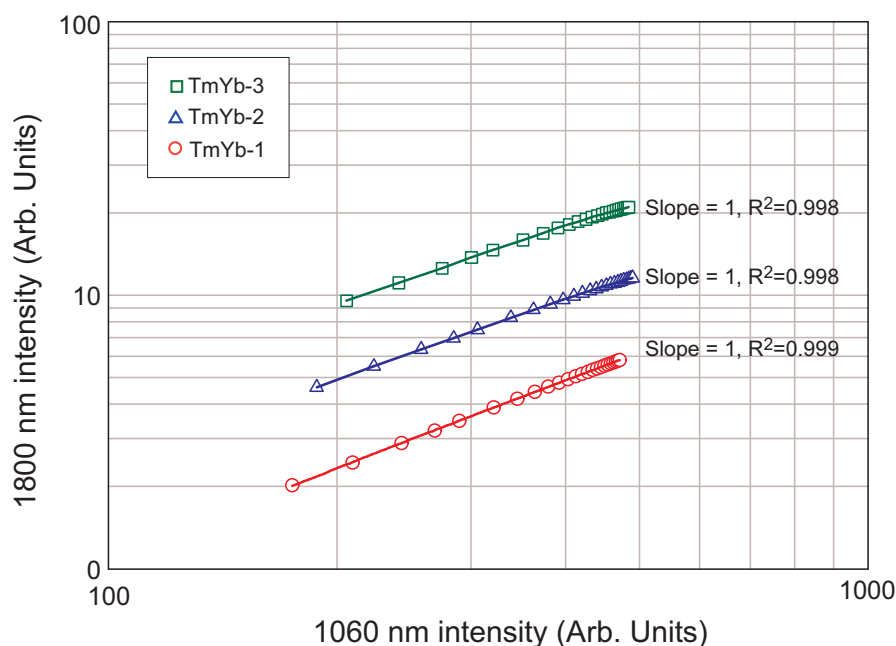


**Figure 6.6:** Log-log plot of the 1800 nm luminescence from  $\text{Tm}^{3+}$  vs. the 1060 nm luminescence from  $\text{Yb}^{3+}$ , for incident pump powers ranging from 3 - 108 mW. The 1800 nm measured data have been offset to aid comparison. Note: the errors associated with these measurements are not shown as they are smaller than the size of the individual data points in the plot.

The equation used to fit the measured data in Figure 6.6 was obtained by solving the rate equations describing the excited state populations of the  ${}^2F_{5/2}$  and  ${}^3F_4$  manifolds. These rate equations are given below, along with the energy man-

ifold labelling which is shown in Figure 6.7, where  $N_{Y_i}$  represents the population of the  $i^{\text{th}}$   $\text{Yb}^{3+}$  manifold and  $N_{T_j}$  represents the population of the  $j^{\text{th}}$   $\text{Tm}^{3+}$  manifold. It should be noted that the populations of the  ${}^3H_5$  and  ${}^3F_{2,3}$  manifolds of  $\text{Tm}^{3+}$  have been ignored in this analysis due to the close spacing to the next lowest energy manifold; any population in these manifolds will decay non-radiatively to the longer lived  ${}^3F_4$  and  ${}^3H_4$  manifolds, respectively.  $\tau_{Y1}$  represents the fluorescence lifetime of the  ${}^2F_{5/2}$  manifold of  $\text{Yb}^{3+}$ , whilst  $\tau_{T_j}$  represents the fluorescence lifetime of the  $j^{\text{th}}$  excited manifold of  $\text{Tm}^{3+}$ .  $W_i$  represents the energy transfer co-efficient describing the interaction between  $\text{Yb}^{3+}$  and  $\text{Tm}^{3+}$  ions for steps  $i = 1$  to 3 and  $\sigma_{T_{i-j}}$  represents the excited state absorption cross sections for transitions from the  $i^{\text{th}}$  to  $j^{\text{th}}$  manifold in  $\text{Tm}^{3+}$ .  $I$  represents the incident pump intensity. Finally,  $\sigma_{Y01}$  is the absorption cross section of the ground to excited state transition of  $\text{Yb}^{3+}$  when excited at 980 nm.

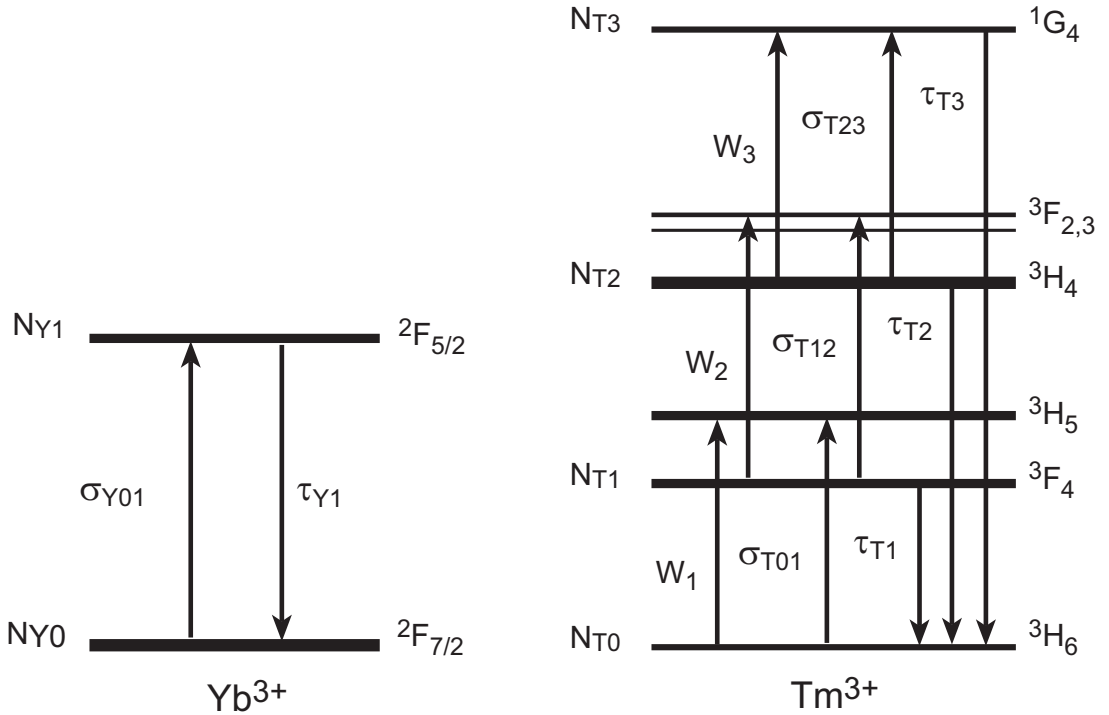


**Figure 6.7:** Energy manifold labelling for the rate equation analysis of the  $\text{Tm}^{3+}/\text{Yb}^{3+}$  - co-doped system.

The rate equations describing the populations of the  ${}^2F_{5/2}$  manifold of  $\text{Yb}^{3+}$  and the  ${}^3F_4$  manifold of  $\text{Tm}^{3+}$  can be written as:

$$\frac{dN_{Y1}}{dt} = I\sigma_{Y01}N_{Y0} - \frac{N_{Y1}}{\tau_{Y1}} \quad (6.1)$$

and

$$\frac{dN_{T1}}{dt} = W_1N_{Y1}N_{T0} - \frac{N_{T1}}{\tau_{T1}} - W_2N_{T1}N_{Y1}, \quad (6.2)$$

with the additional condition that

$$N_{Y0} + N_{Y1} = c_Y \quad (6.3)$$

$$N_{T0} + N_{T1} + N_{T2} + N_{T3} = c_T \quad (6.4)$$

where  $c_Y$  and  $c_T$  represent the concentration of  $\text{Yb}^{3+}$  and  $\text{Tm}^{3+}$  ions, respectively.

It should be noted that Equation 6.1 takes into account the assumption that the energy transfer up-conversion terms (i.e.  $W_1N_{Y1}N_{T0}$ ,  $W_2N_{Y1}N_{T1}$  and  $W_3N_{Y1}N_{T2}$ ) are  $\ll$  than the spontaneous decay term  $N_{Y1}/\tau_{Y1}$ . This assumption is verified by fluorescence decay results from the  ${}^2F_{5/2}$  manifold, reported in Section 6.3.1.1. The second assumption made in this analysis is that, since only a small fraction of ground state  $\text{Tm}^{3+}$  ions are excited by the up-conversion mechanisms,  $N_{T0} \approx c_T$ . The validity of this assumption is discussed further in the text.

Equations 6.1 and 6.2 can be solved in the steady state, i.e. when  $\frac{dN_{Y1}}{dt}$  and  $\frac{dN_{T1}}{dt} = 0$ , to obtain an expression for  $N_{T1}$  as a function of  $N_{Y1}$ :

$$N_{T1} = \frac{W_1N_{Y1}c_T}{1/\tau_{T1} + W_2N_{Y1}}. \quad (6.5)$$

The solution shows that in the limit that  $W_2N_{Y1} \ll 1/\tau_{T1}$ , a linear relationship exists between the population of the  ${}^3F_4$  and  ${}^2F_{5/2}$  manifolds. To test the validity of this solution, the measured data were fit to a linear expression in the form of  $y = Ax + B$ , where  $A$  and  $B$  were the fitting parameters. The excellent agreement, as shown in Figure 6.6, between the fit and measured data over the entire pump

power range for all fibre samples verifies that under 980 nm excitation, the  ${}^3F_4$  manifold of  $\text{Tm}^{3+}$ , is populated by the energy transfer process:



It can also be concluded from the analysis that the energy transfer up-conversion rate,  $W_2N_{Y1}$ , which depopulates the  ${}^3F_4$  manifold is much less than the spontaneous decay,  $1/\tau_{T1}$ .

### 6.2.2 ${}^3H_4$ manifold

The second energy transfer step from the  ${}^3F_4$  to the  ${}^3F_{2,3}$  manifolds could not be determined from the luminescence at 810 nm in this sample set as, upon inspection of the  $\text{Tm}^{3+}$  energy level diagram, see Figure 2.4, it becomes clear that luminescence from the  ${}^1G_4 \rightarrow {}^3H_5$  and  ${}^3H_4 \rightarrow {}^3H_6$  transitions both result in fluorescence bands around 810 nm. Since blue luminescence has been observed in these fibre samples it can be concluded that excited ions have been promoted to the  ${}^1G_4$  manifold of  $\text{Tm}^{3+}$ . With this in mind, the 810 nm luminescence should show the properties associated with the populating mechanisms from both energy manifolds and hence an independent measurement of the population of the  ${}^3H_4$  manifold cannot be obtained. This complication can be avoided by studying the luminescence properties of the 1480 nm transition; unfortunately the luminescence in this wavelength region was too weak to be detected, due to the low  $\text{Tm}_2\text{O}_3$  concentrations and limited pump powers available. A short discussion of the 810 nm luminescence is given following the exploration of the  ${}^1G_4$  manifold. This order has been chosen to aid understanding.

### 6.2.3 ${}^1G_4$ manifold

The populating mechanism responsible for the blue luminescence from the  ${}^1G_4$  manifold can be established in this sample set by studying its dependence on the 1060 nm luminescence from  $\text{Yb}^{3+}$ . The fluorescence at 650 nm from the  ${}^1G_4 \rightarrow {}^3F_4$  transition could also be used to study the mechanism populating the  ${}^1G_4$  manifold. However the branching ratio in silica glass for the 475 nm luminescence is 0.51 compared to

0.069 for the 650 nm luminescence [70], therefore the luminescence intensity of the 475 nm luminescence at least 7 times stronger. Figure 6.8 shows the log-log plot of the 475 nm luminescence as a function of the  $\text{Yb}^{3+}$  luminescence at 1060 nm for a range of input pump powers.

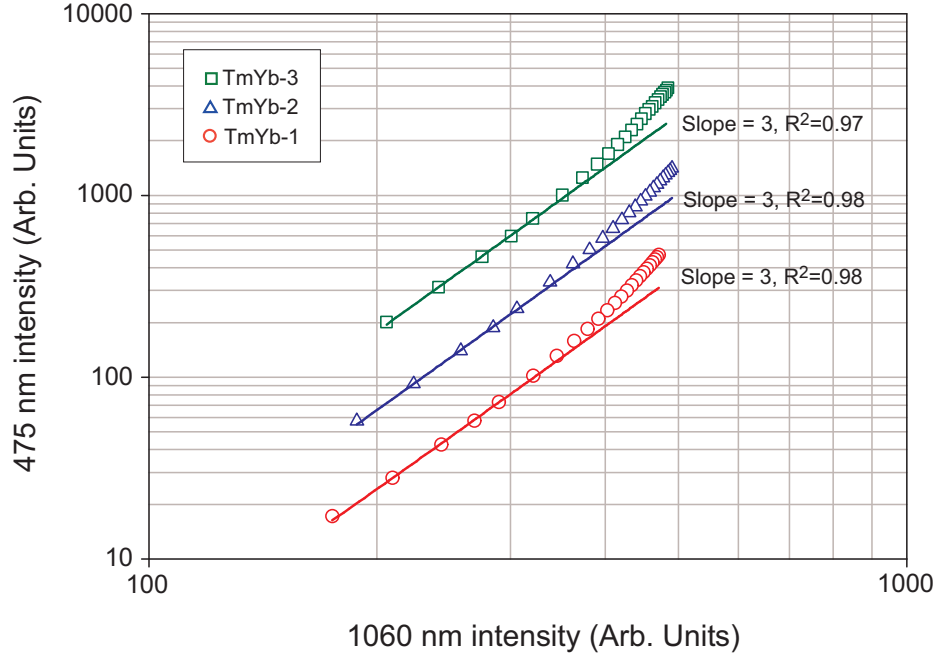


**Figure 6.8:** Log-log plot of the 475 nm luminescence from  $\text{Tm}^{3+}$  vs. the 1060 nm luminescence from  $\text{Yb}^{3+}$ , for incident pump powers ranging from 3 - 108 mW. The 475 nm measured data have been offset to aid comparison. Note: the errors associated with these measurements are not shown as they are smaller than the size of the individual data points presented in the plot. The fits to the data are discussed in the text.

The equation used to fit the measured data in Figure 6.8 was determined from the solution to the rate equation describing the population of the  $^1G_4$  manifold. Since the populating mechanism of the  $^3H_4$  manifold could not be determined from the 810 nm luminescence data, it was assumed that a second energy transfer up-conversion process, involving the energy exchange between an excited  $\text{Yb}^{3+}$  ion and an excited  $\text{Tm}^{3+}$  ion in the  $^3F_4$  manifold, populates the  $^3H_4$  manifold under 980 nm excitation, as shown Figure 6.2. Based on this assumption the rate equation describing the population of the  $^3H_4$  manifold and  $^1G_4$  manifold of  $\text{Tm}^{3+}$  can be written as:

$$\frac{dN_{T2}}{dt} = W_2 N_{Y1} N_{T1} - \frac{N_{T2}}{\tau_{T2}} - W_3 N_{Y1} N_{T2}, \quad (6.6)$$

and

$$\frac{dN_{T3}}{dt} = W_3 N_{Y1} N_{T2} - \frac{N_{T3}}{\tau_{T3}}. \quad (6.7)$$

Equation 6.7 assumes that the  $^1G_4$  manifold is populated by a third energy transfer up-conversion process involving an excited  $\text{Yb}^{3+}$  ion and an excited  $\text{Tm}^{3+}$  ion in the  $^3H_4$  manifold. This assumption was made on the basis of the significant body of work which attributes blue luminescence to the successive 3- step energy transfer up-conversion process [137, 43, 45, 139, 140].

By solving the rate equations for the respective manifolds in the steady state, expressions for the population of the  $^3H_4$  and  $^1G_4$  manifolds can be obtained as a function of  $\text{Yb}^{3+}$  population. These solutions are:

$$N_{T2} = \frac{W_1 W_2 c_T \tau_{T1} N_{Y1}^2}{1/\tau_{T2} + W_3 N_{Y1}}, \quad (6.8)$$

and

$$N_{T3} = \frac{W_1 W_2 W_3 c_T \tau_{T1} \tau_{T3} N_{Y1}^3}{1/\tau_{T2} + W_3 N_{Y1}}. \quad (6.9)$$

Both expressions contain a saturation term, which plays a role only when the energy transfer up-conversion rate is comparable to the spontaneous decay rate from the  $^3H_4$  manifold. It has been established that the energy transfer rate of the second ETU step ( $W_2 N_{Y1}$ ) is much less than the spontaneous decay of the  $^3F_4$  manifold; since the decay rate of the  $^3H_4$  manifold is an order of magnitude greater than the  $^3F_4$  manifold, it is suggested that the ETU rate of the third step from  $^3H_4 \rightarrow ^1G_4$  ( $W_3 N_{Y1}$ ) is much less than the spontaneous rate from the  $^3H_4$  manifold ( $1/\tau_2$ ). Therefore the steady state solutions for the  $^3H_4$  and  $^1G_4$  manifolds can simplify to:

$$N_{T2} = W_1 W_2 c_T \tau_{T1} \tau_{T2} N_{Y1}^2, \quad (6.10)$$

and

$$N_{T3} = W_1 W_2 W_3 c_T \tau_{T1} \tau_{T2} \tau_{T3} N_{Y1}^3, \quad (6.11)$$

Therefore, the population of the  ${}^3H_4$  manifold is dependent on the square of the  ${}^2F_{5/2}$  population whilst, the  ${}^1G_4$  manifold population is dependent on the cube of the  ${}^2F_{5/2}$  population.

Equation 6.11 was used to fit the measured data shown in Figure 6.8. The fit describes the data accurately at low pump powers, but fails to describe the data at high pump powers, for all three fibre samples. Figure 6.8 shows that the 475 nm luminescence continues to grow after the 1060 nm fluorescence begins to saturate. This behaviour cannot be described solely by the successive three step ETU process shown in Figure 6.2. The ETU process is inherently linked to the population of the excited states; hence as the  ${}^2F_{5/2}$  manifold begins to saturate, so too will the other successive excited states of  $Tm^{3+}$ . The fact that the 475 nm luminescence continues to grow indicates that another populating mechanism is occurring within the co-doped system which is not just dependent on the excited state populations, but also the incident pump power. The only energy transfer process which fulfils this requirement is excited state absorption (ESA), as it involves the energy exchange of a pump or fluorescent photon with an ion in an excited state. Since ESA requires only one accepting ion, the process is concentration independent and scales with incident pump or fluorescence power, which is an important difference when compared to ETU. Although ESA of  $Tm^{3+}$  ions has been frequently reported in the literature [141, 85, 142, 143], this has not been the case for  $Tm^{3+}/Yb^{3+}$  -co-doped systems.

For ESA to occur in the  $Tm^{3+}/Yb^{3+}$  -co-doped system, excited  $Tm^{3+}$  ions are required to absorb incident pump photons at 980 nm and/or fluorescing photons at 1060 nm. Of the possible ESA transitions which can occur in  $Tm^{3+}$ , only two are possible in the  $Tm^{3+}/Yb^{3+}$  -co-doped system under 980 nm excitation, namely the  ${}^3F_4 \rightarrow {}^3F_{2,3}$  and  ${}^3H_4 \rightarrow {}^1G_4$  transitions. The ESA cross sections for these two transitions have been calculated [11] and are shown in Figure 6.9, with the  ${}^3F_4 \rightarrow {}^3F_{2,3}$  transition exhibiting stronger absorption strengths compared to the  ${}^3H_4 \rightarrow {}^1G_4$  transition. However, of most interest, is the location of these absorption peaks in regard to the energy available from the incident pump and fluorescing

photons. Included in Figure 6.9 is the emission spectrum of  $\text{Yb}^{3+}$  under 980 nm excitation; the position of this fluorescence band indicates which ESA transition of  $\text{Tm}^{3+}$  has the greatest spectral overlap with the energy available from the pump and fluorescing photons.

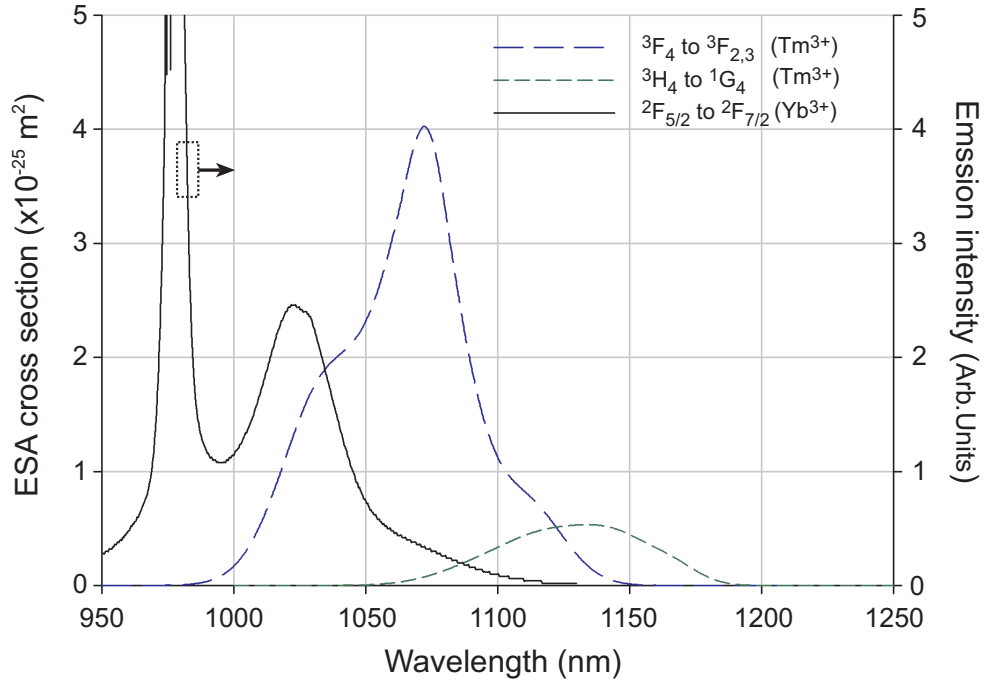


**Figure 6.9:** Spectral overlap of the  $\text{Yb}^{3+}$  fluorescence from the  ${}^2F_{5/2} \rightarrow {}^2F_{7/2}$  transition with the calculated ESA transitions of  $\text{Tm}^{3+}$  [11]. Note: the  $\text{Yb}^{3+}$  fluorescence spectrum of the TmYb-1 sample was measured under 980 nm excitation, using the counter-propagating technique described in Section 3.6.

The  ${}^3F_4 \rightarrow {}^3F_{2,3}$  transition is found to have the greatest overlap with the  $\text{Yb}^{3+}$  fluorescence but, more importantly, it is found to have a larger absorption cross section at the pump wavelength, 980 nm. The absorption cross section at the pump wavelength is the most critical parameter in this case as the number of incident pump photons is many orders of magnitude greater than the number of fluorescent photons. The ESA cross section of the  ${}^3F_4 \rightarrow {}^3F_{2,3}$  transition at 980 nm in silica glass is estimated to be  $5.2 \times 10^{-28} \text{ m}^2$ , compared with  $5.4 \times 10^{-36} \text{ m}^2$  for the  ${}^3H_4 \rightarrow {}^1G_4$  transition. This comparison suggests that the  ${}^3F_4 \rightarrow {}^3F_{2,3}$  transition is the most favourable ESA transition in the co-doped system under 980 nm. This is further supported by the fluorescence lifetime measurements reported in Chapter 4, which found that the

lifetime of the  ${}^3F_4$  manifold was an order of magnitude longer than the  ${}^3H_4$  manifold; this provides the  ${}^3F_4$  manifold ions with a greater opportunity to interact with an incident pump photon, as the ions spend longer in the excited state.

If the  ${}^3F_4 \rightarrow {}^3F_{2,3}$  ESA transition is now considered in the populating dynamics of the  $\text{Tm}^{3+}/\text{Yb}^{3+}$  -co-doped system, the rate equations describing the populations of the  ${}^3H_4$  would be given by Equation 6.12; bearing in mind that the previous analysis determined that the energy transfer rates  $W_2N_{Y1}$  and  $W_3N_{Y1}$  are much less than the spontaneous decay rates from the  ${}^3F_4$  and  ${}^3H_4$  manifolds, respectively.

$$\frac{dN_{T2}}{dt} = I\sigma_{T12}N_{T1} + W_2N_{Y1}N_{T1} - \frac{N_{T2}}{\tau_{T2}}. \quad (6.12)$$

Since ESA from the  ${}^3H_4 \rightarrow {}^1G_4$  manifold is extremely unlikely under 980 nm pumping, the rate equation describing the population of the  ${}^1G_4$  manifold would remain the same as that stated in Equation 6.7. It should be noted that the inclusion of the ( ${}^3F_4 \rightarrow {}^3F_{2,3}$ ) ESA term in the analysis also has implications on the rate equation describing the population of the  ${}^3F_4$  manifold. However the linear dependence of the 1800 nm luminescence on the 1060 nm luminescence indicates that the ESA term is much less than the spontaneous decay rate from the  ${}^3F_4$  manifold. Equations 6.12 and 6.7 can be solved in the steady state to obtain an expression for  $N_{T3}$  as a function of  $N_{Y1}$ , namely:

$$N_{T3} = W_1W_2W_3c_T\tau_{T1}\tau_{T2}\tau_{T3}N_{Y1}^3 + \frac{W_1W_2c_T\sigma_{T12}\tau_{T1}\tau_{T2}\tau_{T3}N_{Y1}^3}{\tau_{Y1}\sigma_{Y01}(c_Y - N_{Y1})}. \quad (6.13)$$

Equation 6.13 is similar to the expression obtained for the successive three step ETU process except for the additional term which results from the inclusion of ESA. The measured 475 nm versus 1060 nm luminescence data were then fitted with the new expression in the form of  $y = Ax^3 + Bx^3/(1 - Cx)$ , where  $A$ ,  $B$  and  $C$  were the fitting parameters. The resulting fits are shown in Figure 6.10 along with the  $R^2$  value which provides an indication of the quality of the fit. The  $A$ ,  $B$  and  $C$  fitting parameters are listed in Table 6.2 for each fibre sample along with their uncertainty.

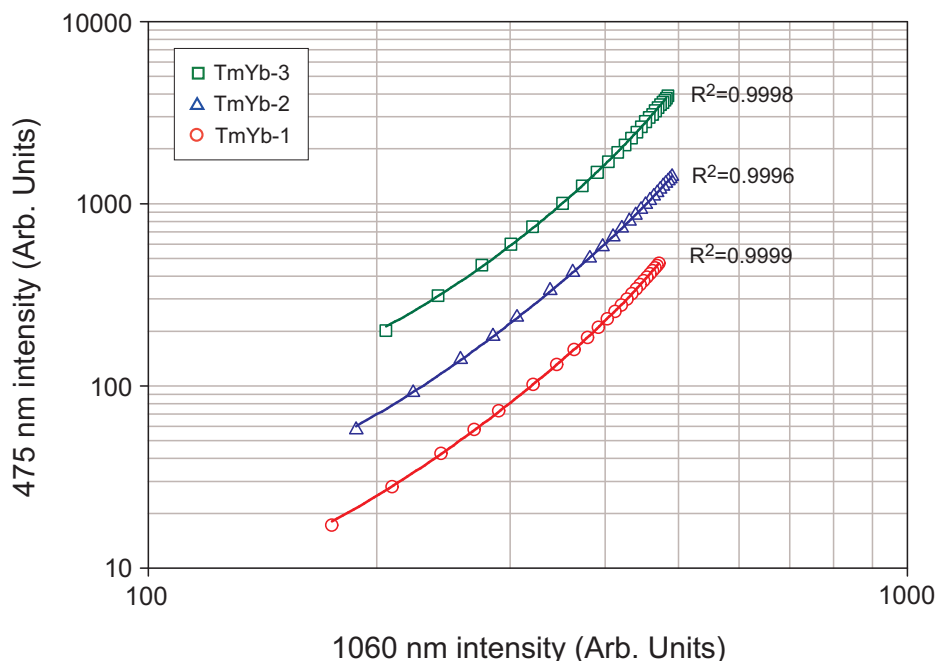


**Figure 6.10:** Log-log plot of the 475 nm luminescence from  $\text{Tm}^{3+}$  vs. the 1060 nm luminescence from  $\text{Yb}^{3+}$ , for incident pump powers ranging from 3 - 108 mW. The data were fitted with Equation 6.13.

Sample	Fitting parameters		
	$A$	$B$	$C$
TmYb-1	$(1.8 \pm 0.1) \times 10^{-7}$	$(5.6 \pm 0.5) \times 10^{-8}$	$(1.67 \pm 0.03) \times 10^{-5}$
TmYb-2	$(1.6 \pm 0.1) \times 10^{-7}$	$(6.0 \pm 0.7) \times 10^{-8}$	$(1.52 \pm 0.03) \times 10^{-5}$
TmYb-3	$(1.5 \pm 0.2) \times 10^{-7}$	$(6.1 \pm 0.9) \times 10^{-8}$	$(1.61 \pm 0.04) \times 10^{-5}$

**Table 6.2:** Parameters obtained by fitting the steady state rate equation model to the 475 versus 1060 nm luminescence data. Note: the uncertainty in each fitting parameter was determined by taking the square root of the sum of the squared errors divided by the degree of freedom of the fit.

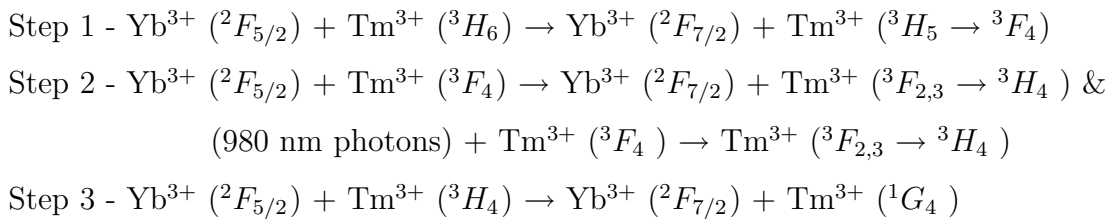
Although the physical parameters associated with the  $A$ ,  $B$  and  $C$  terms cannot be obtained from the fitting parameters due to the coupling of several unknown parameters and proportionality constants, the uncertainty in the fitting parameters validates the model and the quality of the fit for all fibre samples. This establishes for the first time the  ${}^3F_4 \rightarrow {}^3F_{2,3}$ , ESA process as a populating mechanism in  $\text{Tm}^{3+}/\text{Yb}^{3+}$  -co-doped silica glasses under 980 nm excitation.

One point which has not been addressed in this analysis is the possible contribution to the 475 nm luminescence from the double energy transfer of two excited  $\text{Yb}^{3+}$  ions. It has been reported in the literature that under 980 nm excitation,  $\text{Yb}^{3+}$  is observed to emit fluorescence from a so-called “virtual” level around 475 nm [144, 145, 146]. This observation is usually observed in highly concentrated samples under relatively large input pump powers. This process can, however, be ruled out in this analysis since similar outcomes were achieved by studying the 650 nm luminescence properties, providing a separate independent measurement of the  $^1G_4$  manifold population. The possibility of energy transfer between two excited  $\text{Yb}^{3+}$  ions and an unexcited  $\text{Tm}^{3+}$  ion was also investigated as a possible cause of the increase in the  $^1G_4$  manifold population [138]. The steady state solution to the  $^1G_4$  manifold population in the absence of ESA appeared as:

$$N_{T3} = W_1 W_2 W_3 C_T \tau_{T1} \tau_{T2} \tau_{T3} N_{Y1}^3 + W_{2Yb-Tm} N_{Y1}^2 \tau_{T3}, \quad (6.14)$$

where  $W_{2Yb-Tm}$  represented the energy transfer co-efficient for the energy exchange of two excited  $\text{Yb}^{3+}$  ions and one unexcited  $\text{Tm}^{3+}$  ion.

However, this expression failed to describe the measured data well at both low and high incident pump powers, thereby discounting the possibility of the double energy transfer process. It can therefore be concluded that the populating mechanisms involved in promoting  $\text{Tm}^{3+}$  ions to the  $^1G_4$  manifold in  $\text{Tm}^{3+}/\text{Yb}^{3+}$  -co-doped silica glass under 980 nm excitation are:



Although the quantum efficiency of the S-band transition cannot be quantified in this sample set, the spectroscopic study of the system has established two energy transfer processes that act to populate the upper amplifying  ${}^3H_4$  manifold whilst depopulating the lower amplifying  ${}^3F_4$  manifold, under 980 nm excitation.

### 6.2.4 810 nm luminescence

As discussed in Section 6.2.2 the up-conversion luminescence at 810 nm is attributed to the presence of two overlapping luminescence bands, one from each of the  $^1G_4$  and  $^3H_4$  manifolds. In this case, the luminescence at 810 nm should exhibit the characteristics of both excited manifolds with the  $^3H_4$  manifold dominating over the  $^1G_4$  manifold at low excitation powers. Figure 6.11 shows the log-log plot of the 810 nm luminescence as a function of the  $\text{Yb}^{3+}$  luminescence at 1060 nm over a range of input pump powers for each fibre sample.

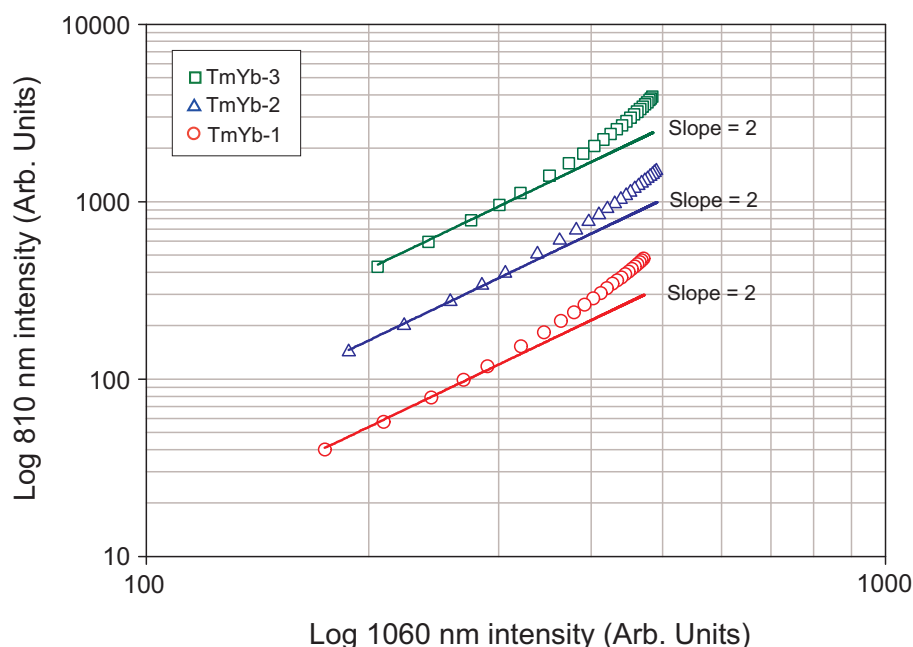


**Figure 6.11:** Log-log plot of the 810 nm luminescence from  $\text{Tm}^{3+}$  vs. the 1060 nm luminescence from  $\text{Yb}^{3+}$ , for incident pump powers ranging from 3 - 108 mW. The 810 nm measured data have been offset to aid comparison. The solid lines represent the fit of a standard quadratic equation to the measured data.

The non-linear nature of the log-log plot suggests the presence of more than one up-conversion process. At low pump powers the measured data exhibits a slope of 2, as seen in Figure 6.11, whilst at high pump powers  $> 50$  mW the slope exceeds 3. The non-linear behaviour is greatest in the TmYb-3 sample which has the highest  $^1G_4$  manifold population. This provides further evidence of the two overlapping transitions from the  $^1G_4$  and  $^3H_4$  manifold and is consistent with the rate equation model proposed in the previous section. Unfortunately, the large number of unknown

parameters prevent the rate equation model from being fitted to the measured data with any degree of certainty. A more accurate account of the population dynamics involved in this luminescence band can be obtained by studying the fluorescence decay characteristics after the pump excitation has been removed.

## 6.3 Fluorescence lifetime measurements

The final stage in the spectroscopic study of the  $\text{Tm}^{3+}/\text{Yb}^{3+}$  -co-doped system was to investigate the fluorescence lifetimes of the excited states of  $\text{Tm}^{3+}$  and  $\text{Yb}^{3+}$ . The fluorescence lifetimes of the  ${}^2F_{5/2}$ ,  ${}^3F_4$ , and  ${}^3H_4$  manifolds were studied under direct excitation at the appropriate wavelength, as outlined in Table 3.1. In addition, the  ${}^3F_4$ ,  ${}^3H_4$  and  ${}^1G_4$  manifolds of  $\text{Tm}^{3+}$  were studied under in-direct pumping at 980 nm. As discussed in Chapter 5, the fluorescence lifetime of an excited manifold can often provide detailed information as to energy transfer processes occurring to and from a particular excited state. By studying the decay characteristics of the excited manifolds under direct and in-direct excitation, meaningful conclusions can be drawn with respect to the dominant populating mechanisms of the system. Of particular interest to this investigation is the possible presence of energy back transfer processes from  $\text{Tm}^{3+}$  to  $\text{Yb}^{3+}$  ions. Energy back transfer processes will have important implications for the efficiency of the  $\text{Tm}^{3+}$  transitions arising from processes established in the previous section.

### 6.3.1 Direct pumping

#### 6.3.1.1 ${}^2F_{5/2}$ manifold

The  ${}^2F_{5/2}$  manifold of  $\text{Yb}^{3+}$  is located  $\sim 10\,200\text{ cm}^{-1}$  above the  ${}^2F_{7/2}$  ground state. The considerably large energy separation between these two manifolds ensures that the decay from  ${}^2F_{5/2}$  manifold is purely radiative in most host materials, including alumino-silicate glass. It was proposed in the previous chapter that excited manifolds which are dominated by radiative decay are insensitive to site-to-site variations caused by the host material; this being the case, the excited manifold will decay as a

single exponential. To verify this proposal the decay characteristics of the  ${}^2F_{5/2}$  manifold of  $\text{Yb}^{3+}$  were studied in the  $\text{Tm}^{3+}/\text{Yb}^{3+}$  -co-doped fibres by directly exciting  $\text{Yb}^{3+}$  ions to the  ${}^2F_{5/2}$  manifold with 980 nm light. Figure 6.12 shows the normalised measured decay waveform from the  ${}^2F_{5/2}$  manifold under 980 nm excitation. The fluorescence decay was measured using 50 ms pulses at a repetition rate of 10 Hz.

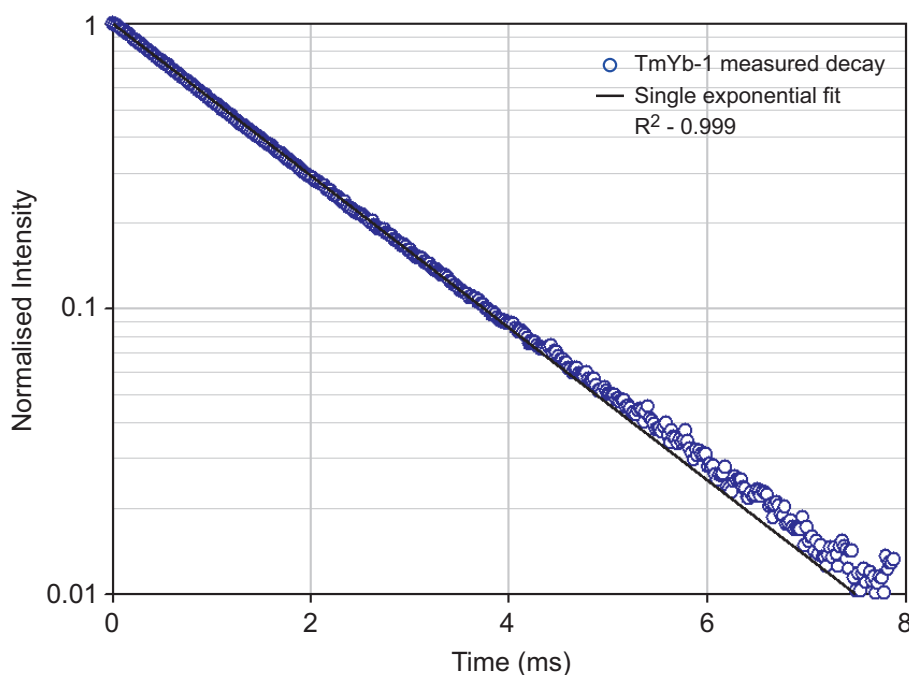


**Figure 6.12:** Semi-log plot of the normalised fluorescence decay waveform from the  ${}^2F_{5/2}$  manifold of sample TmYb-1 under 980 nm pulsed excitation.

The solid line shown in Figure 6.12 was obtained by fitting a single exponential function to the measured data. The single exponential fit is in excellent agreement with the measured waveform. The  $1/e$  lifetimes obtained from the single exponential fit are listed in Table 6.3 for the three  $\text{Tm}^{3+}/\text{Yb}^{3+}$  -co-doped fibres.

Sample	${}^2F_{5/2}$ lifetime ( $\mu\text{s}$ )
TmYb-1	$826.0 \pm 0.6$
TmYb-2	$832.0 \pm 0.6$
TmYb-3	$823.0 \pm 0.5$

**Table 6.3:** Fluorescence lifetimes of the  ${}^2F_{5/2}$  manifold under 980 nm excitation with an incident pump power of 9.3 mW.

To ascertain whether the energy transfer up-conversion processes established in the previous section affect the fluorescence decay from the  ${}^2F_{5/2}$  manifold, the fluorescence decay waveforms were measured over a range of incident pump powers, in a similar manner to the investigation of the  $\text{Tm}^{3+}$  -doped silica fibres. Figure 6.13 shows the fluorescence lifetime of the  ${}^2F_{5/2}$  manifold for the three co-doped samples at incident pump powers ranging from 9 - 113 mW.

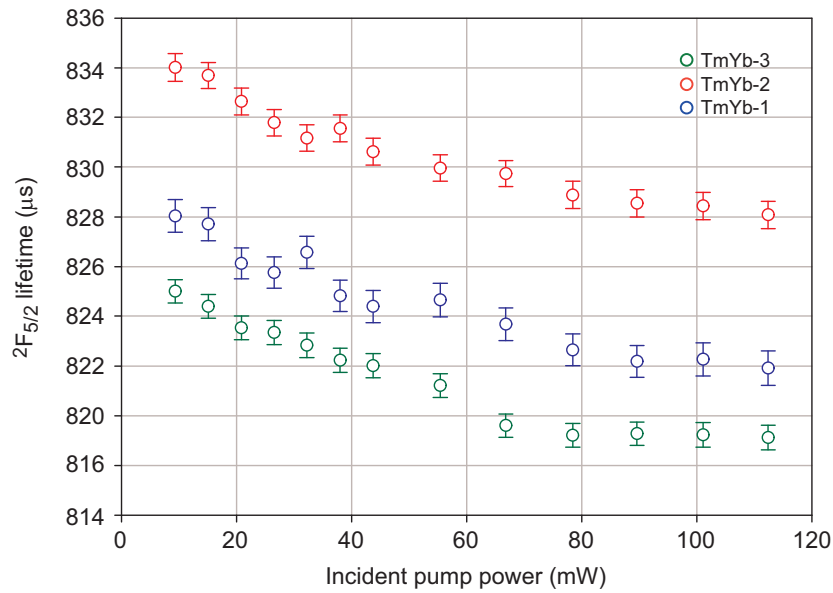


**Figure 6.13:** Fluorescence lifetime of the  ${}^2F_{5/2}$  manifold as a function of incident pump power at 980 nm for the three  $\text{Tm}^{3+}/\text{Yb}^{3+}$  -co-doped alumino-silicate fibres.

Although Figure 6.13 shows a decreasing trend, this effect is minimal with the fluorescence lifetime exhibiting a less than 1% decrease with increasing pump power over the range of available pump powers. Since the ETU processes occurring from the  ${}^2F_{5/2}$  manifold involve a single  ${}^2F_{5/2}$  ion, the fluorescence decay from the manifold will still exhibit single exponential behaviour. However, the characteristic lifetime of the manifold will then contain contributions from three different decay rates, namely the radiative, non-radiative and energy transfer rates. Hence, if the energy transfer rates are significant the characteristic lifetime of the manifold will decrease. The measured lifetimes of the three alumino-silicate samples reported in Table 6.3 are consistent with those reported for  $\text{Yb}^{3+}$  -doped alumino-silicate glass [147], which provides strong evidence that the assumption used in the rate equation analysis that the energy transfer terms  $W_1N_{Y1}N_{T0}$ ,  $W_2N_{Y1}N_{T1}$ , and  $W_3N_{Y1}N_{T2}$  are much

less than  $N_{Y1}/\tau_{Y1}$  is valid. This is also supported by the lack of lifetime dependence on the  $\text{Yb}_2\text{O}_3$  concentration.

### 6.3.1.2 $^3F_4$ manifold

Under direct excitation at 1586 nm the  $^3F_4$  manifold of the  $\text{Tm}^{3+}/\text{Yb}^{3+}$  -co-doped fibres was found to decay in a similar manner to the  $\text{Tm}^{3+}$  -doped alumino-silicate fibres reported in Section 5.3.2. With this in mind, the decays were fitted with both single and stretched exponential functions to provide comparisons with the measured waveforms from the  $\text{Tm}^{3+}$  -doped alumino-silicate fibres. Table 6.4 lists the  $1/e$  lifetime obtained from the single exponential fit as well as the characteristic lifetime and power obtained from the stretched exponential fit.

Sample	Direct pumping @ 1586 nm		
	$\tau_{1/e}$ ( $\mu\text{s}$ )	$\tau_{SE}$ ( $\mu\text{s}$ )	SEP ' $p$ '
TmYb-1	$424 \pm 2$	$352 \pm 2$	$0.804 \pm 0.004$
TmYb-2	$423 \pm 2$	$338 \pm 2$	$0.777 \pm 0.004$
TmYb-3	$377 \pm 2$	$301 \pm 2$	$0.778 \pm 0.004$

**Table 6.4:** Fluorescence lifetimes of the  $^3F_4$  manifold under direct excitation at 1586 nm, where  $\tau_{1/e}$  represents the lifetime obtained from the single exponential fit, whilst  $\tau_{SE}$  and ' $p$ ' represent the characteristic lifetime and power obtained from the stretched exponential fit, respectively. Note: 30  $\mu\text{s}$  pulses at 10 Hz were used for direct excitation.

The  $1/e$  lifetimes and SEP's listed in Table 6.4 are consistent with those reported for the  $\text{Tm}^{3+}$  -doped alumino-silicate fibres in Table 5.5. Sample TmYb-3 did, however, exhibit a decrease of  $\sim 11\%$  in the fluorescence lifetime. This reduction is attributed to the reduced amount of  $\text{Al}_2\text{O}_3$  present in the core, rather than energy back transfer from  $\text{Tm}^{3+}$  to  $\text{Yb}^{3+}$  ions. If energy back transfer was occurring from the  $^3F_4$  manifold, the fluorescence decay would have exhibited a greater degree of non-exponentiality. Since the SEP remained relatively constant in this sample set, it can be concluded that energy back transfer from  $\text{Tm}^{3+}$  to  $\text{Yb}^{3+}$  ions is negligible. This is not a surprising result, as the energy mismatch associated with energy back transfer from the  $^3F_4$  ( $\text{Tm}^{3+}$ )  $\rightarrow$   $^2F_{5/2}$  ( $\text{Yb}^{3+}$ ) is  $\sim 4500 \text{ cm}^{-1}$ , thereby necessitating the simultaneous absorption of at least 4 phonons, which is highly unlikely.

### 6.3.1.3 $^3H_4$ manifold

The direct excitation of the  $^3H_4$  manifold at 780 nm also resulted in decay waveforms similar to those reported for the  $Tm^{3+}$ -doped alumino-silicate fibres. Single and stretched exponential fits were applied to the measured data with the results summarised in Table 6.5.

Sample	Direct pumping @ 780 nm		
	$\tau_{1/e}$ ( $\mu s$ )	$\tau_{SE}$ ( $\mu s$ )	SEP ' $p$ '
TmYb-1	$20.0 \pm 0.1$	$14.7 \pm 0.1$	$0.723 \pm 0.004$
TmYb-2	$20.1 \pm 0.1$	$14.8 \pm 0.1$	$0.724 \pm 0.004$
TmYb-3	$18.7 \pm 0.1$	$14.2 \pm 0.1$	$0.730 \pm 0.004$

**Table 6.5:** Fluorescence lifetimes of the  $^3H_4$  manifold under direct pumping at 780 nm, where  $\tau_{1/e}$  represents the lifetime obtained from the single exponential fit, whilst  $\tau_{SE}$  and ' $p$ ' represent the characteristic lifetime and power obtained from the stretched exponential fit, respectively. Note: 3  $\mu s$  pulses at a repetition rate of 10 Hz were used to excite the samples directly.

The results obtained from the single and stretched exponential fits are again consistent with those reported in Tables 4.5 and 5.2 for  $Tm^{3+}$ -doped alumino-silicate fibres. A considerable reduction ( $\sim 7\%$ ) in the fluorescence lifetime of the TmYb-3 sample was observed compared to the other two co-doped fibres, which is consistent with the reduction seen in the  $^3F_4$  manifold lifetime under direct pumping. If the reduction in the lifetime of the  $^3H_4$  manifold was due to the cross relaxation process, discussed in Section 4.4.1, or an energy back transfer process then the measured decay waveform would exhibit a greater degree of non-exponentiality. On the other hand, if the reduction was due to a host dependent change, then the decay should exhibit less non-exponentiality as the TmYb-3 sample contains less  $Al_2O_3$ . From the increase in the SEP of the TmYb-3 sample, it can be concluded that the reduction in the lifetime is caused by the reduced amount of  $Al_2O_3$  present in the fibre core.

## 6.3.2 In-direct pumping

The in-direct excitation of the  $^3F_4$ ,  $^3H_4$  and  $^1G_4$  manifolds of  $Tm^{3+}$  has been demonstrated in the previous section under continuous wave excitation at 980 nm. In this

section, the fluorescence decay characteristics of the excited manifolds are studied under pulsed excitation. The decay of an excited manifold under in-direct excitation can often provide detailed information regarding the feeding mechanism into the particular excited state. The time dependent rate equation model established in the previous section for continuous wave pumping can be carried over into the fluorescence decay analysis to describe the excited state population over time, allowing the validity of the model to be tested under two energy excitation regimes.

### 6.3.2.1 $^3F_4$ manifold

An example of the fluorescence decay of the  $^3F_4$  manifold under in-direct excitation at 980 nm is shown in Figure 6.14. The decay characteristics of the  $^3F_4$  manifold showed considerable differences to those obtained under direct excitation.

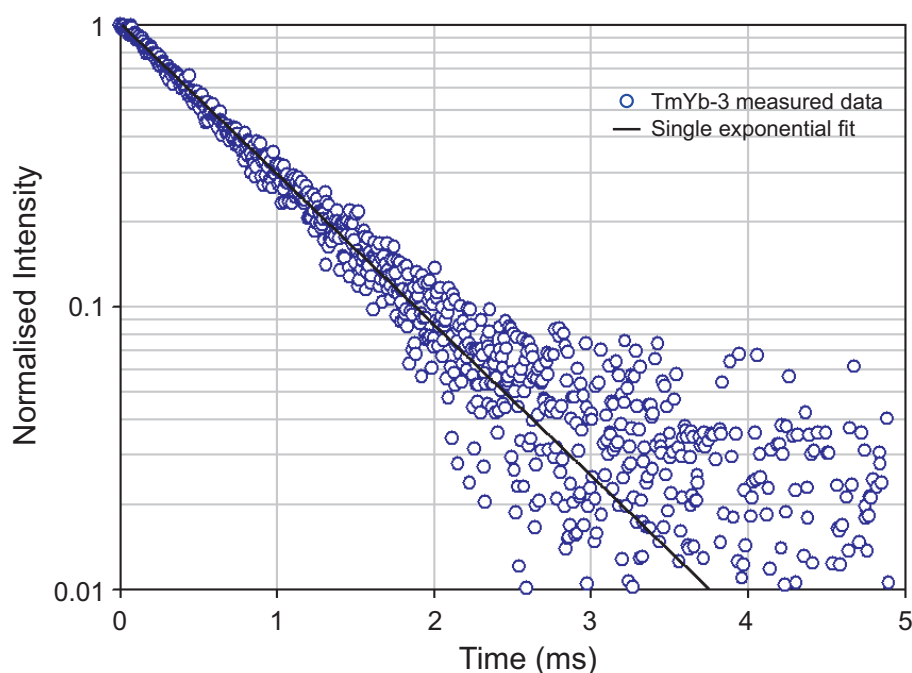


**Figure 6.14:** Semi-log plot of the normalised fluorescence decay waveform from the  $^3F_4$  manifold of sample TmYb-3 under 980 nm excitation.

The fluorescence decay was adequately described by a single exponential function, as seen in Figure 6.14. Similarly, the data for the other two samples could also be described in this way. The characteristic lifetime of the manifold was found to increase

by a factor of two on average, when compared to the lifetimes obtained under direct pumping and were comparable to the fluorescence lifetime of the  ${}^2F_{5/2}$  manifold of  $\text{Yb}^{3+}$  (see Table 6.6).

Sample	In-direct pumping	Direct pumping	${}^2F_{5/2}$ manifold
	$\tau_{1/e}$ ( $\mu\text{s}$ )	$\tau_{1/e}$ ( $\mu\text{s}$ )	$\tau_{1/e}$ ( $\mu\text{s}$ )
TmYb-1	$781 \pm 10$	$424 \pm 2$	$826.0 \pm 0.6$
TmYb-2	$845 \pm 20$	$423 \pm 2$	$832.0 \pm 0.6$
TmYb-3	$812 \pm 10$	$377 \pm 2$	$823.0 \pm 0.5$

**Table 6.6:** Fluorescence lifetime of the  ${}^3F_4$  manifold under in-direct excitation at 980 nm. Note: 50 ms pulses at 10 Hz were used to excite the  ${}^3F_4$  manifold in-directly. The fluorescence lifetimes of the  ${}^3F_4$  and  ${}^2F_{5/2}$  manifolds under direct excitation at 1586 and 980 nm, respectively, are shown for comparison.

The considerably large error associated with the single exponential fit was a result of the poor signal to noise ratio of the 1800 nm luminescence under in-direct pumping, rather than the inability of the fit to describe the waveform accurately. The single exponential nature and longer fluorescence lifetime of the  ${}^3F_4$  decay can be explained using the rate equation analysis outlined in the previous section. By solving the time dependent rate equations after the pump excitation has been removed, expressions describing the decay of the manifold can be obtained. From the steady state analysis in Section 6.2, the time dependent rate equations describing the population of the  ${}^2F_{5/2}$  and  ${}^3F_4$  manifolds can be written as:

$$\frac{dN_{Y1}(t)}{dt} = I\sigma_{Y01}N_{Y0}(t) - \frac{N_{Y1}(t)}{\tau_{Y1}}, \quad (6.15)$$

and

$$\frac{dN_{T1}(t)}{dt} = W_1N_{Y1}(t)c_T - \frac{N_{T1}(t)}{\tau_{T1}}. \quad (6.16)$$

The solutions to Equations 6.15 and 6.16 after the pump excitation has been removed, i.e.  $I = 0$ , are given by:

$$N_{Y1}(t) = N_{Y1}(0)\exp\left(-\frac{t}{\tau_{Y1}}\right), \quad (6.17)$$

and

$$N_{T1}(t) = A \exp\left(-\frac{t}{\tau_{Y1}}\right) + (N_{T1}(0) - A) \exp\left(-\frac{t}{\tau_{T1}}\right), \quad (6.18)$$

where

$$A = \frac{\tau_{Y1}\tau_{T1}N_{Y1}(0)W_1c_T}{\tau_{Y1} - \tau_{T1}}. \quad (6.19)$$

The normalised form of Equation 6.18 is given by:

$$\frac{N_{T1}(t)}{N_{T1}(0)} = B \exp\left(-\frac{t}{\tau_{Y1}}\right) + (1 - B) \exp\left(-\frac{t}{\tau_{T1}}\right), \quad (6.20)$$

where

$$B = \frac{\tau_{Y1}\tau_{T1}N_{Y1}(0)W_1c_T}{(\tau_{Y1} - \tau_{T1})N_{T1}(0)}. \quad (6.21)$$

The single exponential solution to the  ${}^2F_{5/2}$  manifold rate equation is consistent with the measured decay waveform shown in Figure 6.12, with  $\tau_{Y1}$  representing the characteristic lifetime of the decay. From Equation 6.20, it can be seen that the  ${}^3F_4$  manifold of  $\text{Tm}^{3+}$  decays as a double exponential under in-direct pumping, with two characteristic time constants; one being equal to the lifetime of the  ${}^2F_{5/2}$  manifold ( $\tau_{Y1}$ ) and the other being equal to the lifetime of the  ${}^3F_4$  manifold ( $\tau_{T1}$ ). The amplitudes of the respective decay components are given as  $(1 - B)$  for the faster component of the decay dictated by the  ${}^3F_4$  manifold lifetime and  $B$  for the slower component of the decay dictated by the  ${}^2F_{5/2}$  manifold lifetime. Depending on the relevant strengths of amplitudes, the decay from the  ${}^3F_4$  manifold can be a single or double exponential. The measured fluorescence decay from the  ${}^3F_4$  manifold under in-direct excitation was described well by a single exponential function with a characteristic lifetime consistent with the  ${}^2F_{5/2}$  manifold lifetime, as seen in Figure 6.14. This suggests that the parameter  $B$  can be approximated to unity, in which case the fluorescence decay under in-direct pumping at 980 nm is given by:

$$N_{T1}(t) = \frac{\tau_{Y1}\tau_{T1}N_{Y1}(0)W_1c_T}{(\tau_{Y1} - \tau_{T1})N_{T1}(0)} \exp\left(-\frac{t}{\tau_{Y1}}\right). \quad (6.22)$$

The dominance of the  $B$  parameter indicates that the energy transfer rate into the  ${}^3F_4$  manifold ( $W_1 N_{Y1}$ ) is greater than the  ${}^3F_4$  spontaneous decay rate ( $1/\tau_{T1}$ ). This is a promising result as it demonstrates efficient energy transfer between  $Yb^{3+}$  and  $Tm^{3+}$  ions in alumino-silicate glasses.

### 6.3.2.2 ${}^1G_4$ manifold

The in-direct excitation of the  ${}^1G_4$  manifold of  $Tm^{3+}$  can be achieved by the series of successive energy transfer processes established in Section 6.2. The fluorescence decay from the  ${}^1G_4$  manifold under in-direct pumping at 980 nm is shown in Figure 6.15 for the TmYb-1 sample. The measured waveforms for all samples were described well by a single exponential fit, with  $R^2$  values of  $\sim 0.997$  achieved in each case. The characteristic lifetimes obtained from the single exponential fits are listed in Table 6.7 for the three co-doped samples.

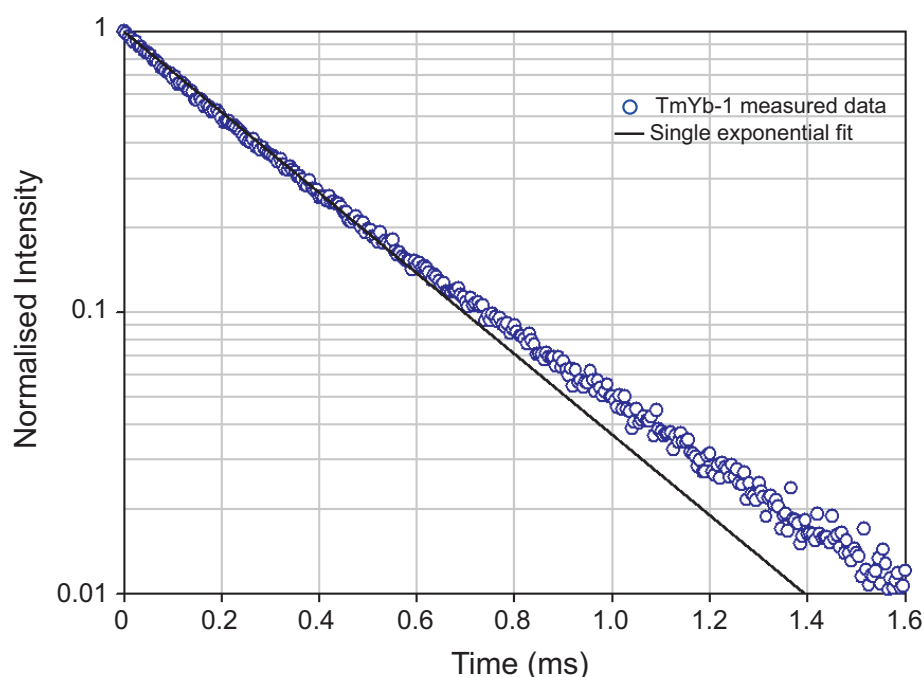


**Figure 6.15:** Semi-log plot of the normalised fluorescence decay from the  ${}^1G_4$  manifold under 980 nm excitation for sample TmYb-1. Note: decay waveforms were recorded using 50 ms pulses at a repetition rate of 10 Hz.

Sample	$\tau_{1/e}$ ( $\mu\text{s}$ )
TmYb-1	$302.4 \pm 0.7$
TmYb-2	$304.3 \pm 0.4$
TmYb-3	$298.2 \pm 0.5$

**Table 6.7:** Fluorescence lifetime of the  $^1G_4$  manifold under in-direct excitation at 980 nm. Note: 50 ms pulses at 10 Hz were used to excite the  $^3F_4$  manifold in-directly.

The single exponential nature of the  $^1G_4$  decay provides information regarding the mechanisms dominating the  $^1G_4$  manifold population after the pump excitation has been removed. The time dependent rate equation describing the population of the  $^1G_4$  manifold is given by:

$$\frac{dN_{T3}(t)}{dt} = W_3 N_{Y1}(t) N_{T2}(t) - \frac{N_{T3}(t)}{\tau_{T3}}. \quad (6.23)$$

Although the solution to Equation 6.23 cannot be obtained without the knowledge of  $N_{T2}(t)$ , it is clear that the solution will contain several exponential components each with their own amplitude and characteristic time constant, resulting in a non-exponential decay waveform. However, the experimentally observed fluorescence decay waveforms were single exponential in nature with characteristic time constants consistent with the  $^1G_4$  manifold lifetime reported in Tm<sup>3+</sup>-doped silica fibres [24, 107]. It can therefore be concluded that the energy transfer rate into the  $^1G_4$  manifold is much less than the spontaneous decay. Therefore, the  $^1G_4$  manifold decay can be described by the single exponential function:

$$N_{T3}(t) = N_{T3}(0) \exp\left(-\frac{t}{\tau_{T3}}\right). \quad (6.24)$$

This is not a surprising result; the lifetime of the  $^3H_4$  manifold is relatively fast and hence, the likelihood of an excited ( $^3H_4$ ) Tm<sup>3+</sup> ion interacting with an excited ( $^2F_{5/2}$ ) Yb<sup>3+</sup> ion after the pump excitation has been removed is extremely low. The other important point is that the lifetime of the  $^1G_4$  manifold remains constant over the Yb<sub>2</sub>O<sub>3</sub> concentration range studied here, providing further evidence that the energy

transfer rate is negligible compared to the spontaneous decay. This also suggests that there is negligible energy back transfer from the  $^1G_4$  manifold of  $\text{Tm}^{3+}$  to the  $^2F_{5/2}$  manifold of  $\text{Yb}^{3+}$ .

Finally, the single exponential behaviour of the  $^1G_4$  manifold decay is expected for both direct and in-direct pumping schemes since the excited manifold is located  $\sim 5950 \text{ cm}^{-1}$  above the next lowest excited manifold ( $^3F_{2,3}$ ). The large energy gap between these two manifolds results in the fluorescence decay from the  $^1G_4$  manifold being dominated by radiative decay; therefore the decay should remain largely unaffected by the site-to-site variations caused by the amorphous nature of the glass. For completeness, the  $^1G_4$  manifold decay waveforms were fitted with the stretched exponential function to provide a comparison against the two other excited states studied in this work. Table 6.8 lists both the stretched exponential lifetime and power obtained from each fit. Note that the stretched exponential power is close to unity consistent with a near exponential decay.

Sample	$\tau_{SE}$ ( $\mu\text{s}$ )	SEP ' $p$ '
TmYb-1	$289.9 \pm 0.5$	$0.896 \pm 0.009$
TmYb-2	$292.7 \pm 0.3$	$0.917 \pm 0.008$
TmYb-3	$288.8 \pm 0.2$	$0.908 \pm 0.006$

**Table 6.8:** Characteristic lifetimes and stretched exponential powers obtained from the stretched exponential fit to the  $^1G_4$  manifold decay waveforms under in-direct pumping at 980 nm.

### 6.3.2.3 810 nm luminescence

The fluorescence decay properties of the 810 nm luminescence were studied in an effort to verify the existence of the two overlapping transitions from the  $^3H_4$  and  $^1G_4$  manifolds. The fluorescence decay of the  $^3H_4$  manifold under in-direct pumping at 980 nm is shown in Figure 6.16 for the TmYb-1 sample.

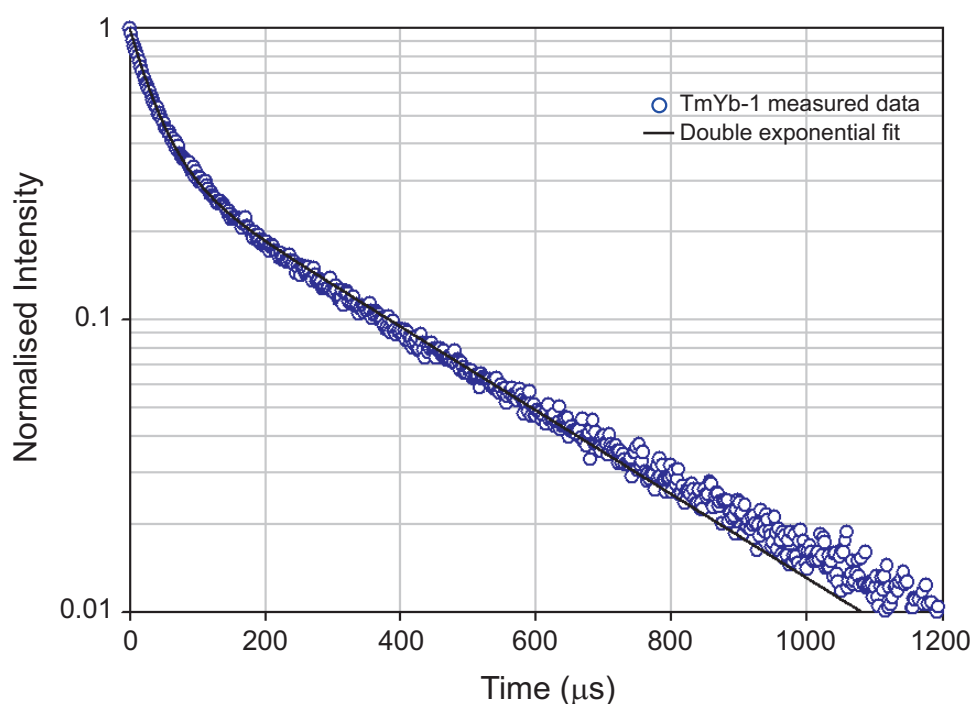


**Figure 6.16:** Semi-log plot of the normalised fluorescence decay at 810 nm under 980 nm excitation for sample TmYb-1. Note: decay waveforms were recorded using 50 ms pulses at a repetition rate of 10 Hz. The double exponential fit is discussed in the text.

The decay waveforms at 810 nm were described accurately by a double exponential function in the form of  $y = (1 - A) \exp(-x/B) + A \exp(-x/C)$ , where  $A$  was the fitting parameter describing the amplitude of the second exponential and  $B$  and  $C$  were the fitting parameters used to obtain the two characteristic lifetimes. The two characteristic lifetimes obtained from the double exponential fit are listed in Table 6.9 for the three co-doped fibres.

Sample	Amplitude $A$	Fast decay $B$ ( $\mu s$ )	Slow decay $C$ ( $\mu s$ )
TmYb-1	$0.355 \pm 0.001$	$37.1 \pm 0.2$	$302 \pm 1$
TmYb-2	$0.406 \pm 0.002$	$36.6 \pm 0.2$	$307 \pm 1$
TmYb-3	$0.434 \pm 0.002$	$30.9 \pm 0.2$	$301 \pm 1$

**Table 6.9:** Amplitude and characteristic lifetimes obtained from the double exponential fit of the 810 nm fluorescence decay for all three samples under in-direct pumping at 980 nm.

There are a number of possibilities as to the cause of the double exponential decay of the 810 nm fluorescence. The first possible cause is based on the assumption that

there are no overlapping transitions and that the 810 nm fluorescence originates solely from the  $^3H_4$  manifold. In this case, the double exponential behaviour may arise from the energy transfer process between  $Yb^{3+}$  and  $Tm^{3+}$  ions which populates the  $^3H_4$  manifold under 980 nm pumping. The time dependent rate equation describing the  $^3H_4$  manifold would then be given by:

$$\frac{dN_{T2}(t)}{dt} = W_2 N_{Y1}(t) N_{T1}(t) - \frac{N_{T2}(t)}{\tau_{T2}}. \quad (6.25)$$

Equation 6.25 can be solved using Equations 6.17 and 6.22 to obtain:

$$N_{T2}(t) = D \exp\left(-\frac{2t}{\tau_{Y1}}\right) + (N_{T2}(0) - D) \exp\left(-\frac{t}{\tau_{T2}}\right), \quad (6.26)$$

where

$$D = \frac{W_1 W_2 c_T \tau_{T1} \tau_{T2} N_{Y1}(0)^2 \tau_{Y1}^2}{(2\tau_{T2} - \tau_{Y1})(\tau_{Y1} - \tau_{T1})}. \quad (6.27)$$

Using this model, the double exponential solution would have two characteristic time constants; one being equal to the lifetime of the  $^3H_4$  manifold ( $\tau_2$ ) and the other being equal to  $(\frac{1}{2}\tau_{Y1})$ , i.e. one half of the  $^2F_{5/2}$  manifold lifetime. Based on the values reported in Tables 6.5 and 6.3, the decay is expected to exhibit a fast and slow component equivalent to  $\sim 20$  and  $\sim 410 \mu s$ , respectively. These time constants are not consistent with the those reported in Table 6.9; therefore it can be concluded that energy transfer up-conversion is not the cause of the non-exponential decay of the 810 nm luminescence.

The second potential cause of the double exponential decay is the presence of two overlapping transitions in the  $810 \pm 10$  nm window. It has been proposed throughout this chapter that the  $^1G_4 \rightarrow ^3H_5$  transition spectrally overlaps the  $^3H_4 \rightarrow ^3H_6$  transition. The fluorescence decay in such a case would exhibit the characteristics from each energy manifold. It was established in the previous section, that the  $^1G_4$  manifold decays in a single exponential form with a characteristic lifetime around  $\sim 300 \mu s$ . Assuming the  $^3H_4$  manifold exhibits similar characteristics

to the  $^1G_4$  manifold, i.e. the energy transfer rates which populate and depopulate the manifold are much less than the spontaneous decay, the resultant decay would be a double exponential with two characteristic time constants equivalent to the lifetimes of the  $^3H_4$  and  $^1G_4$  manifolds. The slow component of the 810 nm luminescence decay is in excellent agreement with the measured  $^1G_4$  manifold lifetime, whilst the fast component of the 810 nm decay is of the order of the  $^3H_4$  manifold lifetime. The  $^1G_4$  manifold contribution to the 810 nm luminescence may explain the increase in the amplitude of the slow component of the decay with increasing  $Yb_2O_3$  concentration. The  $^1G_4$  luminescence intensity was found to increase at a greater rate than the  $^3H_4$  luminescence with increasing  $Yb_2O_3$  concentration (refer to Figure 6.4), and hence the contribution the  $^1G_4$  manifold makes to the overall luminescence at 810 nm increases with increasing  $Yb_2O_3$  concentration. Therefore the amplitude associated with the slow component of the decay, which is attributed to the  $^1G_4$  manifold luminescence, will also increase with increasing  $Yb_2O_3$  concentration.

The slight deviation of the double exponential fit at very long times may be a result of the contribution of the energy transfer up-conversion rate into the  $^3H_4$  manifold; however this contribution is considered to be small in all three fibres studied since the luminescence from the  $^1G_4$  manifold dominates this effect. It can therefore be concluded with confidence that the luminescence at  $810 \pm 10$  nm under in-direct pumping at 980 nm is a result of the spectral overlap of two fluorescence transitions; one originating from the  $^3H_4$  manifold and the other from the  $^1G_4$  manifold. The study of the 1480 nm luminescence would provide much greater detail in regard to the energy transfer rates populating and depopulating the  $^3H_4$  manifold, but this can only be carried out in  $Tm^{3+}/Yb^{3+}$  -co-doped fibres with much higher  $Tm_2O_3$  concentrations.

## 6.4 Conclusion

The spectroscopic study of the  $\text{Tm}^{3+}/\text{Yb}^{3+}$  -co-doped system in alumino-silicate glass identified up-conversion luminescence in the visible and near infra-red regions under 980 nm excitation. The rate equation model used to describe the luminescence intensity as a function of incident pump power enabled the population dynamics of the system to be established. One of the important conclusions to be drawn from the analysis from the point of view of the S-band amplifying transition is that the lifetime and hence the quantum efficiency of the  ${}^3F_4$  manifold was found to increase by a factor of two, due to the energy transfer up-conversion from  $\text{Yb}^{3+}$  to  $\text{Tm}^{3+}$  ions. The increase in the  ${}^3F_4$  lifetime results in the manifold being a virtual ground state. Hence, for optical amplification to occur, efficient processes are required to remove the population from the  ${}^3F_4$  manifold to the  ${}^3H_4$  manifold. The steady state rate equation analysis established two energy transfer processes capable of depleting the  ${}^3F_4$  manifold and populating the  ${}^3H_4$  manifold. A double energy transfer up-conversion process and an excited state absorption process were identified as populating mechanisms in the co-doped system under 980 nm excitation. To the best knowledge of the author, this is the first time the ESA transition from the  ${}^3F_4 \rightarrow {}^3F_{2,3}$  manifold has been identified as a populating mechanism in the  $\text{Tm}^{3+}/\text{Yb}^{3+}$  -co-doped system. These two processes are the key to the  $\text{Tm}^{3+}/\text{Yb}^{3+}$  -co-doped system becoming an efficient S-band amplifying source. The other significant result to come from the analysis was that there was little evidence of energy back transfer from  $\text{Tm}^{3+}$  to  $\text{Yb}^{3+}$  ions under the direct pumping of the  ${}^3F_4$  and  ${}^3H_4$  manifolds.

The only drawback to the  $\text{Tm}^{3+}/\text{Yb}^{3+}$  -co-doped system is the presence of a third energy transfer up-conversion process which quenches population from the upper amplifying manifold to the  ${}^1G_4$  manifold. The rate of quenching from the  ${}^3H_4$  manifold has not been identified in this analysis; however from the fluorescence lifetime results it is considered to be significantly less than the  $\sim 3257 \text{ s}^{-1}$  decay rate of the  ${}^1G_4$  manifold.

## Chapter 7

### CONCLUSION

It was the intention of this work to study two possible techniques for improving the efficiency of the S-band amplifying transition of  $\text{Tm}^{3+}$  in silica based glasses. Significant improvements in the quantum efficiency of the S-band transition were realised by modifying the local environment of the  $\text{Tm}^{3+}$  ion through the incorporation of  $\text{Al}_2\text{O}_3$ . The addition of 9 mol % of  $\text{Al}_2\text{O}_3$  to the silica glass network resulted in an increase of  $\sim 260\%$  in the fluorescence lifetime the  ${}^3H_4$  manifold, when compared to the lifetime in pure silica glass, which is commensurate with an increase of  $\sim 260\%$  in the quantum efficiency of the S-band transition. A similar increase of  $\sim 175\%$  was observed from the  ${}^3F_4$  manifold. The maximum reported lifetimes of the  ${}^3H_4$  and  ${}^3F_4$  manifolds were 32.5 and 573  $\mu\text{s}$ , respectively. The increase in the lifetimes of both manifolds was attributed to the modified local environment surrounding the  $\text{Tm}^{3+}$  ion and the lower phonon energy of the Al-O bonds. The other network modifying elements studied in this work included germanium, antimony and tin; although considerable differences in the shapes and positions of the energy manifolds, particularly the  ${}^3F_4$  manifold, were observed their effect on the fluorescence lifetimes and quantum efficiency of the S-band transition were minimal, when compared to the aluminium co-doping results.

Further spectroscopic studies of the  $\text{Tm}^{3+}$  -doped alumino-silicate glasses found the well known cross relaxation process has a negligible effect on the  ${}^3H_4$  population for  $\text{Tm}_2\text{O}_3$  concentrations as high as 2900 ppm. The study also established the beneficial ( ${}^3F_4, {}^3F_4 \rightarrow {}^3H_4, {}^3H_6$ ) ETU process in silica based glasses for the first time. This process provides an alternative pumping scheme which can be used in conjunction with the traditional pumping techniques for the S-band amplifier in silica glass.

The second stage of the investigation into  $\text{Tm}^{3+}$  -doped silica based glasses involved the study of the non-exponential fluorescence decay characteristics of the  ${}^3H_4$  and  ${}^3F_4$  manifolds. The non-exponential behaviour from these manifolds was explained in terms of multi-phonon decay occurring across varying energy gaps caused by site-to-site variations in the silica glass network. A stretched exponential function was found to accurately describe the non-exponential behaviour from both excited state manifolds. The stretched exponential function enabled the degree of non-exponentiality to be compared between waveforms. The stretched exponential fitting technique was particularly useful when studying the fluorescence decay from excited manifolds dominated by multi-phonon decay, such as the  ${}^3H_4$  manifold. The exponentiality of the  ${}^3H_4$  manifold in the alumino-silicate glasses was found to decrease linearly with increasing  $\text{Al}_2\text{O}_3$  concentration. This effect was attributed to the increase in site-to-site variations and distribution of possible multi-phonon decay rates caused by the incorporation of  $\text{Al}_2\text{O}_3$  into the glass network. Although no quantitative information can be obtained from the analysis, the stretched exponential fitting of decays dominated by multi-phonon processes provides a simple technique for assessing the effects of co-doping in disordered host materials. It should be noted that this technique is not limited to  $\text{Tm}^{3+}$ ; other rare earth ions that have energy manifolds which are dominated by multi-phonon decay will also serve as excellent probing sources.

The second approach taken to improve the efficiency of the S-band transition was co-doping  $\text{Tm}^{3+}$  with the sensitising  $\text{Yb}^{3+}$  ion. The spectroscopic study of the  $\text{Tm}^{3+}/\text{Yb}^{3+}$  -co-doped system in alumino-silicate glass identified up-conversion luminescence in the visible and near infra-red regions under 980 nm excitation. A rate equation model was developed to determine the population mechanisms for the 475, 650 and 800, 1800 nm luminescence bands; the model accurately described the luminescence under both continuous wave and pulsed excitation. In regard to the S-band amplifying transition, a two fold increase in the quantum efficiency of the  ${}^3F_4$  manifold was realised under 980 nm excitation as a result of the energy transfer from  $\text{Yb}^{3+}$  to  $\text{Tm}^{3+}$  ions. Moreover, an ETU and ESA process was established which acts to remove the population from the  ${}^3F_4$  manifold to the  ${}^3H_4$  manifold and

increase the efficiency of the S-band transition. One of the main limitations of the  $\text{Tm}^{3+}/\text{Yb}^{3+}$  -co-doped system is the quenching of the  ${}^3H_4$  manifold population to the  ${}^1G_4$  manifold through a third ETU process. The system showed no signs of energy back transfer from  $\text{Tm}^{3+}$  to  $\text{Yb}^{3+}$  ions for  $\text{Yb}_2\text{O}_3$  concentration up to 1400 ppm. The positive results to come from the spectroscopic study of  $\text{Tm}^{3+}/\text{Yb}^{3+}$  in silica glass suggest this system may have an important role to play in the realisation of an efficient S-band optical fibre amplifier; however careful manipulation of the dopant concentrations and pumping wavelengths will be required in order to maximise the quantum efficiency of this transition in silica glass.

## 7.1 Suggestions for future work

Future work to arise from this body of work could include a detailed concentration study of  $\text{Tm}^{3+}$  in alumino-silicate glasses. One of the failings of this work was its inability to establish the cross relaxation and ETU co-efficients associated with the  $({}^3H_4, {}^3H_6 \rightarrow {}^3F_4, {}^3F_4)$  and  $({}^3F_4, {}^3F_4 \rightarrow {}^3H_4, {}^3H_6)$  processes in  $\text{Tm}^{3+}$  -doped silica glass. These important parameters can be obtained only through a thorough study of the  ${}^3H_4$  and  ${}^3F_4$  manifold lifetimes over a much larger  $\text{Tm}_2\text{O}_3$  concentration range than that studied here. The identification of these parameters in alumino-silicate glass will allow more accurate modelling of S-band amplification in these glass types.

Another important consideration, which may allow further improvements in the quantum efficiency of the S-band transition to be made, is the possible realisation of a fabrication technique which can incorporate large amounts of  $\text{Al}_2\text{O}_3$  ( $> 9$  mol%) without crystallisation of the aluminium salts. The fluorescence lifetimes of the  ${}^3H_4$  and  ${}^3F_4$  manifold showed a linear dependence on the  $\text{Al}_2\text{O}_3$  concentration, for  $\text{Al}_2\text{O}_3$  concentrations up to 9 mol% with, no sign of saturation. This suggests that further improvements can be realised with the incorporation of greater  $\text{Al}_2\text{O}_3$  concentrations. The technique used to fabricate the preforms and fibres in this investigation was limited by the solubility of the aluminium salts in the solution and the upper limit of the  $\text{Al}_2\text{O}_3$  concentration was placed at around 9 mol%.

The promising results obtained from the  $\text{Tm}^{3+}/\text{Yb}^{3+}$  -co-doped silica fibres suggest this system may have an important role to play in S-band amplification in the future. However, before this system can be identified as a possible solution for improving the S-band efficiency in silica glass, important spectroscopic parameters need to be identified. Recent theoretical modelling of a  $\text{Tm}^{3+}/\text{Yb}^{3+}$  -co-doped silica S-band amplifier suggest that significant gains, upward of 20 dB, can be achieved in silica glass through the careful manipulation of the  $\text{Tm}_2\text{O}_3$  and  $\text{Yb}_2\text{O}_3$  concentrations coupled with an optimised pumping scheme [148]. However, the theoretical treatment of this system was constrained by the limited spectroscopic parameters available in silica glass, in particular, the ETU rates relating to the first and second energy transfer steps. These rates were found to have a significant affect on the maximum gain of the amplifier; therefore to permit accurate modelling of this system, experimental energy transfer rates need to be identified in silica glass. The identification of the first energy transfer parameter can be determined easily by studying the fluorescence lifetime of the  ${}^2F_{5/2}$  manifold as a function of  $\text{Tm}_2\text{O}_3$  concentration. This experiment needs to be carried out at much greater  $\text{Tm}_2\text{O}_3$  concentrations than those studied here, an appropriate  $\text{Tm}_2\text{O}_3$  concentration study would range between 500 - 15 000 ppm. The determination of the second ETU co-efficient is a little more problematic but may still be obtained by studying the  ${}^3H_4$  manifold population as a function of incident pump power at various  $\text{Yb}_2\text{O}_3$  concentrations. The need to study the  ${}^3H_4$  population places an increased emphasis on detecting the light from the S-band transition; hence  $\text{Tm}_2\text{O}_3$  concentrations much greater than those studied here are required. From the experimental analysis,  $\text{Tm}_2\text{O}_3$  concentrations as high as 1950 ppm can be used without significant penalty from the Tm-Tm cross relaxation process. A suggested concentration range for the  $\text{Yb}_2\text{O}_3$  study would lie between 1000 and 20 000 ppm, considering the theoretical maximum gain in silica glass was realised with 3 000 ppm of  $\text{Tm}_2\text{O}_3$  and 15 000 ppm of  $\text{Yb}_2\text{O}_3$  under 1060 and 980 nm pumping [148].

The other important issue which needs to be addressed in this system is the management of the third up-conversion step which quenches population from the S-band

transition. Although little can be done in regard to the third ETU process, since the rate is assumed to be independent of dopant concentration and pumping wavelength, the potential for ESA from the  ${}^3H_4$  manifold needs to be taken into account. Based on the theoretical predictions and limited experimental data, it is anticipated that the S-band amplifier will require a dual wavelength pumping scheme, usually a 980 nm source to excite a high percentage of  $\text{Yb}^{3+}$  ions to the  ${}^2F_{5/2}$  manifold and an auxiliary source which is used to excite ions from the  ${}^3F_4$  manifold of  $\text{Tm}^{3+}$  to the upper amplifying  ${}^3H_4$  manifold. The wavelength selection of the auxiliary pump then becomes an important parameter in terms of the population dynamics of the system. To avoid unwanted ESA from the  ${}^3H_4$  manifold, the auxiliary pumping source should be implemented at wavelengths less than 1050 nm, given that longer wavelengths have a significantly greater probability of exciting  ${}^3H_4$  manifold ions into the  ${}^1G_4$  manifold (refer to Figure 6.9). This effect may be explored in greater detail by studying the relative populations of the  ${}^1G_4$  and  ${}^3H_4$  manifolds under various auxiliary pumping wavelengths from 1000 to 1150 nm.

The realisation of an efficient TDFA in silica glass is indeed a challenging task. This work has aimed to address some of the potential solutions towards improving the efficiency of the S-band transition of  $\text{Tm}^{3+}$ . The outcomes and future work to have arisen from this investigation provide optimism in our ability to meet this engineering challenge.

## BIBLIOGRAPHY

- [1] K. C. Kao and G. A Hockham. Dielectric fiber surface waveguides for optical frequencies. *Proc. IEE*, 113(7):1151–1158, 1966.
- [2] A. Werts. Propagation de la lumière cohérente dans les fibres optiques. *L'Onde Electrique*, 46:967–980, 1966.
- [3] J. Hecht. *Understanding Fibre Optics, Forth Edition*. Prentice-Hall, Upper Saddle River, USA, 2002.
- [4] J. C. Palais. *Fibre Optic Communications, Fifth Edition*. Prentice Hall International, Inc., New Jersey, 1998.
- [5] E. F. Schubert. *Light Emitting Diodes, Second Edition*. Cambridge University Press, United Kingdom, 2006.
- [6] R. J. Mears, L. Reekie, I. M. Jauncey, and D. N. Payne. Low-noise erbium-doped fibre amplifier at 1.54  $\mu\text{m}$ . *Electron. Lett.*, 23(19):1026–1028, 1987.
- [7] A. Bjarklev. *Optical Fiber Amplifiers: Design And System Applications*. Artech House, Boston, 1993.
- [8] Alcatel-Lucent achieves a world record 25.6 Terabit/s optical transmission, 2007. [online]. [Accessed 6th June 2007]. Available from the World Wide Web: <<http://www.alcatel-lucent.com>>.
- [9] M. N. Islam. Raman amplifiers for telecommunications. *IEEE J. Select. Topics Quantum Electron.*, 8:548559, 2002.
- [10] J. Hecht. S-band amplification challenges developers. *Laser Focus World*, 38(7):79–84, 2002.
- [11] P. Peterka, B. Faure, W. Blanc, M. Karasek, and B. Dussardier. Theoretical modelling of S-band thulium-doped silica fibre amplifiers. *Opt. Quantum Electron.*, 36(1-3):201–212, 2004.
- [12] J. B. Khurgin, I. Vurgaftman, J. R. Meyer, S. Xu, and J. U. Kang. Reduced crosstalk semiconductor optical amplifiers based on type-II quantum wells. *IEEE Photon. Technol. Lett.*, 14(3):278–280, 2002.
- [13] T. Yamatoya and F. Koyama. Optical preamplifier using optical modulation of amplified spontaneous emission in saturated semiconductor optical amplifier. *J. Lightwave Technol.*, 22(5):1290–1295, 2004.
- [14] M. N. Islam and M. Nietubyc. Raman amplification opens the S-band window. *Laser Focus World*, 3:53–62, 2001.

- [15] K. Rottwitt, M. Du Bromage, and A. J. Stentz. Design of distributed Raman amplifiers. In *Proc. of 26<sup>th</sup> European Conference on Optics and Communications*, page 4.4.1, Munich, September 2000.
- [16] J. Bromage. Raman amplification for fiber communications systems. *J. Lightwave Technol.*, 22(1):79–93, 2004.
- [17] S. Aozasa, T. Sakamoto, T. Kanamori, K. Hoshino, and M. Shimizu. Gain-shifted thulium-doped fibre amplifiers employing novel high concentration doping technique. *Electron. Lett.*, 36(5):418–419, 2000.
- [18] S. Aozasa, T. Sakamoto, T. Kanamori, K. Hoshino, K. Kobayashi, and M. Shimizu. Tm-doped fiber amplifiers for 1470-nm-band WDM signals. *IEEE Photon. Technol. Lett.*, 12(10):1331–1333, 2000.
- [19] B. Bourliaguet, F. Émond, A. C. Jacob-Poulin S. Mohrdiek, P.-Y. Cortês, and J. Lauzon. Thulium-doped fibre amplifier using 1055 nm laser diode pumping configuration. *Electron. Lett.*, 38(10):447–448, 2002.
- [20] R. M. Percival, D. Szebesta, and J. R. Williams. Highly efficient  $1.064\mu\text{m}$  upconversion pumped  $1.47\mu\text{m}$  thulium doped fluoride fibre laser. *Electron. Lett.*, 30(13):1057–1058, 1994.
- [21] T. Komukai, T. Yamamoto, T. Sugawa, and Y. Miyajima. Upconversion pumped thulium-doped fluoride fiber amplifier and laser operating at  $1.47\mu\text{m}$ . *IEEE J. Quant. Electron.*, 31(11):1880–1888, 1995.
- [22] S. Aozasa, H. Masuda, H. Ono, T. Sakamoto, T. Kanamori, Y. Ohishi, and M. Shimizu. 1480-1510 nm band Tm-doped fibre amplifier with high power conversion efficiency of 42%. *Electron. Lett.*, 37(19):1157–1158, 2001.
- [23] T. Kasamatsu, Y. Yano, and T. Ono. Gain-shifted dual wavelength pumped thulium-doped fiber amplifier for WDM signal in the  $1.48\text{--}1.51\mu\text{m}$  region. *IEEE Photon. Technol. Lett.*, 13(1):31–33, 2001.
- [24] A. S. L. Gomes, M. T. Carvalho, M. L. Sundheimer, C. J. A. Bastos-Filho, J. F. Martins-Filho, J. P. Von der Weid, and W. Margulis. Low-pump-power, short-fiber copropagating dual-pumped (800 and 1050 nm) thulium-doped fiber amplifier. *Opt. Lett.*, 28(5):334–336, 2003.
- [25] J. F. Martins-Filho, C. J. A. Bastos-Filho, M. T. Carvalho, M. L. Sundheimer, and A. S. L. Gomes. Dual-wavelength (1050+1550 nm) pumped thulium-doped fibre amplifier characterization by optical frequency-domain reflectometry. *IEEE Photon. Technol. Lett.*, 15(1):24–26, 2003.
- [26] F. Roy, F. Leplingard, L. Lorcy, A. Le Sauze, P. Baniel, and D. Bayart. 48% power conversion efficiency in single pump gain-shifted thulium-doped fiber amplifier. *Electron. Lett.*, 37(15):943–945, 2001.

- [27] F. Roy, A. Le Sauze, and D. Vallart. 0.8  $\mu\text{m}$  + 1.4  $\mu\text{m}$  pumping for gain-shifted TDFA with power conversion efficiency exceeding 50%. In *Tech. Digest of OAA*, page PD4, Italy, July 2001.
- [28] A. S. L. Gomes, M. T. Carvalho, and M. L. Sundheimer. Comparison of distributed gain in two dual-wavelength pumping schemes for thulium-doped fibre amplifiers. *Electron. Lett.*, 39(8):647–648, 2003.
- [29] T. Kasamatsu, Y. Yano, and T. Ono. Laser diode pumped highly efficient gain-shifted thulium-doped fiber amplifier operating in the 1480-1510nm band. *IEEE Photon. Technol. Lett.*, 13(5):433–435, 2001.
- [30] S. S. H. Yam, H. Inoue Y. Kubota, and K. Parameswaran. Novel pumping schemes for fluoride-based thulium-doped fiber amplifier at 690 and 1050 nm (or 1400 nm). *IEEE Photon. Technol. Lett.*, 17(5):1001–1003, 2005.
- [31] E. R. M. Taylor, L. N. Ng, J. Nilsson, R. Caponi, A. Pagano, M. Potenza, and B. Sordo. Thulium-doped tellurite fiber amplifier. *IEEE Photon. Technol. Lett.*, 16(3):777–779, 2004.
- [32] B. N. Samson, N. J. Traynor, D. T. Walton, A. J. G. Ellison, J. D. Minelly, J. P. Trentelman, and J. E. Dickinson. Thulium doped silicate fiber amplifier at 1460-1520nm. In *Optical Amplifiers and Their Applications, Optical Society of America, Trends in Optics and Photonics Series*, pages 247–249, Quebec, July 2000.
- [33] S. Ohara, N. Sugimoto, Y. Kondo, K. Ochiai, Y. Kuroiwa, Y. Fukasawa, T. Hirose, H. Hayashi, and S. Tanabe. Bi<sub>2</sub>O<sub>3</sub>-based glass for S-band amplification. *Proc. SPIE*, 4645:8–15, 2002.
- [34] B. Cole and M. L. Dennis. S-Band amplification in a thulium doped silicate fiber. In *OFC2001:(OSA, Washington DC, USA)*, page TuQ3, Anaheim, Los Angeles, 2001.
- [35] B. Faure. *Fabrication et caractérisation des fibres optiques en silice dopées au thulium:Influence de l'environnement des terres rares sur l'amplification dans la bande S*. PhD thesis, Université de Nice, 2005.
- [36] F. Roy, D. Bayart, A. Le Sauze, and P. Baniel. Noise and gain band management of thulium-doped fiber amplifier with dual-wavelength pumping schemes. *IEEE Photon. Technol. Lett.*, 13(8):788–790, 2001.
- [37] J. Kani, M. Jinno, and K. Oguchi. Fibre Raman amplifier for 1520 nm band WDM transmission. *Electron. Lett.*, 34(18):1745–1747, 1998.
- [38] S. D. Jackson and S. Mossman. Efficiency dependence on the Tm<sup>3+</sup> and Al<sup>3+</sup> concentrations for Tm<sup>3+</sup>-doped silica double-clad fiber lasers. *Appl. Opt.*, 42:2702–2707, 2003.

- [39] J. R. Lincoln, C. J. Mackechnie, J. Wang, W. S. Brocklesby, R. S. Deol, and A. Pearson. New class of fibre laser based on lead-germanate glass. *Electron. Lett.*, 28(11):1021–1022, 1992.
- [40] W. S. Brocklesby, J. E. Townsend, D. J. B Brink, and R. S. Brown. Non-radiative relaxation in Ta-doped silica fibers. *Opt. Mater.*, 3:205–208, 1994.
- [41] R. A Hewes and J. F. Sarver. Infrared excitation processes for the visible luminescence of  $\text{Er}^{3+}$ ,  $\text{Ho}^{3+}$  and  $\text{Tm}^{3+}$  in  $\text{Yb}^{3+}$ -sensitized rare earth trifluorides. *Phys. Rev.*, 182(2):427–436, 1969.
- [42] F. W. Ostermayer, J. P. van der Ziel, H. M. Marcos, L. G. Uitert, and J. E. Geusic. Frequency upconversion in  $\text{YF}_3:\text{Yb}^{3+},\text{Tm}^{3+}$ . *Phys. Rev. B*, 3(8):2698–2705, 1971.
- [43] Q. Y. Zhang, T. Li, Z. H. Jiang, X. H. Ji, and S. Buddhudu. 980 nm laser-diode-excited intense blue upconversion in  $\text{Tm}^{3+}/\text{Yb}^{3+}$ -co-doped gallate-bismuth-lead glasses. *Appl. Phys. Lett.*, 87(17):171911–171914, 2005.
- [44] S. Xu, H. Ma, D. Fang, Z. Zhang, and Z. Jiang. Upconversion luminescence and mechanisms in  $\text{Yb}^{3+}$ -sensitized  $\text{Tm}^{3+}$ -doped oxyhalide tellurite glasses. *J. Luminescence*, 117(2):135–140, 2006.
- [45] J. Mendez-Ramos, F. Lahoz, I. R. Martin, A. B. Soria, A. D. Lozano-Gorriñ, and V. D. Rodriguez. Optical properties and upconversion in  $\text{Yb}^{3+}$ - $\text{Tm}^{3+}$  co-doped oxyfluoride glasses and glass ceramics. *Mol. Phys.*, 101(7):1057–1065, 2003.
- [46] S. Sudo. *Optical Fiber Amplifiers: Materials, Devices, And Applications*. Artech House, Inc., Boston, 1997.
- [47] W. J. Miniscalco. Optical and electronic properties of rare earth ions in glasses. In M. J. F. Digonet, editor, *Rare Earth Doped Fiber Lasers and Amplifiers: 2nd Ed, revised and Expanded*. Marcek Dekker Inc., NY, 2001.
- [48] G. H Dieke. *Spectra And Energy Levels Of Rare Earth Ions In Crystals*. Wiley-Interscience, New York, 1968.
- [49] B. R Judd. *Operator Techniques in Atomic Spectroscopy*. McGraw-Hill, New York, 1963.
- [50] B. G Wybourne. *Spectroscopic Properties Of Rare Earths*. Wiley-Interscience, New York, 1965.
- [51] B. Di Bartolo. *Optical Interactions In Solids*. Wiley, New York, 1968.
- [52] S. Hufner. *Optical Spectroscopy Of Transparent Rare Earth Materials*. Academic Press, New York, 1978.
- [53] L. A. Riseberg and M. J. Weber. Relaxation phenomena in rare-earth luminescence. In *Progress in Optics*, North-Holland, 1976.

- [54] W. T. Carnall, P. R. Fields, and K. Rajnak. Electronic energy levels in the trivalent lanthanide aquo ions. I.  $\text{Pr}^{3+}$ ,  $\text{Nd}^{3+}$ ,  $\text{Pm}^{3+}$ ,  $\text{Sm}^{3+}$ ,  $\text{Dy}^{3+}$ ,  $\text{Ho}^{3+}$ ,  $\text{Er}^{3+}$  and  $\text{Tm}^{3+}$ . *J. Chem. Phys.*, 49(10):4424–4442, 1968.
- [55] A. Kiel. Multi-phonon spontaneous emission in paramagnetic crystals. In *Third International Conference on Quantum Electronics*, pages 765–772, 1963.
- [56] A. Kiel. *Paramagnetic Resonance*. Academic, New York, 1963.
- [57] L. A. Riseberg and H. W. Moos. Multiphonon orbit-lattice relaxation of excited states of rare earth ions in crystals. *Phys. Rev.*, 174:429–438, 1968.
- [58] R. Reisfeld and Jørgensen. Excited-State Phenomena In Vitreous Materials. In K. A. Gschneider and L. Eyring, editors, *Handbook On The Physics And Chemistry Of Rare-Earths*. Elsevier Science, Amsterdam, 1987.
- [59] A. Blumen, J. Klafter, and G. Zumofen. In I. Zschokke, editor, *Optical Spectroscopy Of Glasses*. Reidel, Netherlands, 1986.
- [60] S. D. Jackson. Cross relaxation and energy transfer upconversion processes relevant to the functioning of 2  $\mu\text{m}$   $\text{Tm}^{3+}$  -doped silica fibre lasers. *Opt. Commun.*, 230(1-3):197–203, 2004.
- [61] J. Y. Allain, M. Monerie, and H. Poignant. Red upconversion Yb-sensitized Pr fluoride fiber laser pumped in 0.8  $\mu\text{m}$  region. *Electron. Lett.*, 27(13):1156–1157, 1991.
- [62] X. Zou and H. Toratani. Dynamics and mechanisms of up-conversion processes in  $\text{Yb}^{3+}$  sensitized  $\text{Tm}^{3+}$  - and  $\text{Ho}^{3+}$  -doped fluorozirconaluminate glasses. *J. Non-Cryst. Solids*, 181(1-2):87–99, 1995.
- [63] J. E. Townsend, W. L. Barnes, and K. P. Jedrzejewski.  $\text{Yb}^{3+}$  sensitized  $\text{Er}^{3+}$  -doped silica optical fiber with ultrahigh transfer efficiency and gain. *Electron. Lett.*, 27(21):1958–1959, 1991.
- [64] D. C. Hanna, R. M. Percival, I. R. Perry, R. G. Smart, J. E. Townsend, and A. C. Tropper. Frequency upconversion in Tm- and Yb:Tm-doped silica fibers. *Opt. Commun.*, 78(2):187–194, 1990.
- [65] F. Auzel, G. Baldacchini, L. Laversenne, and G. Boulon. Radiation trapping and self-quenching analysis in  $\text{Yb}^{3+}$  -,  $\text{Er}^{3+}$  -, and  $\text{Ho}^{3+}$  -doped  $\text{Y}_2\text{O}_3$ . *Opt. Mater.*, 24(1-2):103–109, 2003.
- [66] F. Auzel. In B. DiBartolo, editor, *Spectroscopy Of Solid State Laser-Type Materials*. Plenum, New York, 1987.
- [67] B. Henderson and G. F. Imbush. *Optical Spectroscopy Of Inorganic Solids*. Clarendon Press, Oxford, 1989.

- [68] W. E. K. Gibbs and J. L. Holdsworth. Concentration quenching of fluorescence from the (P-3(0)+P-3(1)) manifold in heavily-doped  $\text{Pr}^{3+}$ : ZBLAN glasses. *J. Non-Cryst. Solids*, 344(3):167–169, 2004.
- [69] M. J. F. Digonnet. Broadband fiber sources. In M. J. Digonnet, editor, *Rare Earth Doped Fiber Amplifiers, Second Edition*. Marcel Dekker Inc., New York, 2001.
- [70] B. M. Walsh and N. P. Barnes. Comparison of Tm:ZBLAN and Tm: silica fiber lasers; Spectroscopy and tunable pulsed laser operation around 1.9  $\mu\text{m}$ . *Appl. Phys. B*, 78:325–333, 2004.
- [71] A. S. L. Gomes, C. B. de Araujo, B. J. Ainslie, and S. P. Craig-Ryan. Amplified spontaneous emission in  $\text{Tm}^{3+}$  -doped monomode optical fibers in the visible region. *Appl. Phys. Lett.*, 57(21):2169–2171, 1990.
- [72] R. Vallée P. Laperle and A. Chandonnet. Thulium-doped ZBLAN fiber laser. *Proc. SPIE*, 3611:228–239, 1999.
- [73] A. Tropper, R. Smart, I. Perry, D. Hanna, J. Lincoln, and B. Brocklesby. Thulium-doped silica fiber lasers. *SPIE Fibre Laser Sources and Amplifiers*, 1373:152–157, 1990.
- [74] G. Frith, D. G. Lancaster, and S. D. Jackson. 85 W  $\text{Tm}^{3+}$  -doped silica fibre laser. *Electron. Lett.*, 41(12):687–688, 2005.
- [75] R. G. Smart, J. N. Carter, A. C. Tropper, and D. C. Hanna. Continuous-wave oscillation of  $\text{Tm}^{3+}$  -doped fluorozirconate fibre lasers at around 1.47  $\mu\text{m}$ , 1.9  $\mu\text{m}$  and 2.3  $\mu\text{m}$  when pumped at 790 nm. *Opt. Commun.*, 82:563–570, 1991.
- [76] L. Esterowitz, R. Allen, I. Aggarwal, and R. J. Ginther. Pulsed laser emission at 2.3  $\mu\text{m}$  in a thulium-doped fluorozirconate fibre. *Electron. Lett.*, 24:1104–1106, 1988.
- [77] J. Y. Allain, M. Monerie, and H. Poignant. Tunable cw lasing around 0.82, 1.48, 1.88 and 2.35  $\mu\text{m}$  in thulium-doped fluorozirconate fibre. *Electron. Lett.*, 26:1660–1662, 1989.
- [78] J. N. Carter, R. G. Smart, D. C. Hanna, and A. C. Tropper. Lasing and amplification in the 0.8  $\mu\text{m}$  region in thulium-doped fluorozirconate fibres. *Electron. Lett.*, 26:1759–1761, 1990.
- [79] R. G. Smart. 20 dB gain thulium-doped fluorozirconate fiber amplifier operating at around 0.8  $\mu\text{m}$ . *Electron. Lett.*, 27:1123–1124, 1991.
- [80] S. A. Wade, S. F. Collins, and G. W. Baxter. Fluorescence intensity ratio technique for optical fiber point temperature sensing. *J. Appl. Phys.*, 94(8):4743–4756, 2003.
- [81] J. Y. Allain, M. Monerie, and H. Poignant. Blue upconversion fluorozirconate fibre laser. *Electron. Lett.*, 26:166–168, 1990.

- [82] B. M. Antipenko, S. P. Voronin, and T. A. Privalova. New laser channels of the  $\text{Tm}^{3+}$  ion. *Opt. Spectrosc.*, 68:164–166, 1990.
- [83] R. Paschotta, J. Nilsson, P. R. Barber, J. E. Caplen, A. C. Tropper, and D. C. Hanna. Lifetime quenching in Yb-doped fibers. *Opt. Commun.*, 136:375–378, 1997.
- [84] V. Gaponstev and K. William. Fiber lasers grow in power. *Laser Focus World*, 38:8385, 2002.
- [85] D. C. Hanna, I. R. Perry, J. R. Lincoln, and J. E. Townsend. A 1-Watt thulium-doped cw fibre laser operating at  $2\mu\text{m}$ . *Opt. Commun.*, 80(1):52–56, 1990.
- [86] G. G. Vienne, W. S. Brocklesby, R. S. Brown, Z. J. Chen, J. D. Minelly, J. E. Roman, and D. N. Payne. Role of aluminum in ytterbium-erbium co-doped phosphoaluminosilicate optical fibers. *Opt. Fiber Technol., Mater. Devices Syst.*, 2(4):387–393, 1996.
- [87] S. Tanabe and T. Hanada. Local structure and  $1.5\mu\text{m}$  quantum efficiency of erbium-doped glasses for optical amplifiers. *J. Non-Cryst. Solids*, 196:101–105, 1996.
- [88] B. J. Cole. *Optimization of  $\text{Tm}^{3+}$  in silica for use as active fibre devices*. PhD Thesis, University of New Jersey, 1996.
- [89] F. Hossain. Images of the atomic structure of  $\text{SiO}_2$  and silica glass were drawn using a standard material visualisation program. 2006.
- [90] W. H. Zachariasen. Atomic arrangement in glass. *J. Am. Chem. Soc.*, 54:3841–3851, 1932.
- [91] W. J. Miniscalco. Erbium-doped glasses for fiber amplifiers at 1500 nm. *J. Lightwave Technol.*, 9(2):234–250, 1991.
- [92] K. Arai, H. Namikawa, K. Kumata, T. Honda, Y. Ishii, and T. Handa. Aluminium or phosphorus co-doping effects on the fluorescence and structural properties of neodymium-doped silica glass. *J. Appl. Phys.*, 59(10):3430–3436, 1986.
- [93] S. P. Craig-Ryan, J. F. Massicott, M. Wilson, B. J. Ainslie, and R. Wyatt. Optical study of low concentration  $\text{Er}^{3+}$  fibres for efficient power amplifiers. *Proc. ECOC'90:(OSA, Washington DC, USA)*, 1:571–574, 1990.
- [94] S. R. Nagel, J. B. MacChesney, and K. L. Walker. An overview of the modified chemical vapor deposition (MCVD) process and performance. *IEEE J. Quant. Electron.*, 18(4):459–476, 1982.
- [95] J. Ganem, J. Crawford, P. Schmidt, N. W. Jenkins, and S. R. Bowman. Thulium cross-relaxation in a low phonon energy crystalline host. *Phys. Rev. B*, 60(24):245101, 2002.

- [96] R. S. Quimby. Quantum efficiency of 1460 nm transition and energy transfer in  $\text{Tm}^{3+}$  -doped glass. *J. Appl. Phys.*, 90(4):1683–1687, 2001.
- [97] A. Sennaroglu, A. Kurt, and G. Ozen. Effect of cross relaxation on the 1470 and 1800 nm emissions in  $\text{Tm}^{3+}:\text{TeO}_2\text{-CdCl}_2$  glass. *J. Phys.:Condens. Matter*, 16(5):2471–2478, 2004.
- [98] M. J. Lochhead and K. L. Bray. Rare-Earth Clustering and Aluminum Codoping in Sol-Gel Silica: Investigation using europium(III) fluorescence spectroscopy. *Chem. Mater.*, 7:572–577, 1995.
- [99] B. J. Ainslie, S. P. Craig, and S. T. Davey. The fabrication and optical properties of  $\text{Nd}^{3+}$  in silica-based optical fibers. *Mater. Lett.*, 5:143–146, 1987.
- [100] J. Minelly and A. Ellison. Applications of antimony-silicate glasses for fiber optic amplifiers. *Optical Fiber Technology*, 8(4):123–138, 2002.
- [101] S. D Jackson and T. A. King. Theoretical modeling of Tm-doped silica fiber lasers. *J. Lightwave Technol.*, 17(5):948–956, 1999.
- [102] B. Faure, W. Blanc, B. Dussardier, G. Monnom, and P. Peterka. Thulium-doped silica-fiber based S-band amplifier with increased efficiency by aluminium co-doping. In *Technical Digest of Optical Amplifiers and Their Applications*, page OWC2, San Francisco, 2004.
- [103] F. Wu. *Rare earth doping of silica based optical fibre by the sol-gel method*. PhD thesis, Rutgers University, 1994.
- [104] D. J. T. DiGiovanni and J. B. MacChesney. A new optical fiber fabrication technique using sol-gel dipcoating. In *OSA Technical Digest Series:(OSA, Washington DC, USA)*, page WA2, 1991.
- [105] S. Boj, E. Delevaque, J. Y. Allain, J. F. Bayon, P. Niay, and P. Bernage. High efficiency diode pumped thulium-doped silica fibre lasers with intracore Bragg gratings in the 1.9 - 2.1  $\mu\text{m}$  band. *Electron. Lett.*, 30(13):1019–1020, 1994.
- [106] G. N. van den Hoven, E. Snoeks, A. Polman, C. van Dam, J. W. M. van Uffelen, and M. K. Smit. Upconversion in Er-implanted  $\text{Al}_2\text{O}_3$  waveguides. *J. Appl. Phys.*, 73(3):1258–1266, 1996.
- [107] J. R. Lincoln, W. S. Brocklesby, F. Cusso, J. E. Townsend, A. C. Tropper, and A. Pearson. Time resolved and site selective spectroscopy of thulium doped into germano- and alumino-silicate optical fibres and preforms. *J. Luminescence*, 50:297–308, 1991.
- [108] M. Inokuti and F. Hirayama. Influence of energy transfer by the exchange mechanism on donor luminescence. *J. Chem. Phys.*, 43(6):1978–1989, 1965.
- [109] D. L. Dexter, T. Forster, and R. S. Knox. Radiationless transfer of energy of electronic excitation between impurity molecules in crystals. *Physica Status Solidi*, 21(5):836–850, 1952.

- [110] T. Förster. Energy transfer and fluorescence between molecules. *Ann. Phys.*, 437(1-2):55–75, 1948.
- [111] A. Brenier, C. Pedrini, B. Moine, J. L. Adam, and C. Pledel. Fluorescence mechanisms in  $\text{Tm}^{3+}$ -singly doped and  $\text{Tm}^{3+}$ -,  $\text{Ho}^{3+}$ - doubly doped indium-based fluoride glasses. *Phys. Rev. B*, 41(8):5364–5371, 1990.
- [112] I. R. Martin, V. D. Rodriguez, R. Alcalá, and R. Cases. Cross-relaxation for  $\text{Tm}^{3+}$  ions in indium-based glasses. *J. Non-Cryst. Solids*, 61:294–296, 1993.
- [113] G. Dominiak-Dzik, W. Ryba-Romanowski, S. Golab, and A. Pajaczkowska. Thulium-doped  $\text{Ca}_4\text{GdO}(\text{BO}_3)_3$  crystals. An investigation of radiative and non-radiative processes. *J. Phys.:Condens. Matter*, 12(25):5495–5505, 2000.
- [114] J. R. Lincoln. *Spectroscopy of rare earth doped glasses*. PhD thesis, University of Southampton, 1992.
- [115] W. E. K. Gibbs, D. J. Booth, and V. K. Bogdanov. Population dynamics of the  ${}^3F_4$  and  ${}^3H_4$  levels in highly-doped  $\text{Tm}^{3+}:\text{ZB(L)AN}$  glasses. *J. Non-Cryst. Solids*, 353:1–5, 2007.
- [116] H. Kalaycioglu, A. Sennaroglu, A. Kurt, and G. Ozen. Spectroscopic analysis of  $\text{Tm}^{3+}:\text{LuAG}$ . *J. Phys.:Condens. Matter*, 19(3):036208, 2007.
- [117] J. B. Gruber, M. E. Hills, R. M. Macfarlane, C. A. Morrison, G. A. Turner, G. J. Quarles, G. J. Kintz, and L. Esterowitz. Spectra and energy levels of  $\text{Tm}^{3+}:\text{Y}_3\text{Al}_5\text{O}_{12}$ . *Phys. Rev. B*, 40(14):9464–9478, 1989.
- [118] J. B. Gruber, M. D. Seltzer, M. E. Hills, S. B. Stevens, C. A., and J. Morrison. Energy levels and upconversion fluorescence in trivalent thulium-doped yttrium scandium aluminum garnet. *J. Appl. Phys.*, 74(4):1929–1935, 1993.
- [119] H. P. Jenssen, A. Linz, R. P. Leavitt, C. A. Morrison, and D. E. Wortmann. Analysis of the optical spectrum of  $\text{Tm}^{3+}$  in  $\text{LiYF}_4$ . *Phys. Rev. B*, 11(1):92–101, 1975.
- [120] C. Xueyuan and L. Zundu. Spectroscopic characteristics, magnetic properties and fluorescence dynamics of  $\text{Tm}^{3+}$  in  $\text{YVO}_4$  crystal. *J. Phys.:Condens. Matter*, 9(38):7981–7997, 1997.
- [121] L. D. Merkle, J. B. Gruber, M. D. Seltzer, S. B. Stevens, and T. H. Allik. Spectroscopic analysis of  $\text{Tm}^{3+}:\text{NaLa}(\text{MoO}_4)_2$ . *J. Appl. Phys.*, 72(9):4269–4274, 1992.
- [122] L. B. Shaw and N. Djeu R. S. F. Chang. Measurement of up-conversion energy-transfer probabilities in  $\text{Ho}:\text{Y}_3\text{Al}_5\text{O}_{12}$  and  $\text{Tm}:\text{Y}_3\text{Al}_5\text{O}_{12}$ . *Phys. Rev. B*, 50(10):6609–6619, 1994.
- [123] D. L. Dexter and J. H. Schulman. Theory of concentration quenching in inorganic phosphors. *J. Chem. Phys.*, 22:1063–1070, 1964.

- [124] M. Yokota and O. Tanimoto. Effects of diffusion on energy transfer by resonance. *J. Phys. Soc. Japan*, 22(3):779–784, 1967.
- [125] D. A. Simpson, G.W. Baxter, S.F. Collins, W.E.K. Gibbs, W. Blanc, B. Dusardier, and G. Monnom. Energy transfer up-conversion in  $\text{Tm}^{3+}$ -doped silica fiber. *J. Non-Cryst. Solids*, 352:136–141, 2006.
- [126] M. J. Weber. Luminescence decay by energy migration and transfer: Observation of diffusion-limited relaxation. *Phys. Rev. B*, 4(9):2932–2939, 1971.
- [127] K. B. Eisenthal and S. Siegel. Influence of resonance transfer on luminescence decay. *J. Chem. Phys.*, 41:652–655, 1965.
- [128] M. Bettinelli, F. S. Ermeneux, R. Moncorgé, and E. Cavalli. Fluorescence dynamics of  $\text{YVO}_4:\text{Tm}^{3+}$ ,  $\text{YVO}_4:\text{Tm}^{3+}, \text{Tb}^{3+}$  and  $\text{YVO}_4:\text{Tm}^{3+}, \text{Ho}^{3+}$  crystals. *J. Phys.:Condens. Matter*, 10:8207–8215, 1998.
- [129] V. A. French, R. R. Petrin, and R. C. Powell. Energy-transfer processes in  $\text{Y}_3\text{Al}_5\text{O}_{12}:\text{Tm}, \text{Ho}$ . *Phys. Rev. B*, 46(13):8018–8026, 1992.
- [130] C. Guery, J. L. Adam, and J. Lucas. Optical properties of  $\text{Tm}^{3+}$  ions in indium-based fluoride glasses. *J. Luminescence*, 42:181–189, 1988.
- [131] E. Desurvire. Erbium-doped fiber amplifiers: Basic principles and theoretical modeling. *Int. J. High-Speed electron.*, 2(1-2):89–114, 1991.
- [132] E. Desurvire, J. L. Zyskind, and Simpson J. R. Spectral gain hole-burning at  $1.53 \mu\text{m}$  in erbium-doped fiber amplifiers. *IEEE Photon. Technol. Lett.*, 2(4):246–248, 1990.
- [133] J. L. Zyskind, E. Desurvire, J. W. Sulhoff, and DiGiovanni D. Dertermination of homogeneous linewidth by spectral gain hole-burning in an erbium-doped fiber amplifier with a  $\text{GeO}_2\text{-SiO}_2$  core. *IEEE Photon. Technol. Lett.*, 2(12):869–871, 1990.
- [134] A. S. S. de Camargo, S. L. de Oliveira, D. F. de Sousa, L. A. O. Nunes, and D. W. Hewak. Spectroscopic properties and energy transfer parameters of  $\text{Tm}^{3+}$  ions in gallium lanthanum sulfide glass. *J. Phys.:Condens. Matter*, 14:9495–9505, 2002.
- [135] R. J. Thrash and L. F. Johnson. Upconversion laser emission from  $\text{Yb}^{3+}$  -sensitized  $\text{Tm}^{3+}$  in  $\text{BaY}_2\text{F}_8$ . *J. Opt. Soc. Am. B*, 11(5):881–885, 1994.
- [136] M. A. Noginov, M. Curley, P. Venkateswarlu, A. Williams, and H. P. Jenssen. Excitation scheme for the upper energy levels in a  $\text{Tm}:\text{Yb}:\text{BaY}_2\text{F}_8$  laser crystal. *J. Opt. Soc. Am. B*, 14(8):2126–2136, 1997.
- [137] F. C. Guinhos, P. C. Nobrega, and P. A. Santa-Cruz. Compositional dependence of up-conversion process in  $\text{Tm}^{3+}/\text{Yb}^{3+}$  -codoped oxyfluoride glasses and glass-ceramics. *J. Alloys Comp.*, 323-324:358–361, 2001.

- [138] I. A. Grishin, V. A. Gur'ev, and A. P. Savikin. Visible luminescence of the fluoride glass ZBLAN with thulium and ytterbium under IR diode laser pumping. *Optics and Spectroscopy*, 93(5):709–713, 2002.
- [139] B. Peng and T. Izumitani. Blue, green and 0.8  $\mu\text{m}$   $\text{Tm}^{3+}$ -,  $\text{Ho}^{3+}$  -doped upconversion laser glasses, sensitized by  $\text{Yb}^{3+}$ . *Electron. Lett.*, 4(6):701–711, 1995.
- [140] F. Yan, C. Xiaobo, S. Feng, L. Kun, and Z. Guangyin. Upconversion luminescence of ZBLAN: $\text{Tm}^{3+}$ ,  $\text{Yb}^{3+}$  glass pumped by a 970 nm LD and its concentration effect. *Proc. SPIE*, 3551:116–120, 1998.
- [141] R. Caspary, M. M. Kozak, D. Goebel, and W. Kowalsky. Excited state absorption spectroscopy for thulium-doped zirconium fluoride fiber. *Opt. Commun.*, 259(1):154–157, 2006.
- [142] T. Tamaoka, S. Tanabe, S. Ohara, H. Hayashi, and N. Sugimoto. Fabrication and blue upconversion characteristics of Tm-doped tellurite fiber for S-band amplifier. *J. Alloys Comp.*, 408:848–851, 2006.
- [143] Y. H. Tsang, D. J. Coleman, and T. A. King. High power 1.9  $\mu\text{m}$   $\text{Tm}^{3+}$ -silica fibre laser pumped at 1.09  $\mu\text{m}$  by a  $\text{Yb}^{3+}$ -silica fibre laser. *Opt. Commun.*, 231(1-6):357–364, 2004.
- [144] Y. L. Mao, F. Ding, C. S. Wang, P. Z. Deng, and F. X. Gan. Cooperative luminescence in Yb:YAG crystals. *Spectroscopy and spectral analysis*, 25(8):1199–1202, 2005.
- [145] X. Xua, Z. Zhaoa, P. Songa, B. Jianga, G. Zhoua, J. Xua, P. Denga, G. Bourdetc, J. C. Chanteloupc, J. P. Zouc, and A. Fulop. Upconversion luminescence in  $\text{Yb}^{3+}$  -doped yttrium aluminum garnets. *Physica B*, 357:365–369, 2005.
- [146] E. Nakazawa and S. Shionoya. Cooperative luminescence in  $\text{YbPO}_4$ . *Phys. Rev. Lett.*, 25(25):1710–1712, 1970.
- [147] R. Paschotta, J. Nilsson, A. C. Tropper, and D. C. Hanna. Ytterbium-doped fiber amplifiers. *IEEE J. Quant. Electron.*, 33(7):1049–1056, 1997.
- [148] J. Chang, Q. P. Wang, and G. D. Peng. Optical amplification in  $\text{Yb}^{3+}$  -co-doped thulium-doped silica fiber. *Opt. Mater.*, 28:1088–1094, 2006.

## Appendix A

### LIST OF PUBLICATIONS

Throughout the duration of this thesis, numerous publications were generated. Work was presented in oral and poster form at both international and national conferences. Other publications that the author contributed to are also shown. Journal articles and conference proceedings are listed chronologically, with the most recent first.

#### A.1 Journal articles

**D. A. Simpson**, W. E. K. Gibbs, G. W. Baxter, S. F. Collins, W. Blanc, B. Dussardier and G. Monnom. Energy transfer up-conversion in  $\text{Tm}^{3+}$  -doped silica fibre. *J. Non-Cryst. Solids*, 352:136-141, 2006.

#### A.2 International Conferences

W. Blanc, P. Peterka, B. Faure, B. Dussardier, G. Monnom, I. Kak, J. Kanka, **D. A. Simpson** and G. W. Baxter. Characterization of thulium-doped silica-based optical fibre for S-band amplifier. *Photonics Prague 2005 - Photonics, Devices, and Systems III, Proc. SPIE*, 6180:181-186, 2006.

**D. A. Simpson**, G. W. Baxter, S. F. Collins, W. E. K. Gibbs, W. Blanc, B. Dussardier and G. Monnom. Energy transfer processes related to the S-Band transition in  $\text{Tm}^{3+}$  -doped silica fibres. *Proc. 31st European Conference on Optical Communication (ECOC), Glasgow UK* 3:759-760, 2005.

**D. A. Simpson**, T. B. Nguyen, G. W. Baxter, S. F. Collins, B. Faure, W. Blanc, B. Dussardier, G. Monnom and P. Peterka. Thulium-doped silica fiber for S-band amplifiers: pump power and host composition effect on the  ${}^3H_4 \Rightarrow {}^3F_4$  band. *EPS-QEOD Europhoton Conference 2004, Lausanne, Switzerland*, ISBN 2-914771-18-5, WeC14, 2004.

### A.3 National Conferences

**D. A. Simpson**, W. E. K Gibbs, G. W. Baxter, S. F. Collins, T. B. Nguyen, W. Blanc, B. Dussardier and G. Monnom. Tm<sup>3+</sup>/Yb<sup>3+</sup> -co-doped alumino-silicate fibre: potential for S-band optical amplification. *Proc. International Conference on the Optical Internet held jointly with the 32nd Australian Conference on Optical Fibre Technology, Melbourne, CD-ROM: "COIN-ACOFT 2007 Conference" ISBN 978-0-9775657-3-3 (COIN-ACOFT, Melbourne Australia)*, Oral paper no. TuB2-2, 2007.

**D. A. Simpson**, G. W. Baxter, S. F. Collins, W. E. K. Gibbs, W. Blanc, B. Dussardier and G. Monnom. Energy transfer up-conversion in Tm-doped silica fibres. *16th Biennial Congress of the Australian Institute of Physics incorporating the Conference of the Australian Optical Society, Canberra*, Abstracts p. 104, 2005.

**D. A. Simpson**, G. W. Baxter, S. F. Collins, W. E. K. Gibbs, W. Blanc, B. Dussardier and G. Monnom. Energy transfer processes in Tm<sup>3+</sup> -doped silica fibres relevant to an S-band amplifier. *30th Australian Conference on Optical Fibre Technology, Sydney, CD-ROM: "BGPP/ACOFT 2005" ISBN 1 877040 33 9*, Oral paper no. 327-329, 2005.

**D. A. Simpson**, G. W. Baxter, S. F. Collins, B. Dussardier, G. Monnom and W. Blanc. Host composition effects on the luminescence decay of the  ${}^3F_4$  and  ${}^3H_4$  energy levels of Tm<sup>3+</sup>-doped silica fibres. *CD-ROM: 7th Australasian Conference on Optics, Lasers and Spectroscopy, Rotorua New Zealand*, Abstracts ThP50, 2005.

V. Zeqaj, **D. A. Simpson**, T. B. Nguyen, G. W. Baxter, S. F. Collins, W. Blanc, B. Dussardier and G. Monnom. Absorption and emission characteristics of thulium doped silica fibre. *CD-ROM: 7th Australasian Conference on Optics, Lasers and Spectroscopy, Rotorua New Zealand*, Abstracts ThP61, 2005.

**D. A. Simpson**, G. W. Baxter, S. F. Collins, B. Dussardier, G. Monnom, B. Faure, P. Peterka and W. Blanc. Pump power and host composition effects on the  $^3H_4$  and  $^3F_4$  energy levels in thulium doped silica fibres. *Australasian Conference on Optics, Lasers and Spectroscopy 2003, Melbourne*, Abstracts 275, 2003.

**D. A. Simpson**, G. W. Baxter, S. F. Collins, B. Dussardier, G. Monnom, B. Faure, P. Peterka and W. Blanc. Annealing effects on the  $3H_4$  energy level in thulium doped silica fibres. *Australasian Conference on Optics, Lasers and Spectroscopy 2003, Melbourne*, Abstracts 276, 2003.